



HAL
open science

Numerical simulations of planet-forming disks : theoretical predictions for observational interpretation

Clément Robert

► **To cite this version:**

Clément Robert. Numerical simulations of planet-forming disks : theoretical predictions for observational interpretation. Galactic Astrophysics [astro-ph.GA]. Université Côte d'Azur, 2020. English. NNT : 2020COAZ4071 . tel-03197898

HAL Id: tel-03197898

<https://theses.hal.science/tel-03197898>

Submitted on 14 Apr 2021

HAL is a multi-disciplinary open access archive for the deposit and dissemination of scientific research documents, whether they are published or not. The documents may come from teaching and research institutions in France or abroad, or from public or private research centers.

L'archive ouverte pluridisciplinaire **HAL**, est destinée au dépôt et à la diffusion de documents scientifiques de niveau recherche, publiés ou non, émanant des établissements d'enseignement et de recherche français ou étrangers, des laboratoires publics ou privés.

THÈSE DE DOCTORAT

Simulations numériques de disques protoplanétaires Prédictions théoriques pour interprétation observationnelle

Clément M.T. Robert

Laboratoire Lagrange, Observatoire de la Côte d'Azur

Présentée en vue de l'obtention du grade de docteur
en Sciences de la Planète et de l'Univers
de l'Université Côte d'Azur
Dirigée par : Héloïse Méheut
Co-encadrée par : François Ménard
Soutenue le : 19 novembre 2020

Devant le jury, composé de :
Clément Baruteau, Chargé de Recherche
Richard Nelson, Professor of Astronomy & Mathematics
Myriam Benisty, Astronome adjointe
Sylvie Cabrit, Astronome

Simulations numériques de disques protoplanétaires

Prédictions théoriques pour interprétation observationnelle

Jury

Rapporteurs

Dr. Clément Baruteau, Chargé de Recherche,
Institut de Recherche en Astrophysique et Planétologie

Pr. Richard Nelson, Professor of Astronomy & Mathematics,
Queen Mary University of London

Examinatrices

Dr. Myriam Benisty, Astronome Adjointe,
Institut de Planétologie et d'Astrophysique de Grenoble

Dr. Sylvie Cabrit, Astronome de 1ère classe,
Laboratoire d'Etude du Rayonnement et de la Matière en Astrophysiques et Atmosphères

Résumé et mots clés

Abstract and keywords

Titre : Simulations numériques de disques protoplanétaires, Prédictions théoriques pour interpretation observationnelle

Résumé : A ce jour, plusieurs milliers de planètes ont été identifiées hors de notre propre système solaire. Leur formation n'est donc pas un événement rare. On connaît également nombre de très jeunes étoiles en pleine formation, entourées de reliquats de gaz et de poussière, prenant la forme de disques sous l'action de la force centrifuge. C'est dans ces disques que les planètes naissent, accumulant la matière environnante. Si les différentes étapes de la croissance de ces agrégats, de grains micrométriques jusqu'à des dimensions planétaires sont relativement bien identifiées, de nombreux obstacles parsèment ce chemin. En effet, les solides de petites tailles ont tendance à accrêter rapidement (en quelques millions d'années) sur l'étoile. C'est aussi le cas (mais pour des raisons différentes) des objets de masses planétaires, qui cèdent leur moment cinétique au disque qui entour l'étoile. Dans cette thèse, j'étudie des solutions possibles à de tels problèmes au moyen de simulations hydrodynamiques. Je montre que, contrairement à une idée reçue, la migration des planètes géantes n'accompagne pas le transport visqueux du disque. De plus, je mets en évidence que l'accrétion de la planète elle-même n'affecte pas significativement sa vitesse de migration. Ensuite, je traite d'un scénario favorable à l'agrégation constructive de la poussière, à savoir les vortex de Rossby, dont l'existence est encore débattue du fait d'un manque de contrainte observationnelle. Je montre que de telles structures pourraient être identifiées à travers plusieurs observables, parmi lesquelles les signatures dynamiques par effet Doppler. En m'appuyant sur un post-traitement par transfert radiatif, je prédis en outre des signatures détectables par des observations interférométriques de l'émission thermique, ainsi que les structures polarimétriques attendues pour ces vortex. Enfin, je consacre un ultime chapitre à la description de mes plus importantes contributions aux logiciels libres que j'ai utilisé au cours de ma thèse.

Mots clés : disques protoplanétaires, formation planétaire, simulation numérique, hydrodynamique, transfert radiatif

Title: Numerical simulations of planet-forming disks, Theoretical predictions for observational interpretation

Abstract: To this day, thousands of planets have been identified outside of our own solar system. Their formation is thus not chance events. A number of still-forming young stars are also known, circled by remnants of gas and dust which are shaped by centrifugal forces into disk-like objects. In those disks, planets are born as they accumulate nearby material. Although the successive steps of this evolution, from micrometric grains to planet-sized objects are relatively well identified, remaining challenges are numerous. Indeed, small size solids tend to rapidly accrete (in a few million years) onto the star. It is also the case (albeit for different reasons) of planet-mass objects, which concede their angular momentum to the circumstellar disk. In this thesis, I study possible solutions to such problems through hydrodynamical simulations. I show that, contrary to popular belief, migration of giant planets does not follow the viscous spreading in the disk. Moreover, I highlight that planetary accretion does not significantly affect migration rates. Then, I deal with a scenario that favours constructive aggregation of dust, namely Rossby vortices, whose existence is still debated for we lack observational constraints. I show that such structures could be identified through a handful of observables, among which dynamical signatures seen in Doppler shifts. Using radiative transfer as a post-processing method, I provide additional predictions for signatures in interferometric observations of thermal emission, as well as polarimetric features of those vortices. Finally, I dedicate my last chapter to describing my main contributions to open source projects that I used throughout my thesis.

Keywords: protoplanetary disks, planetary formation, numerical simulations, hydrodynamics, radiative transfer

Cette thèse est dédiée à Florence Porcel.

Remerciements/Acknowledgement

Mes premiers et plus grands remerciements reviennent à Héroïse et François, pour leur encadrement à la mesure de mon admiration pour eux. Leur bienveillance toujours renouvelée et leurs encouragements dans les meilleurs comme les pires instants de cette thèse ont permis son accouchement. Je n'aurais pu souhaiter meilleurs mentors, et je sais que ces trois années à leur côté ont fait de moi un meilleur scientifique. J'espère m'être montré digne de leur confiance, et je les salue de m'avoir hissé à bout de bras quelque centimètres plus près de leur stature. Que soit salué leur art de la maïeutique.

Je remercie évidemment les membres de mon jury pour avoir accepté de prendre sur leur temps de travail pour juger le mien, et en particulier Clément Baruteau dont le rapport très complet participe de la qualité finale de ce manuscrit.

Un immense merci à Aurélien pour m'avoir ouvert les portes de l'Observatoire de Nice en m'offrant la chance de travailler avec lui en tant que stagiaire puis "pré-doc". Un autre à Elena, qui n'est pas étrangère au succès de cette expérience et sans qui mon premier article eut été bien moins pertinent, et encore plus difficile à produire. Morby pour son expertise exceptionnelement vaste de tous les aspects de la formation du système solaire, distillée avec toujours beaucoup de pédagogie et qui fit le sel de tant de discussions, formelles ou non. Je veux aussi remercier Benoît, dont le flegme et le verbe dépassent les miens, et qui a toujours prêté attention au bien être de tous les doctorants de l'équipe.

La compétence de Rose, notre gestionnaire en or, mérite d'être ici saluée. En quatre années de missions nationales et à l'étranger, je ne puis me rappeler aucune faille, erreur ou maladresse de sa part, moi qui en trouve pourtant souvent.

Je remercie bien sûr le service informatique de l'Observatoire pour leur fiabilité et la patience dont ils firent preuve à mon égard, sous l'avalanche de tickets que je leur soumettais. Je dois à Alain les bases de ma rigueur en développement logiciel, mes premières passes d'armes sous git et svn, et en intégration continue. Fabrice puis Mohammed et Christophe qui ont maintes fois empêché mes "bécanes" d'exploser en vol, et moi avec. Jean-Philippe, dont le travail acharné mais souvent invisible contre les failles de sécurité et les défaillances des machines, fréquemment remises en service en moins de temps qu'il n'en fallait pour lire le premier email.

Khaled, notre chef et maître à tous, pour sa gastronomie, sa bonne humeur contagieuse mais surtout pour ses avoines quasi-quotidiennes qui à mon sens font de cet Observatoire le meilleur de France (et donc du monde !). Son soutien psychologique a entretenu en moi la

flamme de la motivation, qui sans lui se serait sans doute éteinte à de nombreuses reprises. Mon troisième directeur de thèse, mentor et ami, salut, et pourvu que ça dure !

Je veux remercier mes professeurs qui du lycée à la fac m'ont inspiré à marcher dans leurs traces. Nicolas, dont les cours à la rigueur infinie, toujours teintée d'humour m'ont donné l'amour de la physique. Son charisme reste à ce jour, et pour autant que je puisse en juger, inégalé. Sa vocation en science sans doute encore beaucoup d'autres, et la mienne parmi elles. Jacques, dont les cours faisaient figure de récréation à mes yeux tant ils émerveillaient mes jours pourtant déjà fantastiques sur les bancs de l'université. Il aurait suffi qu'un chercheur moins talentueux que lui côté enseignement prenne sa place dans mon cursus pour en changer la direction.

Les agents Sastron, Durst et Oliver-Moulin du service culturel de l'Observatoire, et Frédéric que avec qui j'ai pris plaisir à partager la quasi totalité de mes visites grand public de ce site historique.

Au tour de mes camarades, mes frères et soeurs d'armes. Gabe, qui fut mon colocataire en même temps que mon cobureau, et a accompli l'exploit de jouer ces deux rôles pendant près d'un an sans parvenir à me devenir insupportable. Nos "wine-thursdays" et nos polyphonies me manquent, ainsi que ses fous-rires incontrôlables et contagieux.

Adrien, mon jumeau de thèse, mon partenaire de grimpe, pionier du golf-escalade, solide scientifique autant qu'indécrottable bourrin de la programmation, et intrépide compagnon de Donjons et Dragon. Partager un bureau avec lui fut une bénédiction ainsi qu'une épreuve pour mon amour propre. Les bornes de mon admiration à son égard restent à définir. Avec Gabriele, il est de ceux dont je crois fermement être taillés pour la recherche, et je souhaite que la recherche ait l'intelligence de vouloir d'eux.

Merci à Dylan, notre MJ bienveillant, aussi féru des Simpsons que moi et peut-être encore plus prosélyte à ce sujet.

La fine équipe des partis trop tôt, Flo "Jamais de café entre minuit et le jour suivant", Kev "Je ne supporte pas qu'on m'appelle Kev" (qui souffrira d'être remercié au milieu de tous ces autres diminutifs), Antho et Jerem, auteurs quotidiens et passionnés de débats cinématographiques envahissant mon téléphone avec un plaisir toujours renouvelé. Cette thèse doit beaucoup à leurs sarcasmes et fâcheries légères, leur mauvaise foi (looking at you Antho) et leur intarissable badinage, au travers desquels se lisent un soutien permanent. Leur confiance en moi dépasse de loin la mienne-propre, merci à eux de m'obliger à être la personne qu'ils pensent connaître.

Mes amis grenoblois qui m'ont fait une place dans leur groupe de tarot et dans leur slackspace, sans ordre particulier: Nicolas, Manon, Laetitia, Greg, Oriane, Antoine, Marion, Thomas, Marc, Cyprien, Elie, Noemi, Guillaume dit "Bobby", Aloïs (j'espère n'oublier personne). Florent qui m'a logé lors de mes fréquents séjours parmi eux.

Thanks also to Rony for inviting me to Belgium and giving me the opportunity to give a talk in his lab. This extremely welcoming group made my belgian experience my best mission so far, despite the weather !

I wish to thank the Yt developement team for the great experience I had with them as an external contributor, and for naming me one of them. In particular I thank Matt and Madicken for their benevolent mentorship, and Corentin for our stimulating exchanges. Neils carried the AMRVAC frontend project for 6 months and I know I couldn't have made it alone. He deserves a huge shoutout.

Thomas, mon ami éternel, qui m'a abreuvé de questions tant que de son enthousiasme à la relecture anticipée des premiers chapitres de ce manuscrit. Merci merci, merci.

Ma tante et mes cousins Louise, Gabin et Ginette, que je n'ai jamais autant vus que pendant cette thèse et que je prenais tant de plaisir à retrouver à l'occasion de mes missions à Lyon.

Ma soeur, mon père, pour m'avoir continuellement soutenu à distance et particulièrement dans les moments les plus sombres (et il y en a eu).

Mel, pour m'avoir supporté malgré les retombées émotionnelles d'un confinement couplé à la rédaction ce manuscrit; ô combien laborieuse. Merci d'avoir mis de la musique dans ma vie, et d'être resté à mes côté dans le pire. Le meilleur est à venir.

Contents

Notations & conventions	1
1 Introduction	5
1.1 Where do planets come from ?	5
1.1.1 Discovery of outer worlds	5
1.1.2 The environment of a forming star	8
1.2 Observations of proto-planetary disks	10
1.2.1 What's in a disk ?	10
1.2.2 Dust tracing via thermal radiation	11
1.2.3 Surface layers tracing via scattered light	12
1.2.4 Direct gas detection and kinematics capturing	14
1.2.5 The need for simulations	16
1.3 Planetary formation : from dust to planets	17
1.4 An overview of the thesis	18
2 Prerequisites in hydrodynamics	21
2.1 Elements of general hydrodynamics	21
2.1.1 Fundamental equations of hydrodynamics	21
2.1.2 Some useful definitions	23
2.1.3 A word on turbulence	23
2.1.4 A word on Magneto-hydrodynamics	23
2.2 Physics of an accretion disk	24
2.2.1 Rotational motion	24
2.2.2 Vertical structure of a thin disk	28
2.2.3 Accretion and the hypothetical role of viscosity	29
2.2.4 Aerodynamics of solid particles	30
3 Methods: Numerical Hydrodynamics	37
3.1 Discretization and its consequences	38
3.2 Temperature as a prescription	40
3.3 FARGO	41
3.4 MPI-AMRVAC	43
4 A change of views in planetary migration	47
4.1 Planet-disk interactions	47
4.2 The classical paradigm for type II migration	50
4.3 Numerical details	51
4.4 Robert et al 2018	56
4.5 Additional remarks to the published paper	66

4.6	The current state of research on type II	66
5	Dynamics of Rossby Vortices	69
5.1	Context	69
5.1.1	Rossby vortices	69
5.1.2	The role(s) of vortices in the grand scheme of planetary formation	70
5.1.3	Observational context	71
5.2	Robert, Méheut & Ménard 2020	74
5.2.1	Erratum	85
5.2.2	On physical temperature	85
5.3	Violent vortices with rotational instability	85
5.4	Observational difficulties of interpretation	89
6	Simulated disk imaging	91
6.1	Dusty vortex simulations	91
6.1.1	Numerical setup	91
6.1.2	Results	93
6.2	From hydro to radiative transfer (methods)	95
6.2.1	vac2fost: an interface from AMRVAC to MCFOST	95
6.3	Simulated direct observables of a Rossby vortex	101
6.3.1	Thermal continuum prediction	101
6.3.2	Polarimetric predictions	106
6.4	Conclusions	106
7	Open source data analysis, for more reliable science	109
7.1	A plea for open source research tools	109
7.2	A unified and simplified library for data analysis	111
7.3	Data storage and reading: the illustrative case of MPI-AMRVAC	112
7.3.1	Morton curves: unambiguous flat-indexing for arbitrarily refined data	113
7.3.2	A compact linear memory mapping solution	114
7.4	Other contributions to Yt	115
7.5	Conclusions and perspectives	116
8	Conclusions and perspectives	117
	Bibliography	119

Conventions in the manuscript

Typesetting, operators

In equations, I reserve boldface for vectors. Upward typesetting is used in units, as well as indices and exponents labelling quantities attached to a particular object (e.g. m_{star} could denote the mass of a star), which is explicated where needed. “ \equiv ” is used as a special case equality sign, adding the meaning “is defined as”. In the text body, I use italics to mark the first occurrence of each new technical term, usually matching its definition.

Vector calculus

“ \cdot ” denotes scalar product when applied between two vectors, and is elsewhere used as a place holder. “ \times ” is the cross product when applied to vectors, and sometimes used for scalar multiplication. “ e_x ” designates the unit vector along direction x .

For illustrative purposes, we take here a meaningless scalar variable k , and a vector w . Spatial, partial derivatives are noted e.g. “ $\partial_x k$ ”, or simply indicated by an apostrophe “ k' ” when the spatial direction of the derivation is unambiguous. The time derivative can be symmetrically noted “ $\partial_t k$ ”, or simply as a dot “ \dot{k} ”. “ ∇ ” is the spatial derivation operator, where ∇k is a gradient, while “ $\nabla \cdot w$ ” is a divergence and “ $\nabla \times w$ ” is a curl. Δ designates the Laplace operator for double spatial derivatives.

Coordinate systems

I define two coordinate systems relevant to describe two and three-dimensional systems. Specifying an origin O is necessary in all cases. The *position vector* of any given point is noted r .

1. *Cartesian* coordinates are written along three mutually orthogonal axis, with respective unit vectors e_x , e_y and e_z , where $e_z = e_x \times e_y$ in the *orthonormal* convention, implicitly used throughout the manuscript.

2. *Cylindrical* coordinates are defined with respect to cartesian ones, in terms of a distance r to the vertical axis Oe_z , an angle θ (or φ) defined between e_r and e_x , and the vertical axis e_z which is the same as in the cartesian case. *Polar* coordinates are the 2D equivalent of cylindrical, where the vertical dimension is dropped. The cartesian to polar transformation is given by

$$\begin{cases} e_r &= \cos \theta e_x + \sin \theta e_y \\ e_\theta &= \sin \theta e_x - \cos \theta e_y \end{cases} \quad (0.1)$$

so

$$\begin{cases} r &= \sqrt{x^2 + y^2} \\ \theta &= \arctan2(y, x) \end{cases} \quad (0.2)$$

An important consequence of defining the unit vectors as functions of position (r, θ) in polar coordinates implies that, contrary to cartesian axes, they are generally not time invariant. Their respective derivatives write

$$\begin{cases} \dot{e}_r &= \dot{\theta} (-\sin \theta e_x + \cos \theta e_y) = -\dot{\theta} e_\theta \\ \dot{e}_\theta &= \dot{\theta} (\cos \theta e_x + \sin \theta e_y) = \dot{\theta} e_r \end{cases} \quad (0.3)$$

The terms “coordinate system” and “geometry” may be used interchangeably in the thesis.

Dimensional analysis

M , L , T denote mass, length and time dimensions respectively. Moreover, I define $F \equiv MLT^{-2}$ as a convenient alias for a “force dimension”, even though it is not linearly independent of the first three symbols. Dimensionless variables have dimension “1” by convention, as do angles.

symbol	dimension	typical unit(s)	meaning
\mathcal{G}	$FM^{-2}L^2$		universal gravitational constant
x, y, z	L		cartesian space coordinates
r	L		polar radius coordinate (distance to origin)
θ (or φ)	1	rad	polar angular coordinate (conventions vary)
t	T	s, yr	time
ρ	ML^{-3}	g cm^{-3}	density of a fluid (gas)
Σ	ML^{-2}	g cm^{-2}	surface (column integrated) density
P	FL^{-2}	Pa	thermal pressure
p	FL^{-1}	Pa cm	column integrated thermal pressure
\mathbf{v}	LT^{-1}	km s^{-1}	fluid velocity
c_s	LT^{-1}	km s^{-1}	sound speed
μ	FL^{-3}		dynamic viscosity
$\nu \equiv \mu/\rho$	LT^{-2}	$\text{m}^2 \text{s}^{-1}$	kinematic viscosity
T		K	temperature
ρ_d	ML^{-3}	g cm^{-3}	dust density
Σ_d	ML^{-2}	g cm^{-2}	dust surface density
ρ_p	ML^{-3}		dust particle intrinsic density
s_p	L	1 μm to 1 cm	dust particle size
τ_s	T		particle stopping time
$\text{St} \equiv \tau_s/\Omega_K$			Stokes number (i.e. dimensionless stopping time)
m_{label}	M		mass of the -labeled- object
a	L	AU	semi-major axis in a planet's orbit
$\Omega \equiv v_\theta/r$	T^{-1}	rad yr^{-1}	angular velocity
Ω_K	T^{-1}	rad yr^{-1}	Keplerian orbital velocity (i.e. of a test particle)
ℓ	L^2T^{-2}		specific angular momentum

Tab. 0.1: Common notations and definitions used throughout the thesis.

Introduction

“ A human is a system for converting dust billions of years ago into dust billions of years from now via a roundabout process which involves checking email a lot.

— **Rundall Munroe**
xkcd

1.1 Where do planets come from ?

Our sun is a star. With the 8 known planets that orbit it, their satellites, and a myriad of smaller objects ranging from interstellar dust to quasi-spherical asteroids, it forms the Solar System. Using the relative abundances in radioactive elements found in pristine asteroids, we can estimate the age of the system to be about 5 billion years. For the sake of simplicity, let us put this in perspective and scale it down to a single “year”. At this scale, as a species, humans have only been around for about 15 minutes, writing was invented a mere minute ago, and we had no notion of the scientific method until 12 seconds ago. To say that recollecting the memory of everything that came before us is challenging is putting it mildly. Fortunately, we are helped by the fact that not all stars in our galaxy were born at the same time. Some of them are still forming now, and with them, surely some planets. Provided observational techniques are sufficiently advanced, we can look up for other, younger systems and gather clues there about the origin of our own.

1.1.1 Discovery of outer worlds

It was not always an established fact that other stars bear planets as well, for they are extremely hard to detect. The difficulty of directly detecting a planet around a star is often compared to that of finding a firefly in a lighthouse on the other side of the Atlantic (whichever side you stand on). The first known extra-solar planet orbiting an ordinary star (51 Pegasi) was discovered by Mayor and Queloz (1995) in a *radial velocity* survey of nearby stars. As the star moves away from or towards us, its spectral signature is shifted towards the red and blue respectively. This is known as the Doppler effect. By measuring this spectral displacement in well known molecular absorption lines, one can deduce its *radial velocity*, that is, the motion in the direction of the line-of-sight. With enough accuracy and sensitivity, one can detect the wobbling of a star around the system’s barycenter, thus allowing to infer the presence of planetary companions solely by looking at the star itself. This method is of course biased towards systems that we see with an *edge-on* orientation, i.e. with an *inclination* i close to 90° , see fig. 1.1. Mayor’s and Queloz’s discovery came

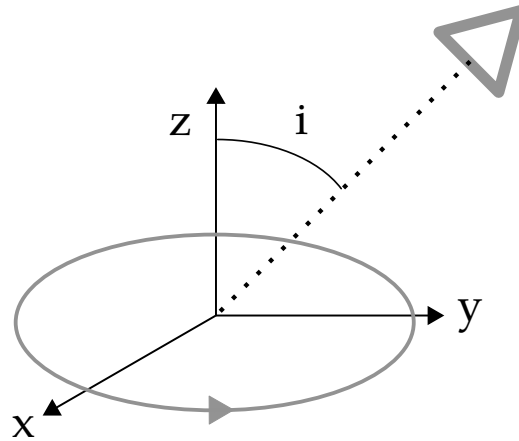


Fig. 1.1: We define the inclination of a target, e.g. a planet orbiting a star, schematically represented here, as the angle i between the local normal z and the direction of the line-of-sight. The observer/instrument is here represented as a triangle.

out as breaking news, not only because it confirmed that our Solar System is not a unique case, but also because the planet itself was very unlike any other we knew. It was estimated to be about the mass of Jupiter, the most massive planet in our system by far, but it goes around its star in a closer orbit than Mercury does the Sun. Since then, hundreds of similar planets were discovered with the same technique. They were nick-named “hot Jupiters”, appropriately enough. Although completely unexpected, there is a good reason why this was the first kind of extra-solar planet we found. Indeed, following Kepler’s third law

$$f_{\text{orbit}} = \sqrt{\frac{\mathcal{G}(m_{\text{star}} + m_{\text{planet}})}{4\pi^2 a^3}} \quad (1.1)$$

where f_{orbit} is the orbital frequency, we see that back-and-forth frequency is higher for massive planets in narrow orbits.

Since then, other techniques have been developed as well, which allow for the detection of different kinds of planets. For instance, another fruitful detection method is based on transit occultations, and is illustrated in fig. 1.2. The aforementioned biases affect this method as well. Additionally, because hot Jupiters are close to their respective host-stars, they also cast larger shadows, making them all the easier to find.

More generally, each technique is sensitive to a range of masses and inclinations. Figure 1.3 shows a summary of known planets by detection methods. Jupiter and Saturn are lying on the edge of the region of current detectability, while terrestrial planets (Mercury, Venus, the Earth and Mars), occupy a uniquely empty space on the graph. This is explained by the fact that most detection techniques are not yet sensitive enough to catch comparable small rocky planets, as their effects on stellar motion, micro-lensing (gravitational light “bending”), flux reduction etc. are smaller. Hence, our system may well be more typical than it appears against existing data. In any case it is now evident that there exists a diversity in the structure of planetary systems, which we need to account for in theories and models built to explain the formation of planets.

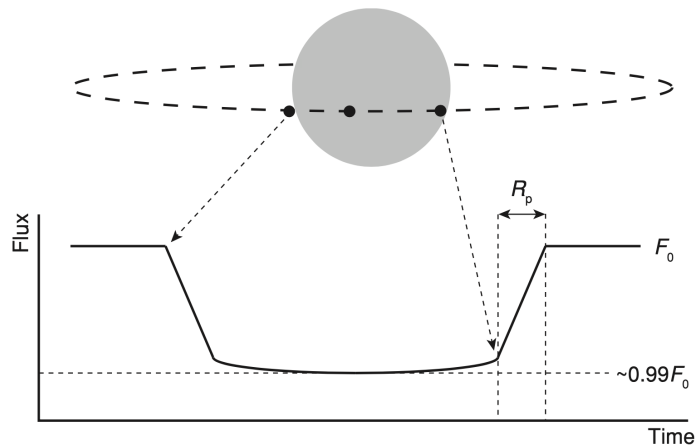


Fig. 1.2: As a planet temporarily eclipses the star it orbits, the total flux received on Earth is diminished by a fraction. The characteristic shape, as well as the periodicity of this signal is a signature of a companion orbiter. Credits: Armitage (2009)

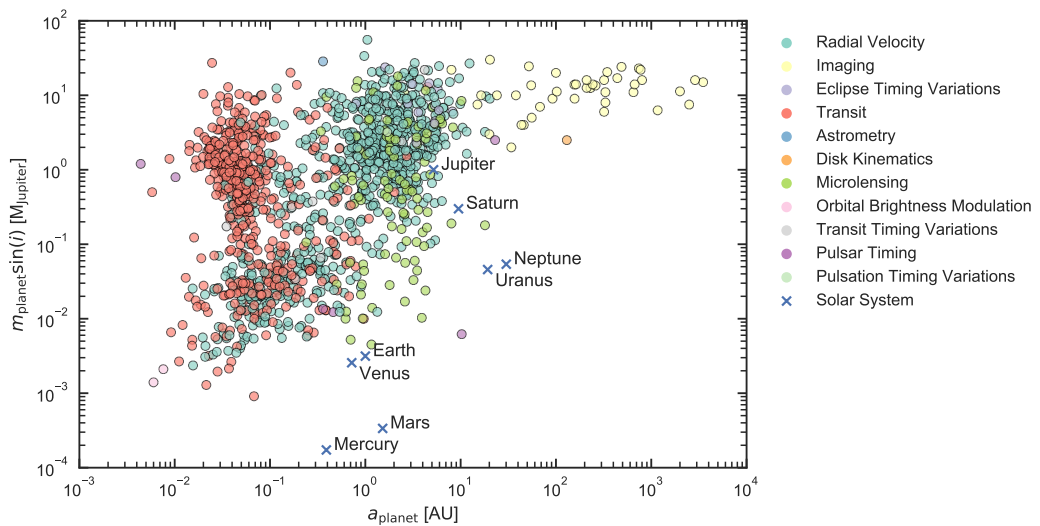


Fig. 1.3: A chart of 1469 confirmed extra-solar planets categorized by detection techniques. The sample is limited to objects for which data is available for each axis. It must be noted that the vertical axis shows $m_{\text{planet}} \times \sin i$ rather than m_{planet} directly. This is because the exact inclinations are virtually impossible to estimate, though in general they must be close to 90° , so $\sin i \simeq 1$. Positions of planets from our system within this chart are indicated as references, assuming i is an exact straight angle.

1.1.2 The environment of a forming star

Stars form in groups when an over-density in the inter-stellar medium provokes a gravitational collapse. The process of forming an individual star can be decomposed into several distinct stages, as illustrated in fig. 1.4. Those stages are defined as an evolution in the spectral energy distribution (SED), that is the curve described by the flux distribution as a function of frequency, and correspond to qualitatively different morphologies in the circumstellar material. In the earliest stage (class 0), gravitationally bound sub-regions in the over-dense region isolate from each other, each creating an even denser core. Each star thus starts its life surrounded by a gas envelope that is approximately spherical and rather opaque. As the cloud collapses further, its total angular momentum is conserved but its size shrinks. Consequently, centrifugal forces grow and eventually lead to the flattening of the gas envelope (class I). The resulting accretion disk still contributes most of the radiated energy. After the central star has reached its final minimal size, the only contribution of the disk remaining material to the total flux is the black-body thermal emission (class II). Later on, after the dissipation of the gas component (99% of the initial mass), only solids remain around the star and form a *debris disk* (class III).

Because multi-planet systems are most often found to orbit their respective host star in nearly co-planar orbits, it is conjectured that they must form during the disk phase, between phase II and III. For this reason, class II objects are what we refer to as *proto-planetary disks*. They are the subject of this thesis. From comparisons of stellar ages against the fraction of stars still featuring a gaseous disk, the transition from class II to class III is estimated to take about 2.5 Myr (Mamajek, 2009). This sets an upper limit to the timescale of planetary formation.

Interestingly, because disks are still detected via SED surveys, and pole-on disks are easier to identify, the distribution of the inclination angle relative to the observer in the population of known targets is biased towards weakly inclined objects. This is illustrated in fig. 1.5.

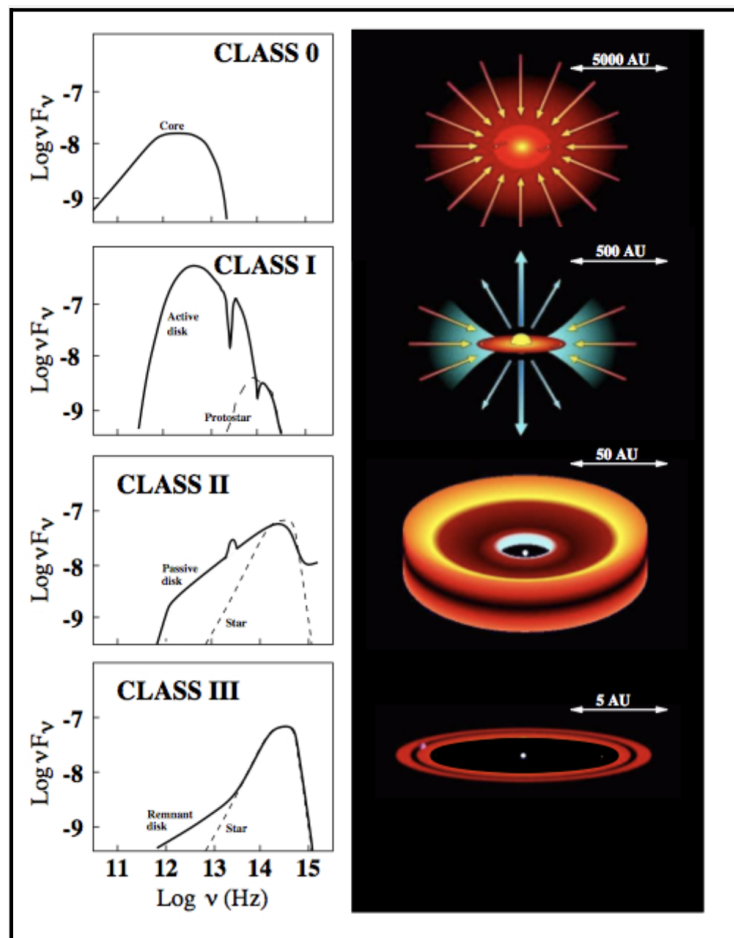


Fig. 1.4: The four stages of stellar formation, as defined by the SED of the envelop (left), and a schematic representation of the corresponding object (right). Class 0: spherical accreting envelop. Class I: active accreting disk. Class II: mostly passive proto-planetary disk. Class III: debris disk, no gas remains. (source: Andrea Isella's thesis (2006), reproduce with permission from the author)

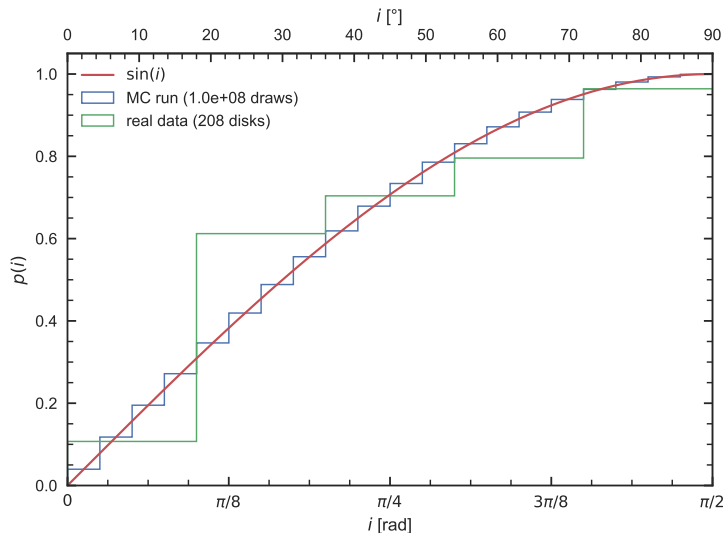


Fig. 1.5: The probability density $p(i)$, where i is the inclination of disks relative to the line of sight, in a sample of known disks (green), against the distribution expected from geometric considerations in an isotropic universe (red). A simple fake population (blue) simulated with the Monte-Carlo method fits the geometric analytical distribution. The effective distribution is skewed towards high inclination disks because in the edge-on cases, a significant fraction of the stellar flux is lost to absorption. As so, it is harder to identify a double-peaked distribution in the observed SED. Data source <http://www.circumstellardisks.org/>

1.2 Observations of proto-planetary disks

1.2.1 What's in a disk ?

A proto-planetary disk's mass is initially comprised of 99 % gas. The remaining ~ 1 % are solid particles (or grains) collectively referred to as *dust*. Gas molecules only interact with light at discrete wavelengths, referred to as *spectral lines*, and can be detected either in emission or absorption.

However, most of the gas in a proto-planetary disk is comprised of molecular hydrogen H_2 . Because this molecule is symmetric, it has a zero electric dipole moment, which implies it has no purely vibrational spectral lines. As a result, H_2 is essentially transparent and untraceable¹. Atomic hydrogen H is not easily detectable from ground-based observatories either because its most common and fundamental emission lines (Lyman series) are found in the ultra-violet part of the spectrum, which the atmosphere is (thankfully for us !) mostly opaque to². On the other hand, dust thermally emits in the radio range ($\lambda \lesssim 1$ mm), which can be captured by modern facilities, the most prominent one being the Atacama Large Millimeter Array (ALMA) interferometer. As a reference for upcoming discussions, I represent the immediate infra-red domains in fig. 1.6, against ALMA observable ranges (bands), and indicate the correspondance between frequency, wavelength, and black body temperature as

¹Though some rare studies have presented detections in weaker ro-vibrational modes, see for instance Carmona et al. (2011)

²Balmer, Paschen and Brackett series are still detectable.

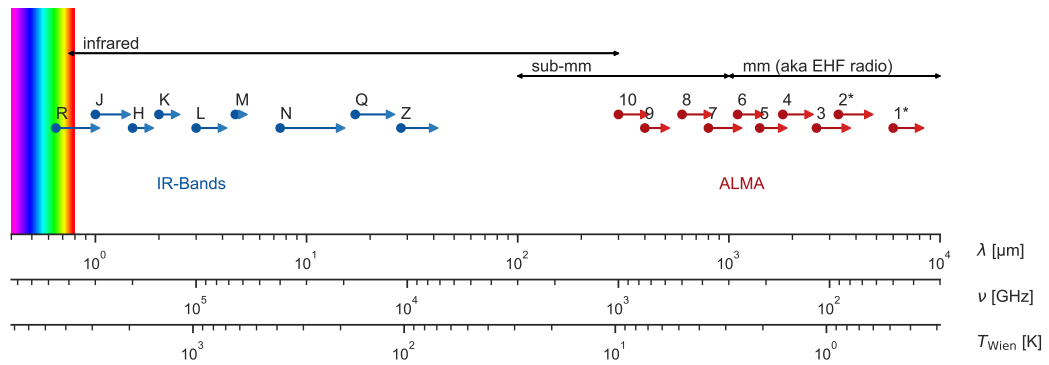


Fig. 1.6: A graphic representation of the immediate infra-red sub-domains of the electromagnetic spectrum. The horizontal axis is labelled in wavelength λ , frequency ν as well as Wien temperature T_{Wien} , i.e. the temperature of a black body peaking at the corresponding wavelength. The visible range is shown as a rainbow, roughly corresponding to the colours as seen by a (non-colorblind) human eye. The generic IR (infra-red) bands as defined in general astronomy are shown as blue arrows, while ALMA's bands in the millimeter and submillimeter domains are shown as red arrows.

defined by Wien's law of displacement. I will now review the different means used to probe proto-planetary disks structure.

1.2.2 Dust tracing via thermal radiation

Observations in the cold thermal continuum part of the SED associated with the disk historically predate direct gas detection. Indeed, thermal radiation as a whole is easier to detect because it covers a continuum in wavelength and produces smooth SED profiles, following Planck's law in the black body approximation, so its detection is not too demanding in terms of spectral resolution. Rather, angular resolution $\Delta\theta$ is the main hurdle. In an interferometer with baseline B , the angular resolution is roughly defined as

$$\Delta\theta(\lambda) = \frac{\lambda}{2B} \quad (1.2)$$

Let us construct a first order estimate for the instrumental requirements. Most of the dust is concealed close to the midplane of a disk, with temperatures typically between a few and a few tens of K. Furthermore, stars are typically a few thousand K (at the surface), and do not radiate significantly in the millimeter range, thus making it desirable to observe in such bands, where there is no need for coronagraphs to isolate the disk's proper signal. With disks typically found at $d \sim 100$ pc and with typical size (disk radius) of $s \sim 100$ AU, we get the typical target angular size as $\alpha = \arctan \frac{s}{d} \simeq \frac{s}{d} = 1''$. Following eq. (1.2) the bare minimal aperture size required to observe at millimeter wavelengths is 100 m, and is of course insufficient to capture the details besides the disk size. One can see why it took time to achieve reasonable resolutions in this domain: the sheer size of the required baseline is not realistically achievable with a single aperture. A solution is found in interferometry, where we combine the signals from an array of antennas effectively acting as one giant instrument, and this is exactly the outline of ALMA.

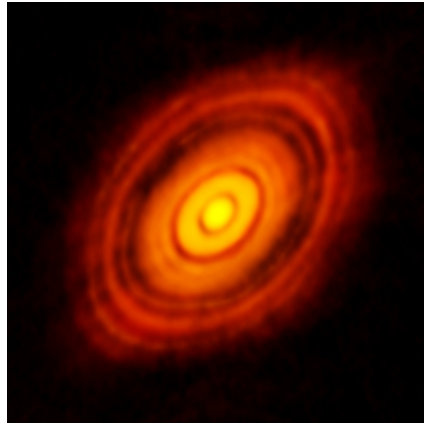


Fig. 1.7: The disk around HL Tau as observed with ALMA and presented by ALMA Partnership et al. (2015). The 140 AU large structure embeds several axisymmetric dust rings, which are potential signposts of planetary formation.

The instrument produced its first light in 2011. Three years later, it was used to produce the first-ever resolved image of a structured disk, presented in ALMA Partnership et al. (2015). It is reproduced in fig. 1.7. This observation, in the millimeter wavelengths, traces the thermal emission of a black body about 30 K. Namely, this represents the distribution of relatively cold solid material that has settled into the disk midplane. We see a collection of thin rings, separated by darker regions. This fits very well the expected effect of interaction with massive perturbers embedded in the structure, namely planets, though they remain undetected to this day.

In fig. 1.8, I show the recent history of imaging, prior to and within the ALMA era, taking the example of the disk around HD 163296, 101 pc from us. One can see that more recent observations are produced further and further away from the visible spectrum. In particular, the first images required the use of a coronagraph, which masks the central area to avoid catching the stellar signal.

The DSHARP survey provided some of the best resolved continuum images produced to this day with ALMA, and were presented in a series of papers lead by (Andrews et al., 2018). This is where panel (d) in fig. 1.8 is from. The showcase gallery from this survey is reproduced as fig. 1.9. Many structures are resolved with sizes 10 AU to 100 AU, most notably rings (r), spirals (s) and asymmetric azimuthal clumps (c). Each and all of these structures are suspected to betray the presence of hidden planets, albeit most if not all are also possible effects of pure hydrodynamics. A conclusion here is that even highly resolved dust location maps do not constitute definitive evidence of planetary formation by themselves, but provide necessary data nonetheless.

1.2.3 Surface layers tracing via scattered light

In the optical and near-infrared domains, a means to abstract from the direct stellar signal is found in polarimetry. Since the light directly emitted by a star is not polarized (i.e. it knows no preferential direction), it can be “switched off” (removed) by measuring the difference in fluxes received in two detectors coupled with linear filters at a straight angle with respect

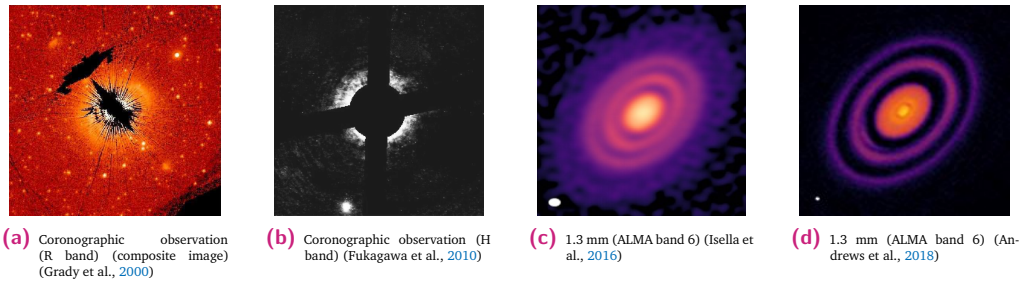


Fig. 1.8: A brief history of continuum imaging of the disk around HD 163296. Prior to the rise of ALMA, observations were conducted in near infrared bands, in which the central star radiates, so that coronagraphs were necessary. This is not the case in the millimeter range observed by ALMA, which allowed for the detection of seemingly axisymmetric rings. They were later captured in even greater details with the DSHARP survey (Andrews et al., 2018), which revealed a non-axisymmetric dust clump in the South of the second to last ring. The visible enhancement in signal to noise ratio as well as improved angular resolution between panels (c) and (d) is due to a sizeable increase in observation time. Note that no two images have the exact same scale. From left to right, the image sizes (squared) are $20''$, $12''$, $\sim 4''$ and $\sim 4''$.

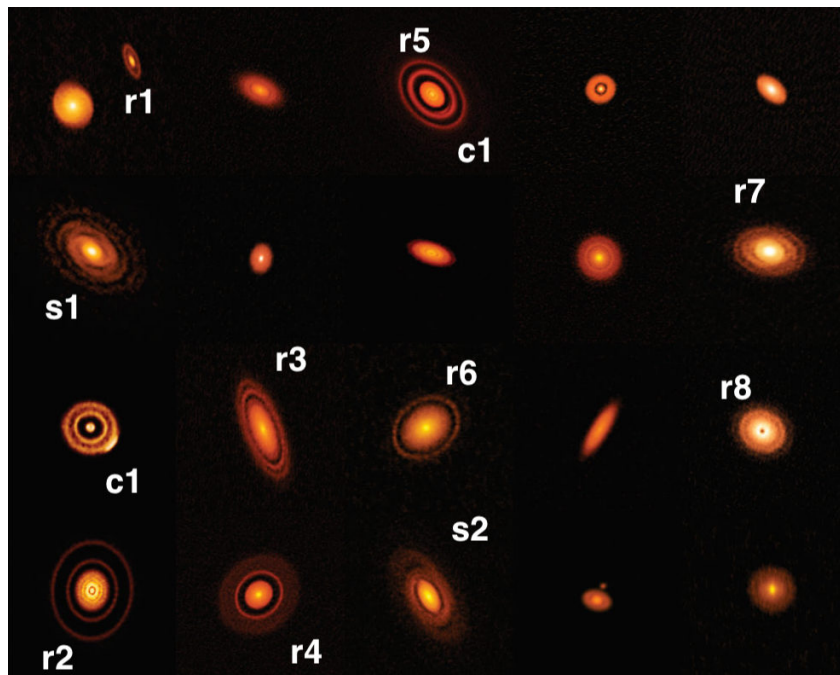


Fig. 1.9: Resolved rings and clumps seen in the continuum. Many structures are visible. Most notably, axisymmetric rings (r), double-armed spirals (s) and dust clumps (c). Credit: ALMA (ESO/NAOJ/NRAO), Andrews et al., 2018; NRAO/AUI/NSF, S. Dagnello. Reproduced with kind permission from Sean Andrews.

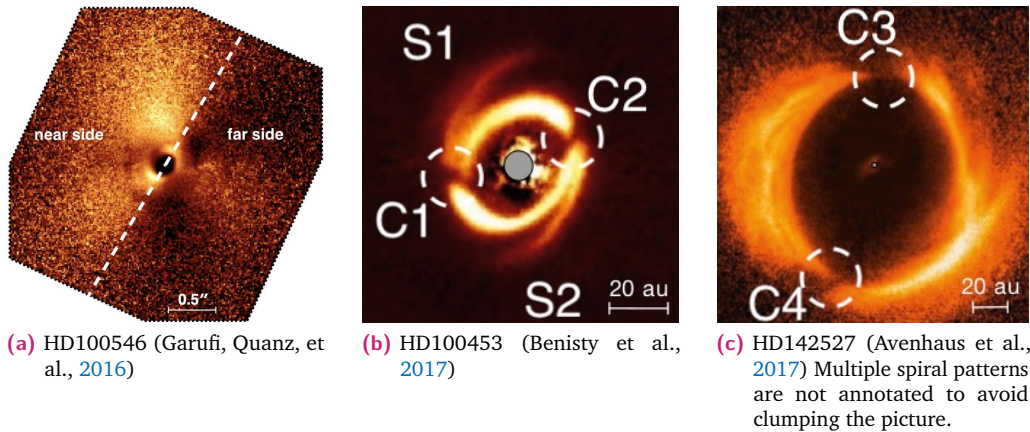


Fig. 1.10: Some examples of polarized intensity maps. Annotations are added to highlight spiral arms (S) as well as azimuthal cut-offs in surface brightness (C). All figures are reproduced with kind permission from their respective authors.

to each other. In other terms, measuring the polarized intensity naturally masks the stellar signal. Meanwhile, stellar light scattered by dust grains is polarized. This process is most efficient for micron-sized dust grains, since their size is comparable to the wavelength. Particles of this size range are not expected to segregate efficiently as they are tightly coupled to the gas (as we will see in section 2.2.4). Moreover, light scattering is extremely efficient in the optical range. As a result, measurements in polarized intensity at wavelengths typically radiated by the star efficiently trace the distribution of small grains in the external layers. This provides geometric insight about the overall shape of a disk (Stolker et al., 2016).

In fig. 1.10, I showcase some examples of polarized intensity maps produced with SPHERE and ZIMPOL. The inclined disk (a) illustrates a geometric bias in the observed intensity ; the surface directly closer to the instrument (near side) appears brighter, because the probability for an individual photon to be scattered in a direction close to the one it originated from is highest. This effect is called *forward scattering*. In panels (b) and (c) one can see some asymmetric structures revealed by SPHERE. Namely azimuthal cutoffs in surface brightness (C), interpreted as shadows cast by a misaligned inner disk, and spirals arms (S), for which many interpretations are possible. They could be signatures from planetary perturbers, or a stellar companion. In heavier disks, spirals may also form via self-gravitational instabilities (SGI). In all cases, hydrodynamic simulations are required to explore these scenarios. A striking example of the complementarity between the two aforementioned observations techniques is illustrated in fig. 1.11.

1.2.4 Direct gas detection and kinematics capturing

Even though H_2 is not detectable, more polar molecules like CO have a range of spectral lines that can be captured with current facilities. CO's distribution cannot in general be assumed to match that of H_2 , in part because their respective chemistry and freezing points are different, but it serves as a useful proxy nonetheless. Furthermore, observing in narrow bands targeting spectral lines is not only about measuring the discrepancy between the dust

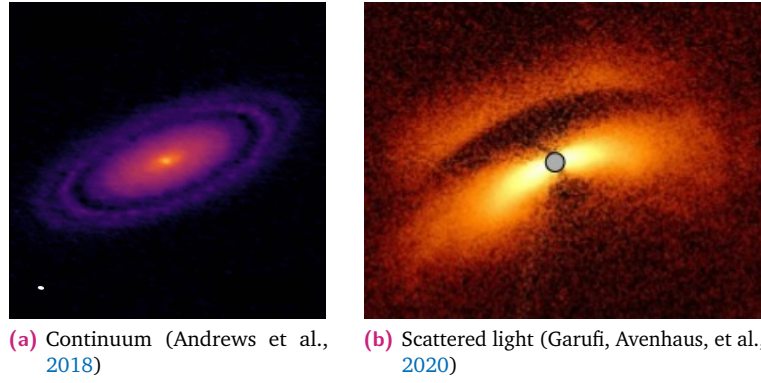


Fig. 1.11: The dichotomy and complementarity of observational techniques, illustrated for the disk around DoAr25. The thermal continuum traces a thin dust layer close to the midplane, while the scattered emission reveals the outer envelope. All figures are reproduced with kind permission from their respective authors.

and gas distributions. Indeed, such observations also convey information on the underlying dynamics of the gas, let us see how.

Spectral lines represent, by definition, discrete parts in the spectrum of a target *at rest relative to the observer*. Actual targets however never quite meet this condition, and have a certain *systemic velocity*, corresponding to the radial velocity of the star itself. On top of this, individual emitting molecules are in motion relative to the bulk (or the star), so each photon's frequency as measured by the observer is in fact Doppler-shifted *relative to this systemic motion*. Accounting for the systemic effect, one can isolate the residual relative component. The velocity dispersion of a patch of gas is thus measurable through the broadening of a line into a Gaussian distribution peaked on the rest-frequency. This is a useful tracer of temperature (Dartois et al., 2003) and turbulence, as a hotter material yields a greater dispersion. More importantly, this provides a means to study the disk dynamics ! Indeed the disk is not at rest with respect to the observer, and the velocity at each location can be decomposed as

$$v_{\text{LOS}} = e_{\text{LOS}} \cdot (v_{\text{star}} + v) \quad (1.3)$$

where v_{star} is the velocity of the star relative to the observer and v the velocity field of the disk relative to the star, and e_{LOS} is the unit vector in the direction of the line-of-sight, so the dot product $e_{\text{LOS}} \cdot$ represents the projection operator. The relevant component in the star velocity along the line-of-sight, namely its *radial velocity*, can be isolated, either by measuring the Doppler displacement in well identified spectral lines in the star spectrum or simply by taking their average value over the whole target. We are thus able to measure the projected velocity of the disk itself ($e_{\text{LOS}} \cdot v$). In practice this is done by sampling images (frames) around the peak of a line (corrected for the star velocity), in *channels* separated by a constant frequency interval $\delta\nu$, called the spectral resolution. Of course a finer velocity measurement requires smaller $\delta\nu$, hence longer exposures. This is because in interferometry, all frequencies are observed simultaneously. The spectral resolution $\delta\nu$ is in fact arbitrarily set at processing time, but the finer it gets, the fewer photons are left in each individual channel, hence the signal to noise ratio is the real limit, and can only be improved with longer runs.

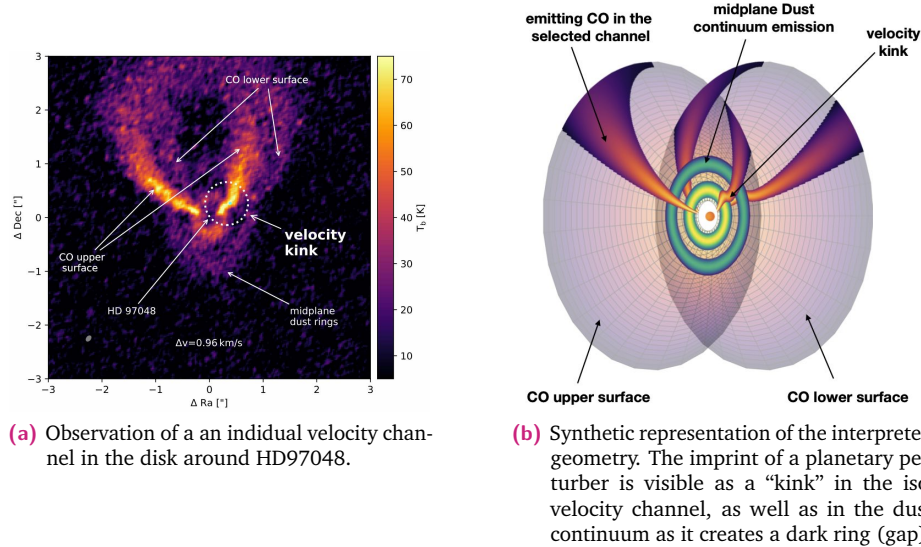


Fig. 1.12: A first candidate for indirect detection of a forming planet via gas dynamics measurements in an individual velocity channel. The perturbation “butterfly pattern” is interpreted as an imprint of an embedded planet’s gravitational disturbance on the disk. This interpretation is further confirmed by the presence of a co-spatial gap seen in continuum dust emission. (a) shows raw observational data while (b) is a geometric representation of the phenomenology in play. Both panels are reproduced from C. Pinte, van der Plas, et al. (2019), and reproduced with the kind permission of the authors.

To first order, this detection method is used to constrain the velocity gradients in a pressure-supported disk (see e.g. (C. Pinte, F. Ménard, et al., 2018)). Recent advancements in data reduction techniques, yielding a much reduced signal to noise ratio for axisymmetric disks, paved the road for extremely accurate pressure measurements (Teague and Foreman-Mackey, 2018; Teague, Bae, et al., 2018).

It was also shown that embedded planets leave visible traces in individual channels (Pérez et al., 2018; Casassus and Perez, 2019), eventually allowing for their indirect detection (Christophe Pinte, Daniel J Price, et al., 2018; C. Pinte, van der Plas, et al., 2019). The first of its kind is reproduced as fig. 1.12. For a cutting edge review of the underlying physics of planet-disk interactions within the scope of dynamics observables, and the pit falls of such detections, see Disk Dynamics Collaboration et al. (2020).

Finally, I note that a promising route to better trace the H₂ distribution directly has been recently opened ; indeed, deuterid (HD or ¹H²H really) is asymmetric and emits much more than the most common isotopic pair, all the while being much rarer. The Herschel Space Observatory has been used to explore this new source of data (McClure et al., 2016).

1.2.5 The need for simulations

As we saw, disks are primarily probed through dust signatures, while the remaining 99 % of their mass remains mostly hidden to observers. Meanwhile, evolution time scales (~ 10 Myr) are far greater than human-life time, as individuals *and* as a species for that matters. Essentially, each target is a fixed frame to us and we do not get to see much change in

a single disk's structure as the years go by³. Both these arguments strongly motivate the use of hydrodynamic simulations to study long-term evolutions and gas dynamics. Direct comparisons between observational and simulated data however require that the dust component be included in hydro models, but this aspect is often left out for simplicity. It should be noted that observations provide constraints on the spatial distribution of grains with respect to their typical size. A useful rule of thumb is that grains interact most efficiently with photons whose wavelength corresponds to their size. As a consequence, the distribution of grains with size s_p can be probed in spectral bands with wavelength $\lambda \sim s_p$. More specifically, a well-known result of the Mie theory (Mie, 1908), which describes scattering of plane waves by compact spheres as a function of wavelength, is that the effective cross-section for this interaction is maximized for $\frac{\lambda}{2\pi s_p} = 1$. This means that grain size is the most essential characteristic of dust when modeling its physical behaviour (Weidenschilling, 1977). Since forming planets are hardly ever directly detected, their effect on dust segregation and the complex interplay with gas dynamics ought to be explored in details in order to assess the existence of planet-specific signatures in actual observables. Most prominently, efforts are being conducted to address the possible connexions between dark rings seen in the continuum (gaps) and planet formation, see e.g. (Dipierro et al., 2015). I will go through the relevant physics connecting dust and gas in section 2.2.4.

1.3 Planetary formation : from dust to planets

Throughout the lifetime of the disk, solids aggregate to form bigger and bigger objects, ranging from mere micrometric particles to full-grown planets, spanning over a mind-boggling ~ 15 orders of magnitude in size ! While this is a necessary condition to the very existence of planets, the details of dust growth in nature are not fully understood yet.

Indeed the physics involved is extremely rich and multi-fields. A simple decomposition of the full story takes microscopic dust to so-called *pebbles* (~ 1 cm) via particle-on-particle coagulation, pebbles to planetesimals ($\gtrsim 1$ km) via streaming instabilities and local gravitational clumping, and finally to planets (~ 1000 km) by large scale gravitational collapse. Each of these stages is the subject of active research and debates, due to apparent obstacles to solid growth.

For instance, it is unclear how solids can reach a scale where gravitation is relevant. A common hypothesis is that ice-coated particles may be able to stick to each other, enabling coagulation-driven growth beyond the ice-line. However, this mechanism becomes less efficient for pebbles, as the ratio of exposed surface to total volume decreases with growth. Velocity dispersion between solids also becomes a hurdle : collisions should become destructive on average, impeding growth (Zsom et al., 2010). This is commonly referred to as the *metre barrier*, or the *collisional barrier*. Another important difficulty is found in the rapid inward drifting undergone by smaller grains and caused by friction with sub-Keplerian gas (this is explained in section 2.2.4). This problem is known as the *drifting barrier*.

³Though the dynamical times scale $\Omega_K^{-1} \sim 100$ yr is short enough that we *do* see some short-term variation.

Finally, the chemical composition of these particles and their physical shapes determine how they interact with each other, but are poorly constrained. For an up-to-date review, see Liu and Ji (2020). The formation of planetesimals is also thoroughly covered in E. Chiang and Youdin (2010).

Because detection of disk-embedded planets are still exceptional⁴, the detailed chronology of their formation is still fuzzy. Nonetheless, in our current understanding as constructed through modeling and simulations, gas giants necessarily co-exist with the gaseous disk phase, but it is not so for terrestrial planets, which could appear in later stages and form out of debris disks.

Giant planets should again be the first ones we can ever witness the birth of. Let me now go over the basics of the theoretical views supporting their formation.

The core accretion model A classic model for planetary formation was derived from simple simulations by Pollack et al. (1996). Assuming a region of local over-density in an otherwise uniform background disk, gravitational collapse builds up the mass of the planet until its sphere of gravitational influence is depleted. This sphere is defined by the Hill radius

$$r_{\text{Hill}} \equiv a_{\text{planet}} (q/3)^{1/3} \quad (1.4)$$

where $q = m_{\text{planet}}/m_{\text{star}}$ is the planet to star mass ratio, so the mass that becomes available to the feeding-zone grows with that of the planet itself, creating a runaway process. The model is summarized by fig. 1.13. Growth proceeds in two phases. First, the “core” is formed by efficient solid accretion, until a mass threshold is attained after which the Hill sphere contains mostly gas. The latter is accumulated over a longer timescale, in an exponential process call *runaway accretion*. In the late stages, gas accounts for most of the final mass.

Although this model is very simple and leaves room for many refinements, it sets a milestone in our understanding of planetary formation. Solid core accretion has been the subject of recent advancements. In the *pebble accretion* model (Lambrechts and Johansen, 2012), cm-sized “pebbles” are efficiently accreted by a forming core as their stopping time is shorter than the fly-by timescale. On the other hand the details of envelop accretion are not yet understood, and in particular we lack a description of the mechanism by which runaway accretion is halted. Recent effort has been invested in exploring this aspect (Lambrechts and Lega, 2017; Lambrechts, Lega, et al., 2019).

1.4 An overview of the thesis

The next chapter introduces the fundamental aspects of theoretical hydrodynamics used to model a proto-planetary disk. In chapter 3, I will go over the technical specifics of solving these models with numerical programs. The two following chapters contain my published results on two very different aspects of disk evolution. Namely, chapter 4 explores the ongoing problems in modeling the orbital evolution of Jupiter-mass planets forming in an

⁴(PDS 70b and PDS 70c being the only cases at the time of writing (Keppler et al., 2018; Müller et al., 2018; Haffert et al., 2019).

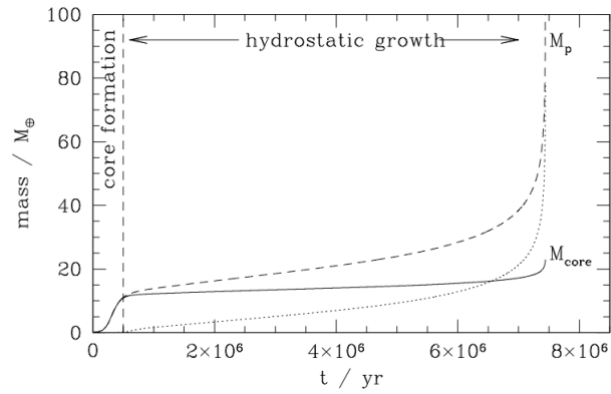


Fig. 1.13: Mass growth of a forming giant planet over time. Accretion of gas (XY) and solid (Z) occur concurrently, but most of the final mass is accreted over a short period of exponential growth, which stops when the resulting planet reaches gravitational isolation from the background. This model is referred to as the "runaway accretion" model for giant planets. This figure was kindly provided by Elena Lega and is adapted from Pollack et al. (1996).

accreting disk. In chapter 5, I derive theoretical predictions for the dynamical signatures of giant vortices, which are proposed to be the formation sites of planetesimals. I then simulate observations of the thermal radiation of dust as well as scattered light from these vortices in chapter 6. Finally, I give a review of my work as a software engineer in developing a promoting open source tools that I used.

Prerequisites in hydrodynamics

” *As the man said, for every complex problem there’s a simple solution, and it’s wrong.*

— **Umberto Eco**
Foucault’s Pendulum

As humans, we are most familiar with the solid state of matter; all the while being ourselves mainly composed of liquid water. However, the vast majority of ordinary matter in the Universe, present and past, exists in fluid states. Namely gas, liquid and plasma. For this reason, fluid dynamics is essential in many branches of astrophysics. It is the fundamental branch of physics that is applied and developed in studying the internal motion of stars and planets, as well as the interstellar medium, individual galaxies and groups they form, up to the very largest scales accessible in the visible universe.

Since the work of Newton, the work of a theoretical physicist consists in describing natural phenomena with *differential equations*, that is, equations whose solutions are functions of space, time, and everything in between. This approach proved fruitful in all branches of physics, from quantum mechanics to general relativity, and hydrodynamics is no exception. *Solving* a differential equation means finding a family of mathematical functions that satisfy it.

2.1 Elements of general hydrodynamics

2.1.1 Fundamental equations of hydrodynamics

The fundamental equations governing fluid dynamics are written as conservation laws for mass and linear momentum respectively. In their Eulerian formulation, the velocity field is attached to space and time rather than individual fluid particles, and we consider small¹ *fluid parcels* as fixed points in space, with a finite volume and external surface. Conservation of mass is captured by the *continuity equation*, which reads

$$\partial_t \rho + \nabla \cdot \mathbf{j} = s \quad (2.1)$$

where $\mathbf{j} \equiv \rho \mathbf{v}$ is the local linear momentum density, and the right-hand side represents various processes (or *source terms*) by which mass is either being added or removed from the system. It has a 0 integral if the system is *closed* (no mass is exchanged at its boundaries),

¹Not infinitely small ! The correct term is mesoscopic. The approximation is valid as long as each fluid parcel contains a statistically representative population of particles (molecules).

and mass is not being created or destroyed internally. For instance nuclear processes may transform mass into other forms of energy and vice-versa.

Conservation of linear momentum itself reads

$$\rho \frac{d\mathbf{v}}{dt} = \rho \mathbf{f} + \nabla \cdot \sigma \quad (2.2)$$

where $\frac{d}{dt} \equiv (\partial_t + \mathbf{v} \cdot \nabla)$ is the *material derivative* operator, and the right-hand side represents forces acting on the fluid, causing it to accelerate, with \mathbf{f} being the density in *body forces* (with the dimension of an acceleration LT^{-2}), while $\nabla \cdot \sigma$ is the divergence of the stress tensor, i.e. *surface forces*. Note that because σ is a matrix, this divergence is a vector.

In the case of fluids, it can be shown that $\nabla \cdot \sigma$ reduces to a pressure term and a viscosity term such as (D. Mihalas and B. W. Mihalas, 1984, pages 68-70)

$$\nabla \cdot \sigma = -\nabla P + \eta \Delta \mathbf{v} \quad (2.3)$$

Pressure is a statistical effect of collisions² between elementary components of a fluids, namely molecules for liquid and gas, and only creates a force at the macroscopic level of study in the presence of a preferential direction, hence the gradient form ; fluid elements are pushed away from higher pressure regions. Usually, pressure is related to temperature and density via a relation called *equation of state*. I will describe the relevant ones for modelisation of proto-planetary disks in the next section. *Viscosity* on the other hand is the property of a fluid that promotes transport of linear momentum through friction between fluid layers. While viscosity is challenging to define at the molecular level, it normally scales with the molecular mean free path in a gas.

Dividing each term in eq. (2.2) by ρ we obtain the Navier-Stokes equation

$$\frac{d\mathbf{v}}{dt} = (\partial_t + \mathbf{v} \cdot \nabla) \mathbf{v} = -\frac{1}{\rho} \nabla P + \nu \Delta \mathbf{v} + \mathbf{f} \quad (2.4)$$

Although it was discovered centuries ago, solving this equation remains to this day extremely challenging. Indeed, we trust that it provides a sufficiently accurate description of Nature because some analytical solutions can be found that are in excellent agreement with experimental measurements, but only in the simplest cases. Proving that the equation always has solutions in three dimensions, or disproving this postulated result by finding a counter example, constitutes one of the seven “Millennium Prize Problems” for which the Clay Mathematics Institute would award more money than a Nobel Prize.

Another conserved quantity is energy. To some extent, the fact that it is conserved through any physical process is the only global definition for energy that we have, and is formalized as the first principle of thermodynamics. There are many reservoirs for energy in a fluid. They can include, but are by no means restricted to *internal energy* (heat), *mechanical energy*, which is the combination of *kinetic* and *potential* energy and convey the energy of movement

²In the context of MHD, the total pressure includes an additional term, namely *magnetic pressure*. To clarify the notation, the term I am defining here is sometimes called *thermal pressure*.

through a potential field, and *magnetic* energy. Because energy is a scalar quantity, its conservation law takes the same form as eq. (2.1)

$$\partial_t e + \nabla \cdot (e\mathbf{v}) = s \quad (2.5)$$

where e is the *energy density* and s is again the sum of source terms, this time accounting for creation and destruction of energy. Unless nuclear processes are at play, s normally represents energy being lost or gained through the system's boundaries. Otherwise, it does not make much sense to separate mass from the rest of energy forms, thus mass conservation is included in that of energy.

In problems where heating and cooling processes are important, this equation needs to be solved along with eqs. (2.1) and (2.4).

2.1.2 Some useful definitions

1. $\nabla \cdot \mathbf{v}$ is the *compressibility* of a flow. It represents the variation of velocity with respect to space. The flow is said to be *incompressible* if and only if $\nabla \cdot \mathbf{v} = 0$ holds at every point in time and space.
2. $\nabla \times \mathbf{v}$, sometimes noted \mathbf{w} , is called the *vorticity* and quantifies locally rotational flows.

2.1.3 A word on turbulence

Flows described by eq. (2.4) can be categorized in two very distinct regimes. Namely, a flow is called *laminar* if fluid parcels move in nearly-parallel layers. Otherwise, it is *turbulent*. In such flows, external excitation will form eddies (or vortices) that cascade to smaller and smaller scales, until it is dissipated as heat. In more formal terms energy is distributed across all scales.

The usual, though insufficient criterion that determines the nature of a flow, is given in terms of the dimensionless Reynolds number Re . It can be defined as a ratio $\frac{L_0 U_0}{\nu}$ where L_0 and U_0 denote a characteristic length and velocity of the flow respectively. Flows with $Re \ll 1$ are expected to be laminar, while turbulence usually arises for $Re \gg 1$. This notion will be useful in the following section. Figure 2.1 illustrates a transition from laminar to turbulent flow.

2.1.4 A word on Magneto-hydrodynamics

In modeling flows of ionized fluids evolving in magnetic fields, additional forces need to be accounted for in eq. (2.4). Magneto-hydrodynamics, or MHD for shorts, is the branch of hydrodynamics that focuses on such flows. It provides a useful description of the hot plasma on stellar surfaces for instance. It is furthermore expected that magnetic forces play an important part at least in the innermost regions of a disk, in close relation with the stellar

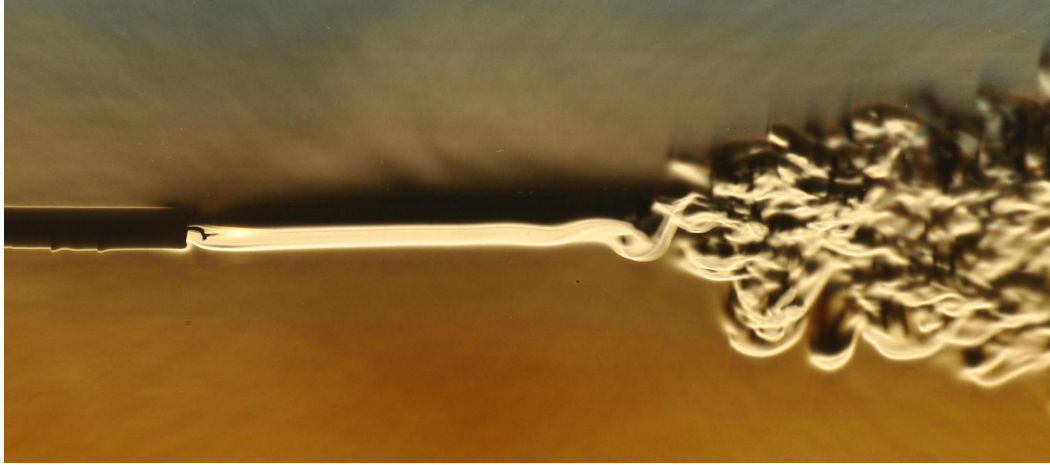


Fig. 2.1: A transition from laminar to turbulent flow in the plume of a candle. Credits: Gary Settles (CC-BY-SA).

surface. However, little to no observational constraints are currently available that would give quantitative hints on the typical magnitude of magnetic fields throughout proto-planetary disks. Moreover, MHD equations are complicated enough that they are usually reduced to facilitate their study, namely bearing the assumption that electric resistivity is negligible. This is called *ideal*-MHD. We will see in the following sections that this fundamental uncertainty sometimes comes in handy to help fill in the gaps of our understanding. However, magnetic fields are not considered in my own work.

2.2 Physics of an accretion disk

Let us now discuss the basics of a disk's physics. Namely, I will here expose the fundamental stationary solution to hydrodynamics equations for a thin disk, and discuss its stability.

2.2.1 Rotational motion

Motion of a massless body

The orbital motion of two point masses m_1 and m_2 , gravitationally bound to one another, is described by Kepler's laws. In particular, the third law gives the angular frequency of motion as a function of r

$$\Omega_K = \sqrt{\frac{\mathcal{G}(m_1 + m_2)}{r^3}} \quad (2.6)$$

This is another formulation than eq. (1.1). Correspondingly, $v_K \equiv r\Omega_K$ is the Keplerian velocity. In studying the motion of a relatively small mass m_2 orbiting a star m_1 , such as a planet, asteroid, or patch of gas, it is useful to reduce the expression to $\Omega_K \simeq \sqrt{\frac{\mathcal{G}m_1}{r^3}}$. Commonly referred to as the Keplerian rotational frequency, this approximation strictly speaking describes that of a massless particle ($m_2 = 0$), otherwise referred to as a *test particle* in the context of numerical simulations.

A stationary disk solution

A flow is said *stationary* and only if it is time-independent ($\partial_t \mathbf{v} = 0$). This notion is useful in studying the evolution of physical processes as perturbations to this equilibrium. A necessary and sufficient condition for it is that forces exerted on a fluid parcel cancel out. It is a fruitful assumption that proto-planetary disks stay close to this state for most of their lifetime, so let us now derive its implications for the velocity distribution in such a disk.

In order to apply the Navier-Stokes equation to a flow around a central mass m_* , gravitational body forces (acceleration) $\mathbf{g} \equiv \mathbf{f}_{\text{gravity}}$ need to be included. In all generality, \mathbf{g} is written as a gradient of the gravitational potential $\mathbf{g} = -\nabla\Phi$, which is itself solution to Poisson's equation (Poisson, 1827)

$$\Delta\Phi = 4\pi\mathcal{G}\rho_{\text{sys}} \quad (2.7)$$

where ρ_{sys} is the whole system's density field, including the central star. Within the approximation of a point-like star, which is valid in the disk where orbital distance is much larger than the stellar radius, Φ itself reads

$$\begin{aligned} \Phi(r, \theta, z) &= \Phi_{\text{star}} + \Phi_{\text{disk}} \\ &= -\mathcal{G}\frac{m_*}{r} - \iiint_V \mathcal{G}\frac{\rho}{r'} dr'^3 \end{aligned} \quad (2.8)$$

where r' is the distance to position (r, θ, z) , V is the integrated volume, which we can approximate by the volume of the disk itself, provided the disk evolves in relative isolation. This potential is defined up to an integration constant, here taken to be zero for simplicity. Solving the Poisson equation along with the hydrodynamics of a disk is extremely challenging. Even in simple cases where solutions can be derived, it was shown that their stability is not guaranteed (J. C. B. Papaloizou and Pringle, 1984). For light disks with mass $m_{\text{disk}} \ll m_*$ however, the contribution of the disk itself to the gravitational potential can be neglected³, which greatly simplifies the problem. Leaving only the contribution of the central star, assumed point-symmetric, the potential outside the star itself reads

$$\Phi(M) = -\mathcal{G}\frac{m_*}{r} \quad (2.9)$$

which yields, finally

$$\mathbf{g} = -\frac{\mathcal{G}m_*}{r^2}\mathbf{e}_r \quad (2.10)$$

If we furthermore assume an inviscid fluid $\nu = 0$, projecting eq. (2.4) along the radial direction, i.e. taking the dot product of every term with \mathbf{e}_r , we obtain

$$\frac{\mathcal{G}m_*}{r^2} + \frac{\partial_r P}{\rho} - \frac{v_\theta^2}{r} = 0, \quad (2.11)$$

where the right-most term stands for centrifugal forces. Hence the angular velocity of a stationary flow reads

$$\Omega \equiv \frac{v_\theta}{r} = \sqrt{\frac{\mathcal{G}m_*}{r^3} + \frac{\partial_r P}{r\rho}} \quad (2.12)$$

³The validity of this approximation is given with higher accuracy by the Toomre number (Toomre, 1964).

In a proto-planetary disk, because gravitation dominates over pressure gradients, the expression reduces as a first order Taylor expansion to

$$\begin{aligned}\Omega &= \Omega_K \sqrt{1 + \frac{1}{v_K^2} \frac{r \partial_r P}{\rho}} \\ &\simeq \Omega_K \left(1 + \frac{1}{2v_K^2} \frac{r \partial_r P}{\rho} \right) \equiv \Omega_K (1 + \eta)\end{aligned}\quad (2.13)$$

where we introduced η , which quantifies the deviation to Keplerian motion. In general, temperature and pressure are lower at large radii, so $\partial_r P < 0$, and so $\eta < 0$. In other words, gas is expected to rotate at slightly sub-Keplerian rates.

Rotational stability

Rotational equilibrium is only perennial if said equilibrium is stable. Let us now consider the case of a test particle evolving on a plane, in an axisymmetric potential $\Phi(r)$. In polar coordinates, the equation of motion writes

$$\ddot{\mathbf{x}} = -\nabla\Phi \implies \begin{cases} \ddot{r} - r\dot{\theta}^2 &= -\partial_r\Phi \\ \partial_t(r^2\dot{\theta}) &= \dot{\ell} = 0 \end{cases} \implies \begin{cases} \ddot{r} &= -\partial_r\Phi_{\text{eff}} \\ \dot{\ell} &= 0 \end{cases}\quad (2.14)$$

where we define an effective potential $\Phi_{\text{eff}} \equiv \Phi + \frac{\ell^2}{2r^2}$. A circular orbit ($\dot{r} = 0$) with constant angular velocity $\dot{\theta}$ is a particular solution to this equation. Now consider a small radial perturbation x to such an equilibrium trajectory with radius r_{eq} ($x \ll r_{\text{eq}}$). A Taylor expansion of the effective potential near the equilibrium orbit writes

$$\Phi_{\text{eff}}(r_{\text{eq}} + x) = \Phi_{\text{eff}}(r_{\text{eq}}) + \frac{1}{2} \partial_r^2 \Phi_{\text{eff}}(r_{\text{eq}}) x^2 + \mathcal{O}(x^3)\quad (2.15)$$

where the first term can arbitrarily be made 0 since Φ_{eff} is defined up to an additive constant. Thus the perturbation itself obeys the following equation of motion

$$\ddot{x} = -\partial_x \Phi_{\text{eff}}(r_{\text{eq}} + x) \simeq -\partial_r^2 \Phi_{\text{eff}}(r_{\text{eq}}) x\quad (2.16)$$

which reduces to the harmonic oscillator equation with natural frequency κ

$$\ddot{x} + \kappa^2 x(t) = 0, \text{ with } \kappa^2 \equiv \partial_r^2 \Phi_{\text{eff}}(r_{\text{eq}}) = 4\Omega^2 + 2r\Omega\Omega'\quad (2.17)$$

Two cases need be distinguished, and are illustrated in fig. 2.2.

- if $\kappa^2 > 0$, then $\kappa \in \mathbb{R}$ and a solution basis is $\{\sin(\kappa t), \cos(\kappa t)\}$, so the perturbation remains bounded through time. κ is the frequency at which the particle oscillates around its equilibrium orbit, and is called the *epicyclic frequency* in reference to geocentric theories.

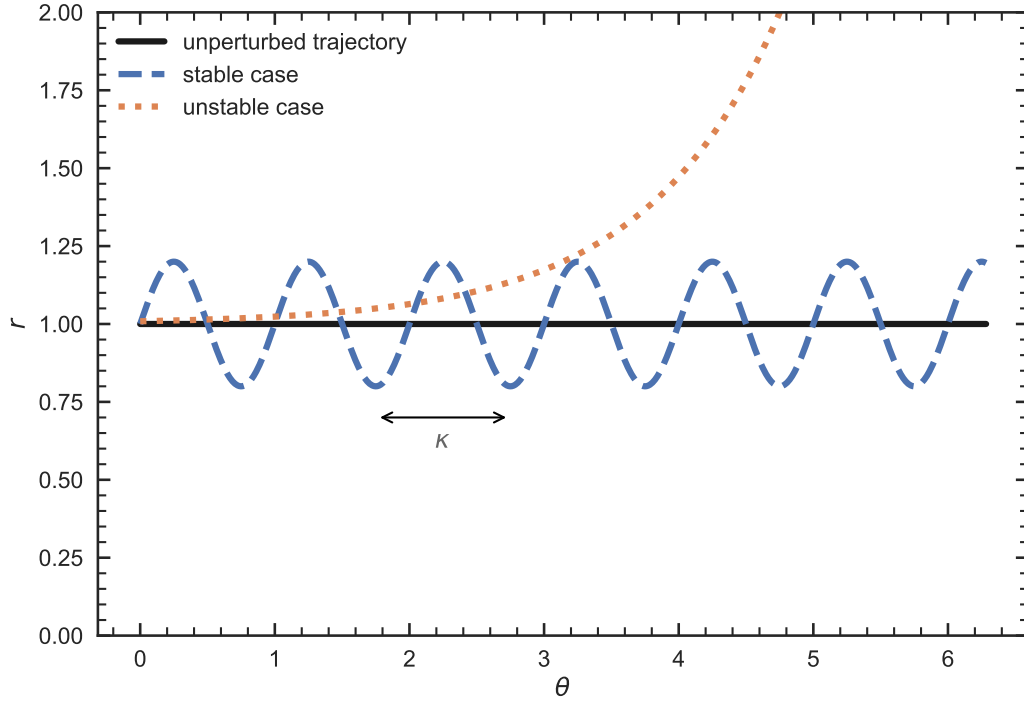


Fig. 2.2: An illustrative case comparison between trajectories of a perturbed fluid element in a rotationally stable and unstable context respectively. The amplitude of the initial perturbation in the unstable case is made 10 order of magnitude lower to help visualize both cases in one scale.

- if $\kappa^2 < 0$, then κ is a pure imaginary number, and a solution basis is given as $\{\exp(qt), \exp(-qt)\}$, where $q \in \mathbb{R}, q^2 = -\kappa^2 > 0$. Those solutions are not bounded, hence the equilibrium is unstable.

A necessary condition for rotational stability is therefore $\kappa^2 > 0$. We refer to this condition as the Rayleigh criterion after Rayleigh (1879). An equivalent phrasing of this condition is that, in a differentially rotating flow, the gradient in specific angular momentum $\ell = r^2\dot{\theta}$ must be positive.

Proof.

$$\begin{aligned}
 \kappa^2 &= 4\dot{\theta}^2 + 2r\dot{\theta}\partial_r\dot{\theta} \\
 &= \frac{2\dot{\theta}}{r}(2r\dot{\theta} + r^2\partial_r\dot{\theta}) \\
 &= \frac{2\dot{\theta}}{r}\partial_r(r^2\dot{\theta}) \\
 &= \frac{2\dot{\theta}}{r}\partial_r\ell
 \end{aligned}$$

□

2.2.2 Vertical structure of a thin disk

Geometrically speaking, a disk is a two-dimensional shape. This somewhat inaccurate term may however hold some validity still, applied to objects of negligible vertical extension. As we have seen in section 1.1.2, and in particular through fig. 1.7, at least the dust distribution in a circumstellar environment is indeed remarkably flat, so the expression seems justified. Let us now consider the vertical distribution of gas density, assumed axisymmetric, and described in cylindrical coordinates r and z . I will further assume a separable density function $\rho(r, z) = \rho_{z=0}(r)f(z)$, where $\rho_{z=0}$ is the density in the midplane ($z = 0$), and focus on the z dependence. In an equilibrium state with no vertical motion, considering only gravitation and pressure forces, we get

$$\begin{aligned} 0 &= \frac{\mathcal{G}m_*}{d^3} \mathbf{q} \cdot \mathbf{e}_z + \frac{\nabla P \cdot \mathbf{e}_z}{\rho} \\ &= \frac{\mathcal{G}m_*}{d^2} \frac{z}{d} + \frac{\partial_z P}{\rho} \end{aligned}$$

where \mathbf{q} is the position vector of the particle, with norm $d \equiv \sqrt{r^2 + z^2} = r\sqrt{1 + \left(\frac{z}{r}\right)^2}$ the local distance to the star. In the thin disk approximation $\frac{z}{r} \ll 1$, we get the Taylor expansion $\frac{z}{d^3} = \frac{1}{r^2} \left(\frac{z}{r} + \mathcal{O}\left(\frac{z}{r}\right)^2 \right) \simeq \frac{z}{r^3}$. Additionally, I will assume that temperature does not depend on elevation z ; the same must hold for the isothermal sound speed as well since $c_s^2 \propto T$. This is consistent with the assumption that the disk is geometrically thin, under the condition that stellar irradiation is the dominant source of heating. This is the *locally isothermal* paradigm, in which pressure relates to density as $P = c_s^2 \rho$, so $\partial_z P = c_s^2 \partial_z \rho$. We obtain, to first order

$$\frac{\partial_z \rho}{\rho} = -\frac{1}{c_s^2} \frac{\mathcal{G}m_*}{r^3} z = -\left(\frac{\Omega_K}{c_s}\right)^2 z \quad (2.18)$$

The solution to this differential equation is a gaussian function $f(z) = e^{-\frac{z^2}{2H^2}}$, and gives us the characteristic vertical size of the disk $H(r) \equiv c_s/\Omega_K$, called the *scale height*. The dimensionless number $h \equiv H/r$ is called the *aspect-ratio* and is usually assumed to be about 5 %.

This notion is widely used in the literature to quantify the spread of gas density around the midplane.

Implications in 2D polar simulations It is important to note that, in “razor-thin” 2D simulations (r, θ polar plane), there exist two incompatible physical interpretations of the density term ρ .

1. Maybe the most common approach is to substitute ρ in Navier-Stokes equations with a *column-integrated surface density* Σ with dimension $M.L^{-2}$, defined as

$$\Sigma(r) \equiv \int_{-\infty}^{+\infty} \rho(r, z) dz \quad (2.19)$$

which in the locally isothermal paradigm reduces to

$$\Sigma(r) = \rho_{z=0}(r) \int_{-\infty}^{+\infty} e^{-\frac{z^2}{2H^2}} dz = \sqrt{2\pi} H(r) \rho_{z=0}(r) \quad (2.20)$$

This is the approach adopted in chapters 4 and 5.

2. Alternatively, one can consider an *unstratified* disk layer. In this approach, the simulation box is assumed invariant along the z axis over a narrow vertical interval. Usually, this is done in studies focusing on the disk midplane, and shearing-box simulations.

This distinction is of particular importance when dust is included in the simulation and the drag force needs to be computed, as we will see in section 2.2.4.

2.2.3 Accretion and the hypothetical role of viscosity

An unknown dissipative mechanism It is currently unknown exactly how the lifecycle of a proto-planetary disk ends. There is observational evidence that the disk's mass is at least in part deposited onto the host star throughout its lifetime. It is characterized as an excess in hot continuum (IR) in the stellar spectrum, as compared to a pure black body SED. Studies conducted over a few hundred young stellar objects set the typical timescale for disk dissipation through accretion at ~ 6 Myr (Hartmann et al., 1998; Gullbring et al., 1998; Haisch et al., 2001). More recent works showed that the typical accretion rate increases with stellar mass and decreases with time (Jayawardhana et al., 2006; Manara et al., 2012), but the conclusion still holds that accretion rarely occurs around stars older than ~ 10 Myr. This is an important constraint on the planet formation timescales.

While mass deposition is observed on the surface of stars, it is commonly assumed that the accretion flow is not local, but rather, takes place globally throughout the disk. Such a flow must however be supported somehow. Angular momentum dissipation by friction is an obvious candidate, and in particular, dissipation through turbulence must be considered.

Turbulent viscosity As I said, viscosity is the physical property of a fluid that promotes transport in momentum. In the broad context of hydrodynamics, the term most often invokes a property emerging at the molecular level, and quantifies friction. Here, I refer to this property as the *molecular viscosity* and denote it ν_{mol} . It is approximately given as $\nu_{\text{mol}} \sim \lambda c_s$ where λ is the molecular mean free path. In the case of a circumstellar disk at $r_0 = 10$ AU, estimating the molecular number density $n = 1 \times 10^{12} \text{ cm}^{-3}$ and the collisional cross section $\sigma_{\text{mol}} = 2 \times 10^{-15} \text{ cm}^2$, we get $\lambda = 1/n\sigma_{\text{mol}} \sim 50 \text{ cm}$ (Chapman and Cowling, 1970; Armitage, 2009). Now to estimate the Reynolds number around r_0 , taking $L_0 = H(r_0) = 0.5 \text{ AU}$, and $U_0 = c_s$, we get

$$\text{Re} = \frac{L_0 U_0}{\nu_{\text{mol}}} = \frac{H c_s}{\lambda c_s}(r_0) = \frac{0.5 \text{ AU}}{50 \text{ cm}} \simeq 1.5 \times 10^{11} \gg 1 \quad (2.21)$$

This stupendously large number indicates that disks should turn highly turbulent, on the condition that some instability is able to excite turbulent motion.

Correspondingly, Shakura and Sunyaev (1973) showed that, at scales larger than the typical eddy size, turbulence could be modeled as a viscous term. From dimensional considerations, the effective viscosity ν (L^2T^{-1}) may not be active at scales larger than that of the disk itself H (L), while the typical velocity of eddies is bounded by the sound speed c_s (LT^{-1}). Thus, we may define a dimensionless number α such as

$$\alpha \equiv \frac{\nu}{Hc_s} \quad (2.22)$$

which in all practical situations should be lower than 1. This is commonly referred to as the α -viscosity model and is widely used throughout the literature.

What is left to answer here is exactly what instability(ies) could excite turbulence. A promising candidate was found in weakly magnetised MHD models. Namely, a rotational instability similar to but distinct from the one illustrated in section 2.2.1 arises when the flow is weakly magnetised. It is called the magneto-rotational instability (MRI) and was first applied to the theory of proto-planetary disks by Balbus and Hawley (1991). Their derivation was conducted within the frame of ideal MHD, and their conclusion was that MRI would efficiently excite turbulence in a reasonable disk model. Unfortunately it has been shown that some regions of the disk were in fact stabilized by non-ideal effects, defining a *dead zone* of magnetically inactive material (Blaes and Balbus, 1994; Gammie, 1996). This conclusion was repeatedly extended in further works (Jin, 1996; Wardle and Ng, 1999; Desch, 2004; Dzyurkevich et al., 2013, e.g.), leading to a progressive extension of the dead zone, to the point that the term is now mostly historical, since in current views, only the surface layers of a disk may still be subject to the instability. After thirty years of intensive research, the hunt for a turbulence-driving mechanism in disks is still going.

2.2.4 Aerodynamics of solid particles

Drag forces

Interaction between solids and the gaseous background occurs through friction. For dust particles up to a few mm, in a proto-planetary disk, the Epstein drag regime is normally relevant, since the mean free path of gas molecules is much larger than the dust particle size (Paardekooper, 2007). Unfortunately, the complete expression of the corresponding drag force is impractical from the numerical standpoint (Schaaf, 1963). Sacrificing a small amount of accuracy however, one can find two asymptotic limits of this law. Assuming the velocities of the background follow a Maxwellian distribution around the thermal velocity v_{th} , and defining the *relative velocity* $\delta v \equiv |v_g - v_d|$, we get

$$\begin{cases} F_{\text{drag}} = c_1 \rho_g s_p^2 \delta v v_{th} & , \quad v \gg v_{th} \\ F_{\text{drag}} = c_2 \rho_g s_p^2 \delta v^2 & , \quad v \ll v_{th} \end{cases} \quad (2.23)$$

where c_1 and c_2 are dimensionless coefficients that encapsulate the shape of the grains, and are close to unity in the case of spheres. Then, the full law is approximated in a digestible

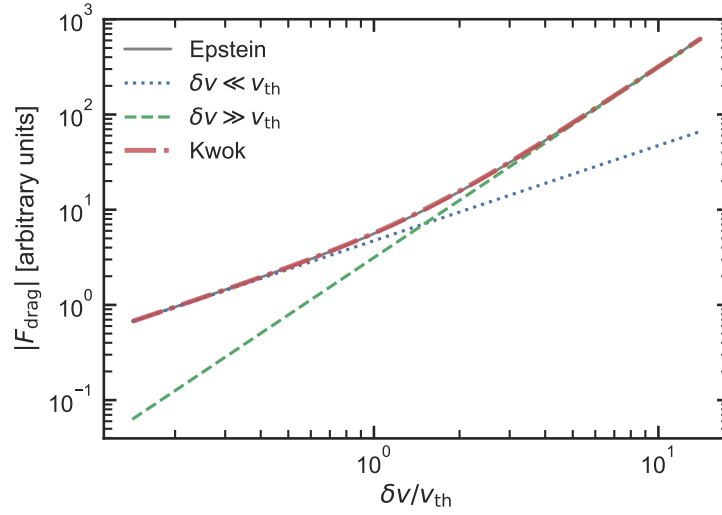


Fig. 2.3: Relative drag intensity in three models as a function of the $\delta v/v_{\text{th}}$ ratio. The Kwok formula connects both classical asymptotic drag regimes. The complete expressions for the Epstein regime and the associated limits are taken from (Paardekooper, 2007). I note that equations 7 (lower velocities case), 8 and 9 therein required a correction of $\times 1/\sqrt{2}$ in order to fit the narrative. I did not inquire further on the source of this error.

form thanks to a useful “adapter” model that connects well with both asymptotic regimes was presented by Kwok, 1975

$$F_{\text{drag,Kwok}} = c_{\text{Kwok}} \rho_{\text{g}} s_{\text{p}}^2 v (v_{\text{th}}^2 + v^2)^{1/2} \quad (2.24)$$

Figure 2.3 represents these practical drag functions graphically, along side with the complete Epstein function, and in the vicinity of the transition.

The typical timescale attached to drag is usually referred to as the particle *stopping time* t_{stop} , over which the relative velocity v is damped out through friction, and can be defined as follows

$$t_{\text{stop}} \equiv \left| \frac{m_{\text{p}} v}{F_{\text{drag}}} \right| \quad (2.25)$$

where m_{p} is the particle mass. In the case of the Kwok drag formula, this expression reduces to

$$t_{\text{stop,Kwok}} = c_{\text{Kwok}} \frac{m_{\text{p}}/s_{\text{p}}^2}{\rho_{\text{g}} (v_{\text{th}}^2 + v^2)^{1/2}} = \frac{4\pi}{3} c_{\text{Kwok}} \frac{\rho_{\text{p}} s_{\text{p}}}{\rho_{\text{g}} (v_{\text{th}}^2 + v^2)^{1/2}} \quad (2.26)$$

where c_{Kwok} not only accounts for the particular geometry, but also for the grain “stickiness”, and ρ_{p} is particle intrinsic density.

The dimensionless ratio between this timescale and the orbital one Ω^{-1} defines the *Stokes number* $St \equiv \Omega t_{\text{stop}}$. We will see in the following that this number is useful to describe the phenomenology of gas-particles interactions.

On the pressureless fluid approximation

There are a handful of ways to include dust dynamics in the hydro simulations. For simplicity, it is often treated as a *pressureless fluid*, which means that the dynamics of solids is assumed to follow the Navier Stokes equations eq. (2.4), without pressure forces, with the drag forces coupling the gas and dust dynamics

$$(\partial_t + \mathbf{v}_g \cdot \nabla) \mathbf{v}_g = -\frac{1}{\rho_g} \nabla P + \nu \Delta \mathbf{v}_g + \mathbf{f}_{\text{gravity}} - \mathbf{f}_{\text{drag}} \quad (2.27)$$

$$(\partial_t + \mathbf{v}_d \cdot \nabla) \mathbf{v}_d = \mathbf{f}_{\text{gravity}} + \mathbf{f}_{\text{drag}} \quad (2.28)$$

where $\mathbf{f}_{\text{drag}} \propto (\mathbf{v}_g - \mathbf{v}_d)$, and in the simplest case of a single dust species. Hersant (2009) and Jacquet et al. (2011) have shown that, in studying the vertical settling (see following paragraph) and streaming instability respectively, this approximation is only valid as long as drag forces do not dominate the dynamics, or equivalently $\text{St} \lesssim 1$. At a given position r (thus fixing Ω), this means that the pressureless fluid approximation is only valid down to a critical particle size s_p^* . It must be observed that, as pointed out by Hersant (2009), pressure in solids is not only an effect of collisions but can also appear as a consequence of velocity dispersion, so it is preferable to refer to this approximation as the pressureless limit rather than the collisionless one.

Solid concentration in pressure traps

Because external forces exerted on solids and gas are the same, if they balance out in an attractor location, or in other terms if there exists a location of stable equilibrium, then *both* gas and solids will tend to accumulate there. Rather counter-intuitively, this is often summarized by saying that dust is attracted into pressure maxima. In particular this can be shown analytically in the simple case of an inviscid gas ($\nu = 0$), within the *terminal velocity approximation*, where time derivatives of relative velocity go to zero, and where eqs. (2.27) and (2.28) can be reduced to

$$\Delta \mathbf{v} = t_{\text{stop}} \frac{\nabla P}{\rho_g} \quad (2.29)$$

In the context of circumstellar disks, this has several implications that are essential to consider within the perspective of forming planets, which I review in the following.

Radial drift Perhaps the most important consequence is that, because gas density and pressure are in general decreasing functions of r , solid particles will drift inwards. As we saw early (see section 2.2.1 and in particular eq. (2.11)), gas is supported by pressure, which is pushing outwards, and as a consequence the background velocity $\Omega < \Omega_K$. On the other hand, since pressure does not apply to solids, their equilibrium rotational speed is exactly Keplerian. Solids then feel a *headwind* from the background, and tend to lose angular momentum, thus they drift inwards (Whipple, 1972). As a consequence, a monotonic (decreasing) radial pressure distribution causes grains to be steadily lost as they reach the

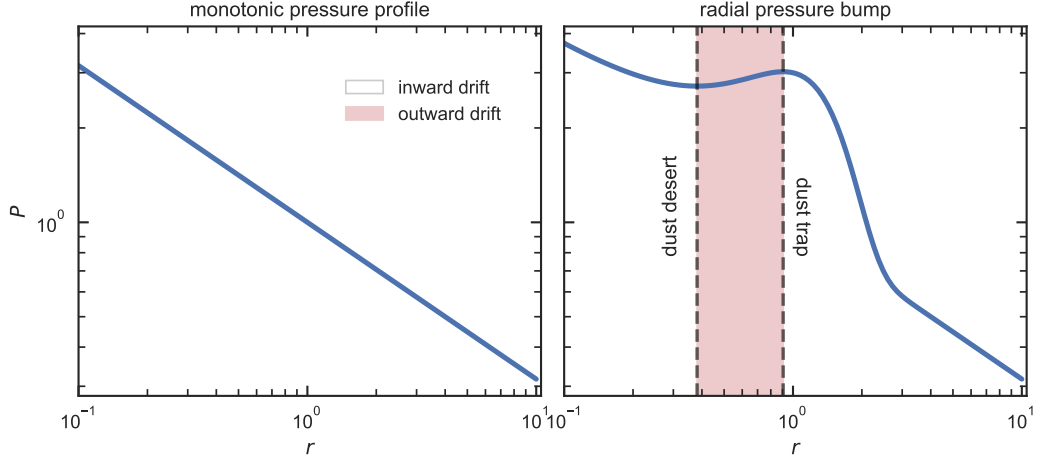


Fig. 2.4: In a non monotonic pressure gradient, the solid drifting direction is locally reversed, creating a pair of stable and unstable orbits where the gas is locally rotating at a Keplerian rate.

innermost regions, hotter than their sublimation temperature (~ 1500 K) in a few million years. This is a major hurdle for planetary formation and is known as the *drift barrier*.

In the particular case where pressure is *not* a monotonic function of r and features a local maximum, the background locally becomes super-Keplerian, which reversely leads to a backwind, reversing the drift direction outward. This is illustrated by fig. 2.4, which schematically shows that such a configuration in the background pressure will effectively act as a radial dust trap, not unlike the dusty rings observed in a large number of resolved systems, see fig. 1.9.

Azimuthal concentration Dust can furthermore concentrate azimuthally. One possible route to achieve azimuthal asymmetries such as seen in fig. 1.9 (c), is found in vortices. A vortex can be defined as a local structure with high vorticity $\omega \equiv \nabla \times \mathbf{v}$ relative to the background flow. In the context of a background in rotation Ω , a vortex can either be rotating flow-wise $\omega \cdot \Omega > 0$, which we refer to a *cyclonic* motion, or anti-flow-wise $\omega \cdot \Omega < 0$ which we call *anti-cyclonic* motion. It is useful here to consider what happens in the reference frame corotating with a vortex. Because such a reference frame is not inertial, fictitious (or geometric) forces apply there, namely Coriolis forces. A simple vortex toy-model can be described in an inviscid fluid $\nu = 0$ in a stationary state $\partial_t \cdot = 0$. Taking $\mathbf{f} = -2\Omega \times \mathbf{v}$ in eq. (2.4) we get

$$2\Omega \times \mathbf{v} + \frac{1}{\rho} \nabla P = 0 \quad (2.30)$$

This condition is called the *geostrophic* approximation, where Coriolis forces and pressure forces cancel out. A direct consequence is that at equilibrium, cyclonic/anti-cyclonic vortices must be local pressure minima/maxima respectively (not unlike cyclones/anti-cyclones in the Earth's atmosphere). This is illustrated schematically in fig. 2.5. Since pressure does not affect solid, it follows that in anti-cyclonic vortices, Coriolis forces tend to concentrate solids, while cyclonic vortices are naturally solid-depleted. Furthermore, because the Keplerian rotation of the background is differential $\Omega_{\mathbf{K}}(r)$, radially extended vortices undergo a shear. This means that cyclonic motion is unstable since it goes against the flow, as illustrated in fig. 2.6. For this reason, it is expected that all large vortices in proto-planetary disks

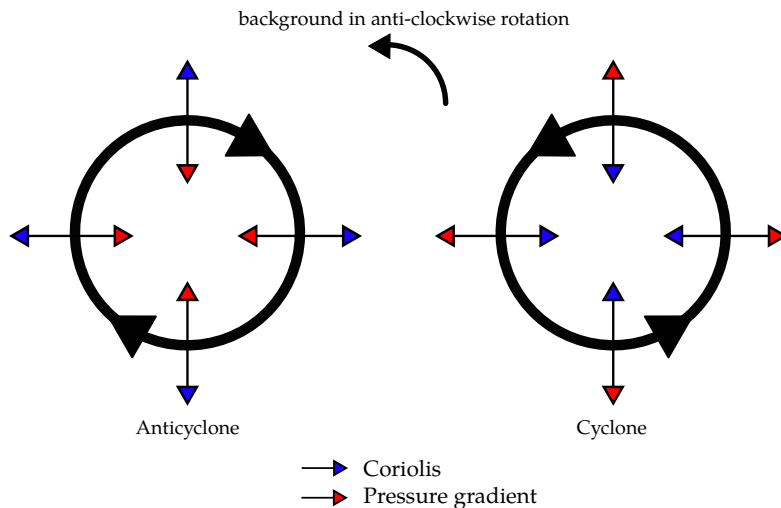


Fig. 2.5: A schematic representation of rotational balance between Coriolis forces (blue) and pressure gradient forces in gaseous vortices in a globally rotating background. Anticyclonic motion correlates with a pressure maximum and vice versa.

are in fact anti-cyclonic, and thus correspond to pressure maxima, and hence act as solid attractors.

The concentration timescale is minimized for grains with $St \simeq 1$. In the limit $St \rightarrow +\infty$ (large grains), grains are barely affected by the gas flow and follow Keplerian trajectories, while in the $St \rightarrow 0$ (small grains), their motion is fully coupled with that of the gas, so they follow elliptical trajectories around the vortex eye (in the frame corotating with it). In both these limits, concentration is infinitely slow.

Because of this effective dust-concentrating mechanism, vortices were proposed to be a promising location for solid growth by coagulation. This is further supported by the fact that, since grains undergo a coherent flow, their relative velocities should be low enough to avoid destructive collisions (Barge and Sommeria, 1995; Tanga et al., 1996; Chavanis, 2000), overcoming the so-called *collisional barrier*. Once trapped, grains will also stop drifting radially (relative to the vortex), so this mechanism also provides a convenient solution to the drifting barrier.

A handful of hydrodynamical instabilities are known to form sizeable vortices in razor-thin 2D setups. Namely the Zombie Vortex Instability (ZVI) (Marcus, Pei, Jiang, Joseph A. Barranco, et al., 2015; Marcus, Pei, Jiang, and Joseph A. Barranco, 2016; Joseph A Barranco et al., 2018), the subcritical baroclinic instability (Geoffroy Lesur and John C B Papaloizou, 2010) or the Rossby Wave Instability (Lovelace et al., 1999; H. Li, Finn, et al., 2000; H. Li, Colgate, et al., 2001). I give further detail about the latter in chapter 5, as this is the instability I used to generate large vortices in my study of their observable dynamics signatures.

Interestingly, the Rossby Wave Instability is expected to occur on the edge of gaps carved by rapidly-formed giant planets. Their longevity against turbulent viscosity is however non-

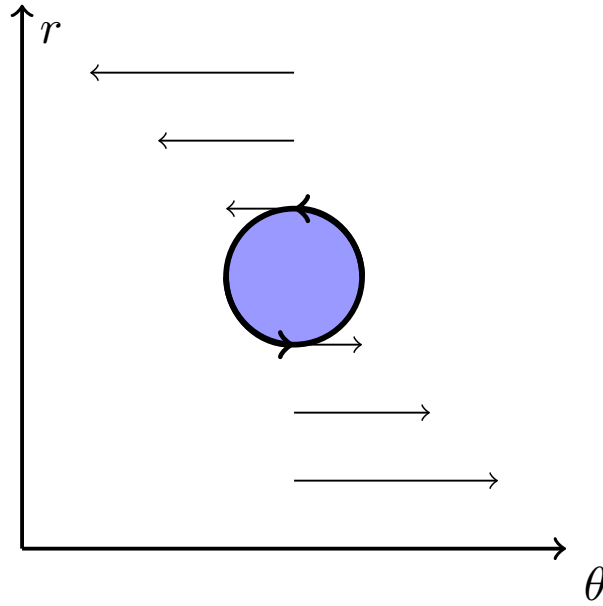


Fig. 2.6: A schematic view of an anti-cyclonic vortex represented in polar coordinates. The background differential flow is shown as arrows in a corotating frame. The vortex (blue) is here rotating anti-clockwise. It can be seen that inverting its rotation direction would make the vortex work against the background flow, which would destroy it.

monotonous (Fu, H. Li, Lubow, and S. Li, 2014), but it is generally accepted that they do not survive for significant time at viscosity $\alpha \gtrsim 1 \times 10^{-5}$. Their ability to survive their inevitable enhancement in dust-to-gas mass ratio up to unity is also debated (Fu, H. Li, Lubow, S. Li, and Liang, 2014; Surville et al., 2016), though it was pointed out that their commonly observed early destruction is most likely a side-effect of two-dimensional studies, while they could be much longer-lived in 3D (Lyra et al., 2018). Overall, it is not widely accepted that vortices obtained in simulations compare well with the reality of proto-planetary disks.

Vertical sedimentation As we saw previously in section 2.2.2, the vertical extension of the gaseous background is supported by vertical pressure gradients. Here again, we can jump to the immediate conclusion that pressureless solids will collapse towards the disk midplane. This is apparent when considering the case of a particle with non-zero inclination $i > 0$. As it is hit by gas particles with planar velocities ($v_g \cdot e_z = 0$), the drag force $f_{\text{drag}} \parallel v_g - v_d$ acts as an upwind and tends to dissipate inclination, as illustrated by fig. 2.7.

Dubrulle et al. (1995) showed that a first order solution for the stationary vertical distribution of solids was still Gaussian, with an effective scale height that depends on the Stokes number and in general $H_d(\text{St}) < H_g$. Follow up works with MHD simulations further showed that the distribution departs significantly from this simple solution for $z \ll r$ (Fromang and Nelson, 2009; Riols and G. Lesur, 2018).

Turbulence, as well as large-scale hydrodynamical instabilities such as the vertical shearing instability (E. Chiang, 2008), or the Kelvin-Helmoltz instability (Joseph A. Barranco, 2009) might hinder the settling process and provide stirring in the dusty layers of a disk. See e.g. (Armitage, 2009, 4.2, p 112) for a quantized discussion about this problem.

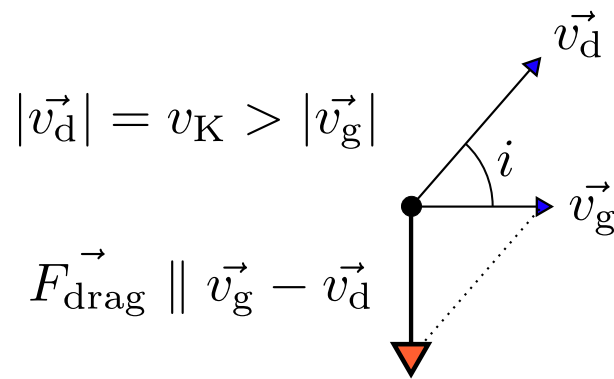


Fig. 2.7: A schematic representation of inclination dampening as a result of drag forces (red).

Methods: Numerical Hydrodynamics

” *In this house we obey the laws of thermodynamics !*

— **Homer J. Simpson**
The Simpsons

Numerical simulations fall somewhere in between theoretical works and experimental physics. They are used to approach solutions to well established equations that are too complicated for analytical solving, when lab experiments cannot be conducted either because of size, time, or money limitations. Most astrophysical systems typically evolve on timescales far greater than human lifespans, which limits the scope of what can be studied purely through observational means, and strongly motivates the resort to numerical experiments.

Moreover, it is often unfeasible to find analytical solutions to eqs. (2.1) and (2.4), which is another reason why simulations are needed. The original equations describe matter as a set of *continuum* fields such as density and velocity, i.e. those quantities are defined at every point of space and time. On the other hand, a computer works with a finite amount of resources, most importantly physical memory. This means that, in order to represent the state of a fluid for a computer to evolve, equations must first be discretized. There are two main approaches to the discretization process for hydrodynamics. One can either represent a finite set of fluid particles, which is the Lagrangian approach of hydrodynamics and correspond to the smoothed-particle hydrodynamics (SPH) numerical paradigm, or rather represent a finite set of spatial positions and attach the state of a fluid to them. This is the Eulerian grid-based approach of hydrodynamics, and the one I used throughout my thesis. The spectral approach is fundamentally different and relies on Fourier formalism. In that paradigm, a finite set of wavelengths are considered in a simulation.

Whatever the approach, the numerical *box* must be restricted to a finite *domain*. Those words may be used interchangeably.

Of course the ability to solve complicated differential equations numerically comes at a price, as there are a handful of ways numerical errors can grow over time and make the end result completely unrealistic.

In this chapter I will cover some of those difficulties for grid-based Eulerian hydrodynamics codes, and the way they are controlled or overcome. I will also introduce the specifics of two such programs that I used throughout my thesis. Namely Fargo and AMRVAC.

3.1 Discretization and its consequences

To solve a set of partial-derivative equations (PDE) as eqs. (2.1) and (2.4), one must write them in discrete form. For the sake of simplicity, let us assume a 1D problem along the direction x . w_n^i denotes the value of a scalar field w at position i at time n , counted as integer multiples of a finite space step and time step respectively. The state of the system is noted as a vector \mathbf{q}_n , which contains all variables w at time n . Partial derivatives operators need discretization too. I will note $\bar{\partial}$ their discrete counterparts. They are obtained by truncating the Taylor expansion of the continuous derivative definition. For instance at first order

$$\begin{aligned}\partial_x w &= \lim_{\delta x \rightarrow 0} \frac{w(x + \delta x) - w(x)}{\delta x} \\ &= \frac{w^{i+1} - w^i}{x^{i+1} - x^i} + \mathcal{O}(\delta x^2)\end{aligned}\tag{3.1}$$

where the first term is the *upwind difference*. An important point is that the definition for the discrete derivative is not unique even with fixed order. For instance the centered difference provides an equally valid expression

$$\bar{\partial}_x w \equiv \frac{w^{i+1} - w^{i-1}}{x^{i+1} - x^{i-1}}\tag{3.2}$$

A *scheme* is an algorithm that evolves the state of the system, from date t to $t + \delta t$, and can be simply represented as

$$\mathbf{q}_n \rightarrow \mathbf{q}_{n+1}\tag{3.3}$$

For algebraic problems, a scheme can be formalized as a matrix operator $\mathcal{M}(\mathbf{q}_n)$, whose coefficients encode the equations to be solved in terms of the chosen discrete derivatives. The *order* of a scheme corresponds to the order of truncation in the Taylor expansion of the derivative operator. Usually, higher order schemes require larger *stencil*, i.e. a larger number of neighboring cells are taken into account in the discrete derivative computation. The matrix is three-diagonal for first order schemes, i.e. information is propagated between immediate neighboring cells over a single time step. It is five-diagonal for second order schemes and so on.

Numerical stability is the property of a scheme that creates bounded errors. As anywhere in the vast realm of science, the quality of a result may be judged by the confidence in the way the errors are controlled or measured. It is thus an essential requirement for any scheme to produce realistic solutions, though obviously not a sufficient criterion.

An *explicit* scheme reads

$$\mathbf{q}_{n+1} = \mathcal{M}\mathbf{q}_n\tag{3.4}$$

which is straightforward to implement but numerically unstable for *stiff* problems, as hydrodynamics. One inelegant way around this problem is to limit the time step to very small values. A better solution is to use *implicit* schemes instead

$$\mathbf{q}_n = \mathcal{M}\mathbf{q}_{n+1}\tag{3.5}$$

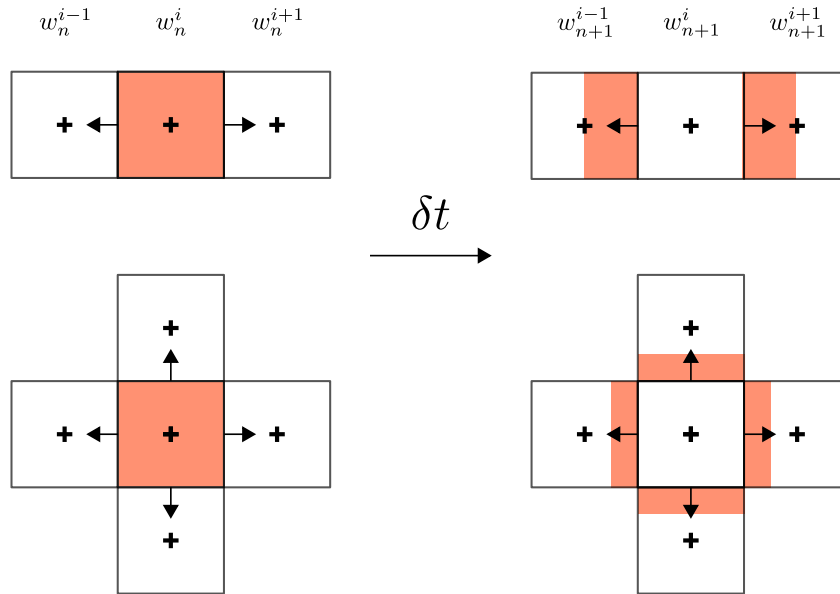


Fig. 3.1: A schematic representation of a pathological case of discrete advection of a scalar field w over time step δt of maximal duration. The one and two-dimensional cases lie on the top and bottom rows respectively. Arrows represent the velocity field. At $t = n$ (left), the density w is zero in neighbor cells, while the velocity field is fully divergent with uniform norm. At $t = n + 1$ (right), the central cell is empty and its “mass” (cell integral for w) is completely distributed over its neighbors. The CFL condition (eq. (3.6)) sets an upper bound to the duration of a time step such that the total mass may be conserved.

This alternative formulation is intrinsically stable, though harder to implement and requires an additional step to compute the inverse matrix \mathcal{M}^{-1} , which further alters the computational speed in a parallel program since it requires frequent communications between processors. For this reason, explicit schemes are still preferred in the field of hydrodynamics¹, but one needs some systematic rule to limit the time step.

Time discretization Numerical stability in explicit schemes is only achievable up to a maximal time step. It is constrained by several criteria. The fundamental one was defined by Courant et al. (1928). Namely, the time step δt can be at most such that the whole mass (or any scalar advected quantity) contained in a cell is transported to its neighbors over one time step. This rule is named the CFL condition (after Courant Friedrichs and Lewy). Formally

$$\delta t \leq \frac{1}{2n_{\text{dim}}} \frac{\delta x}{v_x} \quad (3.6)$$

where $2n_{\text{dim}}$ is the number of neighbors of any given cell in a cubic mesh.

Figure 3.1 illustrates this rule with a pathological case study. One can see that the physics of diffusion is rather poorly mimicked as the central cell winds out completely empty when the time step is strictly maximized. For this reason, the actual time step selected during computation is often written $C \frac{1}{2} \frac{\delta x}{v_x}$ where $0 < C < \frac{1}{n_{\text{dim}}}$ is the Courant number.

¹Unless the time step required for stability is too small to provide numerical results in a reasonable computational time. An example is the diffusion equation which is solved in general with an implicit scheme.

Numerical diffusion It can be shown that an explicit scheme based on centered differences is unstable and produces unbounded numerical oscillations. However, the upwind difference, which yields more stability, can be re-expressed as

$$\begin{aligned}
 \frac{w^{i+1} - w^i}{\delta x} &= \frac{w^{i+1} - w^{i-1}}{\delta x} - \frac{w^i - w^{i-1}}{\delta x} \\
 &= \frac{w^{i+1} - w^{i-1}}{2\delta x} - \frac{w^{i+1} + 2w^i - w^{i-1}}{2\delta x} \\
 &= \frac{w^{i+1} - w^{i-1}}{2\delta x} - \delta x \frac{w^{i+1} + 2w^i - w^{i-1}}{2\delta x^2}
 \end{aligned} \tag{3.7}$$

where the first term in the right-hand side is the centered difference and the second term corresponds to a diffusion term, as would arise from the discretization of a diffusion equation

$$\partial_t w - D \partial_x^2 w = 0 \tag{3.8}$$

where we obtained a diffusion coefficient $D \propto \delta x$. This short demonstration is adapted from (Dullemond, 2009). In other words, the stability of the numerical scheme is only achieved at the cost of an artificial diffusivity that is not found in the equations we solve (for instance inviscid Navier-Stokes), and is inversely proportional to spatial resolution. This is a general property in numerical solvers, and the reason why numerically solving the Euler equation (inviscid Navier-Stokes) is not possible. This *numerical diffusivity* is also called *numerical viscosity*. It is not trivial to estimate it in practice, for it depends on the bulk velocity. However, most studies assume or exhibit a much higher physical viscosity, making numerical diffusion irrelevant and negligible. This becomes an issue when one needs to explore the low viscosity regimes.

3.2 Temperature as a prescription

One important property of a fluid that I eluded in the introduction is temperature. In general, it is described as an internal energy reservoir and is accounted for through the energy conservation equation eq. (2.5). In a proto-planetary disk, thermal energy is not only transported via convection and conduction but also radiation ; light is emitted and absorbed by the medium. In order to account for radiation in a simulation, one needs to include some sort of model for light propagation, namely *radiative transfer*. However solving transfer equations is computationally expensive, so it is generally avoided in most hydrodynamics libraries and codes. Under the assumption that the typical timescale over which thermal equilibrium is restored is much shorter than the dynamical timescale $\tau_{\text{dyn}} = \Omega_K^{-1}$, this simplification is justified.

In this framework one can prescribe temperature as a pure function of pressure and density instead of solving eq. (2.5). In all generality, a mathematical relation between temperature, density and pressure is referred to as an equation of state. A subclass of these are *barotropic* equations, in which pressure is a pure function of density. They constitute the solutions I adopted in my own works, though there remain different prescriptions to choose from. Another quantity that requires a proper definition is soundspeed c_s . In general, soundspeed

and pressure may be regarded as proxies for temperature in simulations that do not include an explicit temperature field.

Locally isothermal prescription In section 2.2.2, I already introduced the locally isothermal paradigm, in which the equation system is closed by $P = \rho c_s^2 = \rho H^2 \Omega^2$. Two-dimensional models often resort to that solution, for it greatly simplifies the set of equations to be solve , and are valid in regions where the cooling timescale is shorter than the dynamical one, so typically from ~ 25 AU on. Strictly speaking, the locally isothermal paradigm removes the need for an equation of state altogether, since pressure is completely defined by density and initial conditions. This also means that temperature is absent from those models, and it is common to defer to the scale-height H as a proxy. I use this prescription in chapter 4.

An isentropic prescription Another way to prescribe pressure and sound speed is to assume an isentropic system such as

$$P = S \rho^\gamma \quad (3.9)$$

where S is a constant that quantifies entropy, and γ is the *adiabatic index* (or *heat capacity ratio*) and reads $\gamma = 1 + \frac{2}{n_{\text{dof}}}$ (n_{dof} is the number of degrees of freedom), so that $\gamma = 5/3$ for a mono-atomic gas such atomic hydrogen and helium that constitute most of the disk mass. In this prescription sound speed reads $c_s^2 = \gamma P / \rho$. This is the model historically used in studies of Rossby vortices (Lovelace et al., 1999; H. Li, Finn, et al., 2000; H. Li, Colgate, et al., 2001) and the one I adopt for my own work with these vortices in chapter 5.

An important aspect that is often eluded in the literature is the dimensionality of the constant S and in particular its effect on the interpretation of results. In particular in 2D, its dimensionality $[S]$ depends on the choice for density and pressure

- with density ρ and pressure P , we get $[S] = M^{1-\gamma} L^{3\gamma-1} T^{-2}$
- however, if we substitute surface density Σ and vertically integrated pressure p , we get $[S] = M^{1-\gamma} L^{2\gamma} T^{-2}$

This distinction is important when one needs to re-inject physical dimensionality in order to interpret the simulation results. In particular, without attention to this aspect, the re-scaling of sound speed is completely biased.

3.3 FARGO

FARGO (Fast Advection in Rotating Gaseous Objects) was designed to study planet-disk interactions (F. Masset, 2000). It is a grid-based code, and integrates point-like masses to represent planets. An integrated n-bodies solver handles the planet-to-planet interactions while planets and the background disk contribute to the gravitational potential.

I review here some specifics of the planet-disk modelisation.

Staggered gridding FARGO uses the *finite elements* discretization paradigm, in which the primary variables (ρ, v) are represented by their exact values at point-like locations. Noting that in eqs. (2.1) and (2.4), the time derivatives in ρ and v contain terms that write as space derivative of one another, it is convenient to define density and velocities at separate locations. Namely, the density is defined at the cell centers while velocity components are defined on the cell edges.

The Fargo algorithm As we saw earlier, the integration time step in a simulation is constrained by the velocities in the fluid. Indeed, the whole grid is constrained by the cell(s) where the CFL criterion is the most strict. Now in a disk close to Keplerian rotation, the fastest cells are always the innermost ones, since motion is in general largely dominated by rotation, and Keplerian azimuthal velocities v_K are greater at lower radii. However, as long as the disk is close to axial symmetry (in density and azimuthal velocities), the *net* azimuthal flux seen by any given cell remains close to zero, since the mass gained over a single time step from the “behind” neighbor is nearly identical to the mass ceded to the “before” cell. F. Masset (2000) first presented a way to exploit this property to improve computational performance by reducing the CFL criterion and apply it to the perturbed azimuthal velocity rather than the full field. Namely, the azimuthal velocity is decomposed as

$$v_\theta = v_K + \tilde{v}_\theta \quad (3.10)$$

where $\tilde{v}_\theta \ll v_K$ and the CFL condition eq. (3.6) becomes

$$\delta t \leq \frac{1}{2n_{\text{dim}}} \frac{r_{\text{min}} \delta \theta}{\tilde{v}_\theta} \quad (3.11)$$

where r_{min} is the lower radial boundary in the grid. This method yields a performance boost of about a factor 15 in terms of computational time². The FARGO algorithm is portable outside of the original implementation in the FARGO code and is available in other libraries as well, such as PLUTO (Mignone et al., 2007) and Athena++ (Stone et al., 2020).

Point-like planets Planets are treated as point-like masses in interaction with each other and the gas. The planet-to-planet interaction is carried out by a fifth order explicit Runge-Kutta integrator. It must be noted that such an integrator is not conservative for angular momentum, hence it is not suited for accurate n-bodies simulations.

Following eq. (2.8), and omitting the arbitrary constant k for simplicity, the total gravitational potential $\Phi(M = (r, \theta))$ reads

$$\begin{aligned} \Phi(r, \theta) &= \Phi_{\text{star}} + \Phi_{\text{planets}} + \Phi_{\text{disk}} \\ &= -\mathcal{G} \frac{m_*}{r} - \sum_k \mathcal{G} \frac{m_k}{|\mathbf{P}_k \mathbf{M}|} - \iiint \mathcal{G} \frac{\rho}{r'} dr'^3 \end{aligned} \quad (3.12)$$

where P_k and m_k label the planets’ positions and masses respectively. It is evident that a true point-like mass inevitably creates a singularity in the gravitational potential, which leads to diverging accelerations for the gas as the planet gets closer to a cell center. A workaround this issue is to smooth out the planets’ contributions by substituting $|\mathbf{P}\mathbf{M}|$ with $\sqrt{|\mathbf{P}\mathbf{M}|^2 + \epsilon^2}$,

²The exact speedup depends on the aspect-ratio h of the disk, and is greater for small values of h .

where ϵ is a parametrized, non-zero *smoothing length*. In 2D, this is geometrically equivalent to stating that planets are orbiting in a plane with a slightly different elevation than the grid (not that it makes any physical sense though). In the limit $|PM| \gg \epsilon$, this hat trick does not affect the results in any measurable way. Close to a planet however, this affects the behaviour of gas in a non-physical way. In order to compensate for this unfortunate side-effect, one usually defines an *exclusion radius* (sometimes called “Hill cut”) around the planet, with size $\simeq r_{\text{Hill}}$. Material lying in this region is simply ignored in the computation of torques applied to the planet.

Reference frame It must be noted that eq. (3.12) is written in an inertial frame. The frame of the simulation however is centered on the star, and is not inertial in general, unless the mass distribution is point-symmetric. In other words, the mass barycenter in the simulation is not to be confused with the star position. In practice, the introduction of planets breaks this symmetry. As a consequence, the effective potential felt by planet number j in the simulation frame includes additional terms (Murray and Dermott, 1999; F. S. Masset, 2002; M.-K. Lin and John C B Papaloizou, 2010) such that

$$\Phi_{\text{eff}} = \Phi - \sum_{k \neq j} \mathcal{G} m_k \frac{\mathbf{r}_k \cdot \mathbf{r}_j}{r_k^3} - \iiint \mathcal{G} \rho \frac{\mathbf{r}' \cdot \mathbf{r}_j}{r'^3} dr'^3 \quad (3.13)$$

with k labeling other planets. These terms are usually referred to as “indirect” terms. Their importance in the evolution of the mass distribution of the disk, in particular in the aspect ratio of lopsided structures (vortices), was shown by (Mittal and Eugene Chiang, 2015; Zhu and Baruteau, 2016; Regály and Vorobyov, 2017a; Regály and Vorobyov, 2017b).

3.4 MPI-AMRVAC

“MPI-AMRVAC” stands for Message Passing Interface (MPI) Adaptive Mesh-Refinement (AMR) Versatile Advection Code (VAC). At the cost of pronounceability, this name has the advantage of being very explicit, at least for a well-informed audience. Let us take it one step closer to layman terms :

- MPI is a protocol for dispatching the computational domain between CPUs, sharing the minimal amount of data when required from time to time.
- AMR is a generic term to denote evolutive simulation grids with heterogeneous resolution levels. MPI-AMRVAC uses *octree* AMR (as opposed to *patch-based*), which means that a grid-cell is refined into $2^{n_{\text{dim}}}$ new ones. The deciding criterion for refinement is in general a weighted function of time variations in conserved quantities and a threshold value.
- VAC is the name of an ancestor code. It means that it can do anything you would expect it to, and much more ! Though in all practicality researchers use it to treat (magneto-)hydrodynamics problems, it can in principle solve any parabolic set of partial differential equations.

In the rest of the manuscript I will refer to the code simply as AMRVAC.

General features AMRVAC features a collection of physics modules (hydrodynamics, MHD, dust ...), finite-volumes resolution methods with Riemann solvers, slope limiters, and is heavily parametrized. In contrast with FARGO, AMRVAC uses *finite volumes* methods, in which advected quantities are represented by their cell-averaged values. A key difference is that finite volume solvers intrinsically conserve the volume integral of advected quantities. It is thus relevant to define linear momentum density $\mathbf{j} = \rho \mathbf{v}$ as a primary variable instead of velocity.

Its core functionalities are written in a modified version of Fortran 90 that allows to write array operations in a dimensionality-agnostic fashion, so the same source code can be used to solve problems in full 3D or reduced dimensions alike. This comes at the cost of preprocessing the source files for a specified dimensionality ahead of compilation, which also makes debugging a lot harder sometimes.

AMRVAC is in fact a programming framework rather than a program, so running a simulation takes more effort than writing a parameter file. Indeed, one first needs to define the problem to be solved with initial conditions and boundary conditions. This is done by writing specific routines required by the main loop, that are not pre-defined. There is also a number of optional entry points, in the form of routines pointers, that allow to override existing routines with user-defined ones. An example of such an entry point is the routine defining the gravity field.

Reducing the geometry of an accretion disk Within the vast possibility tree that MPI-AMRVAC offers, there is indeed a variety of possible geometries and dimensionalities.

For starters, one can solve hydrodynamics on a cartesian, cylindrical or spherical grid, and do either a full-dimensional treatment (3D) or postulate that the simulated system is symmetric in some way (along an axis, or a point) to reduce the dimensionality of the grid to 2D or 1D.

Additionally, AMRVAC uses a decimal notation for dimensionality of problems where velocity has fewer symmetries than density. In this class of problems, the velocity vector typically has more components than the grid has directions. For instance, we will label “cartesian 1.5D” a setup where the grid extends over an x axis, while the velocity vectors writes $\mathbf{v} = v_x \mathbf{e}_x + v_y \mathbf{e}_y$.

Now, as proto-planetary disks are in differential rotation, the most important aspect to disk simulation is capturing the azimuthal velocity. I illustrate in table 3.1 that most non-cartesian setups validate this requirement, while some are invalid for our purpose.

Multi-species Hydrodynamics AMRVAC supports solving hydrodynamics equations for a single real fluid. However, an arbitrary number of pressureless fluids is supported out of the box, that can be coupled to the gas following eqs. (2.27) and (2.28).

	spherical (r, φ, θ)	polar (r, φ, z)	cylindrical (r, z, φ)
3D	✓	✓	✓
2.5D	✓	✓	✓
2D	✓	✓	.
1.75D	✓	✓	✓
1.5D	✓	✓	.
1D	.	.	.

Tab. 3.1: A table of non-cartesian geometries and dimensionalities available in AMRVAC. “✓” marks setups where the azimuthal component of the velocity vector (v_φ) is included, which is a requirement to model an disk. There is some degeneracy as all 1D setups are equivalent to one another, as well as “spherical 2D” and “polar 2D”.

The implemented drag force is the one I wrote as eq. (2.24), which covers both asymptotic drag regimes for small and large dust grains. The dust module originally did not support non-cartesian geometries; centrifugal forces were implemented in a way that did not affect grains, and the gravitational field was also ignored. As a result, I struggled with my first results with dusty-disks simulations for a little while. I can not thank Geoffroy Lesur enough for asking the embarrassing questions during that period, eventually leading to my fixing the library.

A change of views in planetary migration

” *Guard: Are you suggesting that coconuts migrate?*
King Arthur: Not at all. They could be carried.
Guard: What? A swallow carrying a coconut?
King Arthur: It could grip it by the husk!
Guard: It's not a question of where he grips it! It's a simple question of weight ratios! A five ounce bird could not carry a one pound coconut.

— **Monty Python**
Holy Grail

This chapter introduces and completes the project I conducted with Aurélien Crida, Elena Lega, Héloïse Méheut and Alessandro Morbidelli, which was published as Clément Mathieu Trisan Robert et al. (2018), providing a broader context and insight on its development. The article itself is included hereinafter. I will first introduce the general context and define planetary migration, and then discuss the technical difficulties of our study that were eluded in the paper before we dive into it. This work, published at the end of my first year of PhD, is part of a larger ongoing debate in the community, which I discuss by the end of the chapter.

4.1 Planet-disk interactions

As I mentioned earlier, planets are byproducts of stellar formation and form inside the remnant disk of material that surrounds a newborn star. I will show here how the evolution of the disk and that of the planet are closely related.

For the sake of the argument, let us assume for now that planet formation is a very efficient process that accounts for most of the mass lost by the disk as it dissipates. Within the following assumptions

1. planets are formed *in situ*, i.e. at their respective current distances to the Sun.
2. the initial disk's mass distribution is a decreasing function of r .
3. the initial metallicity (solid to gas ratio) is 1%, the classical value in the inter-stellar medium.

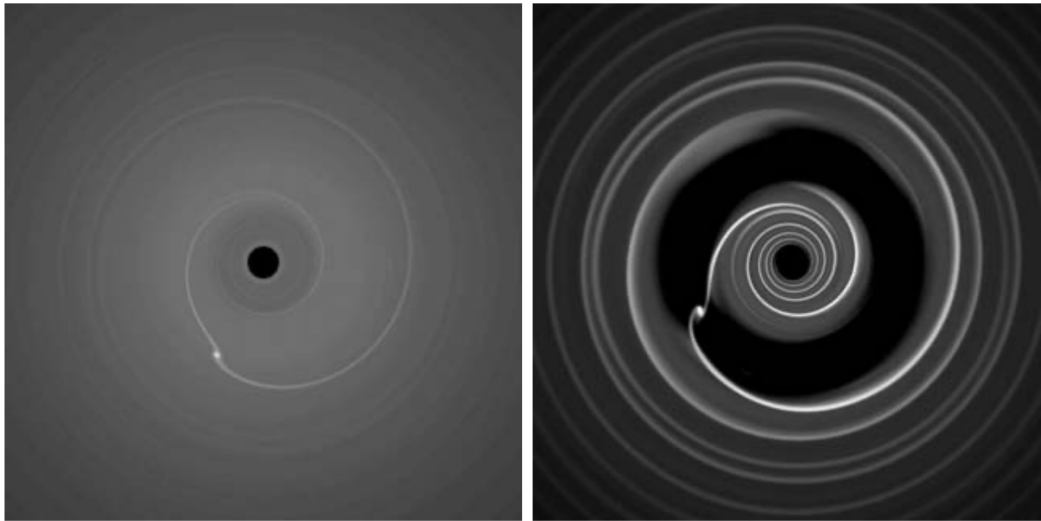


Fig. 4.1: Surface density (greyscale) in 2D simulations as perturbed by a small mass planet (left) and a gap-opening large mass planet (right). A spiral density wave, or *wake*, is induced by a gravitational perturber embedded in a differentially rotating background. Taken from Armitage (2009).

one can build a *minimum mass solar nebula* (or MMSN for short), thus setting a lower bound to the initial mass the proto-planetary disk (Weidenschilling, 1977; Hayashi, 1981).

As noted by Crida et al. (2009) however, the resulting estimation is inconsistent with the first assumption, let us now explain why by exploring the disk-planet gravitational interplay.

If the mass distribution of the disk is axisymmetric, one can show from Gauss’s law that the net force exerted on the planet by the disk is purely radial. In essence, a planet “perceives” the star with a marginally modified effective mass m'_* , and will orbit at a modified rate, following Kepler’s third law, *ceteris paribus*.

However, the reciprocal gravitational pull the planet exerts onto the background material is a symmetry breaking condition, which will change its mass distribution. For small mass planets, it can be regarded as a linear perturbation. In general, gas encountering the planet will “slow down” relative to it, thus creating local “traffic jams” both in its inner and outer vicinity. As these perturbations propagate radially in a differentially rotating background, they result in spiral density waves, called *wakes*. Figure 4.1 (left panel), shows the pattern as seen in density. They can be described more accurately as constructive interference patterns in density waves forced by Linblad resonances (D. N. C. Lin and J. Papaloizou, 1979; Goldreich and Tremaine, 1979; Goldreich and Tremaine, 1980; J. Papaloizou and D. N. C. Lin, 1984). An important point is that the rotation rate of a wake is directly imposed by that of the planet. In other words, the over-density pattern is fixed in a reference frame co-rotating with the perturber.

Wakes are excited both inwards and outwards of the planet’s orbit and correspond to an outwards transport in angular momentum (D. N. C. Lin and J. Papaloizou, 1979) ; from the inner disk to the planet and from the planet to the outer disk. In other words, the planet is subject to two opposing torques. Goldreich and Tremaine, 1980 first demonstrated that

they do not cancel out in general. Hence, the planet will gain or lose angular momentum, leading to a change in its orbit's semi-major axis over time. This is what I will refer to as *planetary migration* from now on. As is done in most if not all existing migration studies, I will now focus on the case of planets forming around a star about as massive as the Sun ($m_{\text{star}} \simeq 1 M_{\odot}$), and a disk close to the MMSN mass.

Now the timescale associated with migration qualitatively depends on the disk to planet (a few Earth masses) mass ratio. In the low planetary mass limit, the gravitational effect on the disk can be treated as a linear perturbation (Goldreich and Tremaine, 1980; D. N. C. Lin and J. Papaloizou, 1979), thus one can derive the net torque analytically, which yields

$$\Gamma_0(r_p) = -C\Sigma_{\text{unperturbed}}(r_p)^4\Omega_p^2(q/h)^2 \quad (4.1)$$

where C is a dimensionless coefficient close to unity which encloses the torque's sensitivity to fine effects such as temperature and turbulent viscosity distribution. This expression will be a useful baseline later. This regime is called *type I migration*. William R. Ward, 1997a showed that the migration timescale in this regime is inversely proportional to the planet mass. Quantitatively, an Earth mass planet would drift all the way to the surface of the sun in about 1×10^4 orbits (William R. Ward, 1997b). These fundamental results cast strong doubts on the survival rate of small planets as they appear to be quickly destroyed. More recent works revealed the co-rotation region also contributes a non-zero torque in non-isothermal models (F. S. Masset, 2002; F. S. Masset and Benítez-Llambay, 2016; Wafflard-Fernandez and Baruteau, 2020). While this contribution indeed mitigates the previous conclusion, it is worth noting that the so-called *co-rotation torque* is prone to saturation when the co-rotation material reaches an equilibrium in isolation.

For high mass planets, however, the disk structure will be significantly altered, and so we have to resort to non-linear numerical simulations to study this other regime, called *type II migration*. The most prominent difference with the linear regime is that more massive planets will create a density-depleted region in the disk, within the vicinity of their orbit, called a *gap* (see right panel in fig. 4.1). At this point, it is worth noting that such a feature is not primarily caused by planetary accretion; as the planet is orbiting at a Keplerian rate (as is the disk's material, in first approximation), it cannot clear its orbit by accreting the material. Instead, the exchange in angular momentum between the planet and the surrounding material promotes their orbital separation. Up to a mass threshold, this effect is normally compensated by the disk viscosity, which spreads the material and tends to even out the distribution. A semi-analytical expression for the threshold condition is derived in Crida (2006), which clarifies the distinction between type I and type II migration. The corresponding migration timescale is expected to be longer than in the type I case, which opens the possibility for massive planets to survive more often, under the condition that they are able to form rapidly. Interestingly, this is supported by the older idea of runaway accretion (Pollack et al., 1996).

F. S. Masset and J. C. B. Papaloizou (2003) further showed that under certain conditions, migration builds into a runaway process itself, which is sometimes referred to as *type III migration*, though the distinction with type II remains controversial to this day.

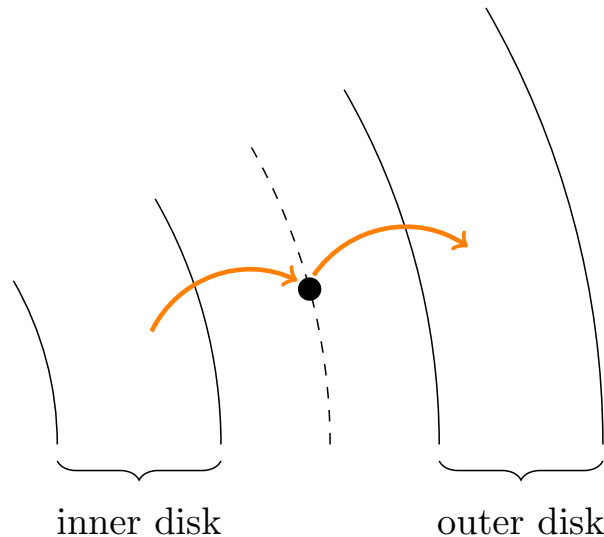


Fig. 4.2: A schematic representation of angular momentum exchanges between gas and a planet. Orange arrows represent angular momentum transport. The planet's instant orbit is shown as a dashed circle arc. This orbit is stationary if and only if the two contributions to its angular momentum gain net zero. In that case, if the planet is displaced inwards (left), the inner torque is increased and the outer one weakens, hence the planet is "pushed" back to its original location. Same goes if the planet is displaced outwards.

4.2 The classical paradigm for type II migration

Type II migration was initially seen a profoundly different from type I. Let me first adopt this point of view before I challenge it. A central idea is that a gap-carving planet is very strongly coupled with the material neighbouring the gap. As angular momentum is transported outwards, from the inner disk to the planet and from the planet to the outer disk, as illustrated in fig. 4.2, the planet is effectively “pushed” away from both parts of the truncated disk. This situation can be schematically compared to that of a ball down in a smooth well, the classic metaphor for a stable equilibrium.

Now, within this paradigm, it is assumed that the disk itself will drift along with the planet, as the gap provides a tight locking mechanism between them. In the presence of a global accretion flow onto the central star $\dot{m}_{\text{disk}}(r, \theta) = 2\pi r \Sigma(r, \theta) v_r(r, \theta)$, it can furthermore be assumed that in the stationary regime, the planet-disk inwards drifting rate will match that of the background flow (W. R. Ward, 1982; Douglas N C Lin and John C B Papaloizou, 1986; D. N. C. Lin and J. C. B. Papaloizou, 1993). This is logically equivalent to assuming the global equilibrium of the disk (be it a dynamical one) is not, in fact, perturbed in significant ways by the planet's presence. Within this assumption, any given tracer particle originally lying on the inner (resp. outer) disk, as compared to the planet's orbital position, will forever stay in this relative radial position with respect to it.

While the very first simulations (Douglas N C Lin and John C B Papaloizou, 1986) showing gap-opening migrators might have verified these assumptions, it recently appeared they did so only out of (ill) luck. Indeed, a few authors before us showed that this tight-locked

relation between the planet and its vicinity's material is not a general rule (Duffell et al., 2014; Dürmann and Wilhelm Kley, 2015; Dürmann and Wilhelm Kley, 2016).

Our primary goal is to address the role of planetary accretion, which is usually omitted in migration studies. The idea is that an actively accreting migrator should inhibit angular momentum transport and reduce migration rates. Since gap-crossing material is transferred through spiral arms, it also closely approaches the planet, hence it should enter the feeding zone (Hill sphere) and be partially accreted, say in fraction $0 \leq f \leq 1$. In that case, one expects the total angular momentum transferred to the planet's orbit by gap-crossing material to be reduced by a factor about $1 - f/2$, while the remaining $f/2$ ends up in the planet's spin or is dissipated as heat. An important and difficult aspect of the simulation we need to control is the global disk accretion rate.

4.3 Numerical details

Navier-Stokes equations (eq. (2.4)) can be extended to take additional physical processes into account, namely body forces such as gravity, rotation, radiation. However, a very general statement in solving differential equation systems is that a problem is unequivocally defined by its initial conditions and boundary conditions. Let me here give more insight on the design of our numerical experiments in these regards.

Initial conditions

In problems to which analytical or semi-analytical equilibrium solutions are known, such solutions constitute a precious source of initial conditions. In order to study the correlation between gas drift velocity v_r and planetary migration rate \dot{r}_p , it is desirable to control the former in the initial state. This condition dictates that we setup the disk in a steady-accretion state. A simple suiting solution is a power-law density distribution $\Sigma(r) = \frac{\dot{m}_{\text{disk}}}{3\pi\alpha h^2 r_0^2 \Omega_0} (r/r_0)^{-1/2}$ (see sec 2.2 in the paper for proof). The numerical stability of this solution depends on the choice of boundary conditions, as detailed in the next paragraph.

At this point we ought to make a distinction between the time-zero of the simulation and the instant migration starts. Indeed, in order to maximize the reproducibility of migration studies, in the case of massive perturbers, it is desirable to wait for the density distribution to stabilize before allowing migration. In fig. 4.3, I graphically represent the accelerations (or forces) caused by each component (disk, planet and star) on each other, as written in the simulation frame, which is centered onto the star. I make a visual distinction between direct interactions and non-inertial terms, which represent the acceleration of the star in an inertial frame. Migration being an effect of the forces (both direct and indirect) exerted by the disk onto the planet, it is artificially prevented by disabling them in the first stage of the simulation, while the reciprocal terms (planet \rightarrow disk) are maintained.

Of course this introductory stage is not physical in that angular momentum conservation is violated. The planet effectively acts as a sink/source to the inner/outer disk respectively, as

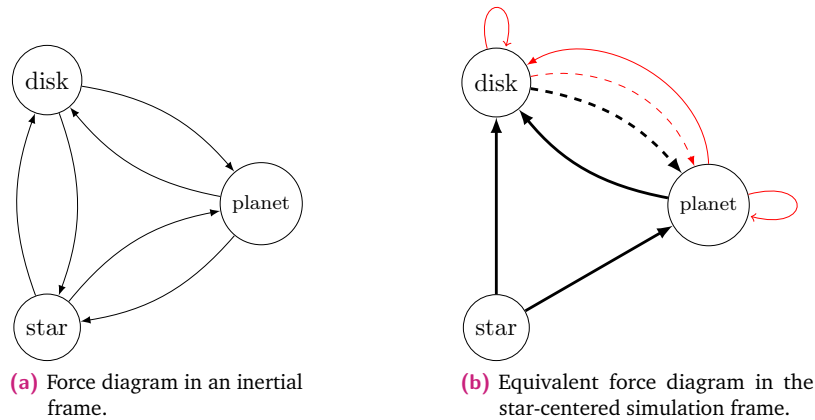


Fig. 4.3: Force diagrams for the three main actors in a simulation. (a) describes the accelerations caused in an inertial frame. (b) is the equivalent diagram in the non-inertial simulation frame. Thick black arrows represent the direct gravitational forces, while thin red arrows represent indirect (non-inertial) terms, namely, the acceleration of the reference frame itself. Those terms are defined in eq. (3.13). Dashed arrows correspond to the two terms that are essential to migration. We turn them off during the first stage of a simulation, allowing the planet to remain on a parametric circular orbit.

illustrated in fig. 4.2. As a consequence, it is illusory to speak about an “equilibrium” state in the physical sense even after this stage of the simulation reaches convergence.

Because the gap-opening process redistributes significant amounts of gas, a rapid introduction of the planet can cause large gas pile-ups at the outer edge of the gap. This delays the system’s relaxation towards a new stationary state in two ways.

1. Since the disk is globally accreting, the accumulated mass excess can not be expelled at the outer boundary of the simulation domain.
2. In most violent cases (a massive planet being introduced instantaneously), the sharpness of the gap may turn Rossby-unstable and generate vortices, which is not what we wish to study in the present chapter (but *is* central in the following one). Such vortices can in fact be excited periodically, causing enormous delays in the relaxation of the system towards an equilibrium state. (Hammer, Kratter, et al., 2017)

The solution to these issues we adopted is to progressively introduce the planet’s mass over a relatively long time (1000 orbits), and monitoring the evolution of \dot{m}_{disk} as a function of r for 4000 additional orbits until a uniform value was satisfyingly approached (see fig B2 in the paper).

Boundary conditions

It is convenient to assume that the physical extension of the disk is greater than the simulation domain. This is for two reasons

1. since the physical edges of the disk, whose shape is not clearly defined, are excluded from the domain, it allows for simpler analytical initial states.
2. the physical inner edge is also imposing the main limitation of the time step through the CFL condition, even using the FARGO algorithm, so cutting it allows for much faster computations. It is also where neglecting magnetic fields is the least relevant.

A drawback is that we then have to prescribe some boundary conditions at the simulation domain radial limits. Let me here give some useful definitions

- *ghost* cells denote a bordering layer of fluid in which extrapolation is required. They are distinct from the *active* domain where evolution is meant to be dictated by laws of physics only. The number of ghost rings n_g is dictated by the order of the highest numerical derivative that we need to compute in the last active ring.
- I note as v_{\parallel} and v_{\perp} the *tangential* and *normal* velocity components respectively, as defined with respect to the cell edge. In the context of this discussion, they correspond to v_{θ} and v_r respectively.

The search for suitable boundary conditions Defining an acceptable treatment for boundaries took a lot of trial and errors. In this section my goal is to provide a synthetic summary of the path I took on the search for a suitable setup.

First, let me recall the desired properties of the final boundary conditions

1. Because we wish to address the alleged correlation between migration speed and viscous spreading (characterized by the radial velocity of the gas), it is required that our boundary conditions allow for a stable (thus, uniform) radial mass flow. Even though this condition is verified in our initial conditions, boundaries play a crucial part in maintaining it with time since mass will typically be added at the outer boundary and removed at the inner boundary.
2. More generally, we want the planet to be the only perturber applied to the initial analytical state. In particular, the analytical disk should be stable against the chosen boundaries.
3. The setup should furthermore be kept as simple as possible.

Controlling the mass inflow is particularly tricky because FARGO defines velocity components on the edges of a cell, while the density is defined at the cell centers. This means that the instant rate of mass gain/loss in each cell n is not simply the product $v_r^i \times \Sigma_n^i$.

Now let us walk through possible treatments of local boundary conditions.

1. The simplest approach would be to initialize ghost cells following the analytical state used throughout the active domain and never update their state. This approach provides an analytically (though not necessarily numerically) stable solution, and

computationally cheap too, but has several important drawbacks in practice. Most notably, this approach will yield a varying mass inflow at the outer boundary as soon as the density and/or the radial velocity in the active domain departs from initial conditions.

2. Another approach would be to extrapolate density, or in other words propagate its first k^{th} numerical derivatives from the active cells into the ghost domain. Doing so, one would need to carefully adjust the radial velocity values in the ghost domain to keep the global inflow time independent. This can be done either locally (in an azimuth-dependent fashion) or globally by using azimuthally averaged values. Unfortunately, none of these possibilities is satisfactory:
 - a) the local approach is heavily time-dependent for a non-axisymmetric disk (e.g. perturbed by a massive planet) and generate numerical oscillations at the boundaries.
 - b) while the global approach is much simpler, it ignores azimuthal asymmetries at the boundary and will in general lead to wave reflections. Moreover, it does not guarantee rotational balance eq. (2.11) is preserved locally, which allows for friction, and thus leads to uncontrolled inflows.
3. In cartesian geometries, it is common practice to set the normal (radial) velocity in the ghost rings following simple prescriptions, such as
 - a) a “wall” condition ($v_{\perp,g} \equiv 0$)
 - b) a “mirror” condition ($v_{\perp,g} \equiv -v_{\perp,l}$)

Though here again, these options allow wave reflection at the boundaries, and essentially negate any mass inflow.

From these considerations, a general conclusion is that strictly local boundaries are unsatisfactory. Now let us consider so called “wave-killing” algorithms such as described in de Val-Borro et al. (2006). The idea is to allocate an intermediate region between the active domain and the actual ghost domain where density waves are artificially damped out. This is done by forcibly changing either density or velocity components (or both) in the transitional region. At each time step, the affected fields are replaced by a weighted average of the current state and a reference state without asymmetries; the reference state could be either the instant azimuthal average or the initial analytical state. The weight of the reference state is a smoothly decreasing function of the distance to the edge of the domain. While the main feature of this pattern is, as the name suggests, to kill off the reflection of waves at the boundary, it also checks out on our other requirements ! Namely, if both density and velocity components are damped out towards their initial states, we obtain stability of the initial conditions against these boundary conditions. The net mass inflow also naturally adjusts to the state of the active domain, so while we cannot fix its value to that of the initial state, it is now possible to achieve a stationary state even after the planet is fully grown. For these reasons, this is the final setup I selected.

Toward a new paradigm for Type II migration

C. M. T. Robert¹, A. Crida^{1,2}, E. Lega¹, H. Méheut¹, and A. Morbidelli¹

¹ Observatoire de la Côte d'Azur, CNRS, Laboratoire Lagrange, Université Côte d'Azur, Bd de l'Observatoire, CS 34229, 06304 Nice Cedex 4, France
 e-mail: clement.robert@oca.eu

² Institut Universitaire de France, 103 Boulevard Saint-Michel, 75005 Paris, France

Received 31 May 2018 / Accepted 15 July 2018

ABSTRACT

Context. Giant planets open gaps in their protoplanetary and subsequently suffer so-called type II migration. Schematically, planets are thought to be tightly locked within their surrounding disks, and forced to follow the viscous advection of gas onto the central star. This fundamental principle, however, has recently been questioned as migrating planets were shown to decouple from the gas' radial drift.

Aims. In this framework, we question whether the traditionally used linear scaling of migration rate of a giant planet with the disk's viscosity still holds. Additionally, we assess the role of orbit-crossing material as part of the decoupling mechanism.

Methods. We have performed 2D (r, θ) numerical simulations of point-mass planets embedded in locally isothermal α -disks in steady-state accretion, with various values of α . Arbitrary planetary accretion rates were used as a means to diminish or nullify orbit-crossing flows.

Results. We confirm that the migration rate of a gap-opening planet is indeed proportional to the disk's viscosity, but is not equal to the gas drift speed in the unperturbed disk. We show that the role of gap-crossing flows is in fact negligible.

Conclusions. From these observations, we propose a new paradigm for type II migration: a giant planet feels a torque from the disk that promotes its migration, while the gap profile relative to the planet is restored on a viscous timescale, thus limiting the planet migration rate to be proportional to the disk's viscosity. Hence, in disks with low viscosity in the planet region, type II migration should still be very slow.

Key words. protoplanetary disks – planet–disk interactions – planets and satellites: formation

1. Introduction

Planetary migration is a key ingredient to understand the architecture of planetary systems. This radial displacement of planets is due to their gravitational interaction with the protoplanetary disk. These disks surround most young stars, and have a lifetime of a few million years. Planetary migration leads to significant changes in the semi-major axis of all planets (see Baruteau et al. 2014; for a recent review) and carves the structure of planetary systems.

Migration of planets has been extensively studied in recent decades. Small mass planets, for which the response of the disk can be considered linear, do not perturb the density profile of the disk, and are in a regime called type I migration. Giant planets, however, are massive enough to modify the disk radial density profile. They deplete the region around their orbit and create a gap (Lin & Papaloizou 1986a), separating the inner disk from the outer disk. Once a gap is open, the planet is repelled inward by the outer disk and outward by the inner disk. The position of the planet within the gap adjusts so that the torques from the inner and out disks cancel out. However, as the disk spreads viscously and the gas accretes onto the central star, the gap, as well as the embedded planet that carved it, is carried with it. This is the classical scheme of the so-called type II migration (Lin & Papaloizou 1986b), responsible for inward motion of giant planets. In this scheme, the planet does not migrate with respect to the gas, but together with the gas, and acts as a gas-proof barrier between the parts of the disk.

This standard scheme of type II migration, where a planet follows exactly the viscous accretion speed of the gas has been questioned by several works. Quillen et al. (2004) note that if the inertia of the planet is much larger than that of the gas originally present in the gap, the disk has a hard time moving the planet, and the migration is slower than the viscous speed. Crida & Morbidelli (2007) add that the corotation torque, exerted on the planet by the gas still present in the gap, may play a role, especially in regions where the background density profile is steep (which promotes a high corotation torque). This could slightly decouple the planet from the gas evolution, but this process relies on a non-empty gap, hence it could be seen as a situation where perfect type II migration is not expected anyway.

Furthermore, Hasegawa & Ida (2013) remark that the assumption that a planet be locked in its gap had no solid physical ground. Lubow & D'Angelo (2006) and Duffell et al. (2014) show that, in simulations, gas is able to cross the gap during planetary migration. Dürmann & Kley (2015; DK15 hereafter) explicitly question the idea that the planet stays in equilibrium in the middle of the gap. They suggest that when the gas reaches an equilibrium gap profile, such that the torques from the viscosity, the pressure, and the planetary gravity balance on each side (Crida et al. 2006), the planet does not necessarily feel a zero torque. Hence, it moves to a different position inside the gap. The motion of the planet then forces the gas to re-adjust the equilibrium profile, by passing through the planet's orbit from the inner part to the outer part of the disk. Because this transfer of gas is due to the planet–gas

interaction and not due to the disk's viscous spreading, the evolution of the planet becomes unlocked from the disk's viscous evolution.

The authors of DK15 find that the migration speed is independent of the disk's drift speed and mainly depends on parameters such as the mass of the disk or that of the planet. Furthermore, [Dürmann & Kley \(2017; DK17 hereafter\)](#) showed that planetary accretion, in some cases, is able to cut the gas flow across the planet's orbit. In these cases the gap acts as a barrier between the inner and the outer disks and classical type II migration regime could be reestablished. However, the authors noticed that even in these cases the migration rate can differ from classical type II migration rate. Both studies (DK15 and DK17) considered a classical α -viscosity disk and focused on the dependence of migration speed on parameters like the disk mass and the planetary mass for a fixed viscosity value.

These studies show that gas is crossing the gap and therefore the migration speed seems to be independent on the disk's drift. Although the authors already provided evidence that migration speeds depend on viscosity, a direct comparison of this dependence with the fundamental assumptions of classical type II remains to be conducted. This is precisely the aim of the present paper.

In fact, though it is now admitted that giant planets' migration does not follow classical type II migration, it is very important to check whether some scaling of migration rate with viscosity is still preserved. Precisely, the existence of giant planets at orbits larger than 1 au in semi-major axis (so-called warm Jupiters) is difficult to explain in the usual paradigm of viscously accreting disks unless considering low viscosity and confirming that migration speed scales with viscosity. Low viscosity is admitted in the central part of the disks, the so-called dead zone, where magneto-rotational instability ([Balbus & Hawley 1991](#)) does not operate. Moreover, recent studies ([Bai & Stone 2013; Bai 2016; Suzuki et al. 2016](#)) have shown that the disk's structure can be very different from that of a viscously accreting disk. Mass accretion onto the star could be ensured by magnetically driven winds providing angular momentum removal. These disks would have very low viscosity. It is beyond the purpose of this paper to model this kind of disks, however these studies motivate the investigation of the migration of giant planets in low viscosity disks. We will also investigate the role of gap-crossing flows on migration.

The paper is organized as follows. In Sect. 2, we present the physical model and the numerical scheme, while the setup of initial conditions is reported in appendices. In Sect. 3, we study the scaling of migration speed with viscosity by performing numerical simulations of Jupiter-mass planets in disks with controlled inflow rates and various viscosities, but same gas surface density. In Sect. 4, the accretion of gas by the planets is modeled by removing, with various efficiencies, the gas entering the Hill sphere; it allows us to find the influence of planetary accretion on migration, and to quantify how important is cutting the gas flow across the gap. Finally, our findings are summarized in Sect. 5, where we propose a new, consistent paradigm to explain giant planet migration.

2. Physical setup

We consider a stationary accreting disk in which a planet is introduced. In this section, we present our background disk model the numerical code used and the prescription for planetary accretion.

2.1. Units and notations

We describe our 2D disk in polar coordinates (r, θ) , centered onto the host star. A subscript “0” denotes values defined at a reference radius $r_0 = 1$. Our time unit, hereafter called an *orbit*, is $t_0 = 2\pi \sqrt{\frac{r_0^3}{Gm_*}} = \frac{2\pi}{\Omega_0}$, where m_* is the mass of the central star. The planet mass is defined as $m_p = qm_* = 10^{-3}m_*$, and its initial semi-major axis as $r_p(t=0) = r_0 = 1$.

2.2. Accretion disk model

Because we are interested in comparing the radial drift of the embedded planet to that of the unperturbed disk, the easiest scheme is to set up a steady-state accreting disk. The local accretion rate is defined as

$$\dot{M}(r) = -2\pi r v_r \Sigma, \quad (1)$$

hence, an accreting disk displays $v_r < 0$ and $\dot{M} > 0$, where r is the distance to the central star, Σ is the gas surface density, and v_r is the gas radial velocity. We use a non-flared disk scale-height $H(r) = hr$, $h = 0.05$ being the uniform aspect ratio, as well as an α -viscosity model ([Shakura & Sunyaev 1973](#)), $\nu = \alpha H^2 \Omega$, and a power law density profile, $\Sigma(r) = \Sigma_0 (r/r_0)^{-s}$. Within those prescriptions, we obtain the radial velocity for a uniform (hence steady) accretion rate as¹

$$v_r = -3(1-s) \frac{v(r)}{r}. \quad (2)$$

Combining Eqs. (1) and (2) gives $\dot{M} = \dot{M}_{\text{ref}}(1-s)\alpha(r/r_0)^{1/2-s}$, where $\dot{M}_{\text{ref}} = 6\pi h^2 r_0^2 \Omega_0 \Sigma_0$. Therefore, the disk model is completely defined by fixing α and \dot{M} . This leads to

$$s = \frac{1}{2} \quad \Sigma_0 = \frac{\dot{M}}{3\pi \alpha h^2 r_0^2 \Omega_0}. \quad (3)$$

Unless specifically stated, all our simulations share this setup, following Eqs. (2) and (3). A summary of different values used in this study may be found in Table 1. In Sect. 2.7, we exhibit boundary conditions compatible with this physically stable initial state, and in Appendix B, we explain how they affect the disk in the presence of a planet.

2.3. Hydro-thermodynamics

The disk evolves along the Navier–Stokes equations:

$$\left(\frac{\partial}{\partial t} + \mathbf{v} \cdot \nabla \right) \mathbf{v} = \nu \Delta \mathbf{v} + \nabla \Phi_G - \frac{\nabla P}{\Sigma}, \quad (4)$$

$$\left(\frac{\partial}{\partial t} + \mathbf{v} \cdot \nabla \right) \Sigma + \Sigma (\nabla \cdot \mathbf{v}) = 0, \quad (5)$$

where \mathbf{v} is the gas velocity, ν is the α -viscosity, Φ_G is the total gravitational potential yielded by the central star and the planet, and P is the pressure. Assuming a cooling time much shorter than the orbital period $2\pi\Omega^{-1} = 2\pi(r/r_0)^{-3/2}\Omega_0^{-1}$, the equation system is closed with a locally isothermal equation of state:

$$P = c_s^2(r) \Sigma = (H\Omega)^2 \Sigma, \quad (6)$$

where c_s is the sound speed and $H(r) = hr$ is the disk scale height.

¹ In all generality, for a $\beta \neq 0$ flared disk $H(r) = hr(r/r_0)^\beta$, the result is changed by replacing $(1-s)$ by $(1-s+2\beta)$.

Table 1. Models parameters.

Simulation name	α	$\dot{M}/(m_* t_0^{-1})$
A1	3×10^{-3}	3.78×10^{-8}
A2	1×10^{-3}	1.25×10^{-8}
A3	7×10^{-4}	8.80×10^{-9}
A4	5×10^{-4}	6.29×10^{-9}
A5	3×10^{-4}	3.78×10^{-9}
B1	3×10^{-3}	0

Notes. In all the cases, the disk mass, or equivalently its surface density Σ_0 is held constant to 5.3×10^{-4} .

2.4. Numerical code

Our experiments were conducted using the 2D hydrodynamic grid code *Fargo* 2D (Masset 2000). This code solves Eqs. (4) and (5) using a finite difference multistep procedure. The fluid advection step is solved using a Van Leer method (Van Leer 1977). The *Fargo* algorithm (Masset 2000) is specifically suited for Keplerian rotation where the traditional Courant–Friedrichs–Lewy (CFL) condition (Courant et al. 1928) provides very small time-steps due to fast orbital motion at the inner boundary of the numerical domain. In the *Fargo* algorithm, the time-step is limited by the perturbed density arising from differential rotation.

Our solver was set with a Courant parameter (Courant et al. 1928) of 0.4. The contribution Φ_p of the planet to the gravitational potential is smoothed as

$$\Phi_p = \frac{Gm_p}{\sqrt{d^2 + \left(\frac{2}{3}R_H\right)^2}}, \quad (7)$$

where d is the local distance to the planet, and $R_H = r_p(q/3)^{1/3}$ is the planet’s Hill radius. As our model does not include the disk’s self-gravity, we exclude the material contained in the Hill region of a planet in the computation of the torque acting on it. To this end, we use the tapering function described by (Crida et al. 2008; Eq. (5)), with $p = 0.6$. This is done to avoid artificial “braking” in the planet’s migration due to the fact that this circum-planetary material does not feel any gravitational torque from the rest of the disk (see Crida et al. 2009).

2.5. Planetary accretion recipe

Accretion onto the planet is handled following the recipe of Kley (1999). At each time step, in every cell located within the Hill radius R_H of the planet, a fraction of the gas is removed. This fraction is given by $K_p f(d) \delta t$, where d is the distance to the planet, δt is the time step, and K_p is an arbitrary accretion efficiency parameter. K_p is typically ~ 1 , and constrained such that $0 \leq K_p \delta t < 1$. In our simulations $\delta t \approx 10^{-3}$. We use the smooth function $f(d)$ proposed by Crida et al. (2016):

$$f(d) = \begin{cases} 1, & \text{if } d \leq 0.3 R_H, \\ \cos^2\left(\pi\left(\frac{d}{R_H} - 0.3\right)\right), & \text{if } 0.3 R_H < d < 0.8 R_H, \\ 0, & \text{if } 0.8 R_H \leq d. \end{cases} \quad (8)$$

For a uniform density around the planet, this function conserves the planetary accretion rate with respect to the original step function proposed by Kley (1999). It furthermore provides better

accuracy when the gas is growing scarce in the planet’s vicinity, without the need for a higher resolution.

This mass taken away from the disk should fall onto the planet, with corresponding momentum. However, here we remove this gas (and its momentum) from the simulation, in order to compare the migration rates of planets of equal, fixed masses. By doing so, we highlight the influence of the gas flow on the migration of the planet. This is reasonable as we are interested in the migration rate of a planet given its mass and not in the planet’s mass accretion rate nor in the final position of an evolving planet.

2.6. Initial conditions for migration

We obtain our initial conditions after two stages, respectively coined *introduction* and *relaxation*, lasting $T_{\text{intro}} = 1000$ and $T_{\text{relax}} = 4000$ orbits, respectively. During *introduction* and *relaxation*, the planet is held at a constant semi-major axis $r_p = 1$.

During *introduction*, the planet mass is slowly increased from 0 to qm_* over T_{intro} , along a smooth function of time

$$m_p(t) = qm_* \sin^2\left(\frac{\pi}{2} \frac{t}{T_{\text{intro}}}\right). \quad (9)$$

Classically, a gap-opening planet quickly expels the gas from its horseshoe region. This gas tends to accumulate at the gap’s edges then to slowly spread at a viscous rate. To avoid this slow phase, we allow the planet to remove gas instead of scattering it, using the planetary accretion recipe described above. We use a smoothly decreasing planetary accretion efficiency

$$K_p(t) = K_p^0 \cos^2\left(\frac{\pi}{2} \frac{t}{T_{\text{intro}}}\right), \quad (10)$$

with $K_p^0 = 1$ in our simulations. As illustrated by Crida & Bitsch (2017), this helps with the gap opening process, and overall saves computational time.

During *relaxation*, we let the system evolve to a near-to-steady state. Convergence is considered achieved when both the mass flow $\dot{M}(r)$ and the gravitational torque Γ_{tot} exerted on the planet reach constant values with respect to time. See Appendix A. Hereafter, we call the time origin $t = 0$, the *release date*, from which the planet is allowed to migrate.

2.7. Boundary conditions

The choice of boundary conditions is a priori of non-negligible importance, and can significantly affect the numerical steady-state the disk relaxes into. Our main concern in choosing appropriate boundaries is that the disk should be left unperturbed far from the planet’s orbital radius. In order to achieve this, we make the further distinction between the domain of interest, in other words, the radial vicinity of the planet, and the broad edges of the simulation domain. A smooth transition is used from the planet’s region of influence to the unperturbed initial state at edges of the simulation domain. This is done through a wave-killing-like algorithm (de Val-Borro et al. 2006) where at each time step and in dedicated regions², perturbations in Σ, v_r, v_θ with respect to the initial state are damped out. This design choice is justified in more extensive details in Appendix B.

² Extending over $r \in [r_{\text{min}}, 1.25r_{\text{min}}]$, and $r \in [0.8r_{\text{max}}, r_{\text{max}}]$ respectively, r_{min} and r_{max} being the limits of the grid.

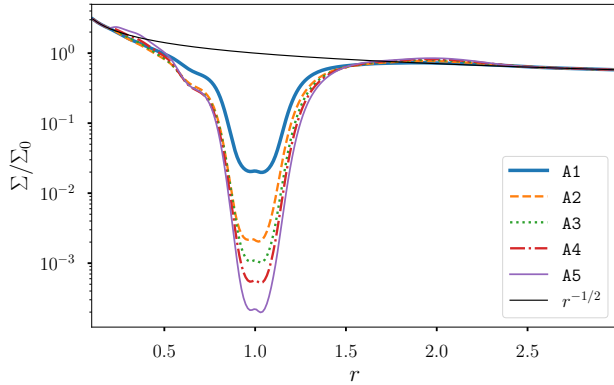


Fig. 1. Azimuthally averaged density profiles at $t = 0$, when the planet is being released. Black thin solid curve corresponds to the power law profile used at initialization.

2.8. Models parameters

The simulation domain spans over $r \in [0.1, 3.0]$. We have chosen an inner boundary at $r = 0.1$, although this choice is very expensive in computational time. The advantage is the possibility to study migration of a planet initially located at $r = 1$ on a large orbital domain, going down in some cases to $r = 0.4$ with no impact of the inner boundary on migration. An arithmetic radial-spacing of grid cells is used with a resolution of $(n_r, n_\theta) = (248, 628)$.

In this paper we aim at testing the scaling of the migration rate with the viscosity and therefore we consider different values of α in the interval $[3 \times 10^{-3} : 3 \times 10^{-4}]$. Table 1 describes in code units our models parametrization. Values are chosen so that $\Sigma_0 = 5.3 \times 10^{-4}$ code units in all simulations. This value is low enough that the co-orbital mass deficit can not exceed m_p , to avoid the runaway type III migration regime (Masset & Papaloizou 2003), but large enough that the disk is still able to push the planet efficiently³. For $m_* = m_\odot$ (hence $m_p = m_J$), and $r_0 = 5$ au, model A1 physically translates into and $\dot{M} = 2 \times 10^{-8} m_\odot \text{yr}^{-1}$.

Figure 1 shows the initial density profiles at the end of the *relaxation* phase at $t = 0$ for simulations A1, A2, A5. As expected, gaps are deeper and wider at lower viscosities.

3. Influence of viscosity on the migration rate

DK15 and DK17 demonstrated that the torque acting on a gap-opening planet is primarily dependent on the disk’s mass rather than its accretion rate $\dot{M}(r) \propto \nu(r)$. Although they showed that viscosity still affected the torque, it remained to be clarify how viscosity’s role compares to the initial assumption of classical type II. A direct comparison with type II is the topic of this section.

“Classical” type II migration rate is given by $\dot{r}_p = v_r$, where v_r is the viscous speed of the unperturbed disk (Eq. (2)); i.e. the planet is assumed to migrate with the drift rate of the gas. We show in Fig. 2 the migration speed measured in simulations A1 to A5 plotted as a function of the semi-major axis of the planet. In all these runs, no planetary accretion is used. The migration speed was normalized in all simulations to $v_r = -\frac{3}{2} \frac{\nu}{r}$ so that scaling of the migration with v_r and/or with viscosity is apparent.

³ We notice that, for $\Sigma_0 r_p^2 / m_p = 0.53$, DK15 obtained a migration speed larger than the disk radial velocity v_r (see Fig. 15 in their paper).

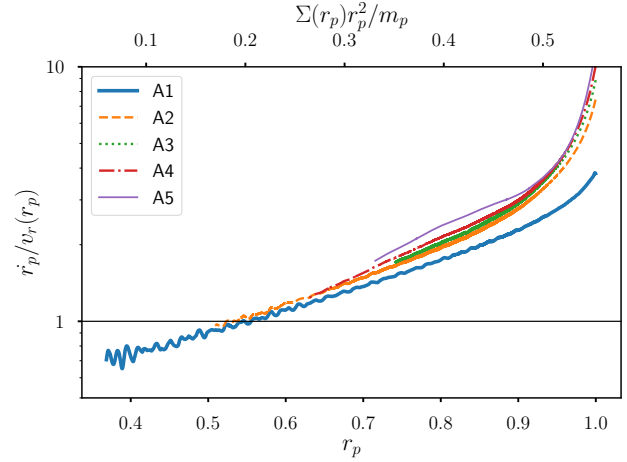


Fig. 2. Normalized migration speed as a function of the semi-major axis for sets A1 to A5 with $K_p = 0$. The normalized local disk mass $\Sigma(r_p)r_p^2/m_p$ is indicated as a secondary graduation for the x-axis.

Because planets do not migrate at identical speeds in different runs, note that a given semi-major axis corresponds to different dates; for instance, A1’s planet reaches $r_p = 0.8$ at $t \approx 1150$, to be compared with $t \approx 8000$ in case A5. Some observations can be drawn from Fig. 2 :

- As pointed out by Duffell et al. (2014), because the planet was first artificially maintained on a circular orbit, the corresponding gas distribution at release date is de facto inconsistent with a migrating perturber. Indeed, within this method, we obtain torques inducing migration timescales much shorter than the viscous spreading timescale of gap edges ; this is a known effect in type II studies. It follows that the transitional stage immediately following release ($r_p \approx 1$) ought to be discarded from our analysis.
- Following this transition, normalized migration tracks converge, demonstrating that steady migration rates scale linearly with the viscosity.
- Because migration speeds scale with viscosity, convergence is reached on timescales $\propto \tau_v = r_p^2/\nu$. Therefore, very long integration times are required at the lower viscosities. In fact, properly comparing situations at different values of α requires snapshots with similar r_p , i.e. similar t/τ_v (and similar local disk mass, see below). In particular, the previously mentioned transitional stage corresponds to $0.9 \lesssim r_p < 1$ for every viscosity.
- At odds with the classical speed expected for type II migration, the migration rate decreases with the semi-major axis and migration becomes slower than classical type II for $r_p \lesssim 0.54$.

This last result is in agreement with DK15 who showed that migration rate decreases with decreasing local disk’s mass $\Sigma_p r_p^2$, Σ_p being the unperturbed surface density at planet position r_p . The top horizontal axis of Fig. 2 shows the local disk mass divided by the mass of the planet. The migration speed is equal to v_r when this mass ratio is ≈ 0.2 , in remarkable agreement with DK15 (Fig. 15 therein).

Besides these observations, Fig. 2 reveals a puzzling fact for the question we are interested in the migration speed of a gap opening planet is proportional to the viscosity of the disk, but not equal to the radial drift of the gas. The fact that the planet migrates slower than the gas when the disk mass is low

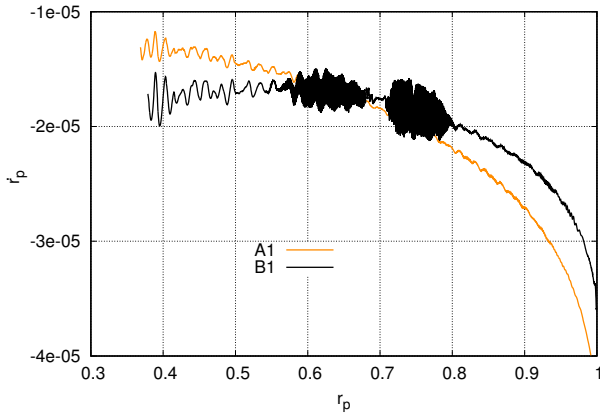


Fig. 3. Migration speed as a function of the semi-major axis in two simulations with $\alpha = 0.003$ and same surface density. Orange curve: case A1 ($s = 1/2$); same curve as Fig. 2 (not normalized here). Black curve: case B1.

is not a surprise, but the reason for a faster migration remains unclear still (although already found by previous studies). To further inquire this possibility, we ran an additional simulation, B1, in a static unperturbed disk, i.e. where Eq. (3) is changed to $s = 1$ so that $v_r = \dot{M} = 0$, Eq. (2), and Σ_0 is arbitrary, hence kept to A1’s value. The migration speed found is displayed in Fig. 3 as the black curve, where it can be compared to the case $s = 1/2$ (orange curve, same data as Fig. 2). Very clearly (and surprisingly), the unperturbed radial velocity of the gas has little influence on the migration speed of the planet.

What pushes the planet is *not* the radial drift of the gas onto the star. This supports DK15’s claim that the planet inside its gap is not necessarily at equilibrium with the gas, when the gas profile is itself at equilibrium with the planet. Hence, the planet can feel a torque, which drives its migration, even if the unperturbed disk has no radial drift. This is already a change of paradigm for type II migration. Why this torque should be proportional to the viscosity, however, is unclear at this point. This suggests that the picture may be more complicated than the one just described, as we will see later.

For the planet to migrate faster than the radial velocity of the unperturbed gas, one would naturally expect that it migrates with respect to the gas. In this picture, gas should cross the planet’s orbit from the inner to the outer disk to sustain migration. The following section is dedicated to studying the influence of planetary accretion on such mass exchanges and its resulting effects on migration.

4. Effect(s) of planetary accretion

Here we test how introducing planetary accretion into our model affects the gas flow through the planet’s orbit, and how the migration rate is changed in turn. Accretion’s efficiency is parameterized by the dimensionless number K_p , which we vary as $K_p \in \{0, 0.2, 1.0, 5.0\}$, using run A2 as the reference case $K_p = 0$. The initial state in all runs is identical to that of A2. Unlike the time-dependent accretion efficiency previously described, here we do not follow Eq. (10), and K_p is instantly switched to a non-zero value at $t = 0$, when the planet is released.

In order to preserve comparability, we emphasize the importance of keeping the global structure of the disk as unperturbed as can be, despite the fact we are adding a sink point to the

hydrodynamical model. Our boundary conditions ensure that the disk’s profile stays unchanged far away from the planet. Hence, we except all changes due to K_p to stay local to the planet’s vicinity.

4.1. Material exchange between reservoirs

The inner and the outer disks constitute our two gas reservoirs of interest. In order to keep track of the planet’s *relative* radial displacement *with respect to* those reservoirs, we use passive, dimensionless, scalar tracers $\eta_{i/o}$. Let us give a non-ambiguous and partly arbitrary definition of their respective initial distributions. We should be concerned about avoiding confusion with material originated from the HorseShoe Region (HSR), whose width is given by Masset et al. (2006) as $w_{\text{HSR}} \approx 2.5 R_H$. Hence, a precautionary choice is to consider only material initially distant of at least $3R_H$ from the planet’s orbit. Within this definition, we define $\eta_{i,o}(r, \theta, t = 0) = r/r_0$, for $r \geq r_p \pm 2.5R_H$, and $\eta_{i/o} = 0$ elsewhere. Let us acknowledge that, as a tracer is advected along with the gas, its value in a given cell becomes the mass weighted average of the tracers that are found in the considered cell at the considered time. Therefore, at $t > 0$, we expect to find mixed material, displaying values of the tracer that do not correspond to the initial value but rather a weighted average of it.

Figures 4 and 5 display, for simulation sets A1 and A2 respectively, the evolution of those tracers, sampling over our parameter K_p from 0.0 to 5.0. Once more, following Duffell et al. (2014) and DK15, we find that, in the non-accreting case, some gas is effectively transported from the inner disk to the outer disk as migration proceeds. Not only does the planet migrate *with respect to* the medium, it also actively ejects some material to larger orbits. This still holds in the weakly accreting case $K_p = 0.2$, although the transport efficiency is being slightly decreased. However, it is not so in the “standard” and “strong” accretion cases ($K_p = 1$, $K_p = 5$), where the outward flow from the inner disk is so efficiently blocked that the outer disk rushes into the planet’s vicinity.

Let us observe that while we successfully introduced accretion as a means to prevent gap-crossing flows, the procedure also profoundly modified the nature of the flow and added complexity to the picture. Indeed, not only did we prevent inner disk material to transfer into the outer disk, we also allowed the outer disk material to reach the planet’s feeding zone, hence causing depletion to happen in both halves of the disk. Additionally, we note that despite the *origin* of gas at a given radius being widely different depending on the accretion rate (see Fig. 5), at lower viscosity values (A2) the disk’s structure stays almost self-similar whatever the planetary accretion efficiency K_p , see Fig. 7. The net effect on migration is unclear at this point and will be discussed in Sect. 4.2. Furthermore, the transition from a naturally occurring gap-crossing flow to a two-way accretion flow with increasing K_p appears to be smooth. Indeed, we see in the weakly accreting case that, as less material flows from the inner disk to the outer disk, the latter immediately reacts and follows the planet more closely than in the non-accreting scenario. From a quick comparison between Figs. 4 and 5’s respective “weak rate” panels, one can see that the stronger the viscosity, the quicker this compensation mechanism (normalizing time to the viscous timescale). This is confirmed in stronger accretion cases $K_p = 1.0, 5.0$. Hence, at least for high values of α , planetary accretion cannot cut the otherwise existing outward⁴

⁴ Relative to the planet.

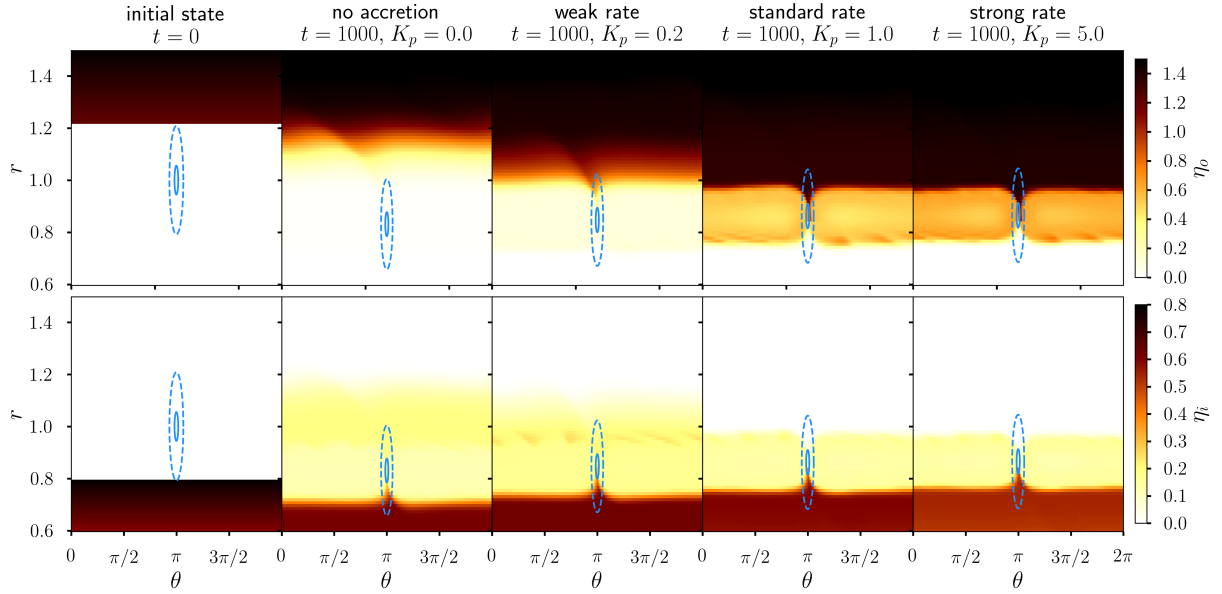


Fig. 4. Evolution of passive tracers $\eta_{i/o}$ for simulation set A1, following material originated in the outer (*top panels*)/inner (*bottom panels*) disk, in polar coordinates. *Left panel*: initial state (white is 0). *All but leftmost column*: 1000 orbits after release, for varying values of K_p . We emphasize that color scales are different across rows. For the sake of readability, the disk is here displayed with angular coordinates such that $\theta_p = \pi$ in every frame. Filled lines show the planet’s feeding zone, $0.8R_H$ in radius; dashed lines are $3R_H$ large in radius, encompassing a somewhat broader region than the typical HSR.

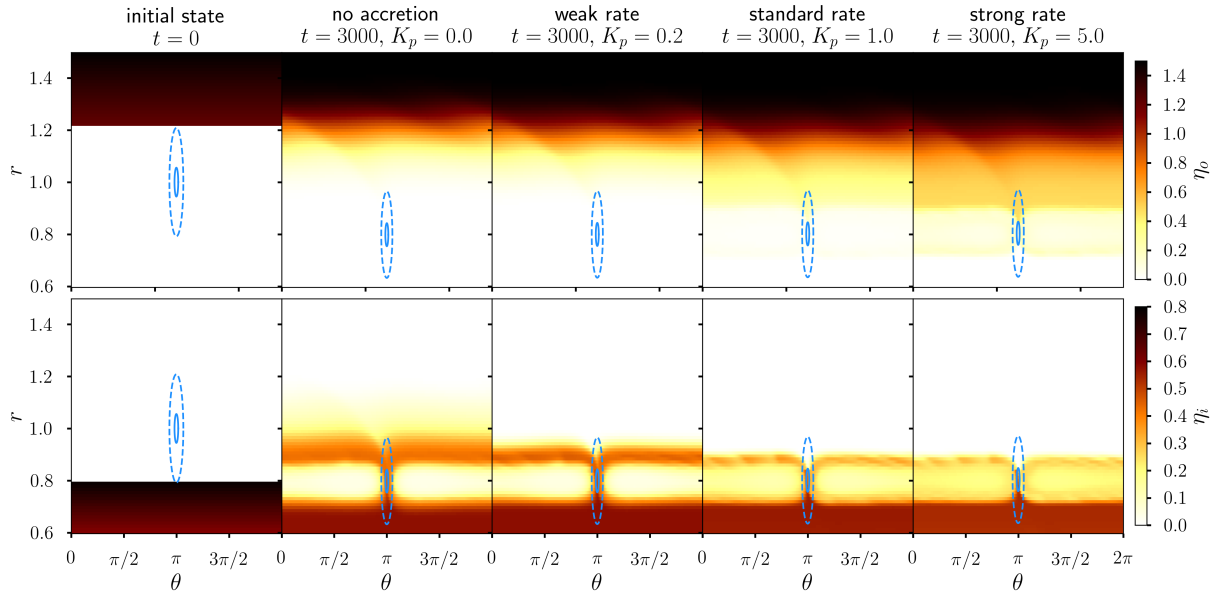


Fig. 5. Same as Fig. 4 for simulation set A2. Snapshots are taken after a α_1/α_2 longer period.

gap-crossing flow without causing a more rapid inward flow of the outer disk.

In short, we find that an accreting planet does not prevent gas from entering its HSR, even though it can nullify gap-crossing flows. Let us now discuss the implications of accretion on the migration speed.

4.2. Impact of accretion on migration

It is clear from our previous observations that the density of the outer disk, hence the negative torque it yields on the planet,

should be reduced by planetary accretion. DK17 already noted that planetary accretion can reduce migration speeds. Nonetheless, we stress that the positive contribution from the inner disk can also diminish as the disk is being forcibly depleted. Here we measure the effective migration rates against accretion efficiency and give further interpretation.

Because planetary accretion stops the gap-crossing gas flow, one may expect it to consolidate the classical type II migration scheme. We recall that in this scheme, the migration rate is given by $\dot{r}_p(r_p) = v_r(r = r_p)$, where v_r is the viscous speed of the

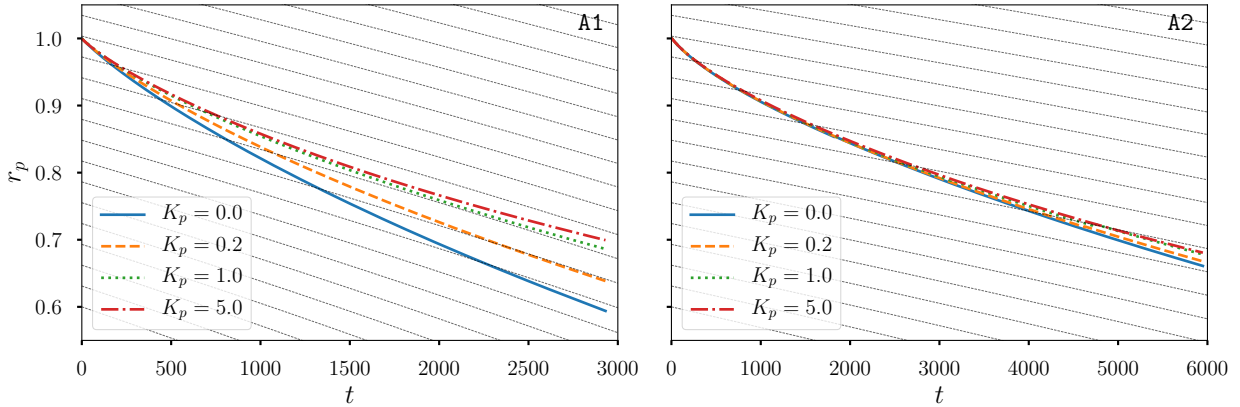


Fig. 6. Radial position of the planet r_p VS time, for varying accretion rates. Panels correspond to simulation sets A1 (left panel) and A2 (right panel). The plot includes analytical migration tracks Eq. (11) with varying time offsets as guidelines.

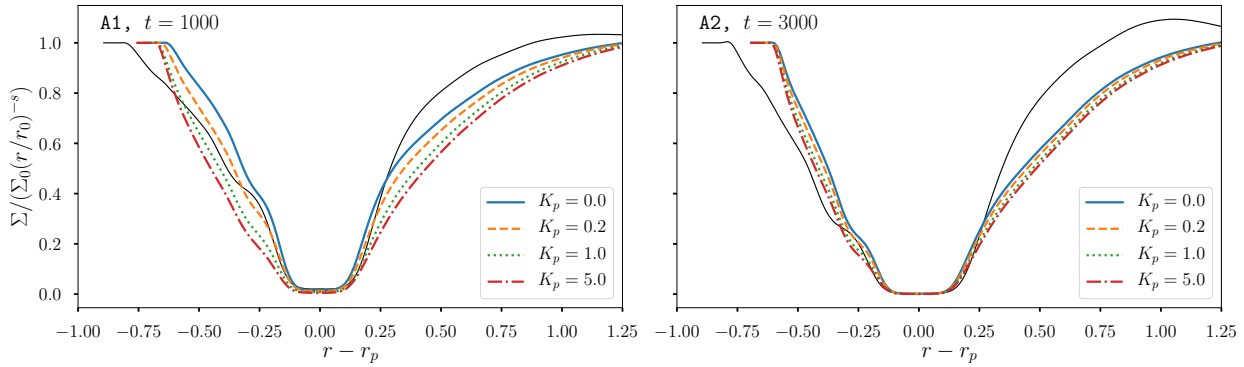


Fig. 7. Density profiles snapshots at fixed time with varying accretion efficiency for simulation sets A1 and A2. Black thin lines indicate the initial states (same as Fig. 1).

unperturbed disk Eq. (2); i.e. the planet is assumed to migrate with the drift rate of the gas. Integrating Eq. (2), we get the analytical evolution of $r_p(t)$ for a planet migrating in a classical type II fashion:

$$r_{p,II}(t) = \left[r_p^{3/2}(t=0) - \frac{9}{4} \alpha h^2 \sqrt{Gm_* t} \right]^{2/3}. \quad (11)$$

Time evolution of r_p is shown in Fig. 6 for various accretion efficiencies (K_p), against this theoretical track, for simulation sets A1 and A2 (1 panel per value of α). We observe that planetary accretion has significant impact only in the highest viscosity case $\alpha = 0.003$, where the migration rate can be reduced below the theoretical rate (cases $K_p \geq 1$) after a few 1000 orbits in agreement with findings from DK17. However, changes in migration are barely noticeable in the second case where $\alpha = 0.001$. We have checked that for lower viscosities (simulations A3, A4, and A5), the migration speed is hardly impacted by planetary accretion as well. Increasing the accretion efficiency of the planet (thus effectively cutting the flow of gas across the gap) does not allow the planet to decrease its migration speed down to v_t if $\alpha \leq 0.001$.

The role of accretion in the viscous case can be understood with corresponding density profiles Fig. 7. For the A1 runs, the local disk's structure is being efficiently affected by the accretion, decreasing both inner and outer disk's densities, hence their respective torques densities (as shown in Fig. 8). In contrast,

the planet can hardly make a dent in the density profile in the lower viscosity cases. This is consistent with that a lower viscosity implies both a wider and deeper gap: as far less material is available in the vicinity of the separatrices of the HSR, the influence of planetary accretion on the dynamical evolution of the disk is hindered.

Except for high values of α , we can conclude from our study that planetary accretion is not of significant importance for the migration of giant planets. Actually, the fact that the curves in Fig. 2 overlap while there is no planetary accretion suggests that the latter is not important in setting the proportionality between the migration rate and the disk's viscosity. The reason why planetary accretion plays a role in the migration speed in the viscous A1 case is not because it cuts the flow, but because it perturbs strongly the density profile and broadens the gap.

5. Conclusion

To summarize, we have found in Sect. 3 that although type II migration speed is proportional to the gas' viscosity, it is not driven by the radial inward drift of the gas. In particular, we confirmed that the giant planet can actually migrate faster than the gas drifts, and even in a stationary disk. We concluded that what drives type II migration is the imbalance between the torques felt by the planet from the inner and outer disks, as pointed out by DK15. However, the width and shape of the gap is not directly linked to the viscosity, especially at low ν where the

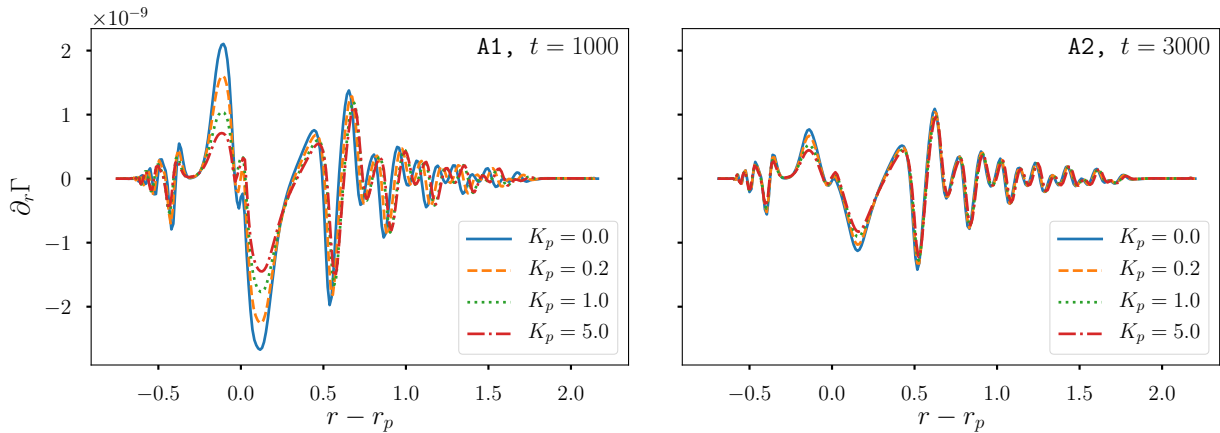


Fig. 8. Radial torque densities for simulation sets A1 and A2.

pressure effects are dominant (Crida et al. 2006); hence, we do not expect this torque imbalance to be proportional to ν , in contrast with the observed migration speed. In Sect. 4, we have seen that gap-crossing flows are actually negligible at low viscosity, and that cutting this small gas flow with planetary accretion hardly impacts the migration speed. Thus, the planet migrates faster than the disk drift, even when no gas is exchanged between the inner and outer disks. Gap-crossing flows cannot be responsible for the observed fast migration, in contrast with the case of case III migration (Masset & Papaloizou 2003).

These two results allow us to draw a new, consistent picture of type II migration. As a giant planet forms, it opens a gap by perturbing the gas profile with the gravitational torque it exerts. The gas reaches a new equilibrium profile on each side of the gap. Nonetheless, the planet inside its gap feels a non-zero torque, because the inner and the outer torques have no reason to balance out (as recently studied by Kanagawa et al. 2018). Thus, the planet has to migrate inward. As it does so, some gas may cross the gap from the separatrix of the HSR, although this is not enough to restore the initial gap profile in the frame of the planet if the viscosity is low and the gap is wide (regardless of whether the planet accretes or not). Therefore, the density distribution has to adapt to the new position of the planet⁵, and this is done over a viscous time. Once the gas is again at equilibrium with the planet, the planet is not in an equilibrium inside the gap anymore, and we are back to the initial situation.

In this scheme, the planet may well migrate faster than the gas drifts, because it is pushed by a torque that has no connection with the drift of an unperturbed disk. But because the gap-crossing flow is negligible, the planet must migrate at a rate proportional to viscosity, otherwise it would pile gas up in the inner disk and leave a depleted outer disk behind, eventually halting its migration.

Although the final result (migration speed of gap-opening planets is proportional to the viscosity) is in line with the standard picture of type II migration, this new scheme is conceptually revolutionary in our understanding of this phenomenon, and allows us to reconcile all the puzzling observations that have been made recently, questioning the standard picture. Additionally, it confirms that even if some gas may cross the gap, a giant planet in a low-viscosity disk should migrate slowly. In

⁵ That is, the bump in the surface density produced at the inner edge of the gap has to be redistributed over the inner disk while the outer disk has to spread down to the new gap's outer edge.

this frame, the abundance of warm Jupiters, who did not migrate all the way toward their star, may suggest that most protoplanetary disks have a low effective viscosity in the planet-forming region.

Acknowledgements. We acknowledge support by the French ANR, project number ANR-13-BS05-0003-01, projet MOJO (Modeling the Origin of Jovian planets). C.M.T.R., H.M., and A.C. acknowledge funding from ANR grant No. ANR-16-CE31-0013 (Planet-Forming-Disks). HPC resources from GENCI [IDRIS] (Grant 2017, [i2017047233]) and from “Mesocentre SIGAMM”, hosted by Observatoire de la Côte d’Azur were used. C.M.T.R. and E.L. wish to thank Alain Miniussi for his valuable help in maintaining and developing the code base used in this work. Figures in this paper were produced with `matplotlib` (Hunter 2007). The authors wish to thank the anonymous referee for their valuable observations and help in making this paper clearer.

References

- Bai, X.-N. 2016, *ApJ*, 821, 80
 Bai, X.-N., & Stone, J. M. 2013, *ApJ*, 769, 76
 Balbus, S. A., & Hawley, J. F. 1991, *ApJ*, 376, 214
 Baruteau, C., Crida, A., Paardekooper, S.-J., et al. 2014, *Protostars and Planets VI*, 667
 Courant, R., Friedrichs, K., & Lewy, H. 1928, *Math. Ann.*, 100, 32
 Crida, A., & Bitsch, B. 2017, *Icarus*, 285, 145
 Crida, A., & Morbidelli, A. 2007, *MNRAS*, 377, 1324
 Crida, A., Morbidelli, A., & Masset, F. 2006, *Icarus*, 181, 587
 Crida, A., Sándor, Z., & Kley, W. 2008, *A&A*, 483, 325
 Crida, A., Baruteau, C., Kley, W., & Masset, F. 2009, *A&A*, 502, 679
 Crida, A., Bitsch, B., & Raibald, A. 2016, in *SF2A-2016: Proc. of the Annual Meeting of the French Society of Astronomy and Astrophysics*, eds. C. Reylé, J. Richard, L. Cambrésy, et al. 473
 de Val-Borro, M., Edgar, R. G., Artymowicz, P., et al. 2006, *MNRAS*, 370, 529
 Duffell, P. C., Haiman, Z., MacFadyen, A. I., D’Orazio, D. J., & Farris, B. D. 2014, *ApJ*, 792, L10
 Dürmann, C., & Kley, W. 2015, *A&A*, 574, A52
 Dürmann, C., & Kley, W. 2017, *A&A*, 598, A80
 Hasegawa, Y., & Ida, S. 2013, *ApJ*, 774, 146
 Hunter, J. D. 2007, *Comput. Sci. Eng.*, 9, 90
 Kanagawa, K. D., Tanaka, H., & Szuszkiewicz, E. 2018, *ApJ*, 861, 140
 Kley, W. 1999, *MNRAS*, 303, 696
 Lin, D. N. C., & Papaloizou, J. 1986a, *ApJ*, 307, 395
 Lin, D. N. C., & Papaloizou, J. 1986b, *ApJ*, 309, 846
 Lubow, S. H., & D’Angelo, G. 2006, *ApJ*, 641, 526
 Masset, F. 2000, *A&AS*, 141, 165
 Masset, F. S., & Papaloizou, J. C. B. 2003, *ApJ*, 588, 494
 Masset, F. S., D’Angelo, G., & Kley, W. 2006, *ApJ*, 652, 730
 Quillen, A. C., Blackman, E. G., Frank, A., & Varnière, P. 2004, *ApJ*, 612, L137
 Shakura, N. I., & Sunyaev, R. A. 1973, *A&A*, 24, 337
 Suzuki, T. K., Ogiwara, M., Morbidelli, A., Crida, A., & Guillot, T. 2016, *A&A*, 596, A74
 Van Leer B. 1977, *J. Comput. Phys.*, 23, 276

Appendix A: Disk relaxation: equilibrium of torques on a fixed-orbit planet

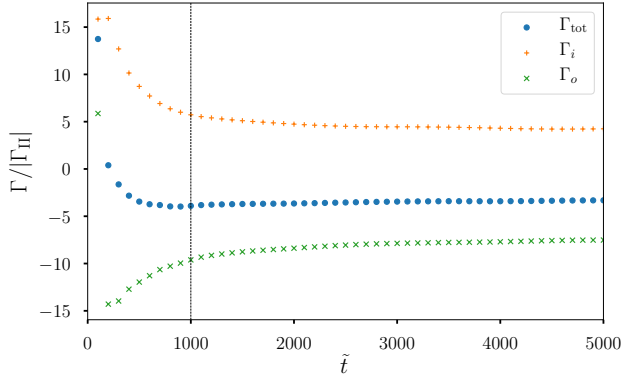


Fig. A.1. Evolution of the gravitational torque Γ_{tot} acting on the planet during *introduction* and *relaxation* (\tilde{t} here denotes time during those stages). Γ_i is the contribution of the inner disk (up to $r = r_p = 1$), Γ_o of the outer disk, and $\Gamma_{\text{tot}} = \Gamma_i + \Gamma_o$. A vertical line indicates the end of the planet’s introduction and starting date of the disk’s relaxation.

Here we give details on the *relaxation* of the disk toward initial conditions for planetary migration. In Fig. A.1, the total gravitational torque Γ_{tot} that the disk exerts on the planet is plotted alongside with its inner and outer components.

While the one-sided torques decrease in absolute value as the gap opens, the total torque remains nearly constant. We measure its final value as only a fraction (~ 0.12) of the differential Lindblad torque:

$$\Gamma_0 = -\Sigma_p r_p^4 \Omega_p^2 (q/h)^2, \quad (\text{A.1})$$

where Σ_p is the *unperturbed* surface density at planetary semi-major axis, r_p . This is expected for a gap-opening planet. For lack of an existing normalization factor for type II migration, let us derive one here. The viscous torque exerted by inner material $r < R$ onto its complementary part $r > R$ in an unperturbed disk may be expressed as

$$\Gamma_v(R) = 3\pi\nu\Sigma R^2\Omega(R) = 3\pi\alpha H^2\Omega^2\Sigma R^2. \quad (\text{A.2})$$

Hence, the expected value the total torque in classical type II can be estimated as the differential viscous torque that a gas annulus occupying the gap would feel as

$$\Gamma_{\text{II}} = 3\pi\Sigma_0\alpha h^2 Gm_* \left[(r_p - w_{\text{HSR}})^{1-s} - (r_p + w_{\text{HSR}})^{1-s} \right], \quad (\text{A.3})$$

where w_{HSR} is the width of the horse-shoe region, estimated as $2.5 R_H$. We observe that Γ_{tot} converges toward $\sim 4 \Gamma_{\text{II}}$. This discrepancy has been tackled by [Dürmann & Kley \(2015\)](#) who showed that in fact, the final value of this torque is primarily determined by the disk mass has little to do with the disk accretion rate \dot{M} , or equivalently its viscous torque $T_v \propto \nu \propto \dot{M}$. Furthermore, they showed that even-though the inner and outer disks reach stationary density profiles, the planet is not in an equilibrium position between them. Indeed, a stationary-state

disk embedding a fixed-orbit planet does not yield the expected type II torque but rather a significantly stronger one.

Appendix B: Design of boundary conditions

Here we provide more insight on how the boundary conditions were selected and acknowledge the consequences of this choice. An obvious choice for boundaries would consist in simply fixing the values of velocities and surface density to their initial state. In principle, this design would allow for conservation of both the total mass in the simulation domain and the initial flow \dot{M} throughout the relaxation. However, this does not hold within the staggered grid scheme used in *Fargo*. Indeed, radial velocities are defined at lower edge of cells while density is center-defined. While this is a convenient design for numerical integration of hydrodynamics equations, it makes it impossible to keep the density, velocities and the net mass flux entering the simulation domain constant all at once. This is because the net mass entering the simulation at the outer edge is effectively defined as a combination of fixed and free numbers. Figure B.1 illustrates this point, and define the two equally problematic possible designs. A solution to this issue would be to correct the imposed value for Σ_n (case 1) or $v_{r,n+1}$ (case 2) at each time step to achieve the desired value in \dot{M} . In practice this proved less than efficient, as $\dot{M}(r)$ is very sensitive to even the most subtle spatial or time variation, convergence was not achieved in practical times.

Although a steady-state is characterized by uniformity in accretion rate $\dot{M}(r)$, there is in fact no strong argument in favor of enforcing its initial value at the grid’s edges. Indeed, DK15 already clarified that the migration rate is not bound to the unperturbed \dot{M} . Furthermore, as previously observed, enforcing a constant mass flow through both radial edges would cause the total mass, dictated solely by s and the radial limits of the grid, $(r_{\text{min}}, r_{\text{max}})$, to be constant. In this case, one would obtain qualitatively different results only by enlarging the simulation domain, corresponding to different physical scenarios. For instance, strong pressure bumps may be found at the edges of the gap for a narrow enough grid, corresponding to a fast planet-formation scenario where a jovian mass would agglomerate over the course of a few 100 orbits.

For these reasons, we chose to relax the assumption that the final uniform value in \dot{M} should be exactly equal to that of the initial, analytical state described in Sect. 2.2, and instead favor the fact that the disk should stay close to unperturbed far from the planet. As explained in Sect. 2.7, we extend the notion of “boundaries” to broad radial domains where perturbations with respect to the initial state are consistently damped out. This artificial process is applied to velocities (both radial and azimuthal) as well as to surface density. A direct consequence of this is that mass is no longer being conserved in wave-killing regions, so that desired uniformity in $\dot{M}(r)$ is only relevant outside those regions. Additionally, this damping process prevents reflections of sound waves, such as spiral wakes, as is its original purpose ([de Val-Borro et al. 2006](#)).

Figure B.2 shows the evolution of the radial flow profile obtained in the case A1. Although not perfectly converged, at $\tilde{t} = 5000$, we settled for what we considered an acceptable level of uniformity to save computational time.

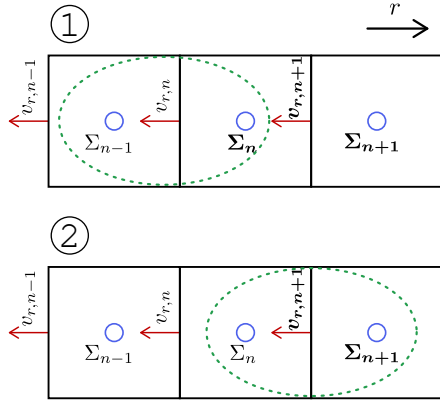


Fig. B.1. Two possible designs for fixed boundary conditions in a 1D grid where radial velocities are defined at inner cell edge (red arrows) and density is center-defined (blue circles). Boldface is used to indicate fixed quantities. The net mass inflow is determined as a combination of quantities inside of a green dashed ellipse, which always contain both fixed and free values. The last cell harbouring free quantities is indexed by n .

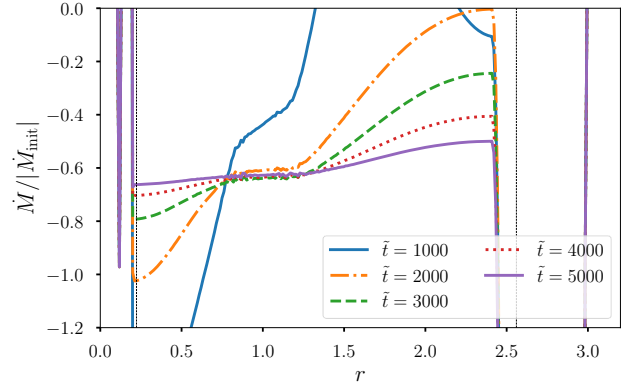


Fig. B.2. Relaxation of the azimuthally averaged radial flow, case A1. \tilde{t} denotes time during introduction and relaxation stages ($\tilde{t} = t + 5000$). Limits of the domain of interest (excluding wave-killing zones) are shown as dashed lines. \dot{M}_{init} denotes the uniform value in the analytic state of the unperturbed disk described in Sect. 2. 628 snapshots covering one orbit were averaged to obtain each line in this figure.

4.5 Additional remarks to the published paper

Here I want to add various remarks that did not fit the scope of the paper, and considerations that I simply did not think of at the time.

- I acknowledge that the planet’s feeding zone, in Figures 4 and 5, is misrepresented as ellipses in polar coordinates, where it should instead take the projection into account and appear larger at lower radius.
- In our simulations, sound speed is time-independent. Yet, this prescription is only relevant if the vertical structure is roughly self-similar with the midplane distribution. When the disk’s structure is significantly perturbed by a planet, this assumption is shattered, and there is no obvious way to characterize the typical size (H) of the disk in the depleted region any more. This is at the core a limitation in the locally isothermal models, in which sound speed can not be updated.
- The instant mass exchange rate can in principle be reconstructed in post-processing, provided that the internal advection algorithm is reproduced. However, such a procedure is error prone and a safer way to measure it is to output it directly at runtime. In contrast, it is not clear how other authors did it.

4.6 The current state of research on type II

Research conducted before and after ours shows an ongoing controversy. Throughout my own paper, I directly used the viscous drift velocity of the gas u_{viscous} as a comparative baseline with migration rate measurements. More nuance is in fact needed, for migration speed indeed depends on the relative masses of the system components. In terms of dimensionless quantities I will use $q_1 \equiv \frac{m_{\text{planet}}}{m_{\text{star}}}$ and $q_2 \equiv \frac{m_{\text{disk}}}{m_{\text{planet}}}$ where the relevant disk mass for comparison can be defined as $m_{\text{disk}} \equiv 4\pi r_p^2 \Sigma_{\text{unpert}}(r_p)$. In the limit $q_2 \ll 1$, called the *inertial regime*, the torque and the migration rate scale linearly with disk mass, as in the type I case; while in the disk dominated limit $q_2 \gg 1$, the net torque is sensitive to disk parameters, but not exclusively to viscosity. This dichotomy is illustrated in fig. 4.4. It can be shown that the correct definition of the *canonical* type II migration speed is in fact

$$u_{\text{II}} = \frac{q_2}{q_2 + 1} u_{\text{viscous}} \quad (4.2)$$

Fortunately, most works focus on $q_1 = 0.001$ which is the mass ratio between Jupiter and the Sun, and helps comparison. However, the way q_2 is chosen varies from study to study. Duffell et al., 2014 developed a unique approach to determine a value of this parameter that allows for self-consistent stationary regime solutions, given an arbitrary migration rate and disk parameters. Their solutions for q_2 fall in the $[1, 100]$ interval. In contrast, this ratio is usually determined by the initial conditions and typically lies within $[5, 20]$ in other works (Dürmann and Wilhelm Kley, 2015; Dürmann and Wilhelm Kley, 2016; Duffell et al., 2014; Kazuhiro D Kanagawa, Muto, et al., 2018; Clément Mathieu Trisan Robert et al., 2018).

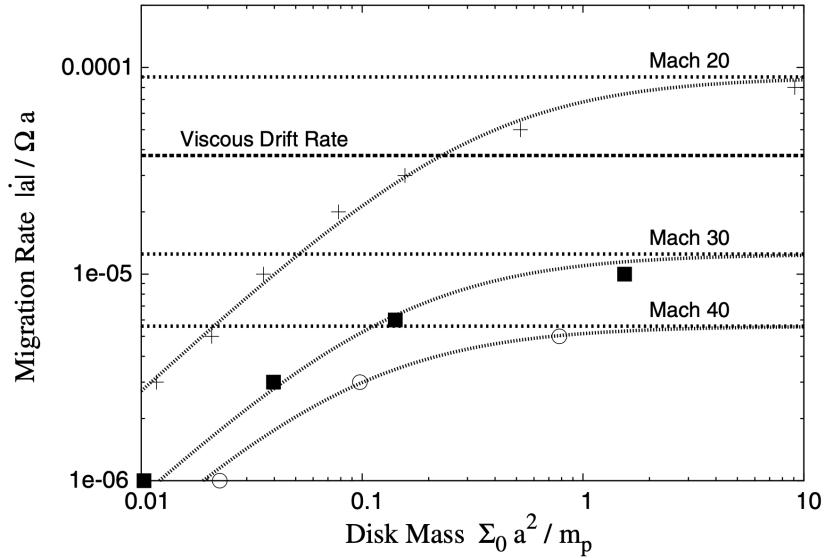


Fig. 4.4: Two distinct asymptotical regimes depending on the disk/planet mass ratio. Here the x-axis unit is $q_2/4\pi$. As the authors vary disk temperature (represented here in Mach number), the asymptotic limit of the normalized migration rate in the disk-dominated regime is changed, and does not in general match the viscous rate. Adapted from (Duffell et al., 2014) (Fig3 therein).

Solutions with lower disk mass should be considered more reliable in studies that do not include the effect of disk self-gravity.

We pointed out that the newly released planet undergoes a transitory fast migration regime. The gap shape needs to dynamically adapt to the planet's position, on a timescale dictated by viscosity as well as pressure gradients (hence shorter than the purely viscous time), until an equilibrium is reached with the migration rate. In my paper, I concluded that migration is still faster than classical type II after this transitory phase ended (see fig 2.). This result has been the subject of recent debate. Scardoni et al. (2020) claim that on longer timescales, migration rate will indeed match the viscous drift rate. However, the migration tracks presented seem to include the later stages of the simulation where the planet approaches very closely the inner edge of the simulation domain. Whatever the boundary conditions are, any measurement performed in such conditions is unreliable. Moreover, the same authors argued that in our zero-accretion case (B1 in the paper), the introduction of a planet modifies the flow state and should induce accretion flow. This argument is in direct contradiction with previous findings of Duffell et al. (2014) and Dürmann and Wilhelm Kley (2015), who remarked that the accretion flow is not in general affected by gap formation, and is not supported by any additional evidence. This work was interestingly directly answered by Kazuhiro D. Kanagawa and Tanaka (2020), who pointed out that novel results were in fact compatible with a semi-analytical model developed earlier in (Kazuhiro D Kanagawa, Tanaka, et al., 2018) (K18). The one figure in the paper is reproduced as fig. 4.5 and completed here with my results. A general conclusion from this is that the classical type II migration rate satisfyingly approximates numerical results in the inertial limit $q_2 \ll 1$, while the disk-dominated asymptotic regime $q_2 \gg 1$ is incompatible with a cohort of results. This important result was hardly spotted within my own data alone, firstly because we used a

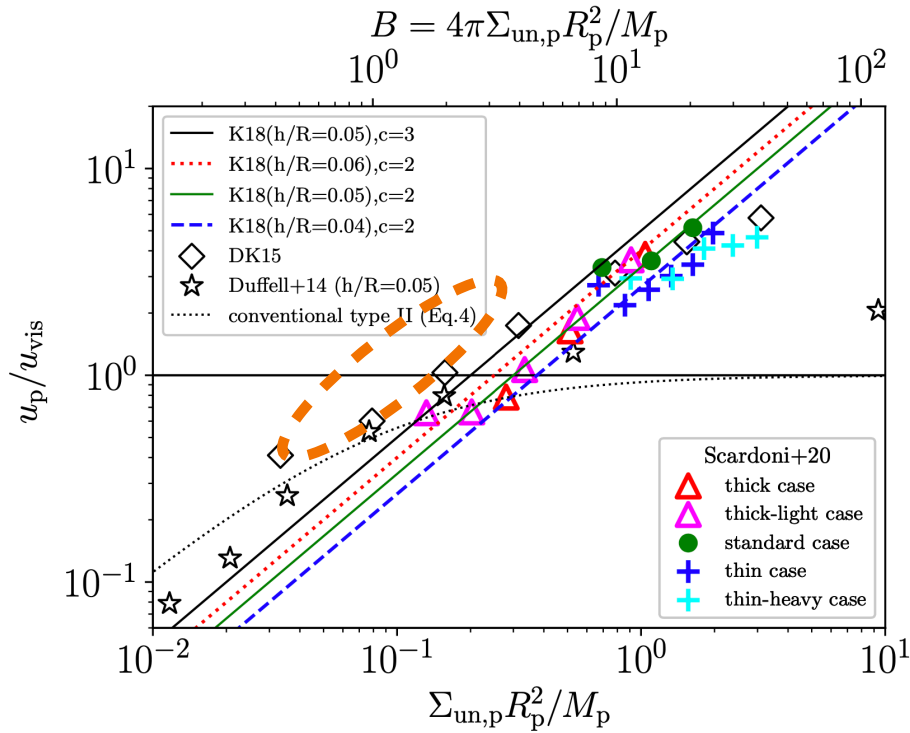


Fig. 4.5: Adapted from (Kazuhiro D. Kanagawa and Tanaka, 2020), fig 1 therein. The semi-analytical model for type II migration developed in Kazuhiro D Kanagawa, Muto, et al. (2018) (K18) is compared with results of numerical experiments from Dürmann and Wilhelm Kley (2015) (DK15) and Scardoni et al. (2020). I overplotted an orange ellipse indicating where my own results fall (using the same data as fig 2 in my paper). The biggest outlier (on the right) comes from Duffell et al. (2014) and corresponds to a critical case where they find a self-consistent solution for rapid migration in a cold disk, leading to an untypically large disk mass.

baseline unsuited to the mass regimes we probed, and secondly because the probed interval was arguably too narrow.

Dynamics of Rossby Vortices

“ It gets harder the more you know. Because the more you find out the uglier everything seems.

— Frank Zappa

This chapter introduces and completes the project I conducted with my supervisors Héloïse Méheut and François Ménard, published in A&A as C. M. T. Robert et al. (2020). As for chapter 4, I will give a broader introduction to the field, discussing the observational context of vortices and their proposed role in planetary formation. In my article, I construct idealized velocity maps of simulated giant vortices, providing a predictive range for the disk around HD 142527 as an example. The paper is followed by a discussion on another one, Boehler et al 2021 (submitted) that I am co-signing, and which presents the most up to date observational data for the dynamics of this disk, as well as the novel difficulties to interpret intermediate resolution data. Finally I present additional results obtained during the production of my own article, and its slightly complicated publication history.

5.1 Context

5.1.1 Rossby vortices

As I mentioned earlier, there are several routes (hydrodynamical instabilities) to vortex formation. Perhaps the most famous vortex-forming mechanism is found in the Kelvin-Helmholtz instability (KHI), where excessive shear between two fluid layers is dissipated as vorticity. Figure 5.1 illustrates the development of KHI in a simple AMRVAC test simulation. See for instance Schaal et al. (2015)¹ for much higher resolution examples. In the work presented hereinafter, I exploit the Rossby wave instability (RWI hereafter) (Lovelace et al., 1999; H. Li, Finn, et al., 2000; H. Li, Colgate, et al., 2001). RWI is akin to KHI within the context of flows in differential rotational, such as proto-planetary disks. RWI results of the excitement of discrete modes $m \in \mathbb{N}$ corresponding to a Fourier decomposition of density along the azimuthal direction. Usually the first mode $m = 1$ dominates once the instability saturates, yielding a single large vortex. The criterion for this instability is that the specific vorticity $(\nabla \times \mathbf{v}) \cdot \mathbf{e}_z / \Sigma$ is locally minimized (Lai and Tsang, 2009; Ono et al., 2016). In practice, this condition is met where the density gradients are sharp. Namely, in a narrow gas ring, or at the edge of a depleted region, e.g. a gap carved by a giant planet, or the inner rim of a so-called “transitional” disk. This expression is a legacy of the historical developments in proto-planetary disk science. It designates a disk with a large (10 AU to

¹and their excellent video <https://www.youtube.com/watch?v=cTRQP6DSaqA>

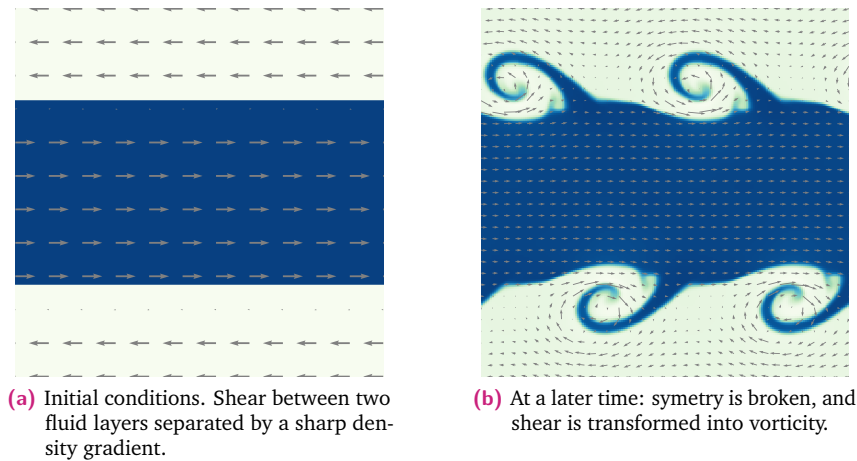


Fig. 5.1: A 2D simulation of the Kelvin-Helmholtz instability performed with AMRVAC and visualized with Yt. Color shows density. The black region is initially 10 times denser and moves in the opposite direction. Arrows indicate the velocity field.

100 AU) gas-depleted inner region, called a *cavity*. Such disks were first thought to represent an intermediate evolution stage between disk formation and complete dissipation of the gas. This view has however been challenged, as it appears that many such structures may in fact be caused by interactions with stellar companions (Daniel J. Price et al., 2018, e.g.). With this in mind, the expression “cavity-hosting disk” seems more appropriate to me, and allows to remain agnostic with respect to the reason why such disks are locally depleted.

5.1.2 The role(s) of vortices in the grand scheme of planetary formation

Planet-forming vortices ? As I explained in section 2.2.4, vortices formed in a shear flow such as a Keplerian disk can only be anti-cyclonic and correspond to local maxima in pressure. As a consequence they behave like solid accumulators. For this reason they were proposed as a possible route to transform micron-sized dust into planetesimals (Barge and Sommeria, 1995; Tanga et al., 1996).

Vortices as signposts of rapidly forming planets ? The other side of the coin is, gap-opening massive planets disturb the density distribution in a disk such that pressure bumps should naturally occur on the edges of such gaps. Their stability against RWI is then compromised if the planet-forming timescale is much less than the viscous timescale. In other terms, vortices should form under the condition that giant planets acquire their mass rapidly (which is supported by runaway accretion models), and that the viscous spreading is low enough that sharp pressure gradients can develop.

This is in fact commonly seen in planet-disk simulations, though it ought to be mentioned that in this context, both timescales are usually arbitrary, as we have seen the previous chapter. The final aspect ratio² of vortices depends on these time scales. Hammer, Paola

²i.e. the ratio between the major and the minor axis of an ellipse in the polar coordinates attached to the disk, that fits an iso-density in the vortex.

Pinilla, et al. (2018) showed that indeed, longer planet introduction periods lead to more elongated and weaker vortices. Nonetheless, (Baruteau, Barraza, et al., 2019) proposed that asymmetries in MWC 758 (see fig. 5.2 panel (a)) are two vortices betraying the presence of as many giant planets.

Moreover, such vortices are not in co-orbital motion with the planets they accompany. This is important when one considers the local density enhancement they represent is relatively strong in terms of density (up to about a factor 2 to 3 in variation in gas density along a ring), and disrupt the wake propagation periodically, affecting planetary migration. McNally et al. (2019) assessed this effect and showed that it can be dramatic at low viscosities as it inhibits the stopping effect of the disk feedback, leading to runaway migration regimes. In the cases of midrange planets (not quite massive enough to open a frank axisymmetric gap), the authors showed that vortices appear in the corotation region and lead to chaotic migration. Lega et al. (2020) (paper accepted after the defense of the present manuscript) pursues the exploration of these regimes in 3D simulations, and unveils that two migration modes arise from vortex-planet interactions. In particular, the authors show that when the planet-induced gap is not very deep, migration is on average much slower than typical type II. This behaviour is enabled in 3D simulations without self-gravitation of the disk and provides an interesting solution to the everlong rapid inward migration problem.

Summary As we can see the link between vortices and planets is two-sided. While none of the alleged connections are currently confirmed, they are not mutually exclusive. Vortex-planet interactions may provide a mechanism to chain planetary formation, in the sense that multiple planetary system may form in a cascade. Additionally, since vortices do not survive small-scale viscosity long enough to be as common as they appear, their detection would provide important constraints on the infamous turbulent viscosity.

5.1.3 Observational context

Vortex candidates seen in thermal dust radiation A handful of targets have been resolved that show lopsided structures in the dust thermal continuum. In fig. 5.2 I showcase 3 of them. As is evident from this sample, the morphology of these asymmetries shows some diversity, and it is not clear whether they originate from similar mechanisms. HD 142527 in particular shows an incredible factor ~ 30 in luminosity between the north side and south side, while the contrast in HD 100546 is much more subtle. The crescent shapes in HD 142527 and MWC 758 are particularly intriguing and closely resemble simulated images of dusty vortices (as we will see in chapter 6). Meanwhile, MWC 758 is showing not one but two clumps, at an inclination close to 0° , allowing to see that the dust distribution of the most inner clump is not symmetric with respect to its maximum. Rather, it shows what I will call a “yin”-like variation. This subtle but important feature is again not unlike what is obtained in hydro simulations (as I will demonstrate in the next chapter). Indeed Baruteau and Zhu (2016) showed that dust does not in general concentrate exactly toward the vortex’s eye but rather piles up ahead of the vortex, at a relative azimuthal position that varies with the Stokes number (or grain size), meaning that the grains are sorted by size so to speak, and that the position of the peak luminosity should vary accordingly with wavelength.

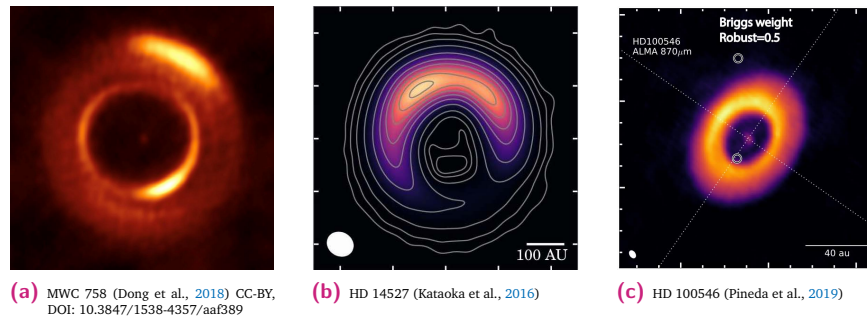


Fig. 5.2: Lopsided structures seen in the thermal radiation of weakly inclined disks. These are primary vortex candidates. Another one is found in the disk around HD 163296 (see fig. 1.8, panel (c)).

While these targets look like excellent vortex candidates, their asymmetries in the distribution of dust may be explained differently. It was proposed by W. Kley and Dirksen (2006) that an eccentric massive ($\geq 3M_{\text{Jupiter}}$) planet in a moderately viscous disk ($\alpha \simeq 4 \times 10^{-3}$) can excite the eccentricity of the disk itself. Following Kepler's second law, the orbital velocity in an eccentric disk is lower at the aphelion. Since mass flux is conserved along the orbit, it implies the density should be higher there, in which case we get a lopsided structure in the gas. However, Ataiee et al. (2013) showed that, contrary to a vortex, an eccentric disk only traps dust radially, not azimuthally, so this scenario can be rejected in most pronounced cases, while it may still fit subtle asymmetries such as seen in HD 100546 (fig. 5.2 panel (c)).

Coincidentally, it appears that cavity hosting disks are not necessarily a transitional state but may in fact result from interactions with binary stars. Daniel J. Price et al. (2018) were indeed able to reproduce most of the features (cavity, spirals, asymmetry) in HD 142527 as effects of a stellar companion.

In fig. 5.3, I summarize the characteristics of 8 targets³ showing azimuthal asymmetries in continuum imaging where vortices are proposed as an explanation. Resolving the dynamics of these structures is one way to assess their nature and provide evidence potentially incompatible with that particular scenario. In my paper (next section), I produce numerical predictions for the projected velocity that should be expected from a large vortex. HD 142527 stands out as the easiest target for dynamics-driven vortex detection a large angular size. Its inclination ($\sim 30^\circ$) is also *a priori* favorable: it is close enough to the face-on limit that column integration should not destruct the signal, while sufficiently inclined that the plane velocity (components other than vertical), are not negated by projection. For these reasons, this disk is the prototype I use in the paper.

Recent progress in gas velocity reconstruction Teague, Bae, et al. (2018) demonstrated a very accurate technique to measure rotation speeds in axisymmetric disks. Although they reach a much better precision than 100 m s^{-1} , the method is not applicable to non axisymmetric features such as vortices.

In an attempt to extract dynamical imprints of planetary perturbers from observational data, Casassus and Perez (2019) ended up building a seemingly very robust approach to

³based on a biased sample of what I managed to unearth from my bibliography

axisymmetric flow $\langle v_\varphi \rangle$ reconstruction. While tailored for an arguably more realistic 3D conical molecular emitting surface, this approach fails to distinguish between the radial and azimuthal components of the flow. Unfortunately, their method is not suited in cases where both components are of comparable amplitudes, as is the case in my simulations.

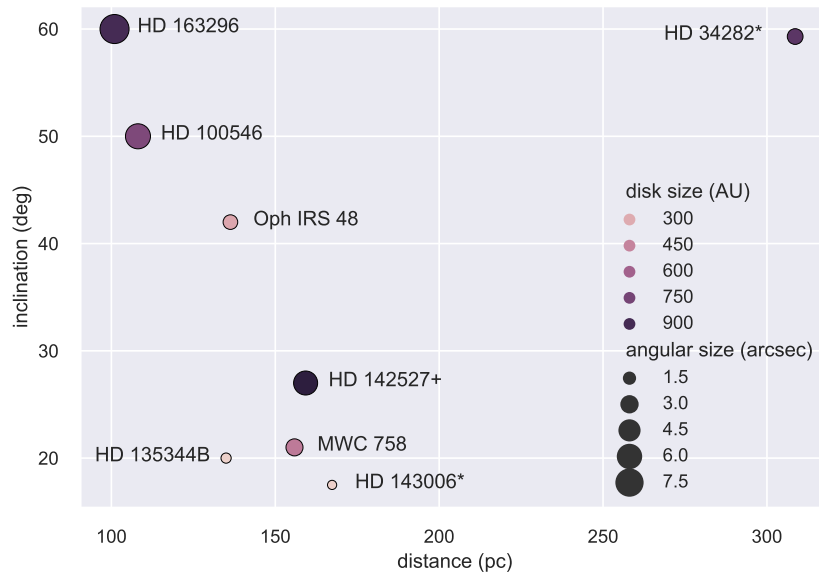


Fig. 5.3: Usual suspects: a spatially organized list of vortex candidates, in a distance (to Earth) VS inclination map. Point size is proportional to the angular size of target as seen from Earth, while color represent their physical size. “*” and “+” in a target name indicate a proposed and confirmed secondary, respectively. Disk “sizes” are estimates in diameter from radio observations, compiled from various sources in the litterature. Distances are obtained via parallax data from Gaia EDR3 (Gaia Collaboration, Prusti, et al., 2016; Gaia Collaboration, Brown, et al., 2020).

5.2 Robert, Méheut & Ménard 2020

A&A 641, A128 (2020)
<https://doi.org/10.1051/0004-6361/201937414>
© C. M. T. Robert et al. 2020

**Astronomy
&
Astrophysics**

Dynamical signatures of Rossby vortices in cavity-hosting disks

C. M. T. Robert¹, H. Méheut¹, and F. Ménard²

¹ Université Côte d'Azur, Observatoire de la Côte d'Azur, CNRS, Laboratoire Lagrange, Bd de l'Observatoire, CS 34229, 06304 Nice Cedex 4, France
e-mail: clement.robert@oca.eu

² Univ. Grenoble Alpes, CNRS, IPAG, 38000 Grenoble, France

Received 24 December 2019 / Accepted 13 July 2020

ABSTRACT

Context. Planets are formed amidst young circumstellar disks of gas and dust. The latter is traced by thermal radiation, where strong asymmetric clumps have been observed in a handful of cases. These dust traps could be key to understanding the early stages of planet formation, when solids grow from micron-size to planetesimals.

Aims. Vortices are among the few known asymmetric dust trapping scenarios. The present work aims to predict their characteristics in a complementary observable. Namely, line-of-sight velocities are well suited to trace the presence of a vortex. Moreover, the dynamics of disks is subject to recent developments.

Methods. Two-dimensional hydro simulations were performed in which a vortex forms at the edge of a gas-depleted region. We derived idealized line-of-sight velocity maps, varying disk temperature and orientation relative to the observer. The signal of interest, as a small perturbation to the dominant axisymmetric component in velocity, may be isolated in observational data using a proxy for the dominant quasi-Keplerian velocity. We propose that the velocity curve on the observational major axis be such a proxy.

Results. Applying our method to the disk around HD 142527 as a study case, we predict that line-of-sight velocities are barely detectable by currently available facilities, depending on disk temperature. We show that corresponding spiral patterns can also be detected with similar spectral resolutions, which will help to test against alternative explanations.

Key words. hydrodynamics – instabilities – planets and satellites: formation – protoplanetary disks

1. Introduction

Planets are formed in circumstellar disks composed of mainly gas and some solid dust components. Many aspects of the processes implied in their formation remain challenging to explain. More specifically, the transition from small dust grains to large planetesimals face two major obstacles: the drift barrier corresponding to fast inward drifting due to gas headwind, and the collision barrier due to destructive collisions (Chiang & Youdin 2010). Pressure bumps provide a solution to the drift barrier, as they act as a barrier stopping the drifting solids and forming dust rings. Concentric dusty rings are a common feature in resolved infrared images of protoplanetary disks (Andrews et al. 2018). Pressure bumps are also known to promote the formation of large-scale vortices, through to the Rossby wave instability (RWI), which are proposed as a solution to the barriers in planetesimal formation. Large vortices both stop the dust drift and harness efficient growth by lowering relative speeds between grains. This is why vortices were proposed as a planet-promoting scenario (Barge & Sommeria 1995; Adams & Watkins 1995; Tanga et al. 1996; Bracco et al. 1999). Moreover, it is well known that massive planets build up pressure bumps in their vicinity, exciting vortex formation (de Val-Borro et al. 2006, 2007; Fu et al. 2014; Hammer et al. 2017; Andrews et al. 2018; Baruteau et al. 2019), which in turn affects planetary migration (Regály et al. 2013; Ataiee et al. 2014; McNally et al. 2018). The study of large vortices is thus key to understanding planetary formation.

The RWI (Lovelace et al. 1999; Li et al. 2000, 2001) is a promising vortex-forming scenario, and is expected where sharp density gradients are found. So-called transitional disks provide

such conditions at the outer edge of large (~5–100 AU) gas cavities they host. Extensive computational effort has been dedicated to studying the long-term evolution of RWI vortices (Fu et al. 2014; Méheut et al. 2012a; Regály & Vorobyov 2017a; Andrews et al. 2018). Overall, eddies tend to form in a few tenths of orbital periods and survive for 10^3 to 10^4 orbital periods.

Concurrently, asymmetric dust crescents are being observed in thermal radiation of a growing number of targets (Cazzoletti et al. 2018; Dong et al. 2018; Isella et al. 2018; Casassus et al. 2019; Pineda et al. 2019) as well as in scattered emission (Benisty et al. 2018). Those clumps are candidates for large vortices, and there have been attempts to explain their formation as vortex-driven (Regály et al. 2012; Birnstiel et al. 2013). Alternatively, disk eccentricity (Ataiee et al. 2013) and excitation by an eccentric companion (Astropy Collaboration 2018) were proposed to explain this azimuthal dust excess, however not reproducing the observed dust-to-gas ratio.

Complementary measurements of the gas dynamics would be of great help in constraining and rejecting concurrent explanations. Continuum emission traces the spatial distribution of dust grains dynamically coupled with the gas, so it provides indirect information concerning the underlying gas dynamics. However, direct measurements of the gas radial velocity can now be achieved through Doppler-shifting of molecular lines, as a result of increasingly sophisticated data reduction techniques (Yen et al. 2016; Teague et al. 2016; Teague & Foreman-Mackey 2018) and ever-enhanced spatial resolution (Andrews et al. 2018). It is becoming possible to use these data to build connections to continuum asymmetries (Casassus et al. 2015a; Casassus & Pérez 2019) or to search for planet-induced

A128, page 1 of 11

Open Access article, published by EDP Sciences, under the terms of the Creative Commons Attribution License (<http://creativecommons.org/licenses/by/4.0>), which permits unrestricted use, distribution, and reproduction in any medium, provided the original work is properly cited.

deviations (Pinte et al. 2018, 2019; Teague et al. 2018a; Pérez et al. 2020).

Hence, observations in molecular line emission are essential to confirm or reject current and future vortex candidates. The present paper aims to characterize the dynamical signatures expected for a single large Rossby eddy forming in the inner rim of a cavity, by the means of hydro simulations.

The paper is organized as follows. First, we describe the numerical setup of our hydro simulations in Sect. 2. We then provide insight into the observability of resulting vortices and propose a method to extract their signature from observational data in Sect. 3. Finally, we discuss the limits of our approach in Sect. 4 and conclude in Sect. 5.

2. Hydro simulations setup

We perform 2D hydro simulations via MPI-AMRVAC 2.2 (Porth et al. 2014; Xia et al. 2018). Namely, we solved Euler equations for an inviscid gas as follows:

$$\partial_t \Sigma + \nabla \cdot (\Sigma \mathbf{v}) = 0, \quad (1)$$

$$(\partial_t + \mathbf{v} \cdot \nabla) \Sigma \mathbf{v} = -\Sigma \nabla \phi - \nabla p, \quad (2)$$

where Σ and \mathbf{v} stand for surface density and velocity, respectively, $\phi \propto -1/r$ is a central gravitational potential, and p is the vertically integrated pressure. The latter is prescribed by a barotropic equation of state $p = S \Sigma^\gamma$, where $S = 86.4$ (code units¹) characterizes the entropy and $\gamma = 5/3$ is the adiabatic index. Sound speed is given as $c_s^2 = \gamma p / \Sigma$. Equations are solved on a linearly spaced polar grid (r, φ) with a fixed resolution $(512, 512)$, ranging from $r_{\min} = 75$ AU to $r_{\max} = 450$ AU and $\varphi \in [0, 2\pi]$. Numerical convergence was checked against runs with double resolution in each direction. The MPI-AMRVAC 2.2 simulations use finite-volumes Reimann solvers. A two-step hllc integration scheme (Harten et al. 1983) and a Koren slope limiter (Koren 1993) are used in our simulations.

The model is physically inviscid. The numerical viscosity, expressed in terms of the widely used “ α ” paradigm (Shakura & Sunyaev 1973), was estimated to lie between $2 \times 10^{-8} \leq \alpha \leq 3 \times 10^{-4}$ in the vortex-forming region. Details on this estimations are given in Appendix B.

The disk is truly “massless” in that both self-gravity and indirect terms due to the motion of barycenter are neglected in the computation of the gravitational potential. Zhu & Baruteau (2016) show that including either or both of these contributions affects the evolution of the vortex. In particular, the inclusion of indirect terms promotes a radial displacement of the structure and overall increases the density contrast with respect to its background. This latter result was also confirmed by Regály & Vorobyov (2017b) for vortices formed in a viscosity transition region. Because of these combined effects, the velocity of the structure is also modified, while a direct comparison is nontrivial.

2.1. Initial conditions

The initial gas surface density features a smooth radial density jump, modeling a disk cavity as

$$\Sigma(r, t = 0) = \Sigma_0 (r/r_*)^{-1} \times \frac{1}{2} \left[1 + \tanh \frac{r - r_j}{\sigma_j} \right], \quad (3)$$

¹ Our code unit system is completely described by mass, length and time normalisation constants respectively $m_* = 1$ solar mass, $r_* = 100$ AU and $t_* = 1$ orbital period of a test particle at $r = r_j$.

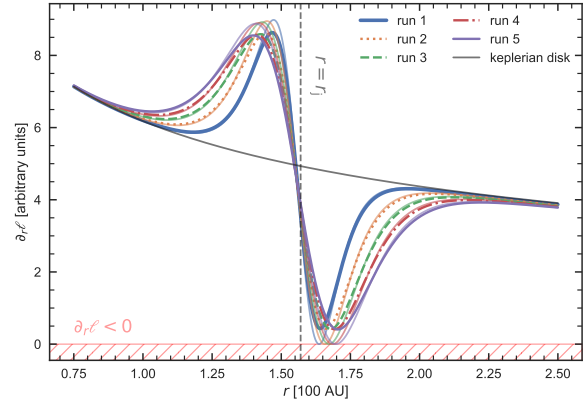


Fig. 1. Initial gradient in specific angular momentum ℓ for our 5 simulations (thick lines, ranked from coldest to hottest) compared to the Keplerian case. The width of the density “jump” region σ_j is adjusted in two steps. First, the critical value σ_j^{crit} for which the global minimum in $\partial_r \ell$ is exactly 0 (thin solid lines) is derived. Any value $\sigma_j < \sigma_j^{\text{crit}}$ would give rise to a rotationally unstable region, characterized by $\partial_r \ell < 0$. An arbitrary 5% margin was applied $\sigma_j = 1.05 \times \sigma_j^{\text{crit}}$ in our runs (thick dashed lines).

where r_j and σ_j are the radial location and the width of the jump respectively, and $r_* = 100$ AU is a normalization factor. The initial equilibrium azimuthal velocity is defined as

$$\frac{v_\varphi^2}{r} = \frac{GM}{r^2} + \frac{\partial_r p}{\Sigma}, \quad (4)$$

where G is the universal gravity constant and M is the mass of the central star.

Observational constraints for HD 142527 are used to tune numerical values, wherever applicable, as we now detail. We assume $M = 2.2 M_\odot$, compatible with existing estimations (Verhoeff et al. 2011; Casassus et al. 2015b). We choose a standard radial density slope in r^{-1} , which is also compatible with estimate from Verhoeff et al. (2011) in the optically thin approximation at 1 mm. Distance to star is now known with good precision 157 ± 6 pc thanks to Gaia Collaboration (2016), which implies the cavity lies at $r_j = 157$ AU for an angular size of $1''.0$ (Casassus et al. 2012). The reference setup has an aspect ratio, or “temperature”² $h \equiv H(r_j)/r_j \approx 0.09$, where $H(r)$ is the disk scale height.

Other simulations with $h \in [0.09; 0.16]$ were performed, and labeled run 1 to run 5 by increasing value in h . These are discussed in Sect. 3.3. The derivation of this parameter is detailed in Appendix A.1. As this temperature is varied, we adjust the density jump’s width σ_j within 5% of its critical value, where the disk becomes rotationally unstable under Rayleigh’s criterion (Rayleigh 1879). Doing so, we approach the physical upper limit in vortex velocity after the RWI saturates. The corresponding signature in the specific angular momentum $\ell = r v_\varphi$ is illustrated in Fig. 1. The computed values for σ_j , and for runs from 1 to 5, are [11.6, 14.7, 16.9, 18.7, 20.2] AU. Even in the hottest case, the simulation box extends at least $4\sigma_j$ away from the density jump center r_j . Unless explicitly stated, all figures show the results for the reference model.

² The vertical spreading of the disk is physically caused by heating and usually characterized by a scale height.

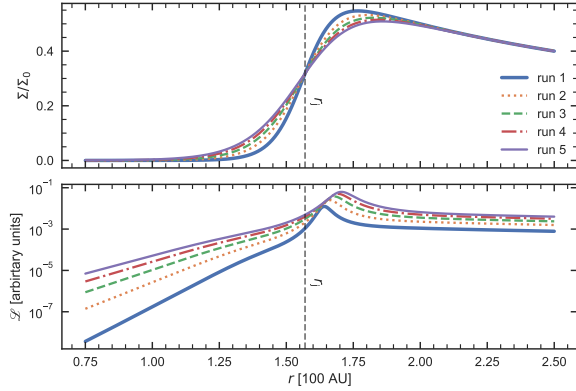


Fig. 2. Initial radial profiles in surface density (*top*) and the $\mathcal{L}(r)$ function (defined in Eq. (5)) for our 5 simulations. In each model, $\mathcal{L}(r)$ features a clear local maximum, which is a necessary condition to RWI growth.

2.2. Boundary conditions

Boundary conditions are imposed through ghost cells outside of the domain and wave-killing region in the active domain. In the radial direction, ghost cells are fixed to the initial equilibrium values for density and azimuthal momentum. The radial momentum is copied from the first cells to the ghost cells at the inner boundary, and extrapolated linearly with no-inflow condition at the outer edge. However, these boundary conditions have low impact as standard damping zones (de Val-Borro et al. 2006) are also used to avoid reflections at domain edges. The domain is periodic in the azimuthal direction.

2.3. Rossby wave instability and vortex formation

Rossby wave instability is similar to the Kelvin-Helmholtz instability in a differentially rotating Keplerian disk. The instability tends to convert excess shear into vorticity. Lovelace et al. (1999) showed that a local extremum in the background potential vorticity is a necessary condition to RWI. More recent works have clarified that a minimum is required (Lai & Tsang 2009; Ono et al. 2016). The key function is defined as

$$\mathcal{L}(r) = \frac{1}{2} \frac{\Sigma}{(\nabla \times \mathbf{v}) \cdot \mathbf{e}_z} S^{2/\gamma}. \quad (5)$$

We exhibit this key function within our initial setup in Fig. 2, showing the existence of a local maximum in $\mathcal{L}(r)$, corresponding to a minimum in vorticity.

We find that, in order to excite the RWI unstable modes, it is useful to add random perturbations. We chose to perturb the radial velocity, which is zero otherwise, as

$$v_r(r, \varphi, t = 0) = c_s \psi(r, \varphi) \exp \frac{-(r - r_j)^2}{2\sigma_j^2}, \quad (6)$$

where $\psi(r, \varphi) \in [-10^{-2}, 10^{-2}]$ is a uniformly distributed random variable drawn for each grid cell. After the instability has saturated, we obtain a single vortex shown in Fig. 3. In a frame that is co-rotating with the vortex, its global structure is quasi-stationary as shown in Fig. 4. The radial density profile at the azimuth of the density maximum is plotted at different times. The orange dotted curve at $t = 10$ features the most noticeable

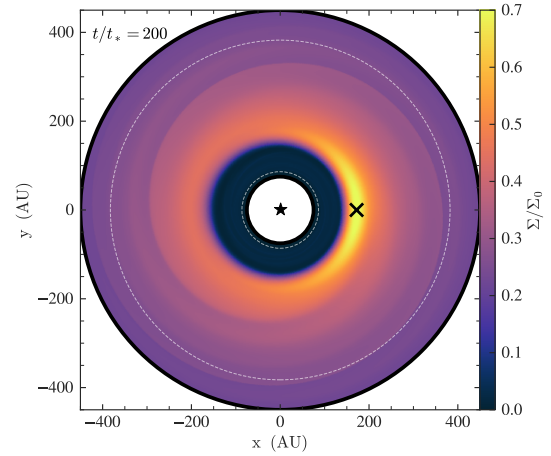


Fig. 3. Gas surface density plotted in Cartesian coordinates (x, y) after $t = 200$ orbital periods (t_*). The global density maximum is indicated by a black cross. The position of the central star is denoted as a “★” symbol. The simulation box radial limits are drawn as solid black circles, while the dashed-line circles indicate the limits of wave damping zones.

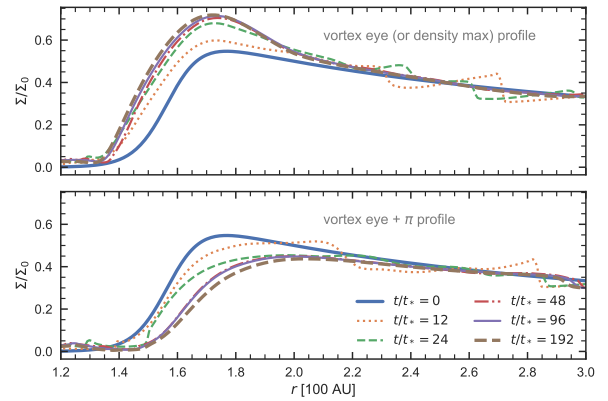


Fig. 4. Time evolution of the radial density profile, plotted as slices at the azimuth of the density maximum where the vortex eye lies (*top*) and its radial opposite (*bottom*). The slices correspond to the $y = 0$ axis in Fig. 3, with $x > 0$ (*top*) and $x < 0$ (*bottom*), respectively. After ~ 40 orbital periods, the disk has practically reached a stationary state. The cavity profile itself has become uneven, showing a non-zero eccentricity.

fluctuations, as smaller eddies are still undergoing a merger and strong spiral waves are launched outward. After 40 orbital periods, the surface density of the vortex is stabilized and does not rapidly evolve any more. Thus we consider this state as quasi-stationary; we take a look at the dynamics of the structure in the next section.

3. Vortex signatures in dynamics

In this section, we provide observational signatures obtained from the dynamics of the vortex. The observable studied in this work is the velocity projected along the line of sight v_{LOS} . We first discuss an adequate decomposition of the velocity field to characterize the signatures. We then study their observability against disk orientation and provide insight into how disk aspect ratio affects observed velocities.

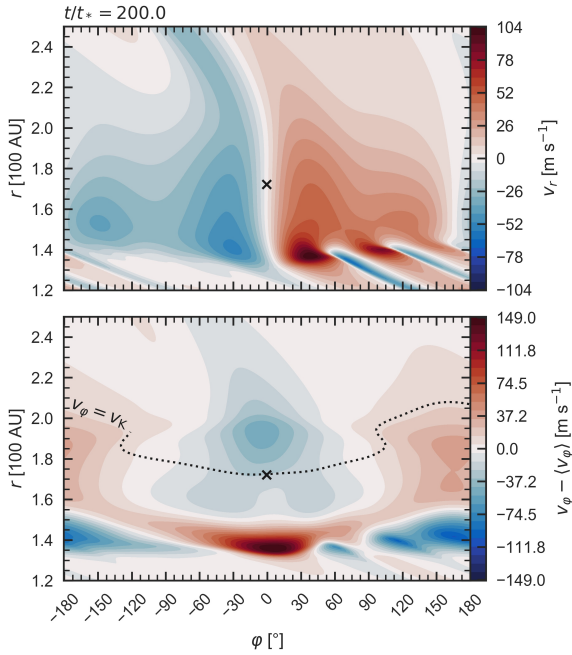


Fig. 5. Polar components of the velocity field of a vortex. *Top*: radial velocity. *Bottom*: azimuthal velocity, where the axisymmetric part $\langle v_\phi \rangle$ is carried out. The pressure maximum is indicated by a black cross. The snapshot is taken at $t = 200$ orbital periods. The dotted line in the *bottom panel* indicates fluid in exact Keplerian rotation.

3.1. Extracting dynamical signatures

The dynamics of a disk is dominated by rotation around the central star. In an axisymmetric stationary state, the net radial force is zero, as in Eq. (4). Owing to pressure gradients, the radial equilibrium slightly departs from Keplerian motion. This is the sub-Keplerian rotation in a disk with negative radial pressure gradient. As a dynamical structure, a vortex exposes little difference to global rotation. Thus, it is useful to decompose the angular velocity v_ϕ as

$$v_\phi = \langle v_\phi \rangle + (v_\phi - \langle v_\phi \rangle) \equiv \langle v_\phi \rangle + v'_\phi, \quad (7)$$

where $\langle \cdot \rangle$ is the azimuthal average operator, and we denote the non-axisymmetric part as v'_ϕ . Hence the total velocity field \mathbf{v} can be decomposed in the polar basis $(\mathbf{e}_r, \mathbf{e}_\phi)$ as

$$\mathbf{v} = v_r \mathbf{e}_r + (\langle v_\phi \rangle + v'_\phi) \mathbf{e}_\phi \equiv \langle v_\phi \rangle \mathbf{e}_\phi + \mathbf{v}'. \quad (8)$$

In the absence of a global accretion flow, there is no relevant axisymmetric part in v_r . Hence we consider that dynamical signatures of non-axisymmetric features reside in $\mathbf{v}' = v_r \mathbf{e}_r + v'_\phi \mathbf{e}_\phi$. Both components of this residual radial and azimuthal velocity are quantified in Fig. 5 and are of similar amplitudes. For comparison, the typical Keplerian speed at the vortex position ($r \sim 180$ AU) is $v_K = 3.3 \text{ km s}^{-1}$, that is, one to two orders of magnitudes larger than the deviation due to the vortex, and one order of magnitude larger than the local sound-speed c_s . The amplitude in the azimuthal velocity is as high as 300 m s^{-1} for this reference (coldest) model. This sets a first upper limit to the spectral resolution required for a direct detection to about 100 m s^{-1} . This is achievable for bright lines with the Atacama Large Millimeter/submillimeter Array (ALMA), for example,

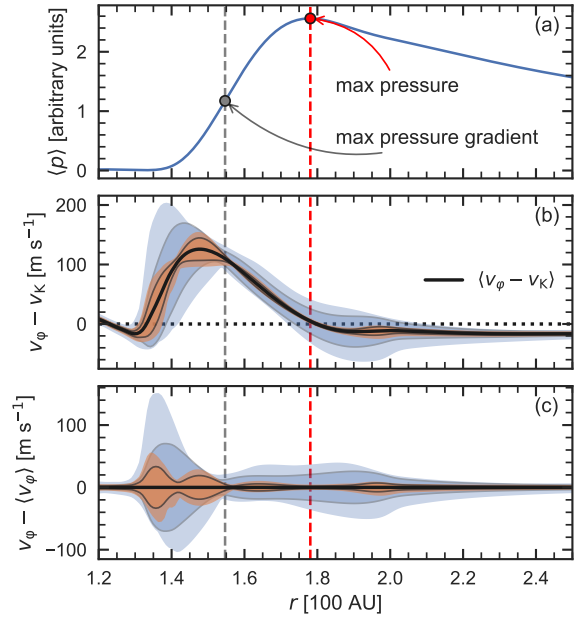


Fig. 6. Comparison between Keplerian velocity v_K and average azimuthal velocity $\langle v_\phi \rangle$ as 1D masks. (a) Pressure profile in arbitrary units. (b and c) Azimuthal velocity cross-sections, with offsets (masks) v_K and $\langle v_\phi \rangle$, respectively. The average $\langle V - \text{mask} \rangle$ is indicated by a thick black line, while shadows show the amplitude and standard deviations in blue ($V = \langle v_\phi \rangle$), and orange ($V = \frac{1}{2}(v_{\phi,\text{left}} + v_{\phi,\text{right}})$). Data are taken at $t = 200$ orbital periods (inspiration for this figure was drawn from Teague et al. 2018a).

for the CO (2-1) or the CO (3-2) transitions, using channel widths of 70 or 120 kHz (or narrower), respectively. For example, van der Marel et al. (2016) successfully detected the ^{13}CO (3-2) and C^{18}O (3-2) lines of SR21, HD 135344B, DoAr44, and IRS 48 with good signal-to-noise ratio (S/N) (peak S/N in the integrated intensity map up to 30 for the ^{13}CO line) with spectral resolution of 0.1 km s^{-1} and angular resolution of $0''.25$. Boehler et al. (2017) obtained data with similar angular and spectral resolutions for HD 142527 but with much higher S/N. All sources are well detected in the lines; increasing the spectral resolution by another factor of 2, as well as the S/N, is possible within a reasonable amount of time ($< 12 \text{ h}$). We note that there is a non-zero azimuthal velocity deviation at the maximum density/pressure (i.e. $v'_\phi \neq 0$), as seen in Fig. 5. Because the vortex is an asymmetric structure, the radial position of the pressure extremum varies with the azimuth. Consequently, the line of exact Keplerian rotation is not circular as shown in Fig. 5.

However, the decomposition proposed in Eq. (8) is vain unless the proposed dominant term $\langle v_\phi \rangle$ can be subtracted from observations. While a Keplerian fit is usually a suiting approximation of the dominant velocity term, it proves insufficient near sharp density jumps. As shown in Figs. 6a and b, subtracting a Keplerian power law leaves systematic velocities caused by pressure gradients. In the density transition region, those systematics dominate over the variability in the remaining signal.

However, we further show (Figs. 6b and c) that averaging two facing cross sections in azimuthal velocities consistently yields a much better approximation for the global azimuthal average $\langle v_\phi \rangle$, with a standard deviation $\leq 20 \text{ m s}^{-1}$. This is a direct sign that the non-axisymmetric parts of the azimuthal velocities v'_ϕ in opposing disk halves are anticorrelated, although not strictly equal in

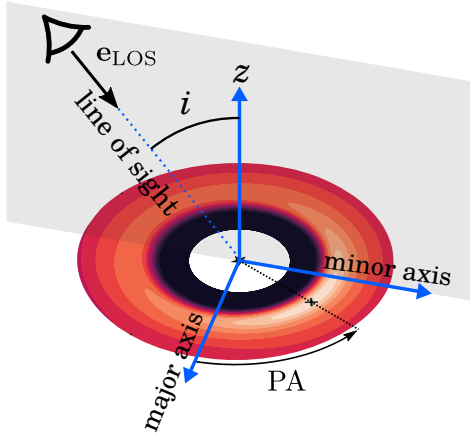


Fig. 7. Sketch view of our notations. The gray shadow shows the plane containing the vertical e_z and the line of sight.

amplitudes. Given that detection is only sensitive to azimuthal velocities on the observational major axis x of the disk, we naturally obtain a satisfying method to subtract $\langle v_\varphi \rangle$ from the whole signal. Consequently, we now confidently assume that the axisymmetric part $\langle v_\varphi \rangle$ of the azimuthal velocity can indeed be removed with good precision from observations, and we only consider the remaining components of \mathbf{v}' exhibited in Fig. 5.

3.2. Vortex detection in line-of-sight velocities

Gas velocity is usually detected through Doppler-shifting in molecular lines. It is therefore the velocity component parallel to the line of sight that is probed. Within optically thick lines, the resulting velocity profile can be blurred by vertical integration over disk height. It is beyond the scope of the present work to investigate this second-order effect, so we neglect both optical and geometrical thickness effects. This approach is reasonable within the assumption that emissive molecular regions are geometrically thin and well resolved (as remarked by Teague et al. 2018b). Furthermore, full 3D simulations showed that, in a stationary state, a vortex tends to be tubular and that its vertical velocity is negligible (Lin 2012; Zhu & Stone 2014; Richard et al. 2013). This comforts us in the idea that, for long-lived vortices, it is reasonable to ignore this component. This also means we ignore the vertical extension in the conical shape of the emissive layer. However, it can easily be shown that for inclinations lower than 45° , even a very high emissive layer $z \approx 5H$ and a large aspect ratio $H/r = 0.2$, can in principle be deprojected as long as it remains spatially thin.

To study vortex dynamical signatures, we use here cylindrical coordinates centered on the star. The radial axis ($\varphi = 0$) is the observational major axis, and the upper part of the disk ($z > 0$) is defined to be the one seen by the observer Fig. 7. Thus, the line-of-sight direction $e_{\text{LOS}}(i, \varphi)$, defined as pointing away from the observer, can be written in the disk cylindrical basis (e_r, e_φ, e_z) as

$$e_{\text{LOS}}(i, \varphi) = -(\sin(i) \cos(\varphi) e_r + \sin(i) \sin(\varphi) e_\varphi + \cos(i) e_z), \quad (9)$$

and it follows that the line-of-sight velocity corresponding to \mathbf{v}' is written as

$$v'_{\text{LOS}} \equiv \mathbf{v}' \cdot e_{\text{LOS}} = -\sin(i) (\sin(\varphi) v_r + \cos(\varphi) v'_\varphi). \quad (10)$$

Hence, the effective observable v'_{LOS} mixes v_r and v_φ . For a 2D vortex disk inclination equally affects all projected velocities and only acts as a scaling factor $\sin(i)$. An inclination $i = 27^\circ$, corresponding to the estimated value for HD 142527 (Fukagawa et al. 2013), is used in the following applications. This choice is arbitrary and used as a textbook case. We note that this inclination is moderate. Deprojection would still be feasible at up to $i = 45^\circ$, where projected velocities would be 1.5 times larger, making detection easier. Figure 8 shows the morphology of the observable v'_{LOS} (large panels), along with corresponding components v_r and v'_φ (small panels), for four different values of PA. This result constitutes an idealized case, built on the assumption that the axisymmetric component $\langle v_\varphi \rangle$ can be exactly subtracted from observational data. We note that we are set in the particular case where the PA rotates in the same direction as the disk. When not so, sign in v'_{LOS} must simply be inverted. At all position angles (PAs), the anticyclonic motion of the vortex around the density maximum is apparent in v'_{LOS} . This point roughly coincides with the maximum luminosity at most wavelengths, and can be located within continuum observations, if not directly in molecular lines used to infer projected velocities.

We note that the eye of the vortex and the region immediately facing it have similar Doppler shifts (e.g., both blue at PA = 0°). This is an expected outcome of subtracting the azimuthally averaged velocity, since the both regions are local extrema along the azimuthal direction. Another signature of the vortex is the azimuthal proximity between the maximum density (black cross) and the projected velocity extrema. The latter two points are determined by the physical on-site velocity as well as the inclination of the system, and hence are virtual positions. Their physical separation is maximized for PA = 90° and minimized for PA = 0° . A direct implication is that detecting a vortex lying on the major axis requires greater angular resolution. However, little dependence of the velocity range on the PA is found. The topography of the signal changes with the PA but the anticyclonic region stands out regardless the orientation. The signature is also typical with a sign reversal in the vicinity of the pressure maximum, along the major axis direction. This characteristic behavior, sign change, is easier to measure in relative than the absolute small velocities and would be observed even with a beam covering the vortex almost entirely (about 100 AU, or 0.6 in the case of HD 142527).

3.3. Detectability against disk temperature

Although our setup is constrained by observations, its temperature (or equivalently h) is not. Indeed the temperature gives the sound speed, which is fundamental to estimate the vortex velocity. To study this dependence, four additional simulations with higher temperatures ($h \in [0.094, 0.119, 0.136, 0.150, 0.161]$) were performed. In Fig. 9, we show contours of projected velocity v'_{LOS} , sampled at an interval corresponding to a tenth of the obtained dynamical range, namely 10 m s^{-1} . The reference, “coldest” setup produces the lowest velocities ranging from -20 to $+20 \text{ m s}^{-1}$, where most of the “detected” structure is within the vortex region. The direct observation of a peak-to-valley velocity shift of about 40 m s^{-1} is challenging but is within reach of ALMA. Boehler et al. (2017) observed HD 142527 for a total of four hours during Cycle 1, targeting the continuum and ^{13}CO (3–2) and C^{18}O (3–2) lines with a spectral resolution of 110 m s^{-1} (after Hanning smoothing). The disk is detected in both lines at high S/N. The angular resolution of the observations was 45 AU (beam 0.27×0.31). The presence of a velocity signature is currently being investigated in that data set (Boehler et al., in prep.).

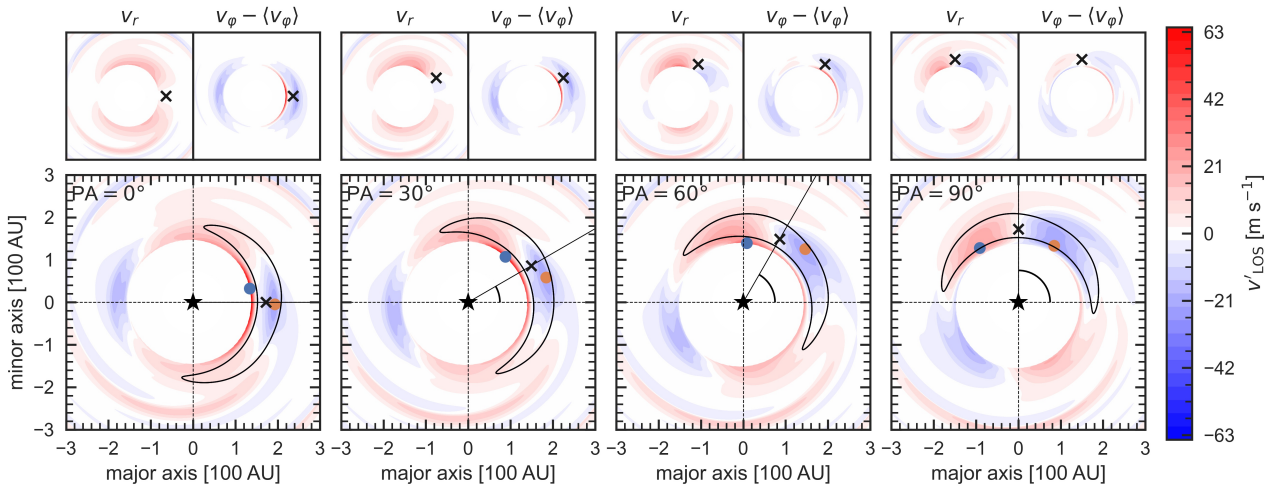


Fig. 8. Line-of-sight velocities (*bottom large panels*) as defined in Eq. (10), applied to HD 142527 with $i = 27^\circ$, and varying PA. *Top panels:* exhibit the corresponding polar components. Color reflects implied Doppler-shifts in molecular lines. Blue/orange dots indicate extreme values in v'_{LOS} . *Leftmost panel:* vortex's spatial extension is shown as a solid contour which corresponds to $\Sigma = 0.5\Sigma_0$, where Σ_0 is the scaling factor used in Eq. (3). The inner cavity, where fast spiral waves are launched but surface density is low, is not shown here: regions with $\Sigma/\Sigma_0 < 0.1$ are masked. As a proxy for the vortex's eye, a black cross indicates the density maximum.

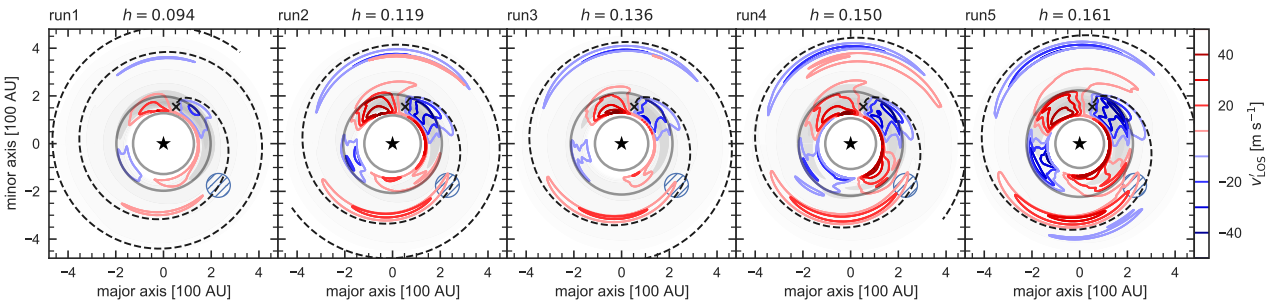


Fig. 9. Comparative view of v'_{LOS} with varying disk temperature h . Disk orientation is taken consistent with values found in the literature on HD 142527 ($i = 27^\circ$ Fukagawa et al. 2013, $PA = 71^\circ$ Kataoka et al. 2016). A mock-up of a spectral resolution of 12.5 m s^{-1} is shown. The reference setup occupies the *leftmost panel*. Velocities in the cavity are masked as in Fig. 8. In dashed lines, the best fit spirals following (Huang et al. 2019; Eq. (2) therein) are overplotted, based on linear perturbation theory (Goldreich & Tremaine 1979; Rafikov 2002; Muto et al. 2012). Those fits were computed using $v_r = 0$ contours as input data. As a visual indicator, surface density is underplotted in grayscale. Additionally, gray circles indicate the $3\sigma_j$ region around the vortex eye, which is used later in Fig. 10. As in other figures, the black cross indicates the density maximum.

This angular resolution is sufficient to resolve the vortex in HD 142527 and the spectral resolution can be improved by a factor of 2 on the brighter ^{12}CO line (Perez et al. 2015), or on the ^{13}CO and C^{18}O lines by increasing the time spent on-source.

At higher temperatures, more structure is revealed as the spiral arm unravels. Figure 10 shows the v'_{LOS} variation amplitude, against temperature (left panel) and time (right panel). Although the upper bound of this range consistently increases with temperature, we note that the mean value is almost unchanged from run 4 to run 5. Indeed, in runs 3 to 5, the amplitude of time variations are significantly higher than for the reference run. These large variations are related to the life cycle of a secondary spiral arm that appears in hot cases, as illustrated in Fig. 11. However, because this secondary spiral is most prominent when the disk itself becomes visibly eccentric, it is likely that this structure would be affected if the indirect gravitational terms were included in the model. A conservative conclusion is that only the lower boundary of the variation interval should be taken into account. Additionally, we observe that between runs 4 and 5, the dynamical range stagnates at 94 m s^{-1} . Indeed, this is the

range shown in Fig. 9, where the simulations are shown at a time ($t/t_* = 200$) that minimizes its amplitude. This saturation is likely caused by the instability in the eccentricity of the cavity, thus we infer that validity of massless disk models is disputable in the hottest case (run 5). We note that a previous study of the gas dynamics in HD 142527 (Casassus et al. 2015b) did not provide evidence of any strong asymmetric structure. This may indeed be due to a lack of spectral resolution ($\sim 1 \text{ km s}^{-1}$).

3.4. RWI spirals

Spirals structures are detected in HD 142527 (Fukagawa et al. 2006; Casassus et al. 2012; Rameau et al. 2012; Avenhaus et al. 2014; Christiaens et al. 2014). Several scenarios have been proposed to understand their origin, such as self-gravitational instability (SGI), excitation by the stellar companion (Biller et al. 2012; Astropy Collaboration 2018), connection to a shadow cast by a misaligned inner disk (Montesinos et al. 2016), or a combination of several effects (Christiaens et al. 2014). Spirals are also a natural outcome of RWI, as Rossby waves are coupled to spiral

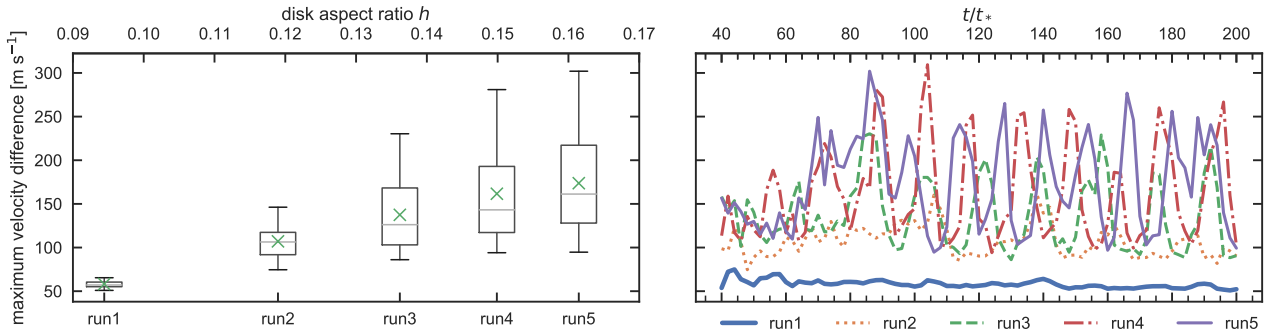


Fig. 10. Amplitude in v'_{LOS} across the annular region shown in Fig. 9, throughout the simulation time, represented as a boxplot (*left*). The whole time series is unraveled in the *right panel*. It is sampled every 2 orbital periods (the output rate of our simulations). Although the first run is remarkably constant, runs 3 to 5 exhibit significant dispersion within this metric, while the mean value (green crosses) itself is stabilized. The period of these oscillations corresponds to the life cycle of a secondary spiral arm, illustrated in Fig. 11.

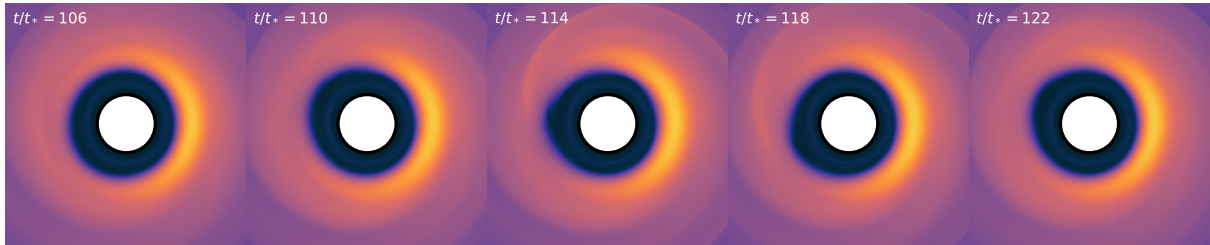


Fig. 11. Formation/dissipation cycle of a secondary spiral arm connected with disk eccentricity, illustrated for the most prominent case, run 5. Color maps density (same scale as Fig. 3). This secondary spiral is a transient and periodic phenomenon, which is responsible for large oscillations in maximum projected velocity as measured in Fig. 10

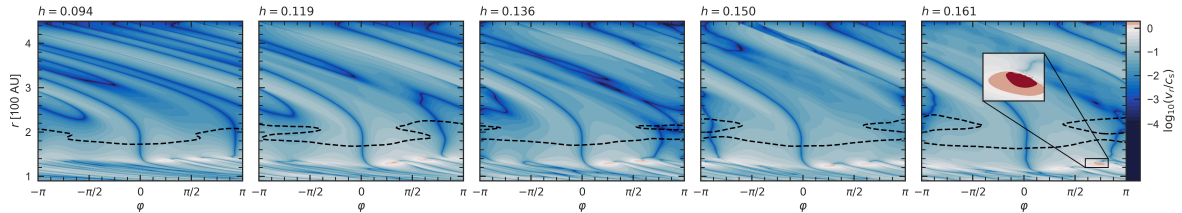


Fig. 12. Radial Mach number vs. temperature (h), seen in polar coordinates. The color mapping is such that sub-(super)sonic regions appear in blue (red). The vortex center is always located at $\phi = 0$. The dashed black lines indicate $v_\phi = v_K$. The global structure is not self-similar when h varies, as one can see the Keplerian line undergoes a reconnection as temperature increases, and spirals in the outer disk are shocking (Mach 1, white) closer to the vortex. Small supersonic (red) regions are found in the inner region of the disk ($r \approx 120$ AU), as is highlighted in an inset in the rightmost panel. The flow remains subsonic everywhere else.

density waves in a Keplerian disk. Such spiral waves would have the same frequency as the Rossby wave creating the vortex.

As opposed to companion-excited spirals, those are not caused by gravitational interaction and are observed in massless disks simulations such as ours (Huang et al. 2019). For Rossby vortices, the launching point is radially close to the vorticity extremum and the spiral corotates with the vortex. As a consequence, for spiral arms with different launching points, the RWI explanation may be safely rejected.

However, it must be noted that the apparent launching point of the spiral, that is, the origin of its detectable part, graphically indicated as a blue hatched mark, departs from its physical origin, namely the eye of the vortex. For instance, Fig. 9 shows a $\sim 90^\circ$ discrepancy between the actual launching point and the apparent origin of the main spiral arm. The figure also shows that, considering only spectral resolution as an experimental limitation, plane-RWI spirals are detectable as soon as the

sensitivity is sufficient to resolve the bulk signature of the vortex. In short, spirals produce projected velocities just marginally smaller than the vortex's bulk. We further note that plane-RWI spirals are a pure tracer of radial velocities v_r , which are observationally characterized by a change of sign in projected velocities across the major axis.

We note that the pitch angle of the spiral increases with h , as a consequence of a higher sound speed. Hence, radial velocities are not self-similar across our models, as hotter disks produce higher Mach numbers, as illustrated in Fig. 12.

4. Discussion

4.1. Numerical versus practical differences

In Sect. 3.1, we showed that a promising data reduction strategy for vortex dynamic extraction in sharp density jumps was to

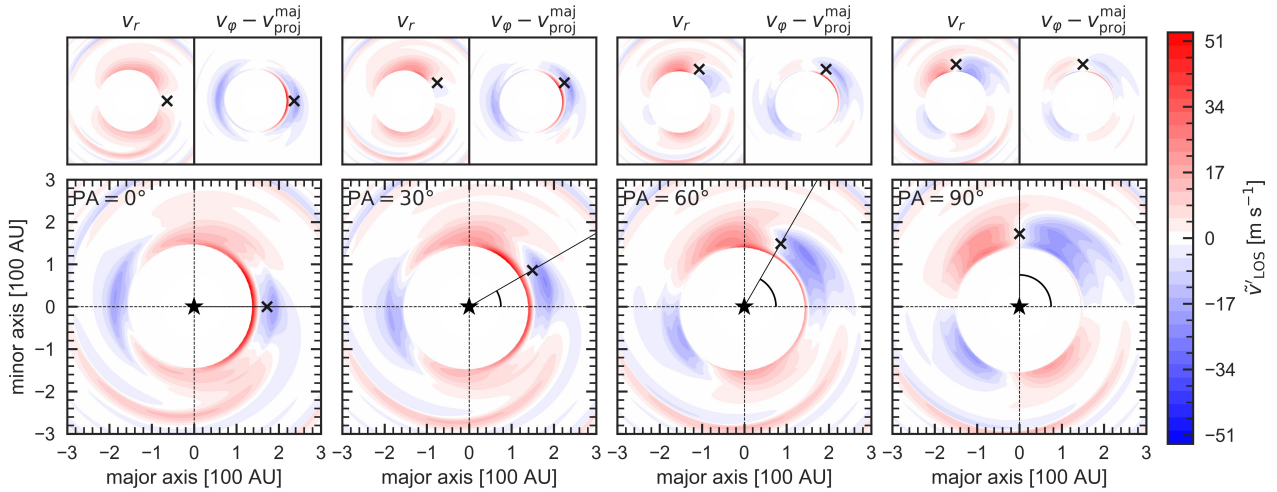


Fig. 13. Practical application of our data reduction method. The figure is similar to Fig. 8 except that v_{proj}^{maj} is subtracted instead of $\langle v_\phi \rangle$.

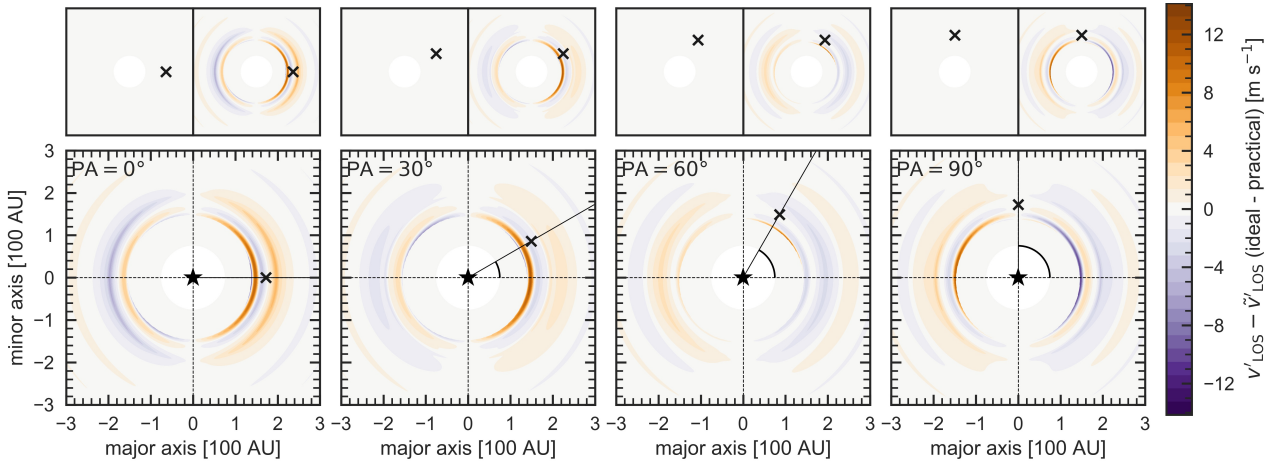


Fig. 14. Difference between numerical (Fig. 8) and practical (Fig. 13) cases. By construction, $v'_{Los} - \tilde{v}'_{Los}$ is a separable function $\text{err}(r, \varphi) = f(r) \cos(\varphi)$ where the density mask is axisymmetric.

subtract $\langle v_\phi \rangle$, and that the projected velocity seen on the major axis (v_{proj}^{maj} for shorts) gives a reasonable proxy for it. In order to test the error implied by this approximation, this strategy is applied in Fig. 13. Consistently with our previous estimation, this more realistic view shows very little difference to the first, idealized estimation (Fig. 8). Figure 14 quantifies that 2D discrepancy as a difference between the numerical and practical cases. We find the discrepancy to reach at most $\sim 7 \text{ m s}^{-1}$.

4.2. Spiral detection

As shown in Sect. 3.4, the projected velocities seen in spiral arms are comparable in amplitude to those attained by the core of the vortex core. However, angular resolution might constitute an additional limitation to identify those secondary structures. In Fig. 15 we simulate a limited angular resolution via Gaussian kernel convolution to the simulated velocity map, where the mean component of azimuthal velocity $\langle v_\phi \rangle$ is subtracted prior to projection. We observe that the contrast sharpness of the main spiral pattern is altered but not destroyed by limited spatial

resolution alone. We note that the spiral arm appears marginally broader in Fig. 13 as compared with the numerical case Fig. 8. The velocity flip pattern however remains visible and is unaltered by the limited spatial resolution.

4.3. Origin of the cavity in HD 142527

The most up-to-date simulations for the thermal emission of HD 142527 were performed in smooth-particle hydro (SPH) by [Astropy Collaboration \(2018\)](#) and do not feature vortex formation. This study was focused on explaining as many features as possible with the excitation provided by the eccentric stellar companion. However, it must be noted that SPH solvers generate numerical viscosities $\sim 10^{-2}$ ([Arena & Gonzalez 2013](#)), which are much greater than typical values used in RWI vortex studies³ ([Lyra et al. 2009](#); [Hammer et al. 2017, 2019](#); [Ono et al. 2016](#)), so this possibility was inherently not included in their study. In

³ The model used in this paper is inviscid. Insights into our evaluation of numerical viscosity are given in Appendix B.

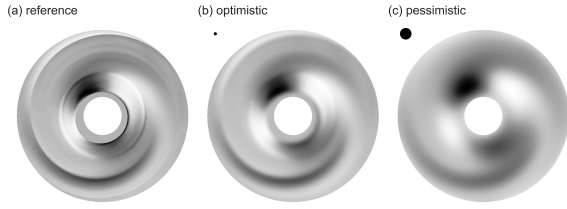


Fig. 15. Qualitative comparison between a simulation-precision velocity map (*left*), and against artificially lowered spatial resolution, simulation with a Gaussian kernel convolution. Kernels with angular size (in proportions of the target) 7% (*center*), and a 3 times larger one 21% (*right*) are shown. With the distance of HD 142527, the center panel corresponds to the recent high resolution obtained by [Keppler et al. \(2019\)](#). No noise is added. Projected velocities are shown in linear gray-scale, where $v_{\text{LOS}} < 0$ is shown in light gray and $v_{\text{LOS}} > 0$ shown in is dark gray. Secondary spiral patterns are lost at low resolution but the primary remains visible. Beam size is shown as a black dot. The velocity map corresponds to the rightmost panel in [Fig. 9](#).

the present work, we remained agnostic regarding how the initial unstable density jump was formed. The stellar companion, while not included in our model, provides a plausible cause to the cavity. However, gravitational perturber-induced Rossby vortices have been studied in the context of circular orbital motion ([Li et al. 2005](#)). How eccentricity and inclination in the orbit of the companion affects the formation of vortices, within an appropriately inviscid medium, remains to be studied.

4.4. Limits of this approach

An important limitation of the model is the lack of a vertical dimension. In a more realistic context, plane velocities (v_r, v_ϕ) are only detectable if the disk is inclined, which in turn affects measurements by line-of-sight integration. This effect would however be mitigated by choosing optically thick molecular lines. Moreover, [Méheut et al. \(2012b\)](#) showed that 3D vortices have a non-negligible vertical velocity component while they form (typically 10% of the characteristic azimuthal velocity signature). As the RWI growth time is typically shorter than the vortex lifetime by one or two orders of magnitude, it seems reasonable to neglect vertical circulation.

It has been shown that the contribution of the disk to the gravitational potential, promotes disk eccentricity ([Regály & Vorobyov 2017b](#)), which in turn amplifies the proper velocity of the vortex. Because this effect is neglected in our model, we expect the resulting velocities to be slightly underestimated in this work.

5. Conclusions

We showed that in cavity-hosting circumstellar disks, large eddies produce dynamical signatures on the verge of detectability for current facilities.

As the dynamical imprint of a vortex resides in the non-axisymmetric part of the velocity field, it is crucial to the detection to be able to subtract the axisymmetric component from observations. In the case of a vortex formed at the inner edge of a cavity-hosting disk, a Keplerian power law is not a correct proxy for the mean azimuthal velocity. This is because pressure gradients prone to vortex formation imply large deviations from Keplerian velocities. Nevertheless, as projected velocities of the observational major axis directly map the azimuthal motion, a

better mask can be obtained by averaging both sides of the velocity profile on this axis. This approach proved to produce small errors when compared with the actual azimuthal mean component of velocity $\langle v_\phi \rangle$. We also observed a saturation in the amplitude of projected velocities as the temperature is increased. This result is to be taken with a grain of salt and may point to a limitation of the model we used. Using this amplitude as an estimator for spectral resolution requirement, we conclude that detection of a single large eddy is achievable under a 50–150 m s^{-1} resolution, while the current maximal resolution with ALMA is $\sim 30 \text{ m s}^{-1}$. We stress that those minimal requirements were obtained within the particular case of the HD 142527 target, with a relatively low inclination (27°). Minimal resolution would be amplified by a factor 150% for a more likely, mean inclination of 45° , ceteris paribus. This demanding requirement may explain the current difficulty elucidate in elucidating the nature of known dust clumps in cavity-hosting disks, yet this is achievable with existing facilities. Vortex-free mechanisms could also explain their formation, although observational constraints for fine gas dynamics are needed to properly discriminate between concurrent scenarios. Full 3D modeling would naturally extend the present work, and allow the study of second order effects in line-of-sight integration.

Acknowledgements. C.M.T.R.’s Ph.D. grant is part of ANR number ANR-16-CE31-0013 (Planet-Forming-Disks). Computations were performed with OCCIGEN CINES (allocation DARI A0060402231), and “Mésocentre SIGAMM”, hosted by Observatoire de la Côte d’Azur. The data presented in this work were proceeded and plotted with Python’s data science ecosystem `scipy`, `numpy` ([van der Walt et al. 2011](#)), `matplotlib` ([Hunter 2007](#)), `pandas` ([McKinney 2010](#)) as well as `astropy` ([Astropy Collaboration 2013, 2018](#)) and the `yt` framework ([Turk et al. 2011](#)). C.M.T. is thankful to Aurélien Crida and Elena Lega for their early proofreading. The authors wish to thank the referee, Zsolt Regály, for helping in improving the quality of the paper.

References

- Adams, F. C., & Watkins, R. 1995, *ApJ*, 451, 314
 Andrews, S. M., Terrell, M., Tripathi, A., et al. 2018, *ApJ*, 865, 157
 Arena, S. E., & Gonzalez, J.-F. 2013, *MNRAS*, 433, 98
 Astropy Collaboration (Robitaille, T. P., et al.) 2013, *A&A*, 558, A33
 Astropy Collaboration (Price-Whelan, A. M., et al.) 2018, *AJ*, 156, 123
 Ataiee, S., Pinilla, P., Zsom, A., et al. 2013, *A&A*, 553, L3
 Ataiee, S., Dullemond, C. P., Kley, W., Regály, Z., & Méheut, H. 2014, *A&A*, 572, A61
 Avenhaus, H., Quanz, S. P., Schmid, H. M., et al. 2014, *ApJ*, 781, 87
 Barge, P., & Sommeria, J. 1995, *A&A*, 295, L1
 Baruteau, C., Barraza, M., Pérez, S., et al. 2019, *MNRAS*, 486, 304
 Benisty, M., Juhasz, A., Facchini, S., et al. 2018, *A&A*, 619, A171
 Biller, B., Lacour, S., Juhasz, A., et al. 2012, *ApJ*, 753, L38
 Birnstiel, T., Dullemond, C. P., & Pinilla, P. 2013, *A&A*, 550, L8
 Boehler, Y., Weaver, E., Isella, A., et al. 2017, *ApJ*, 840, 60
 Bracco, A., Chavanis, P. H., Provenzale, A., & Spiegel, E. A. 1999, *Phys. Fluids*, 11, 2280
 Casassus, S., & Pérez, S. 2019, *ApJ*, 883, L41
 Casassus, S., Pérez, M., S., Jordán, A., et al. 2012, *ApJ*, 754, L31
 Casassus, S., Wright, C., Marino, S., et al. 2015a, *ApJ*, 812, 126
 Casassus, S., Marino, S., Pérez, S., et al. 2015b, *ApJ*, 811, 92
 Cazzoletti, P., van Dishoeck, E. F., Pinilla, P., et al. 2018, *A&A*, 619, A161
 Casassus, S., Marino, S., Lyra, W., et al. 2019, *MNRAS*, 483, 3278
 Chiang, E., & Youdin, A. 2010, *Ann. Rev. Earth Planet. Sci.*, 38, 493
 Christiaens, V., Casassus, S., Pérez, S., van der Plas, G., & Ménard, F. 2014, *ApJ*, 785, L12
 de Val-Borro, M., Edgar, R. G., Artymowicz, P., et al. 2006, *MNRAS*, 370, 529
 de Val-Borro, M., Artymowicz, P., D’Angelo, G., & Peplinski, A. 2007, *A&A*, 471, 1043
 Dong, R., Liu, S.-Y., Eisner, J., et al. 2018, *ApJ*, 860, 124
 Fu, W., Li, H., Lubow, S., & Li, S. 2014, *ApJ*, 788, L41
 Fukagawa, M., Tamura, M., Itoh, Y., et al. 2006, *ApJ*, 636, L153

- Fukagawa, M., Tsukagoshi, T., Momose, M., et al. 2013, *Publ Astron Soc Jpn Nihon Tenmon Gakkai*, 65
- Gaia Collaboration (Brown, A. G. A., et al.) 2016, *A&A*, A595
- Goldreich, P., & Tremaine, S. 1979, *ApJ*, 233, 857
- Hammer, M., Kratter, K. M., & Lin, M.-K. 2017, *MNRAS*, 466, 3533
- Hammer, M., Pinilla, P., Kratter, K. M., & Lin, M.-K. 2019, *MNRAS*, 482, 3609
- Harten, A., Lax, P. D., & van Leer, B. 1983, *SIAM Rev.*, 25, 35
- Huang, P., Dong, R., Li, H., Li, S., & Ji, J. 2019, *ApJ*, 883, L39
- Hunter, J. D. 2007, *Comput. Sci. Eng.*, 9, 99
- Isella, A., Huang, J., Andrews, S. M., et al. 2018, *ApJ*, 869, L49
- Kataoka, A., Tsukagoshi, T., Momose, M., et al. 2016, *ApJ*, 831, L12
- Keppler, M., Teague, R., Bae, J., et al. 2019, *A&A*, 625, A118
- Koren, B. 1993, *Numerical Methods for Advection-Diffusion Problems* (Braunschweig, Wiesbaden: Vieweg), 117
- Lai, D., & Tsang, D. 2009, *MNRAS*, 393, 979
- Li, H., Finn, J. M., Lovelace, R. V. E., & Colgate, S. A. 2000, *ApJ*, 533, 1023
- Li, H., Colgate, S. A., Wendroff, B., & Liska, R. 2001, *ApJ*, 551, 874
- Li, H., Li, S., Koller, J., et al. 2005, *ApJ*, 624, 1003
- Lin, M. 2012, *AGU Fall Meeting Abstracts*, 21, P2 1B
- Lovelace, R. V. E., Li, H., Colgate, S. A., & Nelson, A. F. 1999, *ApJ*, 513, 805
- Lyra, W., Johansen, A., Klahr, H., & Piskunov, N. 2009, *A&A*, 493, 1125
- McKinney, W. 2010, in *Proceedings of the 9th Python in Science Conference*, 51
- McNally, C. P., Nelson, R. P., & Paardekooper, S.-J. 2018, *MNRAS*, 477, 4596
- Méheut, H., Keppens, R., Casse, F., & Benz, W. 2012a, *A&A*, 542, A9
- Méheut, H., Yu, C., & Lai, D. 2012b, *MNRAS*, 422, 2399
- Montesinos, M., Perez, S., Casassus, S., et al. 2016, *ApJ*, 823, L8
- Muto, T., Grady, C. A., Hashimoto, J., et al. 2012, *ApJ*, 748, L22
- Ono, T., Muto, T., Takeuchi, T., & Nomura, H. 2016, *ApJ*, 823, 84
- Perez, S., Casassus, S., Ménard, F., et al. 2015, *ApJ*, 798, 85
- Pérez, S., Casassus, S., Hales, A., et al. 2020, *ApJ*, 889, L24
- Pineda, J. E., Szulágyi, J., Quanz, S. P., et al. 2019, *ApJ*, 871, 48
- Pinte, C., Price, D. J., Ménard, F., et al. 2018, *ApJ*, 860, L13
- Pinte, C., van der Plas, G., Ménard, F., et al. 2019, *Nat. Astron.*, 3, 1109
- Porth, O., Xia, C., Hendrix, T., Moschou, S. P., & Keppens, R. 2014, *ApJS*, 214, 4
- Price, D. J., Cuello, N., Pinte, C., et al. 2018, *MNRAS*, 477, 1270
- Rafikov, R. R. 2002, *ApJ*, 572, 566
- Rameau, J., Chauvin, G., Lagrange, A.-M., et al. 2012, *A&A*, 546, A24
- Rayleigh, J. W. 1879, *Proc. Lond. Math. Soc.*, 1, 57
- Regály, Z., & Vorobyov, E. 2017a, *MNRAS*, 471, 2204
- Regály, Z., & Vorobyov, E. 2017b, *A&A*, 601, A24
- Regály, Z., Juhasz, A., Sándor, Z., & Dullemond, C. P. 2012, *MNRAS*, 419, 1701
- Regály, Z., Sándor, Z., Csomós, P., & Ataiee, S. 2013, *MNRAS*, 433, 2626
- Richard, S., Barge, P., & Le Dizès, S. 2013, *A&A*, 559, A30
- Shakura, N. I., & Sunyaev, R. A. 1973, *A&A*, 500, 33
- Tanga, P., Babiano, A., & Dubrulle, B. 1996, *Icarus*, 121, 158
- Teague, R., & Foreman-Mackey, D. 2018, *Res. Notes Am. Astron. Soc.*, 2, 173
- Teague, R., Guilloteau, S., Semenov, D., et al. 2016, *A&A*, 592, A49
- Teague, R., Bae, J., Bergin, E. A., Birnstiel, T., & Foreman-Mackey, D. 2018a, *ApJ*, 860, L12
- Teague, R., Bae, J., Birnstiel, T., & Bergin, E. A. 2018b, *ApJ*, 868, 113
- Turk, M. J., Smith, B. D., Oishi, J. S., et al. 2011, *ApJS*, 192, 9
- van der Marel, N., van Dishoeck, E. F., Bruderer, S., et al. 2016, *A&A*, 585, A58
- van der Walt, S., Colbert, S. C., & Varoquaux, G. 2011, *Comput. Sci. Eng.*, 13, 22
- Verhoeff, A. P., Min, M., Pantin, E., et al. 2011, *A&A*, 528, A91
- Xia, C., Teunissen, J., Mellah, I. E., Chané, E., & Keppens, R. 2018, *ApJS*, 234, 30
- Yen, H.-W., Liu, H. B., Gu, P.-G., et al. 2016, *ApJ*, 820, L25
- Zhu, Z., & Baruteau, C. 2016, *MNRAS*, 458, 3918
- Zhu, Z., & Stone, J. M. 2014, *ApJ*, 795, 53

Appendix A: Evaluations of aspect ratios

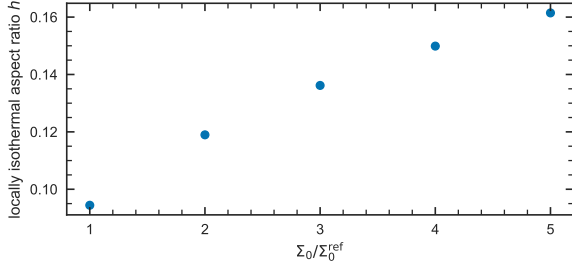


Fig. A.1. Correspondence between locally isothermal aspect ratio and “disk mass” in our simulations. The leftmost model is the reference.

A.1. Equivalence to locally isothermal

Our model differs from the widely used locally isothermal prescription in that it is not defined in terms of scale height

$$H = hr(r/r_*)^\beta, \quad (\text{A.1})$$

where h is the disk aspect ratio and β is the flaring. We can nonetheless draw an equivalence with those parameters for the power-law density distribution at the core of Eq. (3), such that $\Sigma(r) = \Sigma_0(r/r_*)^{-1}$. In the locally isothermal prescription, the scale height is usually defined such that $H^2 = c_s^2/\Omega_K^2$, so we can equate this with Eq. (A.1) to get

$$\begin{aligned} h^2 r^2 (r/r_*)^{2\beta} &= \frac{\gamma p / \Sigma}{GM/r^3} \\ &= \frac{\gamma S}{GM} r^3 \Sigma^{\gamma-1} \\ &= \frac{\gamma S \Sigma_0^{\gamma-1}}{GM} r^3 (r/r_*)^{1-\gamma}, \end{aligned} \quad (\text{A.2})$$

at which point we deduce an effective aspect ratio and disk flaring, in terms of the actual simulation parameters

$$\begin{cases} h^2 = \frac{\gamma S \Sigma_0^{\gamma-1} r_*}{GM}, \\ \beta = 1 - \gamma/2 = 1/6. \end{cases} \quad (\text{A.3})$$

We note that our fixed resolution corresponds to $\Delta r/H(r_j) \approx 0.04$ for the reference model. Figure A.1 shows the resulting variation in h as we scale up Σ_0 , following Eq. (A.3).

A.2. Spiral fitting

In Fig. 9, we fitted the linear-regime spiral wave shape (Goldreich & Tremaine 1979; Rafikov 2002; Muto et al. 2012) given by

$$\begin{aligned} \varphi(r) &= \varphi_o - \frac{\text{sgn}(r - r_o)}{H_o} \\ &\times \left((r/r_o)^{1+\beta} \left[\frac{1}{1+\beta} - \frac{1}{1-\alpha+\beta} (r/r_o)^{-\alpha} \right] - \left[\frac{1}{1+\beta} - \frac{1}{1-\alpha+\beta} \right] \right), \end{aligned} \quad (\text{A.4})$$

where α, β are power-law exponents defined as $\Omega \propto r^{-\alpha}$ and $c_s \propto r^{-\beta}$, respectively. The quantities (r_o, φ_o) are the coordinates of the spiral origin, while H_o is a scale height at this position.

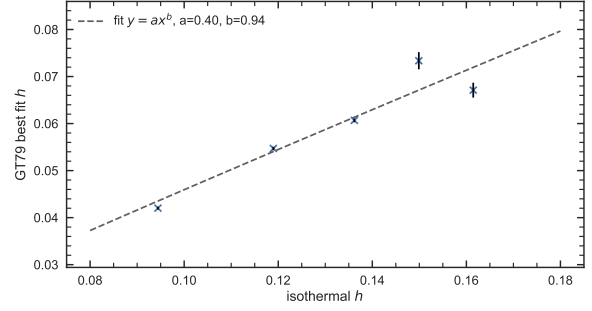


Fig. A.2. Aspect ratios as defined in Appendix A.1 vs. empirical values obtained from fitting Eq. (A.4). The latter is roughly 40% of the former.

The fit was performed with H_o as a free parameter, so the corresponding aspect ratio, differs from the locally isothermal equivalent h value used throughout the paper and described in the previous section. Figure A.2 shows values against each other.

Appendix B: Numerical viscosity evaluation

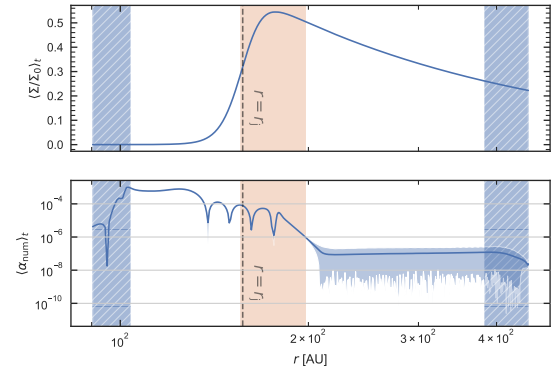


Fig. B.1. Density (*top*) and numerical viscosity equivalent α value (*bottom*) time-averaged over 10 orbital periods ($t/t_* \in [90, 100]$) with a sampling rate of 0.1 orbital periods. The solid blue shadows indicate the variation interval over the sample time series, showing that the profile is very stable in the region of interest. The hatched regions highlight the wave-killing zones, while the orange region loosely indicates the vortex-forming region, spanning one scale height away from the local density maximum.

In order to estimate numerical viscosity $\nu_{\text{num}}(r)$, we performed a 1D run in a 1D run, with identical parameterization as our reference 2D run (run1). The analytical initial conditions constitute a stable equilibrium since RWI cannot grow in 1D. Since our boundary conditions do not impose mass flux, any radial mass transport \dot{M} through the simulation domain is caused by numerical viscosity such that $\nu_{\text{num}}\Sigma = |\dot{M}|/3\pi$. In terms of the Shakura & Sunyaev (1973) alpha viscosity model $\nu_{\text{num}} = \alpha_{\text{num}} H c_s$, thus finally

$$\alpha_{\text{num}} = \frac{2}{3} \left| \frac{v_r}{h c_s} \right|. \quad (\text{B.1})$$

The obtained profile, time-averaged, is plotted in Fig. B.1. The highest numerical viscosities ($\alpha_{\text{num}} \sim 2 \times 10^{-3}$) are reached in the cavity, while α_{num} stays bounded $< 10^{-4}$ in the vortex-forming region, roughly represented in orange.

5.2.1 Erratum

A typing mistake was overlooked in equation (9) of the paper, which is inconsistent with equation (10). Equation (9) should read

$$\mathbf{e}_{\text{LOS}}(i, \varphi) = -(\sin(i)\sin(\varphi)\mathbf{e}_r + \sin(i)\cos(\varphi)\mathbf{e}_\varphi + \cos(i)\mathbf{e}_z)$$

Fortunately, this error only affects the manuscript, not the associated results. I thank my reviewer Clément Baruteau for spotting this error.

5.2.2 On physical temperature

As mentioned in the paper, temperature is not a primitive field in my simulations. However, it is insightful to derive it from existing fields, assuming an ideal gas equation of state

$$T = \frac{\mu m_{\text{H}} p}{k_{\text{B}} \Sigma} \quad (5.1)$$

where $\mu = 2.4$ is the dimensionless average molecular weight, taking a relevant value tailored from the inter-stellar medium chemical composition, mostly H_2 , m_{H} is the mass of a single hydrogen atom, and k_{B} is the Boltzmann constant. Evaluating this expression against my data, I find maximal (time and space) values of 25 K and 67 K in my coldest and hottest runs respectively. Those values are in the realm of plausibility.

5.3 Violent vortices with rotational instability

While in the final version of the paper you just read, initial conditions are designed to ensure instability with respect to RWI and stability against the Rayleigh criterion in all simulations, it was not the case in the first submitted version. I actually checked that those conditions were met in the reference (coldest) run, and then varied Σ_0 (again, affecting only soundspeed really), while σ_j was kept constant across all runs. As a result, 4 of my 5 runs actually had rotationally unstable initial conditions. This was purely accidental and a mistake on my part. However, it did not seem to affect the final aspect of the resulting vortices, which appeared very comparable to what we obtained in the final, corrected version. How did we discover this and why is it important, you may ask? In the first version, we used a lower grid resolution and tested, here again, only against the reference setup for numerical convergence, so it appeared sufficient, when it truly was not in all other runs.

I was able to discover the problem (and fix it) thanks to a seemingly trivial question from our referee, who found that the azimuthal resolution was suspiciously low, so I ran an array of new simulations to check that numerical convergence was indeed reached in all runs; this array is represented as fig. 5.4. In fig. 5.5, I present a comparison between 3 numerical setups for the intermediate run in the paper (run3) with the original paradigm, keeping the cavity width σ_j at the same value than run1. The runs included use, respectively a low azimuthal resolution (A0, left), increased resolution (C2, middle), increased resolution (C2) plus a diffusive solver (right). The key here is that, because we solve physically inviscid

equations, the only viscosity is numerical. As mentioned in this manuscript's introduction, numerical viscosity directly correlates with the grid's resolution! Poor azimuthal resolution indeed proves to have a filtering effect very close to that of a diffusive scheme.

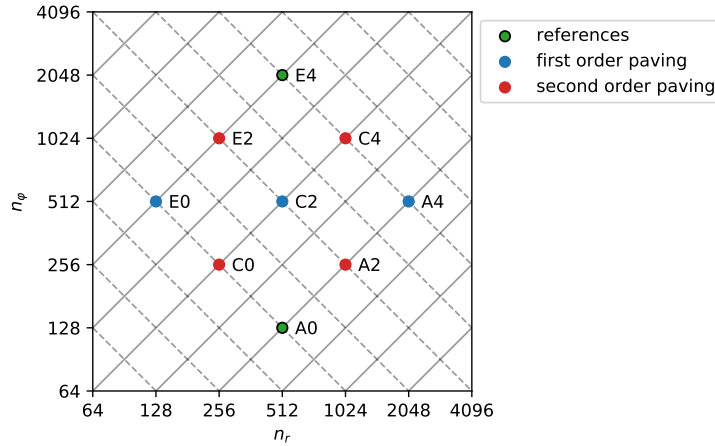
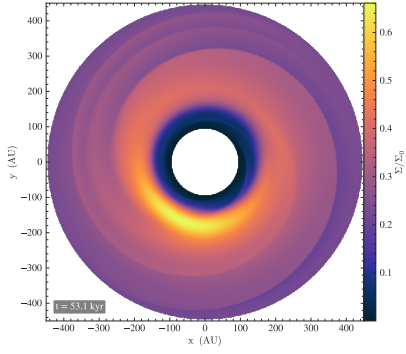


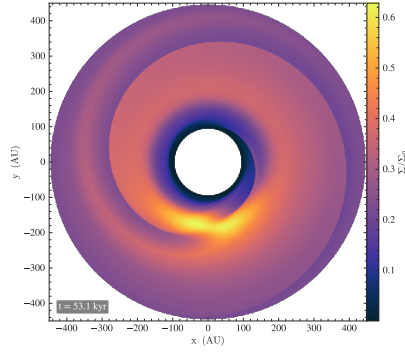
Fig. 5.4: A “battleship” inspired representation of the naming convention I used to explore the resolution parameter space. n_r and n_ϕ are the total number of cells along each direction in the grid. The axes are in \log_2 scale since I am using only powers of two for n_r and n_ϕ . Moving along a full-line (letters) conserves the cell aspect-ratio. Moving along a dashed-line (numbers) conserves the total cell count (hence should not require more CPU power). The setup in the first submitted version was A0, and the final version is using C2.

Namely, vortex-generated spirals are always rotationally unstable ($\kappa^2 < 0$), but in the less diffusive setup (middle column), the core of the vortex also maintains this property. Interestingly, the morphology of this rotationnaly unstable vortex is more complex. In particular, density isocontours around a vortex are usually well approximated by ellipses (as seen in polar coordinates), while here their shape is not convex anymore. The density isocontours are not convex shapes (in polar coordinates).

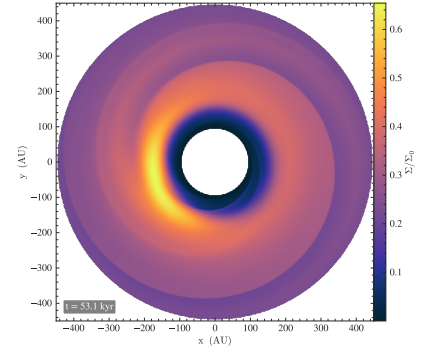
Let us take a look at the time evolution in this case. Figure 5.6 shows a time-series. It becomes obvious that the rotationally unstable region is indeed attached to the vortex. Additionnaly, one can see that the vortex undergoes a radial inward migration, as illustrated by fig. 5.7. This occurs as the spiral waves attached to the vortex, similar to the ones generated by a planet, transport angular momentum outwards. Since the density waves are sharper in a less diffusive setup, the process is more efficient overall, thus the associated migration is visibly quicker. However, as mentionned in the paper, Regály and Vorobyov (2017a) showed that vortex migration rate is slightly exaggerated in such a setup because we are not taking into account the response of the star to the non-axisymmetric disk potential here. Moreover, it is not clear how the inclusion of an excentric binary, a suited initial cause for the forming a Rossby unstable cavity, would affect migration.



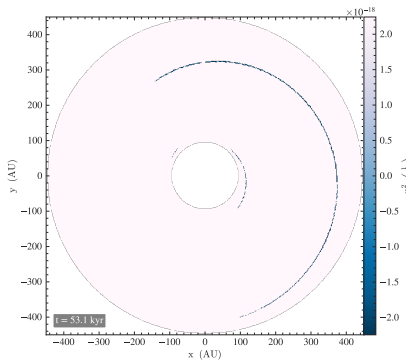
(a) normalized density, low resolution (A0)



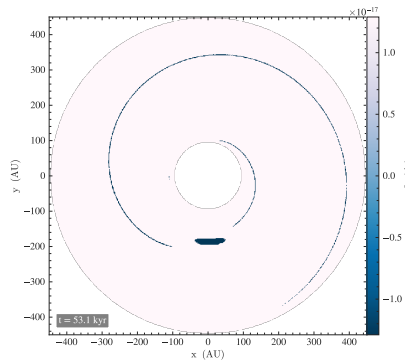
(b) normalized density, moderate resolution (C2)



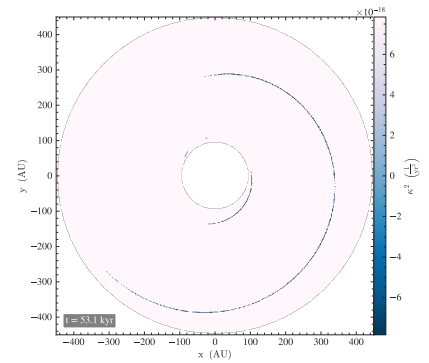
(c) same as panel (b), but with a diffusive solver.



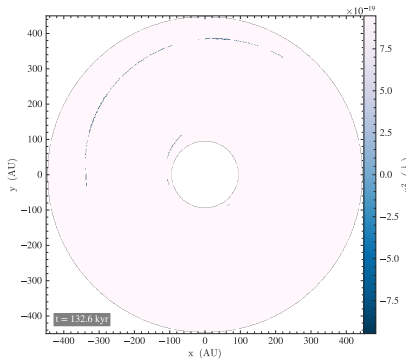
(d) epicyclic frequency squared, low resolution (A0), same time as panel (a)



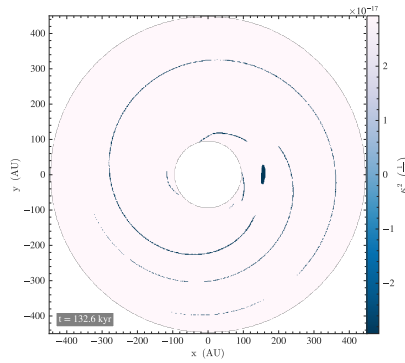
(e) epicyclic frequency squared, moderate resolution (C2), same time as panel (b)



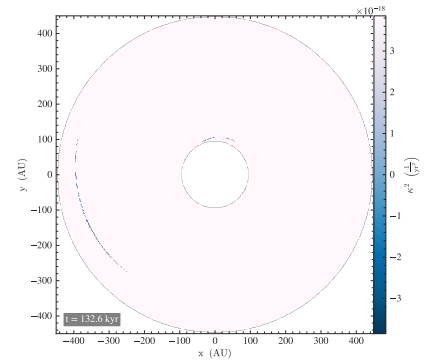
(f) epicyclic frequency squared, diffusive solver, same time as panel (c)



(g) same as panel (d), at a later time



(h) same as panel (e), at a later time



(i) same as panel (f), at a later time

Fig. 5.5: The effect of resolution/numerical viscosity on numerical convergence of rotationally unstable setups. I compare the normalized density (top row) and epicyclic frequency squared, as defined in eq. (2.17) (middle and bottom rows), in three runs, differing only by the solver used and resolution. Left column: original low resolution runs (A0) with a “hllc” solver + “koren” limiter. Middle column: same solver + limiter, with a moderate resolution (C2). Right column: “tvdlf” solver + a “minmod” limiter, same resolution as middle column. The colormap in κ^2 is chosen so has to reveal the location of the rotationally unstable region ($\kappa^2 < 0$), in dark blue.

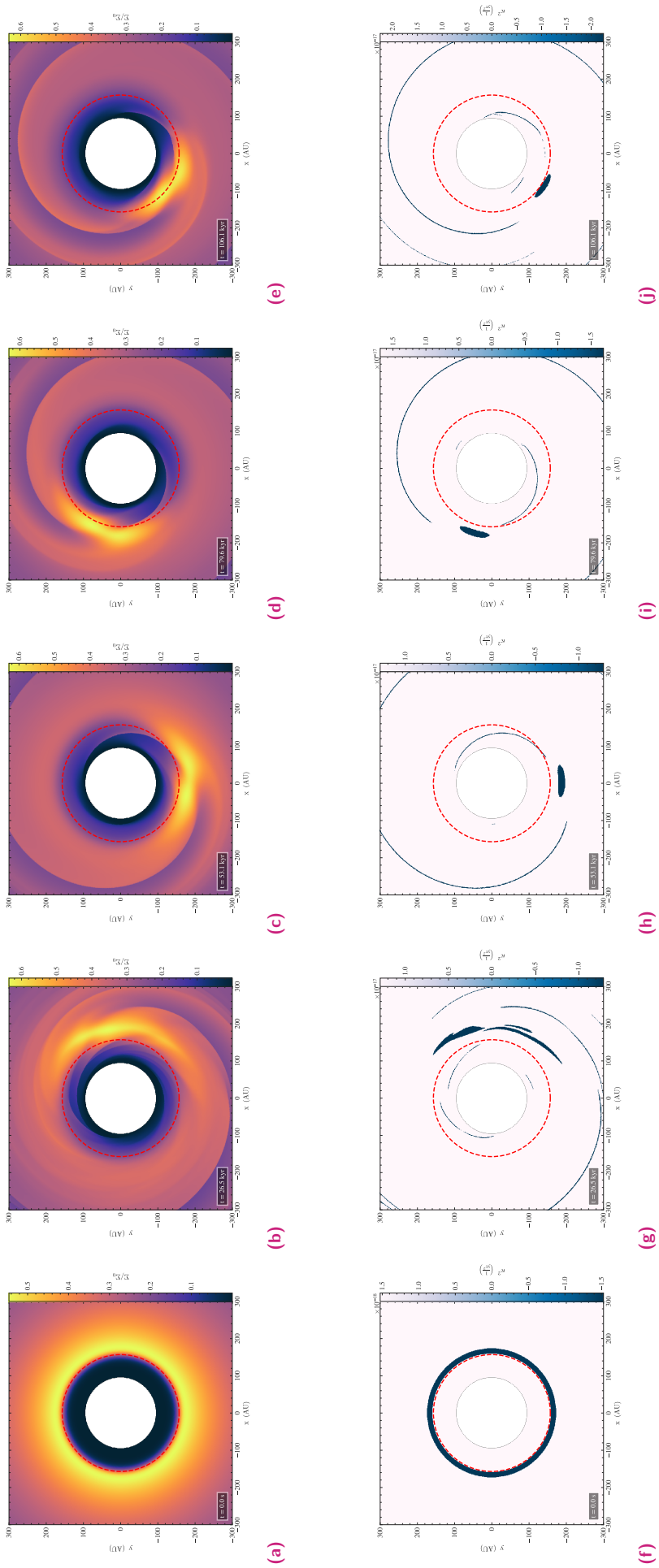


Fig. 5.6: A time-series of normalized density (top row) and the epicyclic frequency squared κ^2 (bottom row) in a rotationally unstable vortex. Time increases linearly toward the right. A red dashed circle indicates the location of the density jump in initial conditions $r = r_1$. The rotationally unstable region is initially an axisymmetric ring but is concentrated over time at the center of the single final vortex. Moreover, vortex migration becomes apparent over the course of the simulation.

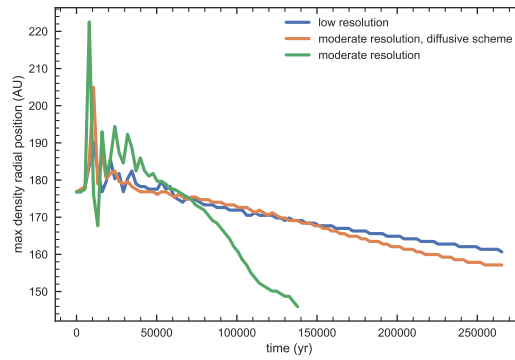


Fig. 5.7: Vortex migration against diffusivity in the numerical setup. The vortex position is assimilated to that of the global density maximum in the grid. Early in the simulation this is not so good of a proxy since the vortex is not fully formed yet, and the maximum basically traces a random point in a spiral arm. After it stabilizes, this traces the inward migration of the vortex itself as the inner rim of the cavity dissipates some of its angular momentum by radiating spiral waves, much akin to what a planetary perturber yields. The x axis spans the whole simulation time (200 orbits) in years.

5.4 Observational difficulties of interpretation

A new observational bias around rims Lead by Yann Boehler, a paper I am cosigning (submitted) provides new observational evidence for the presence of vortex in HD142527, using ^{13}CO and ^{12}CO emission lines to reconstruct the velocity map, included here as fig. 5.8. Once the systemic velocity of the target is removed (left panel), as well as a Keplerian best-fit (right panel), the residuals feature a broad region compatible with the motion expected from an anticyclonic vortex (1) on the north side. A spiral arm (2), coincidentally connected to the alleged vortex also appears, building our confidence in the detection. There are however important reasons to doubt this interpretation. Firstly, the projected velocity such as reduced here is of the order of magnitude of the local speed of sound (of course impossible to evaluate accurately), and goes as high as 300 m s^{-1} .

Moreover, Y. Boehler shows that an observational bias is standing in the way, that may be responsible for the signal we observe, and which is aggravated by limited spatial resolution. This is illustrated using a toy model in fig. 5.9. Assuming a purely Keplerian motion, but a non-uniform luminosity (integrated flux, middle panel) in the radial direction, the *observed* velocity differs from the actual Keplerian. This is because the observed velocity is obtained as a luminosity-weighted average over the width of the synthesized beam. In effect, a region where luminosity decreases is skewed toward lower radii, so the velocity appears greater than it is, or in other words it appears super-Keplerian. Correspondingly, a region where luminosity increases is viewed as sub-Keplerian.

Not only does the detection of vortex signatures require high spectral resolution, it proved demanding in angular resolution as well. Confirming or infirming whether the observed signature is real, and indeed compatible with an anticyclonic vortex is a matter of convergence, and requires yet better resolved images. A proposal to do exactly this was unfortunately rejected (2019).

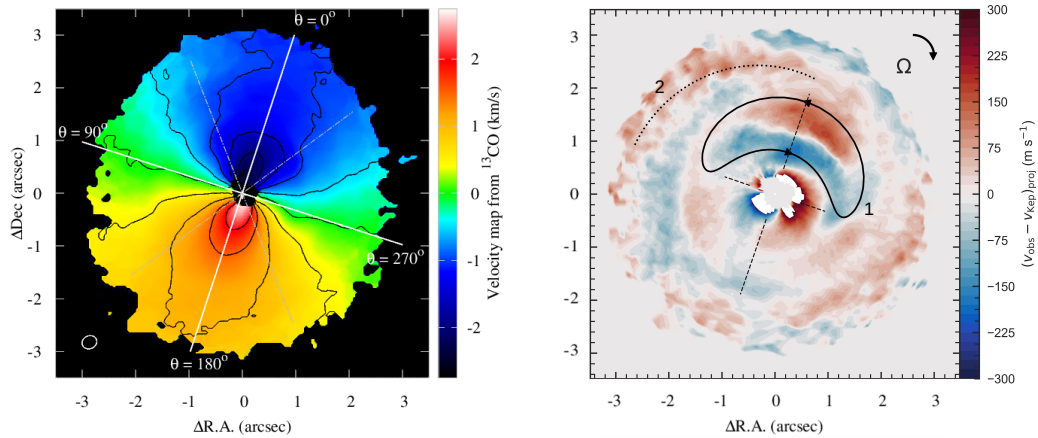


Fig. 5.8: Observational signature compatible with that of a vortex in HD 142527. Left: projected velocity map, systemic velocity removed. right: same as left, but removing a Keplerian best fit as well, leaving only residuals. On the north side of the disk, residuals show dynamical signatures compatible with the anti-cyclonic motion of a vortex. Source Boehler et al 2021 (submitted).

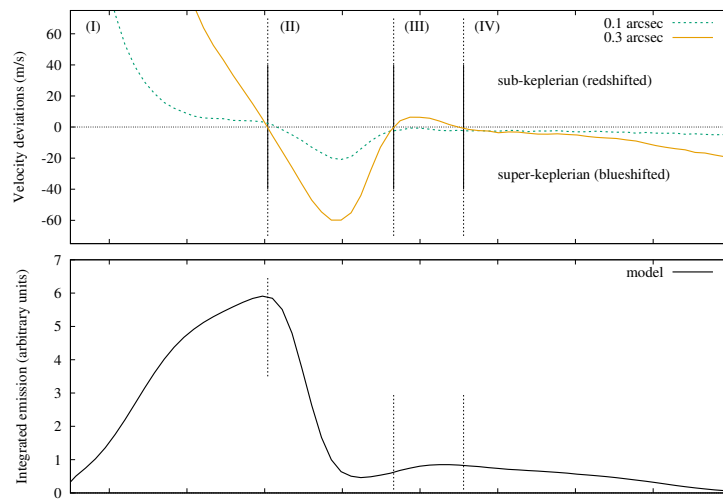


Fig. 5.9: Effect of flux-weighted beam dilution on the detected velocity, for a strictly Keplerian toy model. The horizontal axis represents radius (increasing rightwards). With the exception of local extremum in integrated emission, the detected velocity appears to differ from the underlying Keplerian profile. The effect is however mitigated at higher angular resolution (smaller beam). Source: Boehler et al 2021 (submitted).

Simulated disk imaging

“ *I would rather have questions that can't be answered than answers that can't be questioned.* ”

— Dr. Richard Feynman

In this chapter I present my experiments with radiative transfer applied as post-processing to hydro simulations. I will revisit my vortex simulations from the previous chapter, and produce simulated images with the radiative transfer code MCFOST. This chapter is self-contained and includes a description of additional methods to apply radiative transfer to simulated hydrodynamics data, that I did not invoke earlier. MCFOST (Christophe Pinte, François Ménard, et al., 2006) is used here purely as a black box to produce simulated images and I will only cover its specifics that are relevant to the present problematic. I will however emphasize the inherent difficulties to the exercise I am proposing here, before presenting my results.

6.1 Dusty vortex simulations

As I explained in the introduction (see section 1.2), the primary observables in disks trace the thermal emission of the dust component. Dust also plays a crucial role in the thermal equilibrium and determines the optical depth (opacity) around molecular lines (Boehler et al., 2017), and in turn affects even observations of the gas component. It is thus essential to include dust dynamics in a hydro simulation in order to fill the gap between simulations and observations.

6.1.1 Numerical setup

In order to produce a set of theoretical predictions for a giant Rossby vortex such as modeled in the previous chapter, I ran a new set of simulations with dust included. I will show in following sections that the transformations required to apply radiative transfer to 2D razor-thin model have a important amount of poorly constrained degrees of freedom, so I will restrain the simulation set to two models. Namely, the only difference between them will be the effect of dust back-reaction, that is, whether or not the reciprocal drag force on the gas component is taken into account. Indeed, it is not *a priori* obvious whether this effect should be accounted for or not in the context of vortices. In fact, back-reaction can safely be neglected where the relative abundance of dust compared to gas is low, as is the case in the inter-stellar medium. However, as the ratio approaches one, back-reaction can disrupt the vortex altogether (Raettig et al., 2015). This conclusion was however derived

from 2D simulations only, while Lyra et al. (2018) showed that in 3D, dust concentrates also vertically and which allows vortices to survive.

Parameters The AMRVAC simulations are very similar to the reference run in the previous chapter, so I will only list the differences here. I used a $(n_r, n_\varphi) = (512, 128)$ fixed resolution over a radial domain $r \in [90, 450]$ AU. Although the azimuthal resolution is restrictive here, the results show very little difference to the reference run in the previous chapter as far as the gas component is concerned, so I am confident that the simulations are indeed converged. Because the h11c flux scheme does not support dust as implemented in AMRVAC, I switch to h11 (the difference being that h11 does not perform centered differences). Dust is modeled as a collection of four pressureless fluids with fixed grain sizes equally spaced on a log scale from 1×10^{-3} cm to 1 cm and constant particle density $\rho_p = 1 \text{ g cm}^{-1}$. I solve the equation set eqs. (2.27) and (2.28), with a drag force following Kwok's law eq. (2.24). The back-reaction of dust on gas is the last term in the right-hand side of eq. (2.27) and is turned off and on respectively in the two simulations. Because density of a pressure less fluid can locally decrease dramatically, to the point it becomes the dominant constraint on the time step via the CFL condition, it is set to exactly zero under a given threshold. The initial dust-to-gas mass ratio ϵ_0 is set to 1 %.

Dust binning Setting the relative abundances in each grain discrete population (or "bin") in the most realistic fashion possible is a separate problem. Let us derive the associated constraints in equation form. The grain size s distribution is usually assumed to follow a continuous power law as

$$n(s) \propto s^{-\sigma} \quad (6.1)$$

with $\sigma = 7/2$, following Mathis et al. (1977), and based on the assumption that collisional equilibrium holds, accounting for fragmentation and coagulation. Now in a discretized distribution with N bins, one can express the relative abundance in a discrete bin j as a function of that of another bin i and the associated grains sizes as

$$n(s_j) \equiv n_j = n_i \left(\frac{s_j}{s_i} \right)^{-\sigma} \quad (6.2)$$

Let $m_{d,i} = n_i \frac{4}{3} \pi s_i^3 \rho_p$ be the total mass represented by the i^{th} bin. It immediately follows that

$$m_{d,j} = m_{d,i} \left(\frac{s_j}{s_i} \right)^{3-\sigma} = n_i \frac{4}{3} \pi \rho_p s_i^\sigma s_j^{3-\sigma} \quad (6.3)$$

Likewise, the individual bin-to-gas ratios ϵ_i read

$$\frac{\epsilon_i}{\epsilon_j} = \frac{m_{d,i}/m_g}{m_{d,j}/m_g} = \frac{m_{d,i}}{m_{d,j}} = \left(\frac{s_i}{s_j} \right)^{3-\sigma} \quad (6.4)$$

Additionally, ϵ_i are constrained by the total dust-to-gas mass ratio ϵ as

$$\epsilon_0 = \sum_{i=1}^N \epsilon_i = \epsilon_1 \sum_{i=1}^N \frac{\epsilon_i}{\epsilon_1} = \epsilon_1 \sum_{i=1}^N \left(\frac{s_i}{s_1} \right)^{3-\sigma} \quad (6.5)$$

So finally we obtain the respective bin to gas mass ratios ϵ_i as functions of ϵ_0 and the grain sizes as

$$\begin{cases} \epsilon_1 = \epsilon_0 \left[\sum_{i=1}^N \left(\frac{s_i}{s_1} \right)^{3-\sigma} \right]^{-1} \\ \epsilon_i = \epsilon_1 \left(\frac{s_i}{s_1} \right)^{3-\sigma}, \forall i \end{cases} \quad (6.6)$$

Note that in a simulation without back-reaction, the interaction is one-way from the gas to dust grains, so separate dust populations do not have any influence on each other, and the problem can be overlooked without affecting the results, as long as the relative abundances are properly renormalized during analysis.

6.1.2 Results

I show in fig. 6.1 a comparative view of the two runs as time series. I represent the competition between gas density and total dust-to-gas mass ratio over time. In the run without back-reaction, a single vortex quickly forms and stabilizes, and the dust-to-gas ratio increases smoothly in its center, saturating at unity by the end of the simulation. Meanwhile, as expected, the run with back-reaction differentiates pretty quickly: as dust accumulates in the centers of eddies, the resulting vortex's stability is compromised and we see it becoming more and more elongated. The total dust-to-gas ratio only reaches about $10^{-0.6} \simeq 0.25$ and the azimuthal concentration quickly degenerates into a ring. These simulations will serve as inputs to produce fake observations in the next sections.

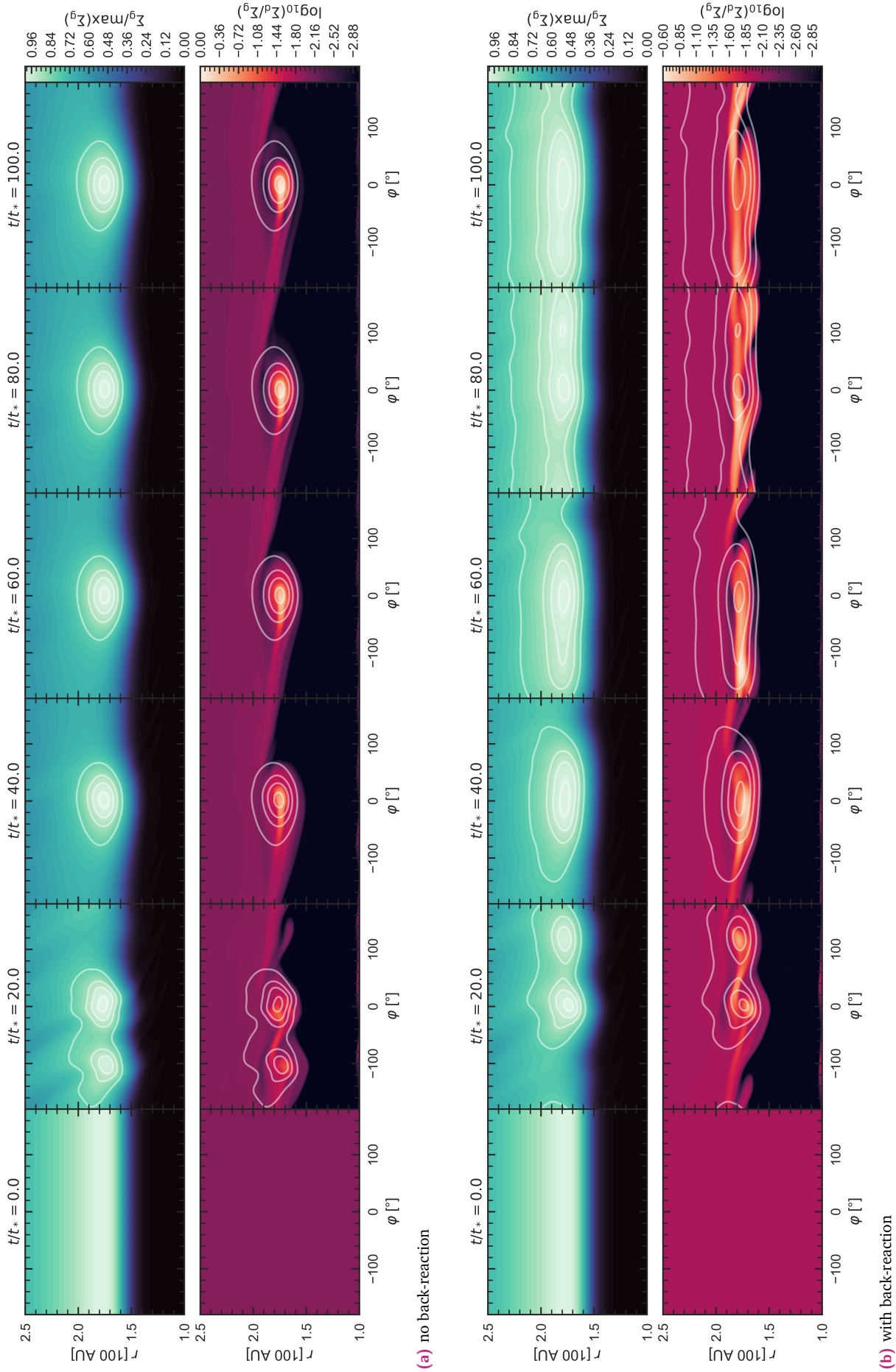


Fig. 6.1: Concurrent evolution of gas and dust density distributions through a Rossby vortex coalescence, represented for two models with feedback turned on (a) and off (b) respectively, in polar coordinates. Normalized gas density occupies the top row, while the metallicity (dust-to-gas ratio) is shown in the bottom row in \log_{10} . Fiducial white contours indicate the normalized gas density levels [0.8, 0.9, 0.95, 0.99].

6.2 From hydro to radiative transfer (methods)

Processing outputs data from AMRVAC to create input files for MCFOST is a complicated multi-step process and not every parameter at play is uniquely defined. To be able to perform this delicate operation reliably and in a reproducible manner, I developed a program dedicated to this task that acts as a glue code, named `vac2fost`. This section details the problems addressed by this interface.

Scale-free hydrodynamics VS radiative transfer In the previous chapter I observed that my vortex simulations are “massless” in the sense that the disk mass is an arbitrary constant that has no direct effect on the physics of the simulation, except through the scaling of soundspeed following eq. (3.9). The important point is that my simulations include neither disk self-gravity nor the acceleration of the reference frame (centered on the star) due to asymmetries in the disk’s mass distribution. More generally, it needs to be noted that hydro simulations are written in a scale-free fashion, because what is solved for is really a dimensionless version of Navier-Stokes’ equations. This means for instance that a single simulation can be equally interpreted as representing a vortex forming at $r_0 = 100$ AU over a period ΔT or a 10 times smaller vortex forming at $r_0 = 10$ AU over a period $(10/100)^{2/3}\Delta T$ (since physical time scales as the Keplerian period). However, the physical intrinsic grain density ρ_p scales as r_0^{-3} , while the realistic range for this value is in fact much narrower than 3 orders of magnitude. This means that despite writing a hydro simulation in dimensionless form, the physical range of interpretation is already very limited when dust is included. Even more importantly, I note that the physics of solids/light interactions (the Mie theory) can not be written in scale invariant form because the positions of spectral lines are independent of the unit system. A conclusion is that the physical scaling factors (length, time and mass) must be chosen in advance and define a unique physical interpretation of the simulation units that is realistic with respect to the physics of radiative transfer.

6.2.1 `vac2fost`: an interface from AMRVAC to MCFOST

In this subsection I cover the important aspects of converting data from the original format outputted by the hydro code, here AMRVAC, to a compliant format that is suitable as input for the radiative transfer code I am using, MCFOST. The control flow of `vac2fost` is then summarized as a flow chart in fig. 6.2.

Radial interpolation AMRVAC and MCFOST both represent density fields on cylindrical grids. However, the radial stepping in MCFOST is irregular as the first few rings in the grids require an increased resolution which varies with r . This means that AMRVAC fields need to be interpolated onto the MCFOST grid.

Unfortunately the analytic formula for this irregular stepping is not documented, susceptible to change as MCFOST is updated, and the source code is cumbersome enough that it is virtually impossible to retro-engineer it. The recommended approach, following MCFOST’s documentation, is actually to dry-run MCFOST with a dedicated flag to output its grid and

exit immediately. In `vac2fost`, this is what I call “prerolling MCFOST” (see the full control flow in fig. 6.2).

The necessity of a vertical dimension Stellar irradiation is fundamentally a function of elevation z . At odds with the prescriptions for temperature that are necessary to run 2D razor thin hydro simulation, it is in fact meaningless to assume invariance along the vertical axis when it comes to heating and cooling processes. While the surface layers receive stellar light directly, they are normally opaque to photons carrying most of the energy, namely the micrometric range, as we saw in section 1.2.3. As a consequence, heating is far less efficient in the midplane’s vicinity.

Indeed, pure radiative transfer models of proto-planetary disks are primarily studied in reduced dimensionality (r, z) (axisymmetric models). A conclusion here is that in order to apply radiative transfer to the output of a razor-thin simulation, the density distribution needs to be extrapolated in the vertical direction. For now on I will simply assume that the 3D gas distribution relates to the surface density following eq. (2.20). However, I showed in the appendix of C. M. T. Robert et al. (2020) (previous chapter) that the scale height H is not uniquely defined in a non-isothermal simulation, so this parameter is left free in the following experiments. Finally, it ought to be remarked that the vertical settling of dust grains normally implies they are distributed over a much shorter vertical height, as a function of their size. However, this phenomenon is extremely demanding in spatial resolution for a full 3D model with MCFOST, and I was not able to run MCFOST on a large enough computing facility, so I will simply sacrifice this to realism and assume all grains follow the vertical distribution of the gas itself.

Dust binning While in hydro simulations, typically only a handful of dust species are taken into account (4 in the runs I presented earlier), MCFOST uses its own binning scheme and parameters. In order to circumvent resonances between radiation and dust grains, it is considered best practice to require the size distribution be spreaded over about 100 bins, equally spaced on a log scale, and specified by a minimal and maximal size. In fig. 6.3, they are noted “rt” min/max sizes for “radiative transfer”, while the limits of the interval covered by the bins from a hydro simulation receive a “hydro” prefix. MCFOST does not in general extrapolate relative abundances of grains outside the range defined by hydro bins if there is more than one, and performs linear (in log scale) interpolations between those. Knowing this, I defined three possible strategies to interface hydro bins into MCFOST, as optional modes for `vac2fost`.

1. The first approach (“gas-only”) simply consists in passing the gas distribution, and let MCFOST extrapolate the relative abundances following eq. (6.1). This was mainly useful in prototyping `vac2fost` as well as setting a baseline for later comparison. It also has the obvious advantage of being applicable to existing datasets that do not include dust, though in practice it is not expected to yield realistic results.
2. Alternatively, one can pass the hydro dust bins only (“dust-only”). This mode is *a priori* relevant to simulate images in wavelengths within the size interval covered by the hydro grains. Since the simulation time step is constrained by the velocity differences between gas and dust, the smallest grains, which are more tightly coupled to the gas

can become prohibitively expensive to simulate for a negligible benefit, and so are excluded from the hydro simulation. This mode remains valid at longer wavelengths.

3. Finally, we can take the best of both worlds in a third composite mode, where the hydro dust bins are passed directly, but an additional one, representing the minimal grain size in the distribution s^* is mocked using gas density distribution directly. This mode is named “mixed”.

These modes graphically represented in fig. 6.3.

User experience While `vac2fost` never knew any other user than myself for now, I wrote it as if for someone else and tried to provide the best user experience possible. Namely, a common pitfall found in tools built by one person over the course of years, and especially in the Python ecosystem, is to neglect things like user input sanitizing, and overlook cryptic error messages when something bad happens. The general solution to these problems is to deliberately and systematically test the software against malformed input data (for instance, check what happens if the one of the input flags has a typo in it). As emphasized in fig. 6.2, the configuration parser is intended to fail immediately in case the requirements make no sense or if currently unsupported combinations of parameters are found. Catching problems as early as possible enables crafting helpful error messages, but requires active decision making in designing the software.

`vac2fost` is primarily designed as a CLI (Command Line Interface) application, mimicking AMRVAC and MCFOST own usage. A basic run is achieved with the following call on the command line

```
vac2fost my_exp.toml --output out/
```

Additionally, `vac2fost` doubles as a simple Python library, which allow to programatically run a series of experiences by overriding a master configuration (.toml) file. For instance one can vary the aspect ratio and the dust binning mode as

```
1 import vac2fost
2
3 # most of the experience parameters are stored in a master configuration file
4 conf_file = "my_exp.toml"
5
6 # programatically run the experience with variations to the master configuration
7 for dbm in ("gas-only", "mixed"):
8     for aspect_ratio in (0.01, 0.05, 0.10):
9         override = {
10             "mcfost_output": {
11                 "scale_height": aspect_ratio,
12                 "reference_radius": 1
13             },
14             "flags": {
15                 "dust_bin_mode": dbm
16             }
17         }
18         vac2fost.run(
19             conf_file,
20             override=override,
21             output_dir=f"{dbm}_{100*aspect_ratio}"
22         )
```

Input file formats The heterogeneous resolution level in an AMR grid was an additional difficulty to overcome. At first, I overlooked this aspect and wrote `vac2fost` within the restriction that input data must be uniformly refined¹, using AMRVAC’s conversion functionalities to write VTK (Visual Tool Kit) compliant data files, and which are supported by the homonym `vtk` Python library. Later in my thesis, I was able to use the `Yt` library (see chapter 7) to read native AMR data from AMRVAC and resample the grid at runtime directly in Python. This resulted in splitting the data reader in `vac2fost` into two separated frontends, one of which can only read VTK files with uniform refinement, and one that reads arbitrarily refined native data from AMRVAC and relies on `Yt` to do the heavy lifting. A sizeable side-benefit is that this second frontend is natively able to read any data format known by `Yt` and is not restricted to AMRVAC, though a lot of other aspects in `vac2fost` would need adjustment in order to truly support inputs from other hydro codes. In the future, I intend to rebuild this software as a general exporter from hydro data to MCFOST.

¹Note that the “AMR” part of AMRVAC is intentionally skipped in `vac2fost`’s name !

User inputs

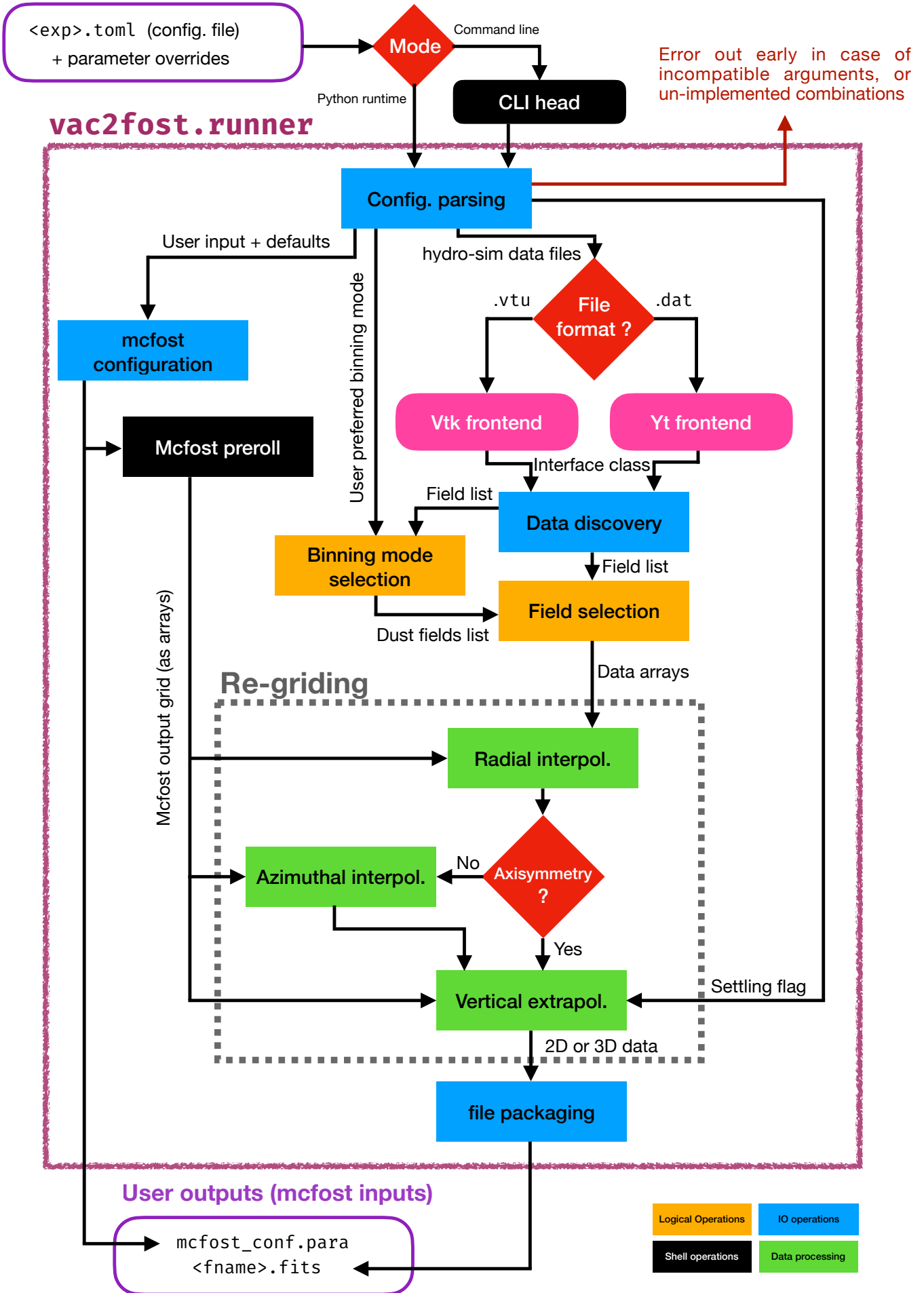
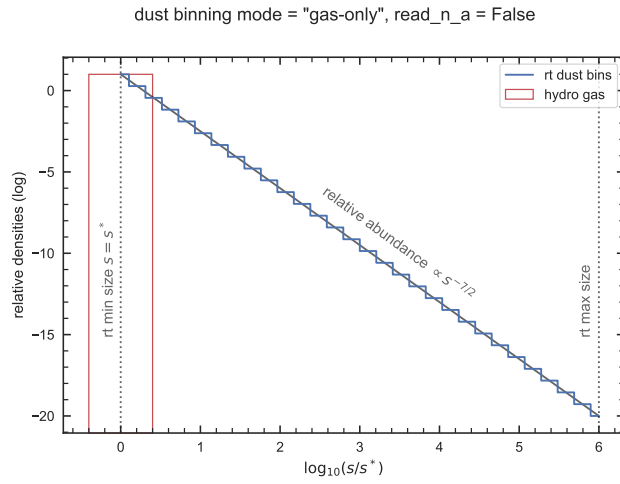
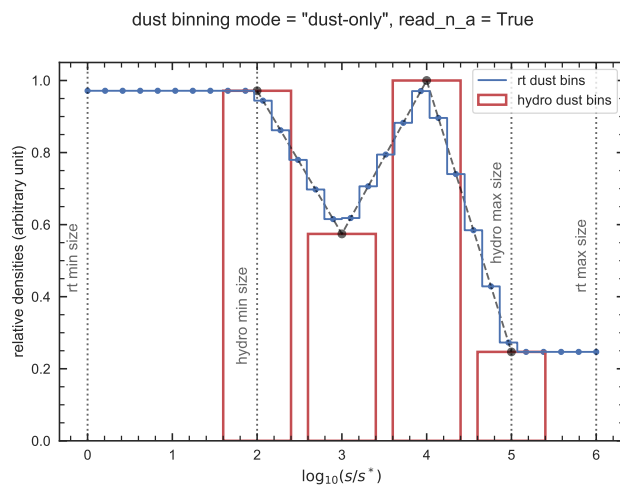


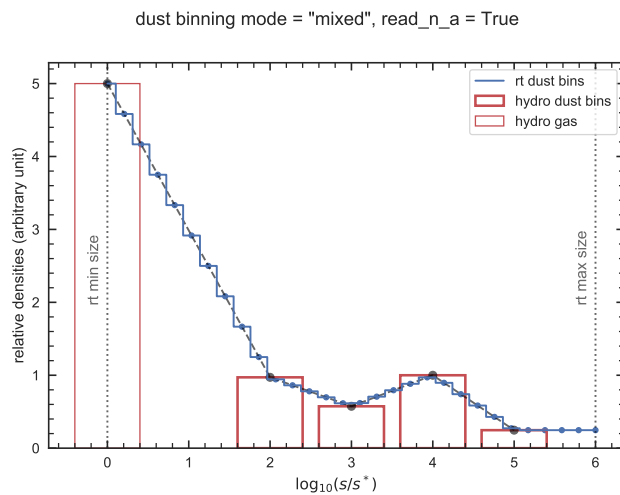
Fig. 6.2: vac2fost's control flow.



(a) gas-only



(b) dust-only



(c) mixed

Fig. 6.3: Three dust rebinning strategies in `vac2fost` from a hydro simulation (4 dust bins + gas density) to a larger number of bins in `MCFOST`. s^* is an other name for “rt min size”. `read_n_a` is a boolean parameter that is passed down to `MCFOST`, which needs to be set to True to avoid renormalizing the densities according to eq. (6.1).

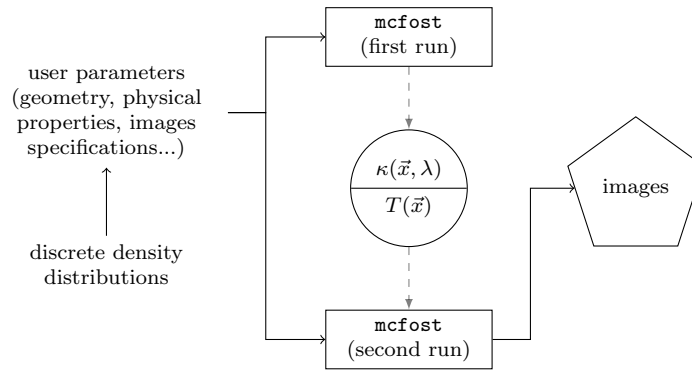


Fig. 6.4: A schematic view of MCFOST’s workflow. Images are obtained in two steps. MCFOST is first run against the density distributions of hydro dust populations, and computes opacity maps (κ) from which it derives temperature (T) in all grid cells. In a second run, the user typically specifies a wavelength at which images should be computed via ray tracing.

6.3 Simulated direct observables of a Rossby vortex

In this section I present images simulated from the aforementioned hydro runs, using vac2fost and MCFOST. In all cases presented thereafter, the temperature of the stellar surface is set to 6650 K to mock that of HD 142527 (Mendigutía et al., 2014), $s_{\min} = 0.1 \mu\text{m}$ and the total dust mass is set to $1 \times 10^{-3} M_{\odot}$. The aspect ratio h is arbitrarily set to 0.1.

The chemical composition of dust grains is assumed to match that of astronomical silicates as described by Draine and Lee (1984), and dust scattering is included in my calculations.

Images presented thereafter are obtained following the workflow schematically represented in fig. 6.4.

6.3.1 Thermal continuum prediction

Intensity maps of a vortex merger In fig. 6.5, I represent intensity maps at various wavelengths for an exactly pole-on disk, using as input the model with dust back-reaction at $t/t^* = 20$, that is, when the simulation contains a pair of vortices undergoing a merger (see fig. 6.1, second to leftmost column). In this snapshot, the dust to gas mass ratio is low enough that the model is still very close to the one without back-reaction. I cover a large range of wavelengths $32 \mu\text{m}$ to $2048 \mu\text{m}$, evenly separated by factors 4. Panels (a) and (b) differ by the dust-binning mode (DBM) used in vac2fost, affecting the size distribution of grains inputted in MCFOST, and I intentionally normalize the color range in every panels so that the overall geometry strikes the eye instead of relative intensities across channels. The same raw data is presented across rows, and is convolved with arbitrarily large gaussian beams, whose sizes are shown as white disks, as an additional step towards observational data. Beam convolution makes structures appear larger as well as less sharp.

The biggest differences between the two models, unsurprisingly, are seen at shorter wavelengths. With the “dust-only” DBM, small grains are under-represented in the overall size distribution. This results in a biased intensity map, where the global maximum as well as the overall azimuthal asymmetry resembles that seen in the actual thermal continuum interval. Indeed, this double peaked azimuthal distribution is in fact not seen in the “mixed” DBM model for $\lambda = 32 \mu\text{m}$, where the global maximum appears on the opposing side of the disk. As smaller grains are more realistically represented in this case, it is indeed expected that the intensity map appears closer to axisymmetric as we approach shorter wavelengths, where stellar irradiation becomes dominant and most of the photons ending in the instrument are scattered by dust that does not pile up in vortices. As expected, the most complex model (“mixed” DBM) appears more realistic overall. At higher wavelengths, while intensity maps are very similar between models, it is also evident that isocontours are visibly narrower in the “mixed” DBM case, which is an encouraging result in that structure is more easily resolved in our most realistic model.

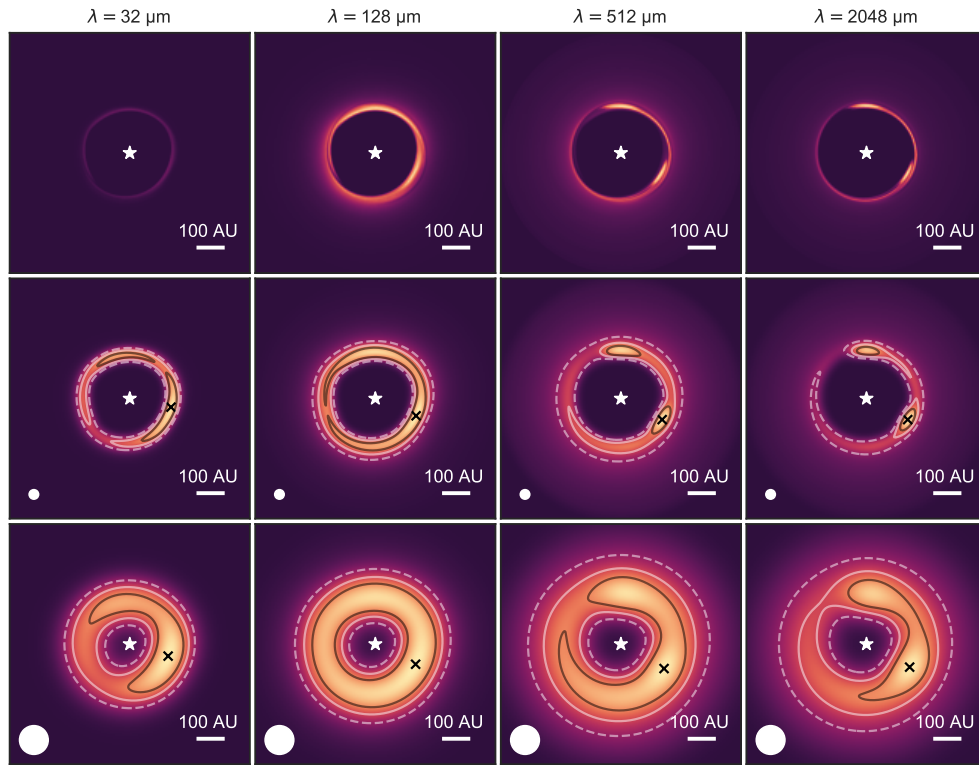
As a sidenote, I remark that this vortex merger event, admittedly a short-term episode in the development of the Rossby wave instability, yields intensity maps not unlike what is observed in HD 142527 (see panel (b) in fig. 5.2), in particular showing a secondary local maximum. Without further inquiry this however may be disclosed as a more plausible explanation is that the double peaked intensity may be due to a shadow, cast by a tilted inner disk, producing a local decrease in heating and hence a minimum in thermal emissivity (Casassus, Wright, et al., 2015).

Intensity maps of a fully grown vortex Now let us compare the late stages of the hydro runs, one of which (without back-reaction) consists in a fully grown vortex. The other model (with back-reaction), where vortex formation is impeded by dust accumulation will serve as a baseline for comparison. The images are displayed in fig. 6.6, and call for a few remarks. In both cases, and at the largest tested wavelengths ($\lambda \in [512, 2048] \mu\text{m}$), the intensity maps show a “yin” shaped azimuthal asymmetry. However, the orientations of these patterns differ. Namely, in the case of an actual vortex, the luminosity is decreasing in the clockwise direction, while the disk is rotating anti-clockwise. This is consistent with the fact that grains spiral into the vortex from behind it, leaving a “trail” of sort, as seen directly in the hydro simulation (fig. 6.1). On the other hand, in the disrupted case, luminosity happens to be decreasing in the anti-clockwise direction. A preliminary conclusion here is that this pattern can be observed even without a vortex, though consistency with the disk rotation solidifies the vortex-explanation of existing candidates.

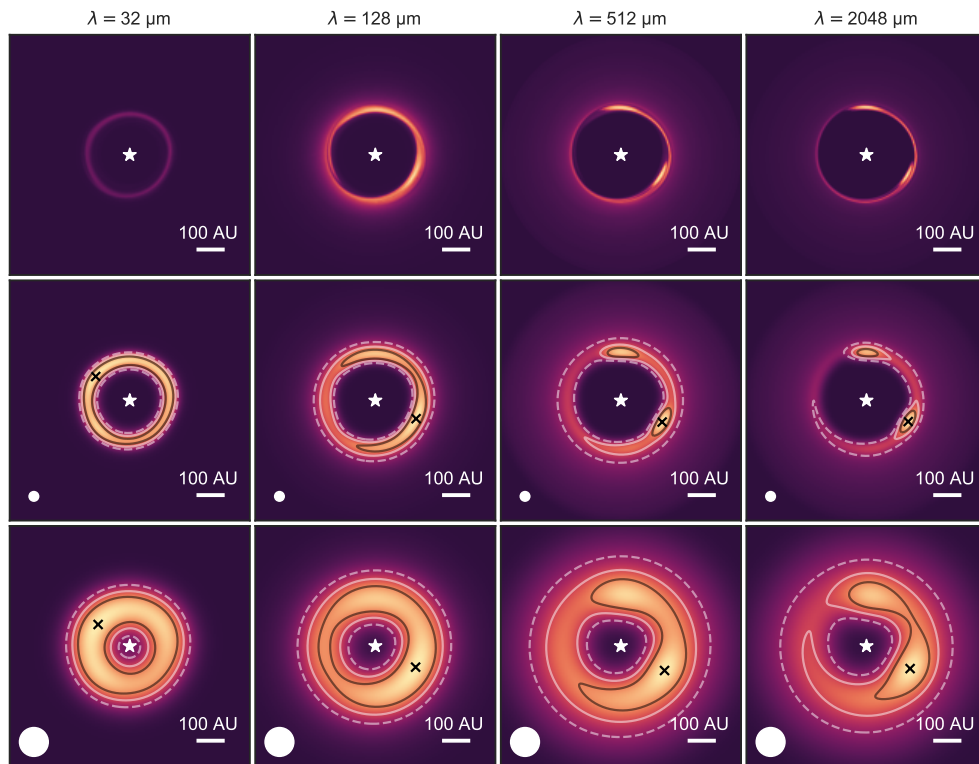
Another noticeable difference is that the location of absolute maxima is clearly consistent across the spectrum in the case of a vortex, while it appears far more random in the disrupted case, since there is no clear concentration site.

Discussion The closest work to this qualitative study is found in Baruteau, Barraza, et al. (2019), which presents quantitative comparisons of continuum observations at $\lambda = 900 \mu\text{m}$ for MWC 758 against 2D lagrangian dust hydro simulations. Other authors (van der Marel, van Dishoeck, et al., 2013; van der Marel, P. Pinilla, et al., 2015; Ohashi et al., 2020) focused on modeling azimuthal dust traps in a geometric fashion, based on an analytic model introduced (Birnstiel et al., 2013). However the model in question only captures

the even modes in azimuthal dust concentration, and fails to reproduce the uneven “yin” shape that characterizes vortex-driven trapping, and which is indeed observed in some real-life targets such as IRS 48 (van der Marel, van Dishoeck, et al., 2013) and MWC 758 (Dong et al., 2018) (at least the inner clump, see panel (a) in fig. 5.2). My results from full hydro simulations provide qualitative evidence that those structures may indeed result from vortices.

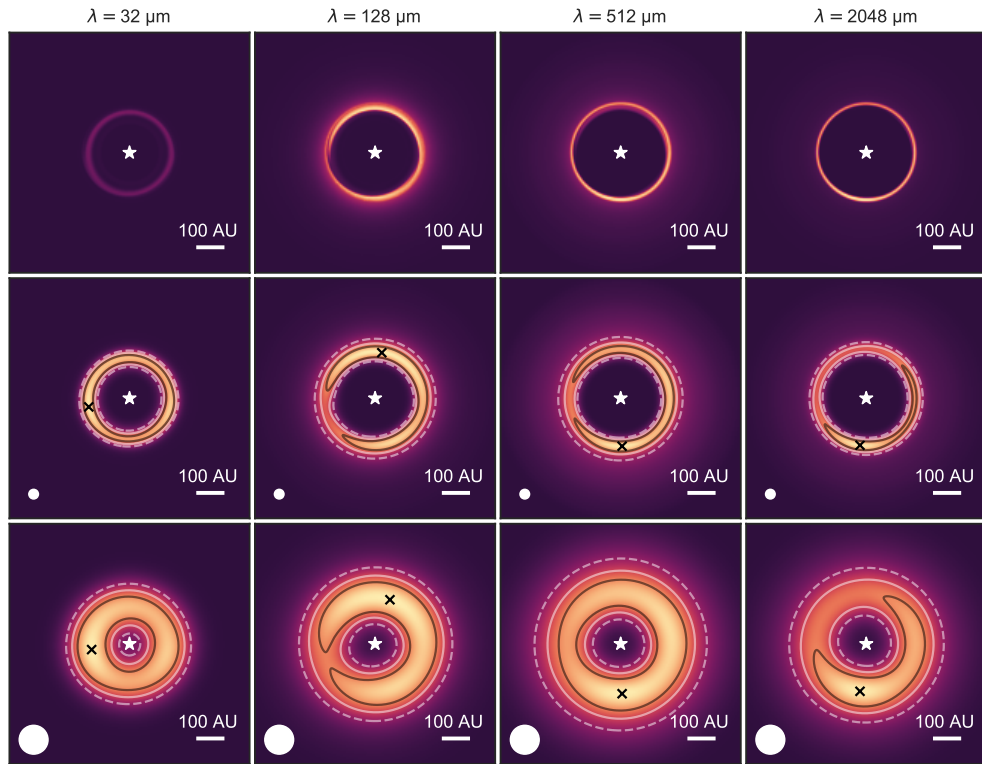


(a) “dust-only” DBM

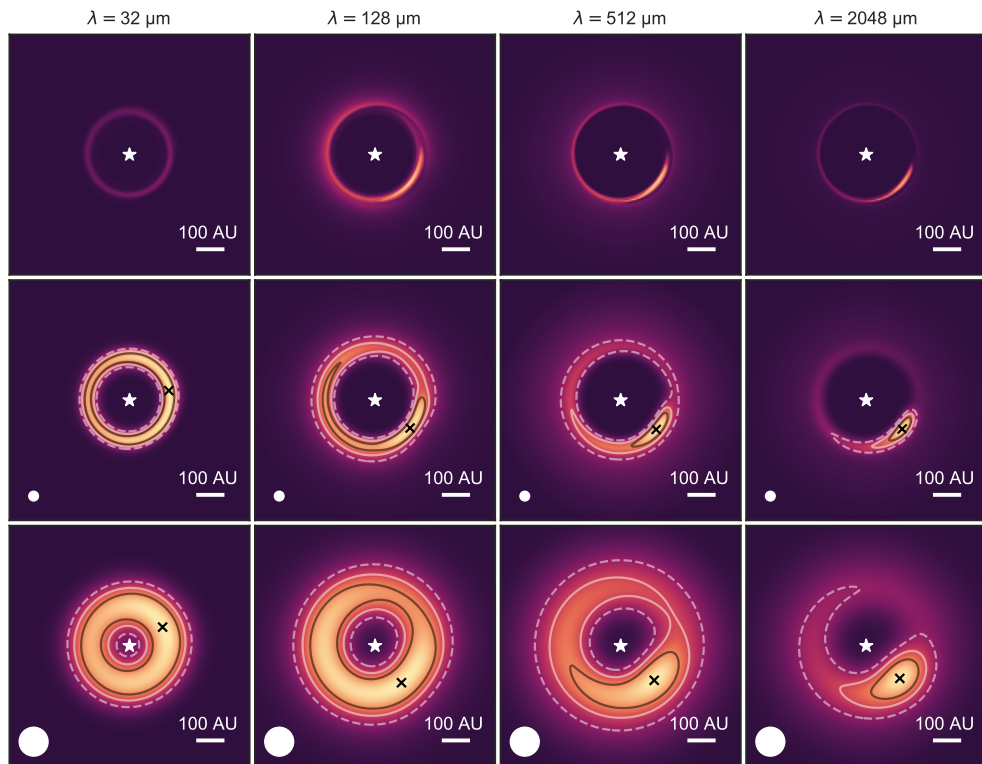


(b) “mixed” DBM

Fig. 6.5: A comparative view of continuum imaging against dust-binning mode (DBM). (a) “dust-only” DBM, (b): “mixed” DBM. Each map represents a flux intensity, color scales are not identical. Wavelength λ is varied across columns while the size of the beam varies across rows. The standard deviation of the 2D gaussian beam is indicated as a white disk in the top row. Fiducial contours indicate intensity levels, relative to the absolute maximum in each frame, at levels 90 % (grey, solid), 50 % (white, solid) and 30 % (white, dashed) respectively. The absolute maximum is indicated by a black “x” mark. The original 2D density snapshot is taken in the hydro model with back-reaction, at $t/t^* = 20$, during vortex coalescence, and corresponds to the second to left-most column in fig. 6.1.



(a) with back-reaction



(b) without back-reaction

Fig. 6.6: Similar to fig. 6.5, but this time comparing the two models with back-reaction (a) and without it (b), at $t/t^* = 100$.

6.3.2 Polarimetric predictions

Polarimetry 101 As discussed in section 1.2.3, the micrometric realm is dominated by stellar thermal emission, though one can probe the disk's surface through scattered light via polarimetric techniques. This is possible because the direct stellar flux is not polarized (e.g. individual photons are uniformly distributed in polarization angle θ_p), while in light scattered by the disk, θ_p is skewed towards directions that are orthogonal to the incident direction. In practice the polarized intensity is measured in two orthogonal directions. These measured intensities are called the Stokes parameters Q and U , and are not intrinsic to the target since they depend on the orientation of the instrument. Intrinsic quantities, name total polarized intensity P and the polarization angle θ_p are recovered as

$$\begin{cases} P \equiv \sqrt{Q^2 + U^2} \\ \theta_p \equiv \frac{1}{2} \arctan2(U, Q) \end{cases} \quad (6.7)$$

Polarimetric signatures of a vortex In figs. 6.7 and 6.8, I display the polarimetric characteristics for 3 inclinations $i \in [0, 30, 60]^\circ$ and two wavelengths $\lambda \in [2, 512]\mu\text{m}$ for the final state of the run without back-reaction. At $\lambda = 2 \mu\text{m}$, the polarized flux is barely enhanced at the vortex location. The polarization angle also seems unaffected and stays locally azimuthal in the face-on case $i = 0^\circ$. The polarized fraction P/I however clearly shows a left-right asymmetry and traces the position of the vortex's bulk at all tested inclinations, reaching 22% of the total intensity.

In the dust's thermal emission domain ($\lambda = 512 \mu\text{m}$) however, my simulated images reveal qualitatively different signatures, and much harder to detect. The polarization fraction barely approaches 1% in the vicinity of the bulk, while the eye of the vortex itself is actually fainter. Note that the total polarized intensity itself is 10 times lower than in the micron domain, but remains detectable. This time the polarization angle reveals the position of the vortex and is locally tangent to the dusty bulk. This is explained by the fact that most of the radiation field at this wavelength is emitted by the cold dusty clump, as is seen in the corresponding total intensity map in fig. 6.6, hence the polarization angle is orthogonal with respect to the local direction to the vortex's eye. This feature is especially striking in the particular case of a perfectly pole-on orientation.

6.4 Conclusions

It should be clear at this point that conclusive evidence in favor of giant vortex formation will not be obtained via a single observable. Rather, concurrency of multiple signatures seems like the most promising route, as it provides many different ways to refute the vortex scenario in individual candidates. Fortunately, it appears that large eddies indeed produce detectable imprints not only in the raw continuum emission but also in polarimetric observables.

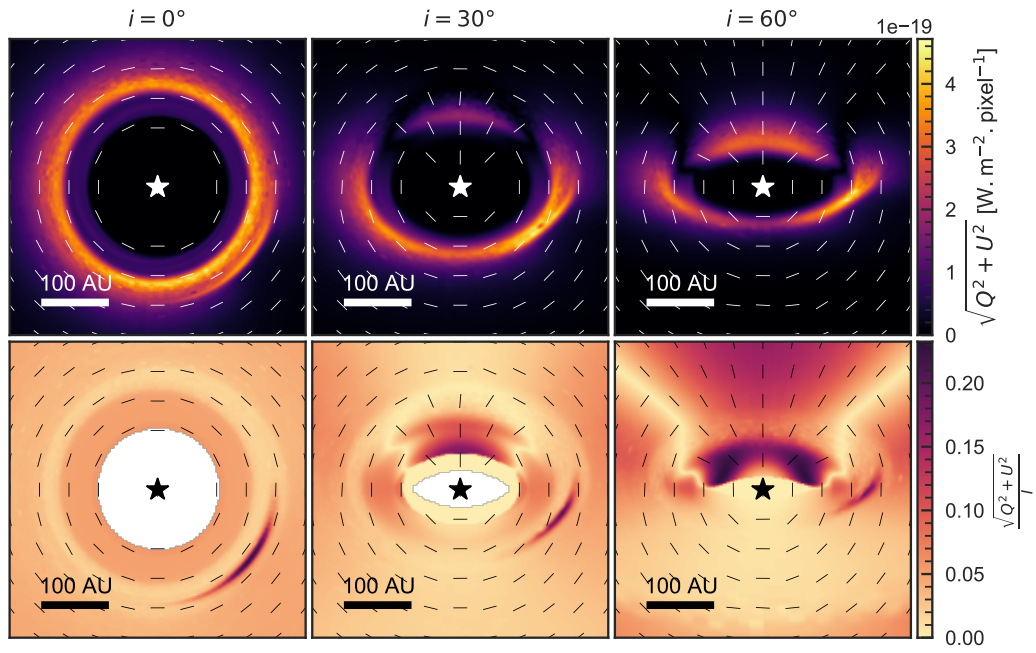


Fig. 6.7: Polarized emission at $\lambda = 512 \mu\text{m}$ for the model without back-reaction, at $t/t^* = 100$. Top row: polarized intensity. Bottom row: polarized intensity fraction (normalized by the total intensity). Inclination varies across columns. The orientation of the polarization is overlaid as a quiverplot.

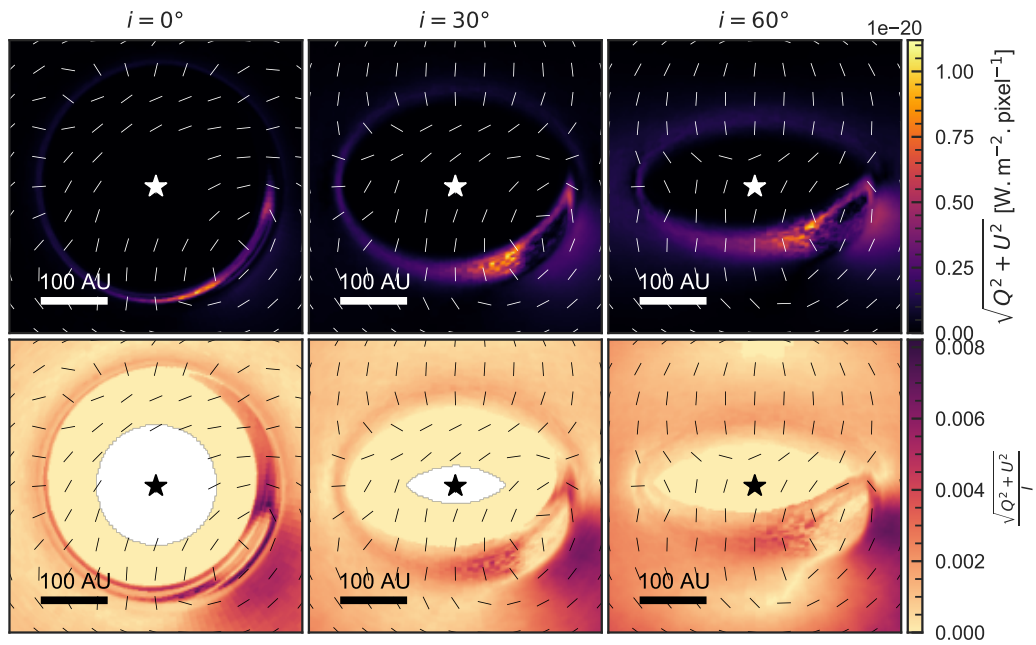


Fig. 6.8: Same as fig. 6.7, at $\lambda = 512 \mu\text{m}$.

Open source data analysis, for more reliable science

“ He may not be perfect, but do we really want some new guy?
I'll stick with the evil maniac I know, thank you!

— Dr. John Zoidberg
Futurama

During my Ph.D., I came across multiple data formats and more solutions to read them. Oftentimes, those solutions were reserved to personal use and provided little to no support for extensions, limiting the depth of inquiry for the analyst. I myself wrote such tools to conduct my own research. Most notably I developed a Python API (Application Programming Interface) to ease IO (input/output, reading and writing data) operations for FARGOCA (our local fork of FARGO developed at the Observatoire de la Côte d'Azur), which was a very useful interface for data analysis with Matplotlib (the de-facto standard plotting library in the scientific Python ecosystem) but saw little use except for the occasional interns after my first paper (chapter 4) was concluded. I also wrote a similar Python API for AMRVAC data which constituted the foundation for vac2fost.

I eventually grew frustrated with *reinventing the wheel*. This expression is common in the programming world, but its application domain grows ever larger by the day. Indeed, what is regarded as game-changing now may become the “wheel” of tomorrow provided enough people need the same software and are given good reasons to trust it.

Hence, and at the cost of an admittedly larger engineering effort, I decided to contribute to a general purpose data analysis library (Yt) and eventually joined the ranks of its maintainers. This chapter is a discussion on the stakes of open source development in science and presents my contribution to it.

7.1 A plea for open source research tools

Because the astrophysics community is highly competitive, a lot of numerical tools and libraries have historically been developed privately and scarcely distributed. This was regarded as a winning strategy for individual researchers having invested significant time developing private tools, providing themselves with cutting-edge technology only available to the closed circle of their immediate collaborators. It can however be argued that this strategy is harmful to the community as a whole as it does not promote reproducibility in numerical experimentation. The wide usage of *proprietary* tools (i.e. of which the source code is hidden from users) furthermore damages the questionability of scientific results, as

bugs can hardly be deciphered or fixed by its end-users. Naturally, results are more difficult to challenge and question when they are obtained through black boxes, which goes against a fundamental principle in the scientific method ; namely the criterion of falsifiability. Another problematic aspect is that testing culture seems under-developed in research. Effectively, writing tests for code that “just works” is undermined as an unnecessary luxury while in the industry, it is a basic requirement in any software worthy of its users’ or clients’ trust. As an advocate for reproducible computational experiments, I wrote tests for existing code in Yt, FARGOCA, AMRVAC (for which I enabled *continuous integration*, i.e. I set up the github repository so that no code contribution would go untested), as well as a handful of tools that I wrote or occasionally contributed to (including astropy and pyMCFOST).

On the other hand, open source development solves all of these issues by exposing the gears of software as well as internal weaknesses. This allows for them to be more quickly discovered and fixed as end-users can more easily get involved in the development process. The resulting software should be more robust as a result.

That being said, open-source projects are all somewhat unique in how they are developed, administrated and maintained. Let me here briefly borrow political power vocabulary to try and make a clear and concise distinction between the codes I have personally used and developed during my thesis. Perhaps AMRVAC’s governance can be described as an *ad hoc-technocracy*, as it is developed by a disorganized group of technical experts, and the distinction between users and developers is relatively sharp. In contrast, Yt’s governance is a *participatory sociocracy*, in which decisions are taken in proactive groups. The quality of contributions must explicitly be reviewed and challenged by peer developers, much like scientific publications, even when emitted by founding members of the projects, avoiding the emergence of a dictatorial regime. Enforcing peer-review not only promotes better code quality, it also participates to the development of a community culture.

As emphasized by Matthew J Turk (2013), community-driven development is best grown by encouraging guidelines and needs to be designed for, rather than wished for. For instance, Yt’s development team provided itself with a set of governing rules that clearly define different roles in the group and enables dynamic decision making processes by embracing a rule of *lazy-consensus*. Namely, unexpressed votes are considered approvals for any given proposal after a set period of time (2 weeks). Important changes that require a well defined frame of discussion are documented throughout their acceptance process via YTEPs (Yt Enhancement Proposals, mimicing Python’s own PEPs). Through this proposal/decisional process I was able to argue for the adoption of several tools to automate part of the code quality validation process and promote coding standards in Yt, which got accepted after internal debates.

On a broader scope, there is an increasing demand for public data management in science. For instance the Observatoire Virtuel¹ initiative aims at providing common access methods to retrieve and explore public data collected by many sources. It also solves the difficulty of archiving enormous chunks of data at the community level. Wilkinson et al. (2016) proposed a fundamental set of principles to promote and develop open science, called FAIR (Findable, Accessible, Interoperable, Reusable data).

¹<https://www.observatoiredeparis.psl.eu/-observatoire-virtuel-.html?lang=fr>

The common theme here is that putting resources in common requires that scientists go the extra mile and pro-actively design empowering rule sets.

7.2 A unified and simplified library for data analysis

Yt (pronounced "whitey") is a Python library that provides general-use abstractions for common low-level processing operations applied to spatially organized data (Matthew J. Turk et al., 2011). Its core functionalities are written as native extensions in Cython and rely on the C API provided by Numpy for efficient array computations. It adds a physical layer to data representation as units are attached to N-dimensional arrays, and comes with functionalities for dimensional analysis and physically meaningful computation. This essential aspect to physical interpretation of simulation-outputted data is easy to get wrong when dealing with the raw computer-representation of quantities (dimensionless numbers), so it is a valuable feature in a general use library.

It is designed to uniformize data processing of small and large datasets alike, offering *lazy-loading* mechanisms, i.e. it allows to only load the computer's memory (RAM) as data is requested. Namely, it allows to selectively load information from user-defined regions and physical quantities of interest. Core functionalities such as data querying are written in Cython (a C-compilable derived version of Python) and support parallel computation. This is achieved thanks to *memory-mapping*, i.e. the on-disk data is typically mapped out to physical space ahead of memory loading.

These general principles are implemented in several paradigms to comply with the existing formal diversity in spatially organized data. Namely grid-based AMR (patch-based as well as octrees), discrete particle sets (e.g. in SPH or PIC simulations), and so-called *unstructured meshes*. Each data format is interpreted by a specialized part of Yt, called a *frontend*, and dedicated to memory-mapping and reading operation. My main and starting contribution to the Yt library was writing such a frontend dedicated to AMRVAC.

Relying on Yt to process data simplifies MPI-AMRVAC's workflow in several ways. First, it suppresses the need to convert data to standard file formats, which saves significant disk space and time. In my own simple applications, I found that converting my data more than tripled my memory usage. It was also reported to me that some very high resolution/AMR refinement research conducted with AMRVAC involved data files so large that their mere conversion to readable formats takes about an hour per snapshot. Additionally, it removes the need for storing *derived fields*² such as sound speed or gradients on hard drives, which makes for further reduction of memory usage, and allows for fully post-processed data analysis. By enforcing this clear separation between simulation runs and post-processing data reduction operations, one does not need to define relevant quantities to explore ahead of the numerical experiment, which saves the pain of having to rerun simulations only to output derived data. Cherry on top, it scales much better than the leading software for visualization (Paraview)

²Derived quantities (or fields) are completely determined by their counterpart *primitive quantities*, density, linear momentum, energy density, and magnetic field, given that equations of state are specified.

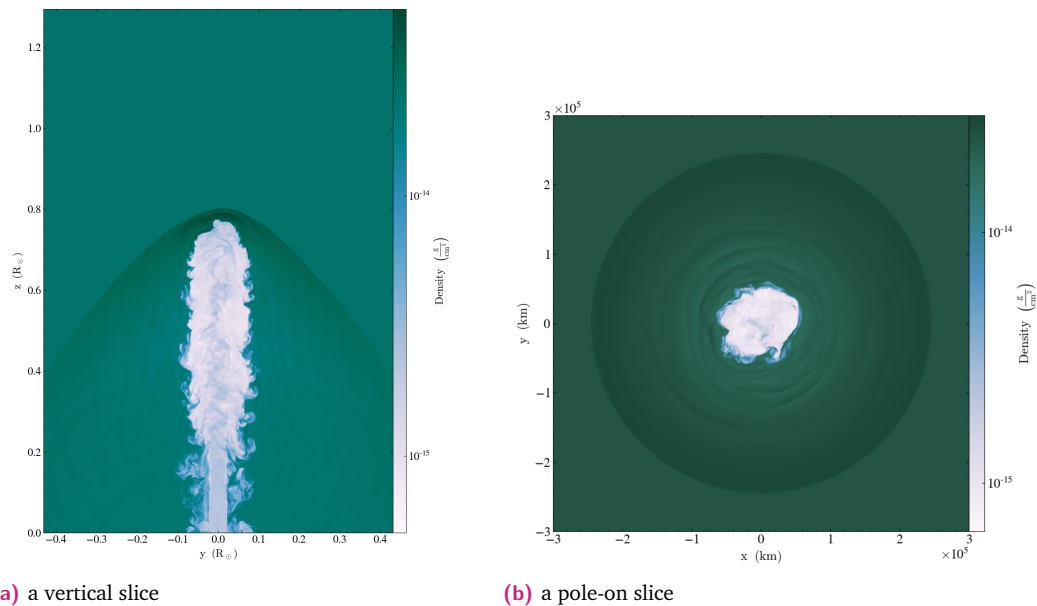


Fig. 7.1: Slice plots for an extremely high resolution 3D jet flow simulation. Each plot can be performed under 30s on a 8 cores laptop. The data file itself is larger-than-RAM and weights 25 Gb; equivalent visualizations with Paraview were not possible with comparable machine specs and required several minutes of acquisition on a larger facility (visualization server). The simulation was run by Rony Keppens and plotted by Niels Claes.

for large datasets (at least running on a highend laptop) see fig. 7.1. The reason is that Paraview loads the whole dataset into the RAM ahead of time and only perform selections at visualization time, while Yt loads nothing initially and queries (and caches) the relevant data chunks as they are needed. I summarize a typical workflow in fig. 7.2. In essence, Yt abstracts away the low-level tasks and allows for writing very simple pure-Python scripts which contain none of the mundane preprocessing and visualization operations and let the user focus on the science part, namely analysis through data-questioning.

In the following section, I summarize keypoints in AMRVAC’s unique data format, exposing the minimal knowledge I needed in order to design a Yt frontend for it.

7.3 Data storage and reading: the illustrative case of MPI-AMRVAC

Among other challenges and dilemmas, authors of simulations codes are faced with a two-sided choice for the file format their codes should write its data to. The trade off is here is that standardized file formats such as `.hdf5` or `.vtu` are recognized by a variety of analysis tools but not necessarily optimized for their applications, while designing a unique dataformat allows for refined optimizations in terms of IO time (reading and writing), but is de-facto unknown to analysis tools and libraries.

AMRVAC implements its own “datfile” format (named after the conventional `.dat` file extension). The library also offers some flexibility and is able to convert its own format to a

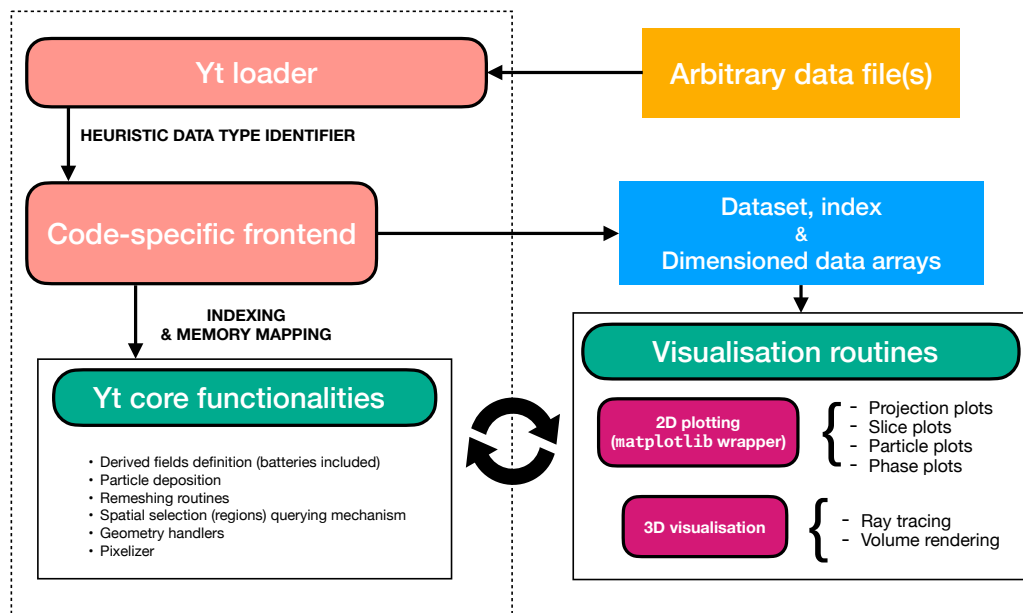


Fig. 7.2: A flowchart representation of a typical workflow with Yt. The graph is divided between the internal library side (boxed, left), and the user side (right). Only the main functionalities of the library are listed here. My contributions to the library include the AMRVAC-specific frontend (collaboratively with Niels Claes), as well as geometry specific support for existing functionalities.

dozen other, more standardized formats. The primarily *raison d'être* for the native datfile format is to allow efficient restarting of large simulations from a previous snapshot. Because this format is optimized for compacity, and is the only one every MPI-AMRVAC user will consistently store, it is the one I design the Yt frontend around. I give here indications on how this is achieved, within the mindset of a Yt frontend developer.

7.3.1 Morton curves: unambiguous flat-indexing for arbitrarily refined data

Computer hard-disk memory is intrinsically 1D. In order to represent information for simulations with arbitrary dimensionality, efficient and reproducible sorting algorithm are needed. While this is straightforward in the case of uniform resolution grids, where data can be represented as tensors, it is less so with AMR.

Multiple resolution levels AMR data can be uniquely sorted using Morton-indexing. Each cells is assigned a unique label specifying its position in space as a $(N + 1)D$ integer vector (where N is the number of spatial dimensions) where the last component specifies the resolution refinement level, while the first 3 indicate the distance with respect to the “left” edge of the domain, in units of the cell’s width.

Cells are then ordered following a depth-first exploration algorithm that systematically visits children cells (deeper, more refined) over neighbours. The resulting curve tracing the visit order shows a typical “z” shape on multiple scales and is appropriately named the z-space

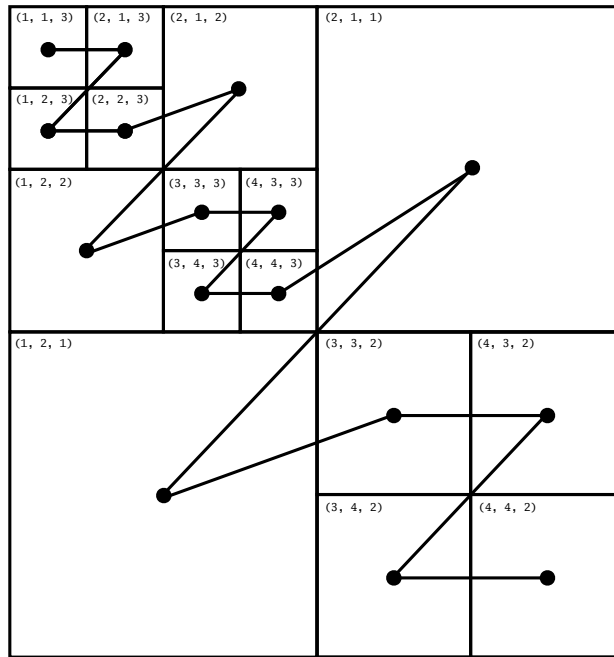


Fig. 7.3: An illustrative case of space-filling Z-curve (Morton indexing) in 2D across 3 levels in resolution refinement. Each cell is uniquely labelled following the Morton indexing (x , y , level).

filling curve, or Morton curve. This is illustrated for a 2D mesh in fig. 7.3, and is trivially generalized to 1D or 3D.

7.3.2 A compact linear memory mapping solution

I give a schematic representation of AMRVAC’s native datfile format in fig. 7.4. It is designed primarily to minimize occupied disk space. The simulation domain is comprised of *blocks*, that each contain a well defined number of cells, written following the Morton-ordering rule. First level (coarsest) blocks are user-defined arbitrary divisions of the simulation domain, and are most useful in parallel computing to dispatch the domain among CPUs. Other, AMR-refined blocks are defined by the program at runtime, following user-parameterized refinement rules.

Each block’s data is reduced to a minimum, where only “primitive” (linearly independent) fields are written to disk such as linear momentum ρv as well magnetic field \mathbf{B} . The *ghost-zones*, i.e. repeated data from neighbouring blocks, which is potentially refined/coarsen to match the current block, are not written to the datfile. This data is used in the program to enable parallel computation, as well as numerical gradients. The fact that it is not stored in the datfile means that it needs to be reconstructed by Yt in order to recover gradients. At the time of writing, this is an existing limitation of our Yt frontend. Gradients can still be derived by resampling the grid to a uniform level first, though this is admittedly a costly operation to perform on large datasets.

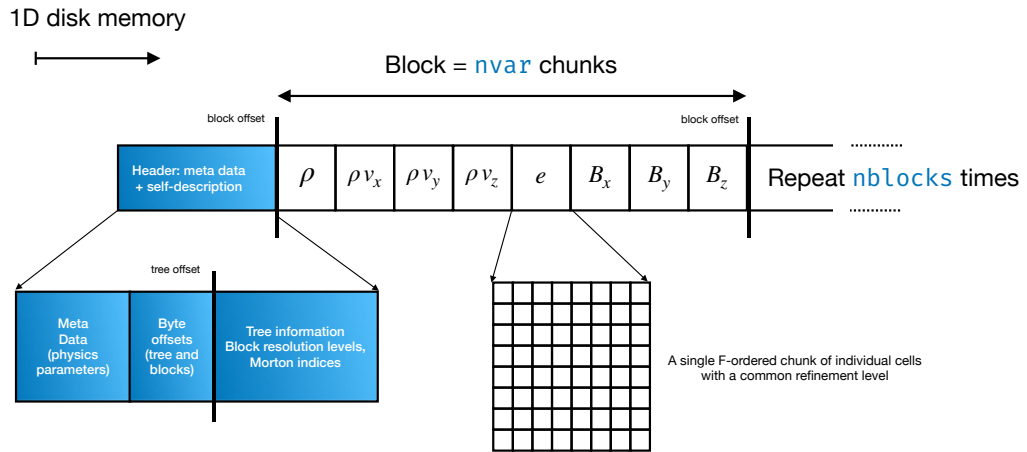


Fig. 7.4: A sketch of how AMRVAC's data file is mapped to linear disk memory, represented here as a ribbon. No data is repeated and the number of panning bytes is kept at a minimal, where bytes offsets for each block and blocks byte width are contained in the header. Each block is described by $nvar$ (for each stored field) chunks of contiguous *F-ordered* (i.e. "column first" array, as per fortran's tradition). Because the byte-width of a single double-precision floating point number (float for shorts) is invariant, it is trivial to compute the byte-offset corresponding to a given block and field. We use this indexing to efficiently retrieve data on-demand within Yt.

The *tree-index*, which describes the location of each block in terms of bytes-offsets from the top of the file, is fully contained in the header's meta-data. This is a trade-off that makes for a more complex writing routine but greatly simplifies reading operations, and in particular memory mapping can be done in one pass in Yt by simply reading this header. I note that this format is also designed to minimize the time needed within AMRVAC to restart from a previous snapshot ; since the block-tree is fully described and then presented in a well defined order, the datfile can be read linearly by the initializer routine. To me, as the frontend developer, it also means that the format prioritizes spatial ordering over physical meaning. A direct consequence is that a given field is never represented as a contiguous data segment, which is an important bottleneck for reading speed optimizations.

7.4 Other contributions to Yt

Additionally to the AMRVAC frontend, I also contributed many bugfixes to the library, affecting all users. I also dedicated some effort in refactoring existing code to improve both the code quality (and its maintainability) and the user experience. Indeed, a pitfall of flexible libraries like Yt is that all possible use cases are not implemented. However, if malformed or incompatible user input is not taken care off early in the control flow, the function calls will fail with somewhat cryptic error messages that are not easily deciphered by the user. Often, when something goes wrong, it is not clear whether what they are attempting to do is not supported, not allowed, or if they just discovered a bug in the library. I improved a number of user-facing functions to include early catching of problems instead, providing meaningful error messages or warnings. This work will be my contribution to the upcoming Yt method paper (in prep).

7.5 Conclusions and perspectives

By making Yt able to read data from AMRVAC's unique format, I enabled the AMRVAC community (a few dozen researchers) to perform data analysis with Python, easing their day to day analysis job (as well as my own) to work with complex AMR data. To this day, a few months after the frontend was publicly released and announced, around 20 people in the AMRVAC community have completely switched to Yt for data analysis, and we expect more are to come when we add support for more features in AMRVAC (such as stretched grids, ghost zones, particle data ...). I also intend to pursue development of vac2fost as a more general exporter for MCFOST, and make it open source once I am confident enough in its stability.

Conclusions and perspectives

In this thesis I scratched the surface of several important aspects of the evolution of planet-forming disks. I investigated the role of planetary accretion in their early migration, and showed that the cuts in angular momentum budgets were indeed not significant even for unrealistically efficient accretion. Performing this study allowed me and my co-authors to reassess the importance of disk viscosity, and we were able to show that, while migration rates indeed correlate to viscous accretion, it is not caused by it in any way. These results are however still disputed in the community, while a number of limitations of 2D simulations cast legitimate doubts on their validity. Fortunately, this work set a baseline for following publications with 3D studies, currently in the making at the Observatoire de la Côte d'Azur. I hope my work on Rossby vortices contributes to building necessary bridges over the overwhelmingly large gap that separates simulations and observations. Again, the works presented in chapter 5 and chapter 6 would strongly benefit from being revisited in full 3D simulations. Nonetheless, I was able to show that the alleged existence of large eddies in proto-planetary disks is refutable, thus testable. I expect the following years will see the first multi-technique unambiguous confirmation of a vortex, and that we should be able to reject part of the candidates, excluding one of the many proposed scenarios to explain dusty clumps. Doing so, we will get one step closer to understanding the conditions under which planets are born.

The challenges ahead are countless, but it is my conviction that one of the most crucial one is in answering the question: how do disks dissipate? Viscosity generating mechanisms are still looked for, and the very idea of globally accreting disks may prove a dead-end. I believe recent and future developments in wind-driven disk accretion models will shake the way we think about these objects once again, and perhaps demonstrate that the role of magnetic fields, which is often overlooked as in the present thesis, is indeed crucial. I will take part on this journey as a post-doc.

Bibliography

- ALMA Partnership, C. L. Brogan, L. M. Pérez, et al. (July 2015). „The 2014 ALMA Long Baseline Campaign: First Results from High Angular Resolution Observations toward the HL Tau Region“. In: *The Astrophysical Journal Letters* 808, p. L3 (cit. on p. 12).
- Andrews, Sean M., Marie Terrell, Anjali Tripathi, et al. (2018). „Scaling Relations Associated with Millimeter Continuum Sizes in Protoplanetary Disks“. In: *ApJ* 865, p. 157. arXiv: [1808.10510](https://arxiv.org/abs/1808.10510) (cit. on pp. 12, 13, 15).
- Armitage, Philip J. (Dec. 2009). „Planet Formation“. en. In: *Am. Inst. Phys. Conf. Ser.* 1192, p. 3 (cit. on pp. 7, 29, 35, 48).
- Ataiee, S., Paola Pinilla, A. Zsom, et al. (2013). „Asymmetric Transition Disks: Vorticity or Eccentricity?“ In: *A&A* 553, p. L3 (cit. on p. 72).
- Avenhaus, H., Sascha P Quanz, H. M. Schmid, et al. (May 2017). „Exploring Dust around HD142527 down to 0.025“ / 4au Using SPHERE/ZIMPOL“. In: *Astron. J.* 154. arXiv: [1705.09680](https://arxiv.org/abs/1705.09680) (cit. on p. 14).
- Balbus, Steven A. and John F. Hawley (July 1991). „A Powerful Local Shear Instability in Weakly Magnetized Disks. I. Linear Analysis“. en. In: *ApJ* 376, p. 214 (cit. on p. 30).
- Barge, Pierre and J. Sommeria (1995). „Did Planet Formation Begin inside Persistent Gaseous Vortices?“ In: *A&A* 295, pp. L1–L4 (cit. on pp. 34, 70).
- Barranco, Joseph A. (Feb. 2009). „Three-Dimensional Simulations of Kelvin-Helmholtz Instability in Settled Dust Layers in Protoplanetary Disks“. In: *The Astrophysical Journal* 691, pp. 907–921 (cit. on p. 35).
- Barranco, Joseph A, Suyang Pei, and Philip S Marcus (2018). „Zombie Vortex Instability. III. Persistence with Nonuniform Stratification and Radiative Damping“. In: *ApJ* 869, p. 127 (cit. on p. 34).
- Baruteau, Clément, Marcelo Barraza, Sebastián Pérez, et al. (June 2019). „Dust Traps in the Protoplanetary Disc MWC 758: Two Vortices Produced by Two Giant Planets?“ In: *MNRAS* 486.1, pp. 304–319 (cit. on pp. 71, 102).
- Baruteau, Clément and Zhaohuan Zhu (June 2016). „Gas and Dust Hydrodynamical Simulations of Massive Lopsided Transition Disks – II. Dust Concentration“. In: *MNRAS* 458.4, pp. 3927–3941 (cit. on p. 71).
- Benisty, M., T. Stolker, A. Pohl, et al. (Jan. 2017). „Shadows and Spirals in the Protoplanetary Disk HD 100453“. In: *Astronomy and Astrophysics* 597, A42 (cit. on p. 14).
- Birnstiel, T, Cornelis P. Dullemond, and Paola Pinilla (2013). „Lopsided Dust Rings in Transition Disks“. In: *A&A* 550, p. L8 (cit. on p. 102).
- Blaes, Omer M. and Steven A. Balbus (Jan. 1994). „Local Shear Instabilities in Weakly Ionized, Weakly Magnetized Disks“. In: *The Astrophysical Journal* 421, pp. 163–177 (cit. on p. 30).

- Boehler, Y., E. Weaver, A. Isella, et al. (May 2017). „A Close-up View of the Young Circumbinary Disk HD 142527“. en. In: *ApJ* 840.1, p. 60 (cit. on p. 91).
- Carmona, A., G. van der Plas, M. E. van den Ancker, et al. (Sept. 2011). „A Survey for Near-Infrared H₂ Emission in Herbig Ae/Be Stars: Emission from the Outer Disks of HD 97048 and HD 100546“. In: *Astronomy and Astrophysics* 533, A39 (cit. on p. 10).
- Casassus, Simon and Sebastian Perez (Oct. 2019). „Kinematic Detections of Protoplanets: A Doppler Flip in the Disk of HD 100546“. In: *The Astrophysical Journal Letters* 883, p. L41. arXiv: 1906.06302 (cit. on pp. 16, 72).
- Casassus, Simon, Chris Wright, Sebastian Marino, et al. (May 2015). „A Compact Concentration of Large Grains in the HD142527 Protoplanetary Dust Trap“. In: *ApJ* 812.2, p. 126 (cit. on p. 102).
- Chapman, Sydeny and T. G. Cowling (1970). „The Mathematical Theory of Non-Uniform Gases. an Account of the Kinetic Theory of Viscosity, Thermal Conduction and Diffusion in Gases“. In: *Cambridge: University Press, 1970, 3rd ed.* (Cit. on p. 29).
- Chavanis, P. H. (Apr. 2000). „Trapping of Dust by Coherent Vortices in the Solar Nebula“. en. In: *Astron. Astrophys.* 356, p. 1089 (cit. on p. 34).
- Chiang, E. (Mar. 2008). „Vertical Shearing Instabilities in Radially Shearing Disks: The Dustiest Layers of the Protoplanetary Nebula“. In: *The Astrophysical Journal* 675, pp. 1549–1558 (cit. on p. 35).
- Chiang, E. and A.N. Youdin (2010). „Forming Planetesimals in Solar and Extrasolar Nebulae“. In: *Annu. Rev. Earth Planet. Sci.* 38.1, pp. 493–522 (cit. on p. 18).
- Courant, R., K. Friedrichs, and H. Lewy (1928). „Über Die Partiellen Differenzgleichungen Der Mathematischen Physik“. In: *Math. Ann.* 100.1, pp. 32–74 (cit. on p. 39).
- Crida, Aurélien (Dec. 2006). „Planetary Migration in Solar System Formation“. en. PhD thesis. Université Nice Sophia Antipolis (cit. on p. 49).
- Crida, Aurélien, Frédéric Masset, and Alessandro Morbidelli (2009). „Long Range Outward Migration of Giant Planets, with Application to Fomalhaut b“. In: *ApJ* 705.2 PART 2, pp. 148–152. arXiv: 0910.1004 (cit. on p. 48).
- Dartois, E., A. Dutrey, and S. Guilloteau (Feb. 2003). „Structure of the DM Tau Outer Disk: Probing the Vertical Kinetic Temperature Gradient“. In: *Astronomy and Astrophysics* 399, pp. 773–787 (cit. on p. 15).
- de Val-Borro, M., R. G. Edgar, P. Artymowicz, et al. (May 2006). „A Comparative Study of Disc-Planet Interaction“. In: *MNRAS* 370.2, pp. 529–558 (cit. on p. 54).
- Desch, S. J. (June 2004). „Linear Analysis of the Magnetorotational Instability, Including Ambipolar Diffusion, with Application to Protoplanetary Disks“. In: *The Astrophysical Journal* 608, pp. 509–525 (cit. on p. 30).
- Dipierro, Giovanni, Daniel Price, Guillaume Laibe, et al. (Oct. 2015). „On Planet Formation in HL Tau“. In: *Monthly Notices of the Royal Astronomical Society* 453, pp. L73–L77 (cit. on p. 17).
- Disk Dynamics Collaboration, Philip J. Armitage, Jaehan Bae, et al. (Sept. 2020). „Visualizing the Kinematics of Planet Formation“. In: *arXiv e-prints* 2009, arXiv:2009.04345 (cit. on p. 16).
- Dong, Ruobing, Sheng-Yuan Liu, Josh Eisner, et al. (2018). „The Eccentric Cavity, Triple Rings, Two-Armed Spirals, and Double Clumps of the MWC 758 Disk“. In: *ApJ* 860, p. 124 (cit. on pp. 72, 103).
- Draine, B. T. and H. M. Lee (Oct. 1984). „Optical Properties of Interstellar Graphite and Silicate Grains“. In: *The Astrophysical Journal* 285, pp. 89–108 (cit. on p. 101).

- Dubrulle, B., G. Morfill, and M. Sterzik (Apr. 1995). „The Dust Subdisk in the Protoplanetary Nebula“. In: *Icarus* 114.2, pp. 237–246 (cit. on p. 35).
- Duffell, Paul C, Zoltan Haiman, Andrew I Macfadyen, Daniel J. D’Orazio, and Brian D Farris (2014). „The Migration of Gap-Opening Planets Is Not Locked to Viscous Disk Evolution“. In: *ApJ Lett.* 792.1, p. L10. arXiv: [1405.3711](#) (cit. on pp. 51, 66–68).
- Dullemond, C. P. (2009). *Numerical Fluid Mechanics* (cit. on p. 40).
- Dürmann, Christoph and Wilhelm Kley (2015). „Migration of Massive Planets in Accreting Disks“. In: *A&A* 574, A52. arXiv: [1411.3190](#) (cit. on pp. 51, 66–68).
- (2016). „The Accretion of Migrating Giant Planets“. In: *A&A* 598, A80. arXiv: [1611.01070](#) (cit. on pp. 51, 66).
- Dzyurkevich, Natalia, Neal J. Turner, Thomas Henning, and Wilhelm Kley (Mar. 2013). „Magnetized Accretion and Dead Zones in Protostellar Disks“. In: *The Astrophysical Journal* 765, p. 114 (cit. on p. 30).
- Fromang, Sebastien and Richard P. Nelson (Jan. 2009). „Global MHD Simulations of Stratified and Turbulent Protoplanetary Discs. I. Model Properties“. In: *A&A* 496, pp. 597–608. arXiv: [astro-ph/0606729](#) (cit. on p. 35).
- Fu, Wen, Hui Li, Stephen Lubow, and Shengtai Li (2014). „Long-Term Evolution of Planet-Induced Vortices in Protoplanetary Disks“. In: *ApJ Lett.* 788, p. L41 (cit. on p. 35).
- Fu, Wen, Hui Li, Stephen Lubow, Shengtai Li, and Edison Liang (2014). „Effects of Dust Feedback on Vortices in Protoplanetary Disks“. In: *ApJ Lett.* 795, p. L39 (cit. on p. 35).
- Fukagawa, Misato, Motohide Tamura, Yoichi Itoh, et al. (Apr. 2010). „Subaru Near-Infrared Imaging of Herbig Ae Stars“. In: *Publications of the Astronomical Society of Japan* 62, pp. 347–370 (cit. on p. 13).
- Gaia Collaboration, A. G. A. Brown, A. Vallenari, et al. (Dec. 2020). „Gaia Early Data Release 3: Summary of the Contents and Survey Properties“. In: *arXiv e-prints* 2012, arXiv:2012.01533 (cit. on p. 73).
- Gaia Collaboration, T. Prusti, J. H. J. de Bruijne, et al. (Nov. 2016). „The Gaia Mission“. In: *Astronomy and Astrophysics* 595, A1 (cit. on p. 73).
- Gammie, Charles F. (Jan. 1996). „Layered Accretion in T Tauri Disks“. In: *The Astrophysical Journal* 457, p. 355 (cit. on p. 30).
- Garufi, A., H. Avenhaus, S. Pérez, et al. (Jan. 2020). „Disks Around T Tauri Stars with SPHERE (DARTTS-S). II. Twenty-One New Polarimetric Images of Young Stellar Disks“. In: *Astronomy and Astrophysics* 633, A82 (cit. on p. 15).
- Garufi, A., S. P. Quanz, H. M. Schmid, et al. (Apr. 2016). „The SPHERE View of the Planet-Forming Disk around HD 100546“. In: *Astronomy and Astrophysics* 588, A8 (cit. on p. 14).
- Goldreich, P. and S. Tremaine (Nov. 1979). „The Excitation of Density Waves at the Lindblad and Corotation Resonances by an External Potential“. In: *The Astrophysical Journal* 233, pp. 857–871 (cit. on p. 48).
- (Oct. 1980). „Disk-Satellite Interactions“. In: *The Astrophysical Journal* 241, pp. 425–441 (cit. on pp. 48, 49).
- Grady, C. A., David Devine, B. Woodgate, et al. (Dec. 2000). „STIS Coronagraphic Imaging of the Herbig AE Star: HD 163296“. In: *The Astrophysical Journal* 544, pp. 895–902 (cit. on p. 13).
- Gullbring, Erik, Lee Hartmann, Cesar Briceño, and Nuria Calvet (Jan. 1998). „Disk Accretion Rates for T Tauri Stars“. In: *The Astrophysical Journal* 492, pp. 323–341 (cit. on p. 29).
- Haffert, S. Y., A. J. Bohn, J. de Boer, et al. (June 2019). „Two Accreting Protoplanets around the Young Star PDS 70“. In: *Nature Astronomy* 3, pp. 749–754 (cit. on p. 18).

- Haisch Jr., Karl E., Elizabeth A. Lada, and Charles J. Lada (June 2001). „Disk Frequencies and Lifetimes in Young Clusters“. In: *The Astrophysical Journal Letters* 553, pp. L153–L156 (cit. on p. 29).
- Hammer, Michael, Kaitlin M Kratter, and Min-Kai Lin (Oct. 2017). „Slowly-Growing Gap-Opening Planets Trigger Weaker Vortices“. In: *MNRAS* 466.3, pp. 3533–3543 (cit. on p. 52).
- Hammer, Michael, Paola Pinilla, Kaitlin M. Kratter, and Min-Kai Lin (2018). „Observational Diagnostics of Elongated Planet-Induced Vortices with Realistic Planet Formation Time-Scales“. en. In: *MNRAS* 482.3, p. 3609 (cit. on p. 70).
- Hartmann, Lee, Nuria Calvet, Erik Gullbring, and Paola D’Alessio (Mar. 1998). „Accretion and the Evolution of T Tauri Disks“. In: *The Astrophysical Journal* 495, pp. 385–400 (cit. on p. 29).
- Hayashi, C. (1981). „Structure of the Solar Nebula, Growth and Decay of Magnetic Fields and Effects of Magnetic and Turbulent Viscosities on the Nebula“. In: *Progress of Theoretical Physics Supplement* 70, pp. 35–53 (cit. on p. 48).
- Hersant, F. (2009). „On the Pressure of Collisionless Particle Fluids. The Case of Solids Settling in Disks“. In: *A&A* 502, pp. 385–389. arXiv: 0905.0959 (cit. on p. 32).
- Isella, Andrea, Greta Guidi, Leonardo Testi, et al. (Dec. 2016). „Ringed Structures of the HD 163296 Protoplanetary Disk Revealed by ALMA“. In: *Phys. Rev. Lett.* 117, p. 251101 (cit. on p. 13).
- Jacquet, Emmanuel, Steven Balbus, and Henrik Latter (Aug. 2011). „On Linear Dust-Gas Streaming Instabilities in Protoplanetary Discs: Linear Dust-Gas Streaming Instabilities“. en. In: *Mon. Not. R. Astron. Soc.* 415.4, pp. 3591–3598 (cit. on p. 32).
- Jayawardhana, Ray, Jaime Coffey, Alexander Scholz, Alexis Brandeker, and Marten H. van Kerkwijk (Sept. 2006). „Accretion Disks around Young Stars: Lifetimes, Disk Locking, and Variability“. In: *The Astrophysical Journal* 648, pp. 1206–1218 (cit. on p. 29).
- Jin, Liping (Feb. 1996). „Damping of the Shear Instability in Magnetized Disks by Ohmic Diffusion“. In: *The Astrophysical Journal* 457, p. 798 (cit. on p. 30).
- Kanagawa, Kazuhiro D. and Hidekazu Tanaka (Apr. 2020). „Comments on ‘Type II Migration Strikes Back - an Old Paradigm for Planet Migration in Discs’ by Scardoni et Al.“ In: *Monthly Notices of the Royal Astronomical Society* 494, pp. 3449–3452 (cit. on pp. 67, 68).
- Kanagawa, Kazuhiro D, Takayuki Muto, Satoshi Okuzumi, et al. (2018). *Impacts of Dust Feedback on a Dust Ring Induced by a Planet in a Protoplanetary Disk*. Tech. rep. (cit. on pp. 66, 68).
- Kanagawa, Kazuhiro D, Hidekazu Tanaka, and Ewa Szuszkiewicz (2018). „Radial Migration of Gap-Opening Planets in Protoplanetary Disks. I. The Case of a Single Planet“. In: arXiv: 1805.11101v1 (cit. on p. 67).
- Kataoka, Akimasa, Takashi Tsukagoshi, Munetake Momose, et al. (Oct. 2016). „Submillimeter Polarization Observation of the Protoplanetary Disk around HD 142527“. In: *ApJ Lett.* 831.2 (cit. on p. 72).
- Kepler, M., M. Benisty, A. Müller, et al. (Sept. 2018). „Discovery of a Planetary-Mass Companion within the Gap of the Transition Disk around PDS 70“. In: *Astronomy and Astrophysics* 617, A44 (cit. on p. 18).
- Kley, W. and G. Dirksen (Feb. 2006). „Disk Eccentricity and Embedded Planets“. In: *Astronomy and Astrophysics* 447, pp. 369–377 (cit. on p. 72).
- Kwok, Sun (1975). „Radiation Pressure on Grains as a Mechanism for Mass Loss in Red Giants“. In: *ApJ* 198, pp. 583–591 (cit. on p. 31).

- Lai, Dong and David Tsang (Mar. 2009). „Corotational Instability of Inertial-Acoustic Modes in Black Hole Accretion Discs and Quasi-Periodic Oscillations“. en. In: *MNRAS* 393.3, pp. 979–991 (cit. on p. 69).
- Lambrechts, M. and A. Johansen (Aug. 2012). „Rapid Growth of Gas-Giant Cores by Pebble Accretion“. In: *Astronomy and Astrophysics* 544, A32 (cit. on p. 18).
- Lambrechts, M. and E. Lega (2017). „Astronomy & Astrophysics Reduced Gas Accretion on Super-Earths and Ice Giants“. In: *A&A* 606 (cit. on p. 18).
- Lambrechts, M., E. Lega, R. P. Nelson, A. Crida, and A. Morbidelli (Oct. 2019). „Quasi-Static Contraction during Runaway Gas Accretion onto Giant Planets“. In: *Astronomy and Astrophysics* 630, A82 (cit. on p. 18).
- Lega, E., R. P. Nelson, A. Morbidelli, et al. (Dec. 2020). „Migration of Jupiter Mass Planets in Low Viscosity Discs“. In: *arXiv e-prints* 2012, arXiv:2012.12930 (cit. on p. 71).
- Lesur, Geoffroy and John C B Papaloizou (Apr. 2010). „The Subcritical Baroclinic Instability in Local Accretion Disc Models“. en. In: *A&A* 513, p. 60 (cit. on p. 34).
- Li, Hui, S. A. Colgate, B. Wendroff, and Richard Liska (2001). „Rossby Wave Instability of Thin Accretion Disks. III. Nonlinear Simulations“. In: *ApJ* 551, pp. 874–896 (cit. on pp. 34, 41, 69).
- Li, Hui, J M Finn, R V E Lovelace, and S. A. Colgate (2000). „Rossby Wave Instability of Thin Accretion Disks. II. Detailed Linear Theory“. In: *ApJ* 533.2, pp. 1023–1034 (cit. on pp. 34, 41, 69).
- Lin, D. N. C. and J. Papaloizou (July 1979). „On the Structure of Circumbinary Accretion Disks and the Tidal Evolution of Commensurable Satellites“. In: *Monthly Notices of the Royal Astronomical Society* 188, pp. 191–201 (cit. on pp. 48, 49).
- Lin, D. N. C. and J. C. B. Papaloizou (1993). „On the Tidal Interaction between Protostellar Disks and Companions“. In: pp. 749–835 (cit. on p. 50).
- Lin, Douglas N C and John C B Papaloizou (1986). „On the Tidal Interaction between Protoplanets and the Protoplanetary Disk. Hi. Orbital Migration of Protoplanets“. In: *ApJ* 309, pp. 846–857 (cit. on p. 50).
- Lin, Min-Kai and John C B Papaloizou (2010). „Type III Migration in a Low-Viscosity Disc“. In: *MNRAS* 405, pp. 1473–1490 (cit. on p. 43).
- Liu, Beibei and Jianghui Ji (Sept. 2020). „A Tale of Planet Formation: From Dust to Planets“. In: *arXiv e-prints* 2009, arXiv:2009.02321 (cit. on p. 18).
- Lovelace, R V E, Hui Li, S. A. Colgate, and A F Nelson (1999). „Rossby Wave Instability of Keplerian Accretion Disk“. In: *ApJ* 513, pp. 805–810 (cit. on pp. 34, 41, 69).
- Lyra, Wladimir, Natalie Raettig, and Hubert Klahr (Oct. 2018). „Pebble Trapping Backreaction Does Not Destroy Vortices“. In: *Res. Notes AAS* 2.4, p. 195. arXiv: 1810.07941v1 (cit. on pp. 35, 92).
- Mamajek, Eric E. (Aug. 2009). „Initial Conditions of Planet Formation: Lifetimes of Primordial Disks“. In: 1158, pp. 3–10 (cit. on p. 8).
- Manara, C. F., M. Robberto, N. Da Rio, et al. (Aug. 2012). „Hubble Space Telescope Measures of Mass Accretion Rates in the Orion Nebula Cluster“. In: *The Astrophysical Journal* 755, p. 154 (cit. on p. 29).
- Marcus, Philip S., Suyang Pei, Chung-Hsiang Jiang, and Joseph A. Barranco (Dec. 2016). „Zombie Vortex Instability. II. Thresholds to Trigger Instability and the Properties of Zombie Turbulence in the Dead Zones of Protoplanetary Disks“. en. In: *ApJ* 833.2, p. 148 (cit. on p. 34).

- Marcus, Philip S., Suyang Pei, Chung-Hsiang Jiang, Joseph A. Barranco, et al. (July 2015). „Zombie Vortex Instability. I. a Purely Hydrodynamic Instability to Resurrect the Dead Zones of Protoplanetary Disks“. en. In: *ApJ* 808.1, p. 87 (cit. on p. 34).
- Masset, F. S. (May 2002). „The Co-Orbital Corotation Torque in a Viscous Disk: Numerical Simulations“. In: *Astronomy and Astrophysics* 387, pp. 605–623 (cit. on pp. 43, 49).
- Masset, F. S. and P. Benítez-Llambay (Jan. 2016). „Horseshoe Drag in Three-Dimensional Globally Isothermal Disks“. In: *The Astrophysical Journal* 817, p. 19 (cit. on p. 49).
- Masset, F. S. and J. C. B. Papaloizou (May 2003). „Runaway Migration and the Formation of Hot Jupiters“. In: *ApJ* 588, pp. 494–508 (cit. on p. 49).
- Masset, Frédéric (2000). *FARGO: A Fast Eulerian Transport Algorithm for Differentially Rotating Disks*. Tech. rep., pp. 165–173 (cit. on pp. 41, 42).
- Mathis, John S, William Rumpl, and Kenneth H Nordsieck (1977). „The Size Distribution of Interstellar Grains“. In: *ApJ* 217, pp. 425–433 (cit. on p. 92).
- Mayor, Michel and Didier Queloz (Nov. 1995). „A Jupiter-Mass Companion to a Solar-Type Star“. In: *Nature* 378, pp. 355–359 (cit. on p. 5).
- McClure, M. K., E. A. Bergin, L. I. Cleaves, et al. (Nov. 2016). „Mass Measurements in Protoplanetary Disks from Hydrogen Deuteride“. In: *The Astrophysical Journal* 831, p. 167 (cit. on p. 16).
- McNally, Colin P, Richard P Nelson, Sijme-Jan Paardekooper, and Pablo Benítez-Llambay (Mar. 2019). „Migrating Super-Earths in Low-Viscosity Discs: Unveiling the Roles of Feedback, Vortices, and Laminar Accretion Flows“. en. In: *MNRAS* 484.1, pp. 728–748 (cit. on p. 71).
- Mendigutía, I, J Fairlamb, B Montesinos, et al. (2014). „Stellar Parameters and Accretion Rate of the Transition Disk Star HD 142527 from X-Shooter“. In: *ApJ* 790, pp. 21–29 (cit. on p. 101).
- Mie, Gustav (1908). „Beiträge Zur Optik Trüber Medien, Speziell Kolloidaler Metallösungen“. en. In: *Ann. Phys.* 330.3, pp. 377–445 (cit. on p. 17).
- Mignone, A., G. Bodo, S. Massaglia, et al. (May 2007). „PLUTO: A Numerical Code for Computational Astrophysics“. In: *The Astrophysical Journal Supplement Series* 170, pp. 228–242 (cit. on p. 42).
- Mihalas, Dimitri and Barbara Weibel Mihalas (1984). *Foundations of Radiation Hydrodynamics*. en. Courier Corporation (cit. on p. 22).
- Mittal, Tushar and Eugene Chiang (Jan. 2015). „Fast Modes and Dusty Horseshoes in Transitional Disks“. In: *The Astrophysical Journal Letters* 798, p. L25 (cit. on p. 43).
- Müller, A., M. Keppler, Th. Henning, et al. (Sept. 2018). „Orbital and Atmospheric Characterization of the Planet within the Gap of the PDS 70 Transition Disk“. In: *Astronomy and Astrophysics* 617, p. L2 (cit. on p. 18).
- Murray, C. D. and S. F. Dermott (1999). *Solar System Dynamics* (cit. on p. 43).
- Ohashi, Satoshi, Akimasa Kataoka, Nienke Van der Marel, et al. (July 2020). „Solving Grain Size Inconsistency between ALMA Polarization and VLA Continuum in the Ophiuchus IRS 48 Protoplanetary Disk“. In: *arXiv e-prints* 2007, arXiv:2007.15014 (cit. on p. 102).
- Ono, Tomohiro, Takayuki Muto, Taku Takeuchi, and Hideko Nomura (2016). „Parametric Study of the Rossby Wave Instability in a Two-Dimensional Barotropic Disk“. In: *ApJ* 823, p. 84. arXiv: 1603.09225 (cit. on p. 69).
- Paardekooper, S.-J. (Jan. 2007). „Dust Accretion onto High-Mass Planets“. In: *Astronomy and Astrophysics* 462, pp. 355–369 (cit. on pp. 30, 31).

- Papaloizou, J. C. B. and J. E. Pringle (June 1984). „The Dynamical Stability of Differentially Rotating Discs with Constant Specific Angular Momentum“. In: *Monthly Notices of the Royal Astronomical Society* 208, pp. 721–750 (cit. on p. 25).
- Papaloizou, J. and D. N. C. Lin (Oct. 1984). „On the Tidal Interaction between Protoplanets and the Primordial Solar Nebula. I - Linear Calculation of the Role of Angular Momentum Exchange“. In: *The Astrophysical Journal* 285, pp. 818–834 (cit. on p. 48).
- Pérez, Sebastián, S. Casassus, and P. Benítez-Llambay (Oct. 2018). „Observability of Planet–Disc Interactions in CO Kinematics“. en. In: *Mon Not R Astron Soc Lett* 480.1, pp. L12–L17 (cit. on p. 16).
- Pineda, Jaime E, Judit Szulágyi, Sascha P Quanz, et al. (2019). „High-Resolution ALMA Observations of HD 100546: Asymmetric Circumstellar Ring, and Circumplanetary Disk Upper Limits“. In: *ApJ* 871, p. 48 (cit. on p. 72).
- Pinte, C., F. Ménard, G. Duchêne, et al. (Jan. 2018). „Direct Mapping of the Temperature and Velocity Gradients in Discs - Imaging the Vertical CO Snow Line around IM Lupi“. en. In: *A&A* 609, A47 (cit. on p. 16).
- Pinte, C., G. van der Plas, F. Menard, et al. (July 2019). „Kinematic Detection of a Planet Carving a Gap in a Protoplanetary Disc“. en. In: *ArXiv E-Prints*, arXiv:1907.02538 (cit. on p. 16).
- Pinte, Christophe, François Ménard, Gaspard Duchene, and P. Bastien (2006). „Monte Carlo Radiative Transfer in Protoplanetary Disks“. In: *A&A* 459, pp. 797–804. arXiv: astro-ph/0606550v1 (cit. on p. 91).
- Pinte, Christophe, Daniel J Price, François Ménard, et al. (2018). „Kinematic Evidence for an Embedded Protoplanet in a Circumstellar Disk“. In: *ApJ Lett.* 860, p. L13 (cit. on p. 16).
- Poisson, Siméon Denis (1827). *Mémoires de l'Académie (royale) des sciences de l'Institut (imperial) de France*. French. Vol. T.6(1827). Paris.: Académie royale des sciences, pp. 1–814 (cit. on p. 25).
- Pollack, James B., Olenka Hubickyj, Peter Bodenheimer, et al. (Nov. 1996). „Formation of the Giant Planets by Concurrent Accretion of Solids and Gas“. en. In: *Icarus* 124.1, pp. 62–85 (cit. on pp. 18, 19, 49).
- Price, Daniel J., Nicolás Cuello, Christophe Pinte, et al. (June 2018). „Circumbinary, Not Transitional: On the Spiral Arms, Cavity, Shadows, Fast Radial Flows, Streamers, and Horseshoe in the HD 142527 Disc“. en. In: *MNRAS* 477.1, pp. 1270–1284 (cit. on pp. 70, 72).
- Raettig, Natalie, Hubert Klahr, and Wladimir Lyra (2015). „Particle Trapping and Streaming Instability in Vortices in Protoplanetary Disks“. In: *ApJ* 804, p. 35 (cit. on p. 91).
- Rayleigh, J W (1879). „On the Stability, or Instability, of Certain Fluid Motions“. In: *Proc. Lond. Math. Soc.* 1.1, pp. 57–72 (cit. on p. 27).
- Regály, Zs. and E. Vorobyov (May 2017a). „The Circumstellar Disk Response to the Motion of the Host Star“. In: *A&A* 601, A24 (cit. on pp. 43, 86).
- (Oct. 2017b). „Vortex Stretching in Self-Gravitating Protoplanetary Disks“. In: *MNRAS* 471, pp. 2204–2215 (cit. on p. 43).
- Riols, A. and G. Lesur (Sept. 2018). „Dust Settling and Rings in the Outer Regions of Protoplanetary Discs Subject to Ambipolar Diffusion“. en. In: *Astron. Astrophys.* 617, A117 (cit. on p. 35).
- Robert, C. M. T., H. Méheut, and F. Ménard (Sept. 2020). „Dynamical Signatures of Rossby Vortices in Cavity-Hosting Disks“. en. In: *A&A* 641, A128 (cit. on pp. 69, 96).

- Robert, Clément Mathieu Trisan, Aurélien Crida, Elena Lega, Héloïse Méheut, and Alessandro Morbidelli (Sept. 2018). „Toward a New Paradigm for Type II Migration“. en. In: *A&A* 617, A98 (cit. on pp. 47, 66).
- Scardoni, Chiara E., Giovanni P. Rosotti, Giuseppe Lodato, and Cathie J. Clarke (Feb. 2020). „Type II Migration Strikes Back - an Old Paradigm for Planet Migration in Discs“. In: *Monthly Notices of the Royal Astronomical Society* 492, pp. 1318–1328 (cit. on pp. 67, 68).
- Schaaf, S. A. (1963). „Mechanics of Rarefied Gases“. In: *Handbuch der Physik* 3, pp. 591–624 (cit. on p. 30).
- Schaal, Kevin, Andreas Bauer, Praveen Chandrashekar, et al. (Nov. 2015). „Astrophysical Hydrodynamics with a High-Order Discontinuous Galerkin Scheme and Adaptive Mesh Refinement“. In: *Monthly Notices of the Royal Astronomical Society* 453, pp. 4278–4300 (cit. on p. 69).
- Shakura, N. I. and R. A. Sunyaev (June 1973). „Black Holes in Binary Systems. Observational Appearance.“ en. In: *A&A* 500, p. 33 (cit. on p. 30).
- Stolker, T., C. Dominik, M. Min, et al. (Dec. 2016). „Scattered Light Mapping of Protoplanetary Disks“. In: *A&A* 596, A70 (cit. on p. 14).
- Stone, James M., Kengo Tomida, Christopher J. White, and Kyle G. Felker (July 2020). „The Athena++ Adaptive Mesh Refinement Framework: Design and Magnetohydrodynamic Solvers“. In: *The Astrophysical Journal Supplement Series* 249, p. 4 (cit. on p. 42).
- Surville, Clément, Lucio Mayer, and Douglas N C Lin (2016). „Dust Capture and Long-Lived Density Enhancements Triggered by Vortices in 2D Protoplanetary Disks“. In: *ApJ* 831, p. 82. arXiv: [1601.05945](https://arxiv.org/abs/1601.05945) (cit. on p. 35).
- Tanga, Paulo, A. Babiano, and B. Dubrulle (May 1996). „Forming Planetesimals in Vortices“. In: *Icarus* 121.1, pp. 158–170 (cit. on pp. 34, 70).
- Teague, Richard, Jaehan Bae, Edwin A. Bergin, Tilman Birnstiel, and Daniel Foreman-Mackey (June 2018). „A Kinematical Detection of Two Embedded Jupiter-Mass Planets in HD 163296“. en. In: *ApJL* 860.1, p. L12 (cit. on pp. 16, 72).
- Teague, Richard and Daniel Foreman-Mackey (Sept. 2018). „A Robust Method to Measure Centroids of Spectral Lines“. en. In: *Res. Notes Am. Astron. Soc.* 2.3, p. 173 (cit. on p. 16).
- Toomre, Alar (1964). „On the Gravitational Stability of a Disk of Stars“. In: *ApJ* 139, p. 1217 (cit. on p. 25).
- Turk, Matthew J (2013). „How to Scale a Code in the Human Dimension“. In: arXiv: [1301.7064v1](https://arxiv.org/abs/1301.7064v1) (cit. on p. 110).
- Turk, Matthew J., Britton D. Smith, Jeffrey S. Oishi, et al. (Jan. 2011). „Yt: A Multi-Code Analysis Toolkit for Astrophysical Simulation Data“. en. In: *ApJ Suppl. Ser* 192.1, p. 9 (cit. on p. 111).
- van der Marel, Nienke, P. Pinilla, J. Tobin, et al. (Sept. 2015). „A Concentration of Centimeter-Sized Grains in the Ophiuchus IRS 48 Dust Trap“. In: *The Astrophysical Journal Letters* 810, p. L7 (cit. on p. 102).
- van der Marel, Nienke, Ewine F. van Dishoeck, Simon Bruderer, et al. (June 2013). „A Major Asymmetric Dust Trap in a Transition Disk“. In: *Science* 340, pp. 1199–1202 (cit. on pp. 102, 103).
- Wafflard-Fernandez, Gaylor and Clément Baruteau (Feb. 2020). „Intermittent Planet Migration and the Formation of Multiple Dust Rings and Gaps in Protoplanetary Disks“. In: *Monthly Notices of the Royal Astronomical Society* 493, pp. 5892–5912 (cit. on p. 49).
- Ward, W. R. (Mar. 1982). „Tidal Barriers in the Solar Nebula“. In: 13, pp. 831–832 (cit. on p. 50).

- Ward, William R. (Apr. 1997a). „Protoplanet Migration by Nebula Tides“. In: *Icarus* 126, pp. 261–281 (cit. on p. 49).
- (June 1997b). „Survival of Planetary Systems“. In: *The Astrophysical Journal Letters* 482, pp. L211–L214 (cit. on p. 49).
- Wardle, Mark and Cindy Ng (Feb. 1999). „The Conductivity of Dense Molecular Gas“. In: *Monthly Notices of the Royal Astronomical Society* 303, pp. 239–246 (cit. on p. 30).
- Weidenschilling, S. J. (July 1977). „Aerodynamics of Solid Bodies in the Solar Nebula“. In: *Monthly Notices of the Royal Astronomical Society* 180, pp. 57–70 (cit. on pp. 17, 48).
- Whipple, F. L. (1972). „On Certain Aerodynamic Processes for Asteroids and Comets“. In: p. 211 (cit. on p. 32).
- Wilkinson, Mark D., Michel Dumontier, IJsbrand Jan Aalbersberg, et al. (Dec. 2016). „The FAIR Guiding Principles for Scientific Data Management and Stewardship“. en. In: *Sci. Data* 3.1 (cit. on p. 110).
- Zhu, Zhaohuan and Clément Baruteau (June 2016). „Gas and Dust Hydrodynamical Simulations of Massive Lopsided Transition Discs – I. Gas Distribution“. In: *MNRAS* 458.4, pp. 3918–3926 (cit. on p. 43).
- Zsom, Andras, Chris Ormel, Juergen Blum, Carsten Guettler, and Cornelis Dullemond (May 2010). „The Outcome of Protoplanetary Dust Growth: Pebbles, Boulders or Planetesimals?“. In: 12, p. 2966 (cit. on p. 17).

List of Figures

1.1	A geometric definition of the inclination angle.	6
1.2	A schematic view of the transit detection method for exoplanets.	7
1.3	A chart of 1469 confirmed extra-solar planets categorized by detection techniques.	7
1.4	The four stages of stellar formation, as defined by the SED	9
1.5	Probability density distribution of the inclination angle in a sample of 208 disks.	10
1.6	A graphic representation of the immediate infra-red sub-domains of the electromagnetic spectrum	11
1.7	The disk around HL Tau as observed with ALMA and presented by ALMA Partnership et al. (2015)	12
1.8	A brief history of continuum imaging of the disk around HD 163296	13
1.9	Resolved rings and clumps seen in the continuum, from the DSHARP survey.	13
1.10	Examples of polarized intensity maps.	14
1.11	The dichotomy and complementarity of observational techniques, illustrated for the disk around DoAr25.	15
1.12	A first candidate for indirect detection of a forming planet via gas dynamics measurements in an individual velocity channel.	16
1.13	Mass growth of a forming giant planet over time in the runaway accretion model.	19
2.1	A transition from laminar to turbulent flow in the plume of a candle.	24
2.2	Stability of orbital motion of a fluid element.	27
2.3	Relative drag intensity in three models as a function of the $\delta v/v_{\text{th}}$ ratio.	31
2.4	Radial drift of solids VS pressure gradients.	33
2.5	A schematic representation of rotational balance in a vortex.	34
2.6	A schematic view of an anti-cyclonic vortex represented in polar coordinates.	35
2.7	A schematic representation of inclination dampening as a result of drag forces (red).	36
3.1	A schematic representation of a pathological case of discrete advection of a scalar field w over time step δt of maximal duration.	39
4.1	Surface density in 2D simulations as perturbed by a small mass planet and a gap-opening large mass planet	48
4.2	A schematic representation of angular momentum exchanges between gas and a planet.	50
4.3	Force diagrams for the three main actors in a simulation.	52
4.4	Two distinct asymptotical migration regimes depending on the disk/planet mass ratio.	67
4.5	A semi-analytical model for type II migration developed in K18 against previously obtained results.	68

5.1	A 2D simulation of the Kelvin-Helmholtz instability.	70
5.2	Lopsided structures seen in the thermal radiation of weakly inclined disks. . .	72
5.3	Usual suspects: a spatially organized list of vortex candidates.	73
5.4	A “battleship” inspired representation of the naming convention I used to explore the resolution parameter space.	86
5.5	The effect of resolution/numerical viscosity on numerical convergence of rotationally unstable setups.	87
5.6	A time-series of normalized density and κ^2 in a rotationally unstable vortex. .	88
5.7	Vortex migration against diffusivity in the numerical setup.	89
5.8	Observational signature compatible with that of a vortex in HD 142527. . . .	90
5.9	Effect of flux-weighted beam dilution on the detected velocity.	90
6.1	Concurrent evolution of gas and dust density distributions through a Rossby vortex coalescence.	94
6.2	vac2fost’s control flow.	99
6.3	Three dust rebinning strategies in vac2fost.	100
6.4	A schematic view of MCFOST’s workflow.	101
6.5	A comparative view of continuum imaging against dust-binning mode (DBM). .	104
6.6	Similar to fig. 6.5, but this time comparing the two models with back-reaction (a) and without it (b), at $t/t^* = 100$	105
6.7	Polarized emission at $\lambda = 512 \mu\text{m}$ for the model without back-reaction, at $t/t^* = 100$	107
6.8	Same as fig. 6.7, at $\lambda = 512 \mu\text{m}$	107
7.1	Slice plots for an extremely high resolution 3D jet flow simulation.	112
7.2	A flowchart representation of a typical workflow with Yt	113
7.3	An illustrative case of space-filling Z-curve (Morton indexing) in 2D across 3 levels in resolution refinement. Each cell is uniquely labelled following the Morton indexing (x, y, level).	114
7.4	A sketch of how AMRVAC’s data file is mapped to linear disk memory, represented here as a ribbon.	115

List of Tables

0.1	Common notations and definitions used throughout the thesis.	3
3.1	A table of non-cartesian geometries and dimensionalities available in AMRVAC.	45

Colophon

This thesis was typeset with $\text{\LaTeX}2\epsilon$. It uses the *Clean Thesis* style developed by Ricardo Langner. The design of the *Clean Thesis* style is inspired by user guide documents from Apple Inc.

Download the *Clean Thesis* style at <http://cleanthesis.der-ric.de/>.

